NANOMATERIAL MODIFIED ELECTRODES: OPTIMIZATION OF VOLTAMMETRIC SENSORS FOR PHARMACEUTICAL AND INDUSTRIAL APPLICATION

RORY DENNIS BRIMECOMBE

NANOMATERIAL MODIFIED ELECTRODES – OPTIMIZATION OF VOLTAMMETRIC SENSORS FOR PHARMACEUTICAL AND INDUSTRIAL APPLICATION

A thesis submitted in fulfillment of the requirements of the degree of

DOCTOR OF PHILOSOPHY

of

RHODES UNIVERSITY

By

RORY DENNIS BRIMECOMBE

January 2011

ABSTRACT

Nanomaterials, in particular carbon nanotubes have been shown to exhibit favourable properties for the enhancement of electrochemical detection of target analytes in complex matrices. There is however scope for improvement in terms of the optimization thereof in electrochemical sensors surface modification. The aim of this thesis was to examine methods that would result in increased current response, lowered passivation and application of such modified surfaces with application to pharmaceutically and industrially relevant analytes.

Current methods for enhancing the performance of carbon nanotubes include acid functionalization which not only increases the hydrophilicity of the nanotubes, and consequently their ability to provide stable (aqueous) suspensions, but also introduces electrochemically active sites. This particular approach is however not normalized in the literature. Over-exposure to acid treatment results in loss of structural integrity of the carbon nanotubes, and as such a fine balance exists between achieving these dual outcomes. Guided by high resolution scanning electron microscopy, atomic force microscopy, voltammetric and impedance studies, this thesis examined the role of the length of time of the acid functionalization process as well as the impact of activation of carbon nanotubes and fullerenes on electrochemical sensor performance. Based on desired charge transfer resistances, rate transfer coefficients and sensitivity towards redox probes the optimal length of acid functionalization for multi-walled carbon nanotubes was 9 hours and 4 hours for single-walled carbon nanotubes. Further improvements in the desired outcomes were achieved through electrochemical activation of the modified electrode surface by cycling in the presence of catechol, in a novel approach. By employing electrochemical impedance spectroscopy it was observed that catechol activation resulted in lowered charge transfer resistance, before and after activation, with functionalized multi-walled carbon nanotubes (9 hours) exhibiting the greatest decrease of 90 % and functionalized single-walled carbon nanotubes (4 hours), a 50 % decrease. Corresponding increases in the heterologous rate transfer coefficient showed a 770 % increase for functionalized multi-walled carbon nanotubes (9 hours), following catechol activation. Comparative observations for fullerenes following partial reduction in potassium hydroxide yielded a 30 % decrease in charge transfer resistance, with an increased heterologous rate transfer coefficient at a fullerene modified surface.

The performance of the nanomaterial modified electrodes was applied to the detection of wortmannin with applications in bioprocess control and in the pharmaceutical sector as well as to the detection and monitoring of the industrial dye Reactive red. Of particular relevance to these analytes was the assessment of the nanomaterial modified electrodes for enhanced stability, reproducibility, sensitivity and decreased passivation effects.

In this study the first known account of wortmannin detection through electrochemical methods is reported. Voltammetric characterization of wortmannin revealed an irreversible cathodic process with a total number of 4 electrons and a diffusion coefficient of 1.19×10^{-7} $cm^2.s^{-1}$. At a functionalized multi-walled carbon nanotubes modified glassy carbon electrode a limit of detection of 0.128 $nmol.cm^{-3}$ was obtained, and with limited surface passivation the detection scheme afforded pertinent analyses in biological media representing a substantial improvement over chromatographic detection methods. This study also provided the first account of the voltammetric detection of reactive red, competing favourably with traditional spectroscopic methods for monitoring biodegradation of this compound in real time.

ACKNOWLEDGEMENTS

First and foremost, my sincerest gratitude goes to my Supervisor: Professor Janice Limson, who has been with me every step of the way and has helped nurture my love for diagnostics and sensors, for being there since the commencement of my postgraduate career, and for the work put into making this project a success. Thank you.

To my family, the Brimecombes (Mom, Dad, Gerald, Monique), thank you for being the support and guidance that I have required throughout, for instilling a sense of pride and perseverance, I am forever indebted.

To the Moore family I extend a special thank you, in particular Robin and Ron Moore. You have been my second family, thank you for your support and care. I am forever grateful for the supporting role you played throughout my PhD.

To Jo Burgess I would like to say a special thank you for everything from feeding my fascination with bioreactors, being supportive and proofreading this dissertation, to being a dear friend.

To the laboratory mates of the Biosensor Research Group: Ronen, Shane, Michael, Steve (Shaun), Kelly-Ann, Mary, and all the rest that spent some time in the group.

To the Biochemistry, Microbiology and Biotechnology Department of Rhodes University I extend my gratitude for the years of nurturing and support. Prof Dorrington: thank you for pushing me to getting my Honours application on your 'desk before 5' – thank you for recognizing my passion before I knew about it.

To Mintek, South Africa, thank you for the employment and training me on the HRSEM. In addition thank you for allowing me to nurture my fascination with nanotubes by using the HRSEM. A special word of thanks to Robert Tshikhudo, who saw potential in me during his visits and offered me employment in the fascinating field of electrochemical sensor diagnostics. To my colleagues at Mintek, thank you.

To the National Research Foundation, the Ernst and Ethel Trust fund, Rhodes University and Messel for the scholarships and bursaries acquired during the course of this PhD.

To Dr Peter Clayton, Prof John Duncan, Mr John Gillam and Dr Steve Fourie for playing critical roles during the course of my PhD studies. Thank you for your support, effort and guidance.

To my Grahamstown friends, Clint and Jo de la Mare (and all the related Gtownians), Pierre du Plessis, Michelle Coupé, Greg Short, Michelle and Shaun Bradfield, The Bosch Brothers, Garth Cambray, I say thank you for all the special memories and laughs.

To my Rhodes and Vtown friends, Peter Cromberge, Richard Chapman, Chris Thurman, Terrence Allwright, Mark Neville, Neil Coetzee, Quinton Knoetze: Thank you for the memories, laughs and support.

To Prof P. Ajayan, Professor Inaki Mondragon, thank you for permission to re-publish your images, and to Dr. Jeremy Knapp, and Jeffrey Hays thank you for sending me images.

To the examiners of this script, thank you for taking the time and effort to read and examine this work, and in good time. I appreciate it.

And a final big thank you to my life partner Bronwyn Moore, who has been everything from the PhD widow to the sounding board to my friend and my partner. Thank you for the work you did in helping me get through this dissertation, the editing and the moral support. I do and always will appreciate it.

TABLE OF CONTENTS

CHAPTER 4

LIST OF ABBREVIATIONS AND SYMBOLS

In alphabetical order:

°C	Degrees Celsius
A	Amperes
Ω	Ohm
%	Percentage
2,4-DMA	2,4-Dimethylaniline
3-MBQ	3-methyl-*o*-benzoquinone
A	Surface area
AA	Ascorbic Acid
AC	Alternating current
AE	Auxiliary electrode
AFM	Atomic force microscopy
Ag|AgCl	Silver|Silver chloride
ATP	Adenosine-5'-triphosphate
a.u	Arbitrary units
b	Tafel slope
BAS	Bioanalytical Systems
BF	Bisoprolol fumarate
BR	Britton Robinson
BSE	Back-scattered electrons
C	Concentration
C_{60}	Fullerene
$C_{60\text{-}ACT}$	Activated fullerene
C_{DL}	Double layer capacitance
CE	Counter electrode
Cm	Centimetre
CNTs	Carbon nanotubes
CPE	Constant phase element
CSTR	Continuously stirred tank reactor
CV	Cyclic voltammetry
CVD	Chemical vapour deposition
D	Diffusion coefficient
D	Dissipation
DCC	Dicyclohexylcarbodiimide
DCM	Dichloromethane
dH_20	Distilled water
DMF	Dimethylformamide
DSMZ	Deutsche Sammlung von Mikroorganismen und Zellkulturen
E	Potential
EC	Electrochemical Chemical
ECE	Electrochemical Chemical Electrochemical
ECP	Electrochemical Pretreatment
EDC	Endocrine disrupting compound
E_f	Final potential
E_i	Initial potential
EIP	Electrochemically irreversible process
EIS	Electrochemical Impedance Spectroscopy
E_{pa}	Anodic peak potential
E_{pc}	Cathodic peak potential
EPGE	Edge plane pyrolytic graphite electrode
EQP	Electrochemical quasi-reversible process
ERP	Electrochemically reversible process
ES	Electrochemical sensor

EST	Electrochemical sensor technology
f	Frequency
*f*CNT	Functionalised carbon nanotube
FDA	Food and Drug Administration
FET	Field-effect transistors
FMA	Ferromethylamine
FRA	Frequency response analyser
GC	Gas chromatography
GCE	Glassy carbon electrode
GLU	Glucose
GPES	General purpose electrochemical system
H_2SO_4	Sulphuric acid
HIV	Human immunodeficiency virus
HiVac	High vacuum
HNO_3^-	Nitric acid
HOPG	Highly ordered pyrolitic graphite
HPLC	High performance liquid chromatography
HRSEM	High resolution scanning electron microscopy
HV	High voltage
HV	Hydrodynamic voltammetry
Hz	Hertz
I	Current
IC	Inhibitory concentration
I_{pa}	Anodic current
I_{pc}	Cathodic current
k_{app}	Electron transfer efficiency
K	Kelvin
KCl	Potassium chloride
KOH	Potassium hydroxide
LAC	Laccase
LBL	Layer by layer
LiP	Lignin peroxidase
Ln	Natural logarithm
LOD	Limit of detection
Log	Logarithm
LSV	Linear sweep voltammetry
LYS	Lysine
M	Molarity
m/v	Mass per volume
MnP	Manganese-dependent peroxidase
MS	Mass spectroscopy
mV	Millivolts
MWCNTs	Multi-walled carbon nanotubes
NaOH	Sodium hydroxide
Nm	Nanometer
NME	Nanomaterial-modified electrode
NNLS	Non-linear least squares
O	Oxidant
OH	Hydroxyl
OSWV	Osteryoung square wave voltammetry
PAH	Polyaromatic hydrocarbon
PDA	Potato dextrose agar
PI3-k	Phosphoinositide 3-kinase
POC	Point of care
r	Radius
R	Reactant
R_Ω	Polarisation resistance
R 2	Correlation coefficient
R_{ct}	Charge transfer resistance
RDE	Rotating disk electrode
RDS	Rate determining step
RE	Reference electrode
RLS	Rate limiting step
Rms	Root mean squares

R_p	Polarisation resistance	TLD	Through-lens detector
RPM	Revolutions per minute	TMB	Tetramethylbenzidine
RR	Reactive Red	UA	Uric Acid
SABS	South African Bureau of Standards	UV-O	Ultra violet ozone
SD	Standard deviation	UV-VIS	Ultra violet-visible
SDS	Sodium dodecyl sulphate	V	Volt
STM	Scanning Tunneling Microscopy	v/v	Volume per volume
STP	Standard temperature and pressure	WE	Working electrode
SV	Staircase Voltammetry	Z	Impedance
SWCNTs	Single-walled carbon nanotubes	Z_W	Warburg impedance
TBA^+	Tetra-*n*-butylammonium		
TCA	Tricarboxylic Acid		

LIST OF EQUATIONS

[2.01] $$E = E^{\circ} - \frac{0.05916\,V}{n}\log_{10}\quad\frac{[R]}{[O]}$$

[2.02] $$I_p = (2.99\ \times 10^5)n[(1-\alpha)n]½A.c.(Dv)½$$

[2.03] $$\Delta E_p = E_{o'} - \frac{RT}{\alpha nF}\left[0.78 - ln\left(\frac{k_o}{D^{½}}\right)\times\left(1+\frac{\alpha nF}{RT}\right)^{½}\right]$$

[2.04] $$\Delta m = -C \times \Delta f$$

[3.01] $$I_{pa} = 2.69 \times 10^5 . n^{3/2} . A . C_o . D^{½} v^{½}$$

[3.02] $$\%\ S.D = \frac{S.D}{Average\ I_p}\times 100$$

[3.03] $$R\ (\%) = 100 - \%\ S.D$$

[3.04] $$LOD = \ 3\ (S.D/m)]$$

[3.05] $$\Gamma = \frac{Q}{nFA}$$

[4.01] $$R_{ct} = (R_{\Omega} - R_s)$$

[4.02] $$k_{app} = \frac{R.T}{F^2 A.C.R_{ct}}$$

[4.03] $$C_{calc} = \ (Y_o R_{ct})^{\ 1/\alpha}/R_{ct}$$

[5.01] $$b = 2\left(\frac{\delta E_{pc1}}{\delta log v}\right)$$

[5.02] $$b = 2.303\ \frac{R\,T}{F\alpha n_a}$$

[5.03] $$I_{pc} = 2.98 \times 10^5 n_t (\propto n_a)^{½} A D^{½} C v^{½} \ (at\ 298K)$$

[5.04] $$E_p = E_0 + \frac{RT}{\alpha nF}\left[ln\left\{\frac{RTk_s}{\alpha nF}\right\} - lnv\right]$$

[5.05] $$-\frac{RT}{\alpha n_a F} = slope\ (of\ a\ plot\ of\ E_{pc} vs.\ lnv)$$

[5.06] $$E_p - E_{\frac{p}{2}} = \frac{47.7}{\alpha n_a}$$

[5.07] $$k_s = \frac{\alpha n_a F}{RT} e^{\frac{\alpha nF}{RT}(E_p - E_o)}$$

[5.08] $$E_p = E_o' + \left(\frac{RT}{\alpha n_a F}\right)\left[0.780 + ln\left(\frac{D_R^{½}}{k_o}\right) + \ln\left(\frac{\alpha n_a F v}{RT}\right)½\right]$$

[5.09] $$D^{½} = k_o e^{\left(\frac{\alpha nF}{RT}[Intercept - E_o'] - 0.780 - ½ln(\alpha n_a F) + ½ln(RT)\right)}$$

[5.10] $$I_{pc} = 0.620 nFAD^{⅔}\omega^{½} C\mathrm{v}^{-}$$

[7.01] $$Decolorisation\ extent\ (\%) = \left(\frac{OD_1 - OD_t}{OD_1}\right) x\ 100$$

LIST OF FIGURES

LIST OF SCHEMES

LIST OF TABLES

CHAPTER 1

OVERALL SYNOPSIS AND OBJECTIVES

"Even if I knew that tomorrow the world would go to pieces, I would still plant my apple tree"

– Martin Luther King Jr

1.1 Synopsis

Process biotechnology is an ever expanding field that searches to address market related demands for the development of improved products and sustainable systems. The applications of process biotechnology are diverse, ranging from pharmaceutical, industrial as well as environmental. Cutting edge research has resulted in many fundamental breakthroughs, which have led to the demand for accurate measurement and control systems, to allow for compliance with stringent validation and accreditation regulations. These requirements have directly impacted on the demand for accurate and sensitive diagnostic systems.

The challenges with current and traditional diagnostic approaches are predominantly based on overcoming interferences that co-exist with the target analyte in complex matrices, lowering the response time of the diagnostic, reducing operator involvement, and in some cases, developing a diagnostic that can be utilised in the field by an untrained person.

Electrochemical sensor technology (EST) has shown promise for being inherently sensitive, capable of detecting a target analyte in a complex matrix even under turbid conditions. Additionally, EST has allowed for less operator involvement through a lowered requisite for sample pretreatment, a significant advantage for the development of in-line monitoring technology. The ability to miniaturise the analytical recognition interface has further resulted in the development of diagnostics technology that is portable.

Real time monitoring of a target analyte can be performed either as a quantitative or qualitative assessment. The incorporation of EST provides useful information on the state, concentration and nature of a target analyte; as well as the effects external conditions have on its stability, whether the intention is to synthesise the target analyte (such as in pharmaceutical bioprocessing) or degrade it (such as in environmental bioremediation).

While EST offers promise as a dynamic alternative, significant scope remains for optimisation as well as overcoming challenges such as electrode surface passivation, enhancement of sensitivity and optimisation of environmental parameters. A continuous search for improved methods and materials that could overcome the aforementioned challenges pertaining to sensor development therefore ensues. Nanomaterials, in particular: carbon nanotubes and C_{60} fullerenes have shown unmatched promise as electrode materials for incorporation into EST. The attraction of using these nanomaterials is based on taking advantage of their enhanced conductive properties, as well as their capacity to increase surface areas significantly given their nano size. These properties afford greater sensitivities as well as enhanced reproducibility and reusability. Many applications of utilising these nanomaterials have recently been published; however extensive fundamental studies are in demand and are required in order to better understand their behavioural characteristics and ultimately utilise these materials to their capacity.

Properties of nanomaterials of particular interest in this study were the effect of material modification, doping and immobilisation onto an electrode surface. Visualisation of the nanomaterials was examined through using high resolution scanning electron microscopy (HRSEM) and atomic force microscopy (AFM).

This study therefore serves to gain a better understanding of nanomaterials for use as electrode materials. Additionally, the performance of electrodes modified with nanomaterials was assessed through their utilisation as a diagnostic for target analytes representative of 2 different prominent sectors, namely: pharmaceutical and environmental. These are highlighted.

<u>Case study 1: Pharmaceutical sector. Target analyte: Wortmannin</u>

Wortmannin, a secondary metabolite biosynthesised by many fungal species, is being examined in medical research as a potent anticancer agent given its ability to inhibit key targets involved in tumour formation. Its laboratory-based synthesis is typically through batch mode fermentation. Biosynthesis of wortmannin in a fed-batch or continuous manner is possible, however at present no monitoring system is available that can continuously provide feedback of the concentration of wortmannin in the biological

system. Biological studies of wortmannin are also complicated by operational challenges, such as the diagnostic difficulties afforded by potential coexisting compounds that could ultimately interfere with analyses, the most rational solution being pretreatment of the sample, an approach that is not feasible for continuous monitoring systems. The challenge is further compounded by the relative instability of wortmannin in biological growth media, attributed in literature to be pH sensitive. The voltammetric detection of this compound has thus resulted from an inherent real world demand for a sensor that is capable of quantitative monitoring of wortmannin in regular intervals. Recent discoveries regarding the apparent superior conductive and electrocatalytic properties of nanomaterials has further motivated their utilisation in this study as a possible means of wortmannin detection in complex matrices, as a potential model sensor surface for future concomitant studies.

Case study 2: Industrial and environmental sector. Target analyte: Reactive red dye

One of the key applications for biosensors is within the industrial and environmental sector. Of particular relevance is the biodegradation of harmful industrial effluent contaminants. Bioremediation strategies aimed at achieving the biodegradation of these toxins is reliant on efficient sensing technology to not only confirm degradation intermittently but also to provide insight into the process through continuous monitoring. Since such analyses require detection within complex matrices such as those typically found in the biological reactors, there is a need for analytical tools such as EST which can potentially circumnavigate many of the concerns associated with traditional spectroscopic and HPLC based sensing tools. In this study, the voltammetric detection of the biodegradation of the industrial dye Reactive red by *Pleurotus ostreatus* was examined.

The overarching goal of this thesis was to explore the application and enhancement of electrochemical sensor technology, through the utilisation of nanostructured materials, for the improved detection and monitoring of the fate of the aforementioned target analytes of particular real world application. Chapter 2 provides an overview of the literature. Chapter 3 provides a brief outline of the experimental approach common to most of the work, with specific methodologies outlined in the relevant chapters. Chapter 4 focuses on the effects of treatment and modification of the nanostructured materials. Chapter 5 is a fundamental electroanalysis of wortmannin since this is the first account of its electrochemical detection. Chapter 6 applies nanostructured modified electrodes (NMEs) to the

detection of wortmannin. Chapter 7 focuses on an assessment of the feasibility of NMEs for the detection of actual effluent samples obtained from a local tannery containing Reactive red (RR), and subsequently electrochemically monitor the fate of RR in a bioreactor inoculated with *P. ostreatus*. Chapter 8 summarises the outcomes and suggestions for future possibilities are highlighted.

CHAPTER 2

INTRODUCTION

"I don't know how to do this on a small scale in a practical way, but I do know that computing machines are very large; they fill rooms. Why can't we make them very small, make them of little wires, little elements---and by little, I mean <u>little</u>"

– Richard Feynman (There's plenty of room at the bottom speech, 1959)

2.1 Electrochemical diagnostics

With the advancement in information technologies has come a demand for real time and constant feedback regarding the status of systems affecting various aspects of our daily activities. Accordingly, feedback is required rapidly and without the technology being confined to a laboratory or requiring professional interpretation. In many instances sensors are required to react to conditions where human input is not required, such as those found in the breaking and steering systems of many vehicles.

Sensors, in particular: electrochemical sensors (ES), are rapidly being recognised in many sectors due to their track record of comparable sensitivity, selectivity, reproducibility as well as being capable of integration into a wide range of applications. What is predominantly in the favour of ES is the capacity to miniaturise the technology which is highly sought after for the development of portable sensor technology. Additionally, ES have been of particular interest due to the array of possibilities that can be incorporated into solving many challenges of traditional techniques (such as reducing the effects of co-existing interferents) and subsequently achieving greater selectivity, and sensitivity with smaller error margins.

The ES market has been dominated by the glucose biosensor since its initial introduction by Clark in 1956. In 2008 it was estimated that by 2012 the electrochemical biosensor industry, which then comprised at least 90 % of the sensor market, would be worth $6.1 billion, predominantly invested in blood glucose biosensors. Analysts have attributed the glucose biosensor monopoly to technology transfer limitations as a result of the cost of sensor research and development and to the intrinsic technical barriers that exist in sensor development (Luong *et al.*, 2008).

Even though the third generation of sensors was dominated by glucose biosensors, the first and second generations are largely geared towards a wider range of electrochemical biosensors and chemosensors. Highly sensitive real time and continuous monitoring and detection for incorporation in health and food, environmental, industrial processes, defence as well as quality assurance are key areas and factors that are being addressed in the new generation of sensing devices.

In healthcare, ES are predominantly comprised of point of care (POC) diagnostics such as those used for rapid screening and early disease detection (HIV) as well as routine analyses (blood glucose and cholesterol levels). In the environmental sector ES are being integrated into the in-*situ* detection of, for instance, endocrine disrupting compounds (EDCs) (Wang *et al.*, 2005; Xia *et al.*, 2010) in drinking water as well as monitoring the efficacy of bioremediation attempts of polyaromatic hydrocarbon (PAH) contaminated soil. In the industrial (process) sector, ES are being utilised to monitor and qualitatively assess the real time synthesis of a desired product, such as organic acids or enzymes. In defence ES are being utilised to detect biowarfare agents (Pohanka *et al.*, 2007) such as anthrax or landmines, with many ES being installed into airports for the detection of an array of banned and dangerous substances. In sport and recreation ESs are being used to detect performance enhancing steroids or drug abuse. Presently sensors are being used in environmental monitoring (Dennison & Turner, 1995), health care (Alcock & Turner, 1994), food, defence, as well as in the process industry (White & Turner, 1997).

Electrochemical sensors rely on the redox activity of a target analyte. A variety of electrochemical techniques exist, such as potentiometric, amperometric and coulometric. The choice of which electrochemical technique to adopt is based on knowledge of the analyte of interest as well as related contributing factors notwithstanding the desired outcome.

A conventional ES consists of a working electrode (WE) where the target analyte recognition occurs, and is accompanied by an auxiliary electrode (AE) and a reference electrode (RE). Typical WE surfaces include glassy carbon, gold and platinum. The modification of WE surfaces enhances sensitivity and selectivity, and decreases the effects of interferents with a rich source of modifiers (synthetic or natural), and with a plethora of immobilisation strategies. The utilisation of nanostructured materials (SW- , MWCNTs and C_{60} fullerenes) have been the subject of intense research activity in recent years and will be discussed further here.

2.2 Introduction to Carbon Nanotubes

Carbon nanotubes (CNTs) have received a considerable amount of attention given their unique structural, electronic, chemical, mechanical and functional properties (Odom, 1998; Ajayan, 1999;

Baughman *et al.*, 2002). In addition, CNTs (inclusive of other carbon analogues such as fullerenes) are renowned for their rapid reaction rate and high degree of stability in each of the redox states (Jehoulet *et al.*, 1991; Campbell *et al.*, 1999; Gavalas & Chaniotakis, 2000; Marken *et al.*, 2001; Nugent *et al.*, 2001; Sotiropoulou & Chaniotakis, 2003; Vamvakaki *et al.*, 2006; Vamvakaki & Chaniotakis, 2007).

In a publication in 1991, Iijima described multi-walled carbon nanotubes (MWCNTs), however it was only in 1993 that single-walled carbon nanotubes (MWCNTs) were first documented (Iijima, 1993). It remains contentious as to whether Iijima in 1991, pioneered the first visualisation of carbon nanotubes (His publication in *Nature* in 1991 is cited by many journal articles and reports as being the first documented account of the description of nanotubes). In 1978 Peter Wiles and John Abrahamson visualised, using a transmission electron microscope, carbon fibres and crystallites between 4 and 100 nm in diameter, observed on carbon and graphite anodes following low current arc operation under nitrogen atmosphere (Wiles & Abrahamson, 1978). What is indisputable is the novel account made by Iijima on the different helical arrangements of these nanotubes (figure 2.1) (Iijima, 1991; 1993). The significance of this discovery is the basis on which sensor surface fabrication is based, as helicity in conjunction with nanotube diameter determine the properties of the carbon nanotube (Ajayan, 1999).

2.2.1 Properties of Carbon Nanotubes

Carbon nanotubes (CNTs) are sheets of graphene rolled into a seamless tube. The internal diameter of CNTs can be a few nanometers, with the length reaching micrometers (Grobert, 2007). Typically, the carbon moieties are arranged in hexagonal rings consisting of single bonds between carbon molecules (Rubianes & Rivas, 2003). In the case of SWCNTs, a single graphene sheet is rolled into a seamless tube, whereas with MWCNTs, either a single graphite sheet is rolled up like a parchment (parchment model), or could exist as a series of SWCNTs of decreasing diameter fitting into each other concentrically (Russian doll model). The distance between adjacent walls of MWCNTs is in the order of 0.34 nm (Ajayan, 1999). Figure 2.1 shows SWCNTs (A) and the more common Russian doll MWCNTs (B) typically produced. Figure 2.2 shows a high resolution scanning electron micrograph of unfunctionalised multi-walled carbon nanotubes captured during the course of these studies.

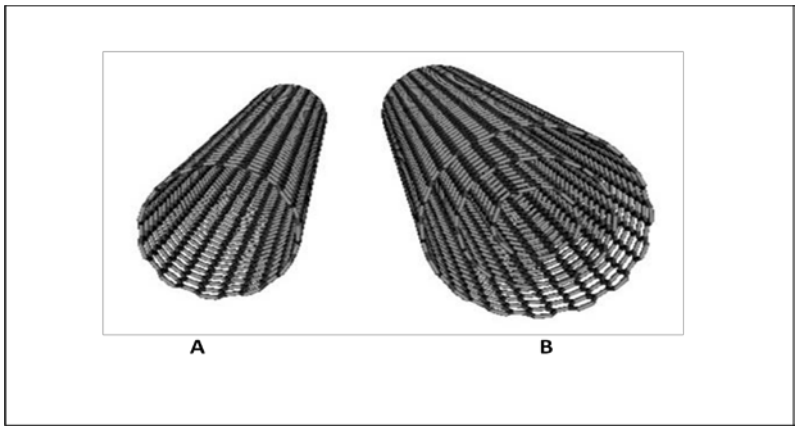

Figure 2.1 Carbon nanotubes, A): single – walled carbon nanotubes, B): multi – walled carbon nanotubes; Russian doll model, (Reproduced with permission from P. M. Ajayan).

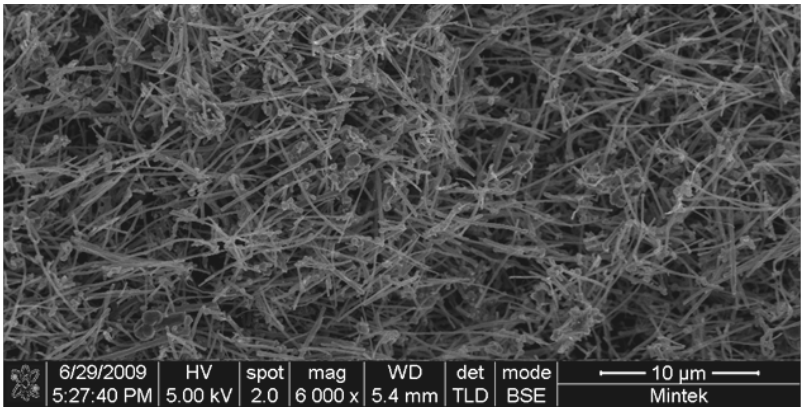

Figure 2.2 High resolution scanning electron micrograph of unfunctionalised multi-walled carbon nanotubes. Detection mode: back scatter emission. HiVac. Operating parameters: High voltage: 5 kV, working distance: 5.4 mm, spot size: 2.0. Image taken during the course of this study.

The structure of CNTs is primarily based on covalent linkage between adjacent carbon atoms creating a nanotube lattice, with a strong bond between adjacent carbon atoms. The alignment of the carbon lattice with the tube axis is of importance, because it is this sound alignment that credits nanotubes with being highly conductive, acquiring significant mechanical strength and rigidity, as well as chemical specificity and unique electronic and electrocatalytic properties (Ajayan, 1999).

2.2.1.1 The Electrocatalytic Properties of Carbon Nanotubes

In their recent reviews of the role of CNTs in electroanalytical chemistry, Valcárcel *et al.* (2005), and Trojanowicz (2006), attribute high electronic conductivity and high mechanical resistance as the prominent characteristics that make CNTs attractive in electrochemical sensor engineering. The enhanced electrochemical response as a result of increased surface area and the electrocatalytic activity of CNTs (inclusive of the demonstrated anti-fouling capabilities of CNTs), relative chemical inertness in most electrolyte solutions, in addition to having a wide working potential window are all additional attractive properties for consideration in the design and development of an electrochemical sensor surface (Merkoc *et al.*, 2005; Valcárcel *et al.*, 2005; Wang, 2005; Trojanowicz, 2006; Wildgoose *et al.*, 2006).

A significant amount of discrepancy exists amongst observations and claims found in literature regarding the source of CNTs' electrocatalytic properties. Various schools of thought exist on the source of CNTs' paramount electrocatalytic properties, each with their own feasible attributes. Early fundamentalists attribute the electrocatalytic properties of CNTs to the presence of reactive groups on the walls of the CNTs (Britto *et al.*, 1999), while others attribute the electrocatalytic properties to impurities, carbonaceous material found together with the CNTs or metallic catalysts used in the CNT synthesis process (Banks *et al.*, 2006). In the case of defects, Britto *et al.* (1999) report that, through *ab-initio* calculations, they had found that the pentagonal regions (defects) on the tubular structure of CNTs yield regions of high charge density.

The electrocatalytic effects of topological surface defects was further demonstrated by Britto *et al.* (1999), to be ascribed to the structural curvature of the tubes which leads to the origination of energy bands close to that of the Fermi level. Assessment of the electrocatalytic source of CNTs by Wildgoose *et al.* (2006) was performed using the well-established redox reactions for ferricyanide and epinephrine. They attributed to the electrocatalysis of CNTs to edge plane sites and side wall defects.

The electrocatalytic properties exhibited by CNTs are attributed to structural characteristics, the activity of basal-plane graphite sites on the CNT walls (Liu *et al.*, 2005), similar to that exhibited by the graphitic basal plane of highly orientated pyrolitic graphite (HOPG), with the open ends of the tubes exhibiting

similar characteristics of the edge plane of HOPG (Wildgoose *et al.*, 2006). According to Banks *et al.* (2005), MWCNTs would, in principle, have a greater degree of electro-catalytic properties since more CNT ends in the MWCNT would terminate in an edge-plane. In accordance, Wildgoose *et al.* (2006) corroborate with this principle stating that in their opinion the chemical and electrochemical activity that is noted with CNTs is as a result of the terminating edge-plane sites. Figure 2.3 shows a schematic to illustrate the difference between edge- and basal-planes on a graphite layer as compared to a carbon nanotube.

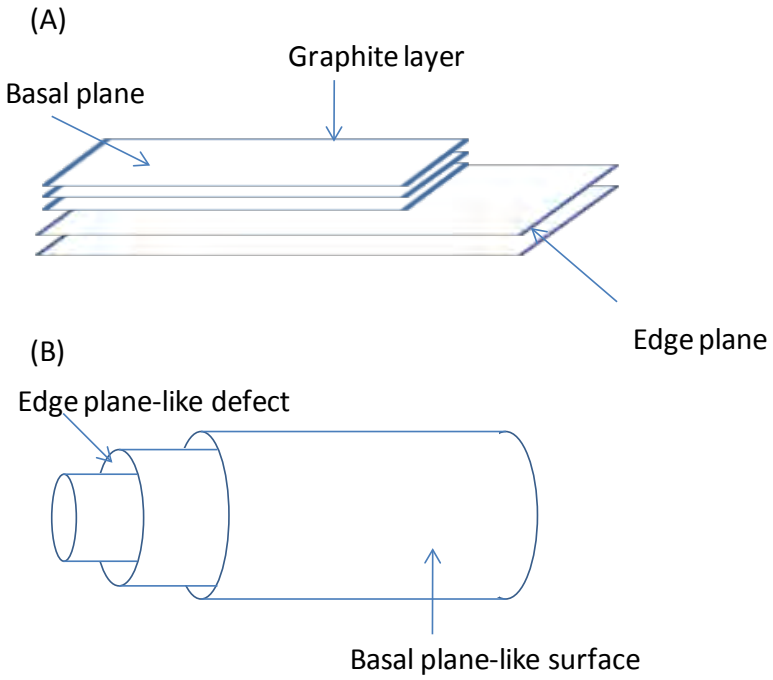

Figure 2.3 The difference between edge-planes and basal-planes on a graphitic surface (A) as compared to a multi-walled carbon nanotube (B) (*Adapted*: Wildgoose *et al.*, 2006).

In agreement with Wildgoose *et al.* (2006) added that the electrocatalytic activity of MWCNTs strongly depended on, (i) the fabrication method (in particular: arc discharge or chemical vapour deposition, CVD), (ii) on the dispersing agent that was used to immobilise the synthesised CNTs on to the electrode surface as well as, (iii) the dispersion and chemistries of these coatings.

Banks *et al.* (2004) and Moore *et al.* (2004) dismiss observations that the electrocatalytic capacity of CNTs is attributed to their structure or due to peripheral functional groups attached at site defects incorporated into the CNTs as a result of acid treatment, but rather that it is the presence of impurities found in the CNT preparation that are responsible for the enhanced electrical conductivity. Banks *et al.* (2006) and Sjukic *et al.* (2006) strongly suggest through their studies on the electro-oxidation of hydrazine and the electro-reduction of H_2O_2 that the electrocatalysis observed in this instance is attributed to iron oxide impurities found in the CNT preparation, rather than site defects of functionalised CNTs. Banks *et al.* (2006) further state that CNTs are no more conductive than conventional edge plane pyrolytic graphite. Goyal *et al.* (2008) experimentally assessed whether the electrochemical enhancement of the detection of bisoprolol fumarate (BF) was due to metal impurities within the CNTs or due to edge-plane defects on the CNT walls. Their studies concluded that the electrocatalytic signal observed at the SWCNTs modified GCE did not correspond to the current response at an EPGE, attributing the catalytic capacity to metallic impurities within the nanotubes.

Conversely, Zare & Nasirizadeh (2007), attribute their observations of an increase in electrocatalytic activity towards hydrazine to the defects created on CNT surfaces as a result of acid treatment. Interestingly, Banks *et al.* (2005) state that metallic particles present as a by-product of CNTs synthesis would undergo oxidation during the acid treatment process and would subsequently be removed during filtration. According to Coleman *et al.* (2006), and Gobert (2007), the greater the purity of the CNTs, the higher their conductivity as a result of the metals being removed during the acid treatment process. CNTs of pristine quality have exhibited enhanced conductor qualities, and are classified as being one-dimensional due to their extraordinary aspect ratio (Banks *et al.*, 2005). This quality allows for the transport of a significant amount of current with densities in the order of 100 $MA.cm^{-2}$. It should however be noted that 'pristine' SWCNTs are not readily available, since CNTs tend to aggregate into highly condensed indiscriminate bundles that are destroyed using purification protocols, with purification yields being as low as 1 % (Coleman *et al.*, 2006).

Other reports have suggested that shortened nanotubes containing functional groups at the open ends may block the adsorption of species on the CNTs (Kuznetsova *et al.*, 2000). Applications of MWCNT modified electrodes where these criteria have been achieved are well documented, and include deductions published by Wang *et al.* (2003), Gooding (2005), Merkoci (2006) and Jurkschat (2007).

It is clear that significant scope remains for unravelling the mechanism by which CNTs exert their effects, however (and as discussed further) there does appear to be common consensus that the rationale for their immobilisation onto existing electrode surfaces is to increase the surface area of the electrode, increase the sensitivity of the electrode response, and as a consequence lower the limit of detection and hinder the passivation of the electrode surface.

This study seeks to improve the understanding of the electrochemical properties of CNTs for improved sensor surface engineering. Additionally, the strategies for CNT modification and immobilisation onto conventional working electrode surfaces were explored further, and form the basis of the focus of section 2.4.

2.3 Introduction to C_{60} Fullerenes

Interest in fullerene applications has grown exponentially since their discovery in 1985 by Kroto *et al.* (Scharff, 1998; Hirsch & Brettreich, 2005). It was during fullerene synthesis (using the carbon arc discharge method) that Iijima first visualised MWCNTs adsorbed to the graphite electrode (Ajayan, 1999). Fullerene C_{60}, as named after Richard Buckminster Fuller (an engineer who coined the term geodesic to describe dome-like structures of high tensile strength), are nanomaterials with a unique spherical conformation of 0.71 nm diameter (molecular weight = 720.64 $g.mol^{-1}$), and consisting of sp^2 bonding structures of 12 pentagons and 20 hexagons of carbon (figure 2.4).

Other forms of fullerenes exist, and were named according to the number of carbon atoms that comprise the spherical structure, namely C_{28} C_{60}, C_{72}, and C_{84}, of which C_{60} is the most stable and most widely used in electrochemical sensor development (Ajayan, 1999; Csiszár *et al.*, 2001; Tan *et al.*, 2003; Li *et al.*, 2006).

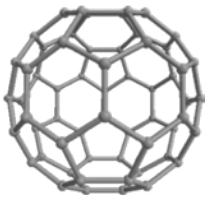

Figure 2.4 Structure of C_{60} fullerene.

Applications of fullerenes are vast and include their use as a treatment of skin cancer due to their photosensitivity (Guldi & Prato, 2000). They have shown promise as a potent HIV-protease inhibitor (DeRosa & Crutchley, 2002), are potent antioxidants (Gharbi *et al.*, 2005) and act as drug delivery vectors in physiological systems (Goyal *et al*., 2008). What is of pertinent interest for the purpose of this study is the capacity of C_{60} to promote electron transfer (Csiszár *et al.*, 2001; Tan *et al.*, 2003; Li *et al.*, 2006). Their inherent capacity to catalyse the transfer of electrons has been demonstrated. For instance the Goyal group exhibited the adsorption of C_{60} onto GCE for the detection of paracetamol (Goyal & Singh 2006 a), atenolol (Goyal & Singh 2006 b), nandrolone (Goyal *et al.*, 2007 a), adenosine and guanosine (Goyal *et al.*, 2007 b) as well as bisoprolol (Goyal *et al.*, 2008), all with a high level of sensitivity in physiological and biological media.

Fullerene C_{60} has been shown to be excellent electron mediators (Goyal *et al.*, 2009). However, this property has only been observed following the electrochemical pretreatment of the C_{60} modified layer in the presence of strong alkaline conditions (preferably KOH or NaOH). This process has been termed partial reduction, and a well-established protocol for it has been documented (Szűcs, 2008; Goyal *et al.*, 2009). The efficiency of the approach is further discussed in Chapter 4.4.3.

2.4 Strategies for Electrode Modification

Designing the electrode surface is achieved with a specific target analyte in mind, as well as the complex matrix wherein it is found. There are many approaches to designing a sensor surface. One of the common approaches is the layer-by-layer (LBL) method, where the electrode surface is systematically constructed from the bottom up. Additionally, many approaches to LBL sensor surface design exist. Scheme 2.1 highlights the factors considered in the construction of a LBL sensor in this study.

Scheme 2.1 General steps employed in the preliminary approach to electrode construction.

The choice of working electrode can be governed by cost, the working potential window of the electrode, its robustness as well as its performance in the target matrix. The mediator is not a compulsory addition, however if sensitivity, selectivity and less surface passivation are required, or the target analyte exhibits low electroactivity, then mediators should be utilised. In the scope of this study, the nanomaterials examined (SWCNTs, MWCNTs and C_{60}) are referred to as mediators. Keeping the aforementioned nanomaterials in mind, surface activation is typically required to enhance the electroactive properties of the mediator and provide a more homogeneous surface in terms of charge and structural morphology. The modified electrode is assessed for the detection of a pure form of the target analyte so as to improve the understanding of its behaviour and performance towards the target analyte. Following preliminary optimisation of the electrode towards the detection of a pure form of the target analyte, the electrode is assessed for the detection of the target analyte in a complex matrix, which could be biological in nature (serum, blood), environmental (water), or process (growth medium for pharmaceutical product biosynthesis).

Each of the steps in the sensor surface construction (LBL) is elaborated on in the subsequent section.

2.4.1 Choice of Working Electrode

Many primary electrode surfaces exist that can be used as substrates to immobilize nanomaterials onto. For the purposes of this study, glassy carbon was adopted due to its inherent electrochemical and chemical properties and characteristics.

Glassy Carbon Electrode

Conventionally glassy carbon electrodes (GCE) have been one of the preferred electrode surfaces for electroanalysis since their working potential window is broad, with inter-scan and inter-electrode reproducibility being high. The GCE is also cheaper than the conventional metal electrodes which are an important consideration in bulk sensor fabrication, and unlike many metal electrodes (except the expensive noble metal electrodes) GCEs do not corrode easily. The surface of a GCE is activated and modified with a relative degree of ease. Depending on the surface treatment of the GCE, the highly electrocatalytic nature of a GCE surface can be attributed to its surface being dominated by reactive quinone derivatives, phenols and carboxylated groups. A clean GCE surface can be obtained with relative ease by polishing with alumina slurry on a Büehler felt pad followed by an ethanol rinse and sonication. For the purposes of this work, physical adsorption of functionalized carbon nanotubes onto the polished GCE surface was adopted, and this approach is described briefly.

Physical adsorption

Physical adsorption, otherwise known as the drop dry method, is the simplest method of electrode modification, and involves either aliquoting a known volume of the electrode modification solution onto an electrode surface and allowing it to dry, or dipping the electrode into an electrode modification solution for an allotted time and allowing the surface to dry. While inter-electrode reproducibility may be lower by employing this technique, the simplicity of preparation as well as the yield of high levels of sensitivity and selectivity makes it a useful technique to use for initial proof of concept analyses. The inter-electrode reproducibility can be improved by employing the utilisation of molecules that self-assemble and configure on the electrode surface.

2.4.2 Choice of Mediator Surface Modification

2.4.2.1 Modification of SWCNTs and MWCNTs

Carbon nanotubes produced through the arc discharge method contain basal end caps (hemispheres of C_{60} fullerenes, figure 2.5), which need to be cleaved off to generate an edge-plane, while in the case of carbon vapour deposition (CVD), the CNTs produced are already uncapped and contain some oxygen containing moieties in the edge-plane positions (typically carboxyl, hydroxyl and quinonyl) (Pelekourtsa *et al.*, 1997; Estrade-Szwarckopf, 2004; Wildgoose *et al.*, 2005). The number of functional groups

decorating the edge-plane of the CNT are few and do not assist significantly in the conductivity of the CNT. In order to increase the number of carboxyl groups at the edge-plane, a number of techniques have been employed.

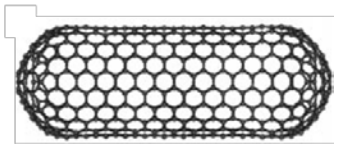

Figure 2.5 An as-produced single-walled carbon nanotube prior to functionalisation (Reproduced with permission from P. M. Ajayan)

In an unfunctionalised state, CNTs exhibit only semi-conductive properties at best, with the majority of unfunctionalised CNTs being described as being near-insular in nature (Tekleab, 2000; Jang, 2003). The addition of functional groups to the nanotubes allows for the efficient and repaid shuttling of electrons between the electrode surface and the bulk solution (Nugent *et al.*, 2001; Gong *et al.*, 2005; Merkoc *et al.*, 2005; Wang, 2005). What is of important consideration for the fabrication of continuous monitoring systems is the capacity of CNTs to decrease the adsorption of redox species through reactions occurring with peripheral functional groups on shortened CNTs (Kuznetsova *et al.*, 2000; Goyal *et al.*, 2008); and therefore allowing for their reusability, which is highly sought after in remote in-line systems demanding low maintenance and robustness.

Techniques such as surface functionalisation of the CNT walls have become common practise as a process incorporated into CNT preparation for electrochemical sensor applications. Functionalisation typically increases the conductivity of the CNTs, allowing for the efficient and rapid shuttling of electrons between the electrode surface and the bulk solution (Nugent *et al.*, 2001; Gong *et al.*, 2005; Merkoc *et al.*, 2005; Wang, 2005). Koehne *et al.* (2004), state that CNTs are typically inert and highly insoluble when they are not functionalised and tend to aggregate as a result of high surface energy and tubular flexibility (Coleman *et al.* 2006). The aggregated bundles of CNTs are characterised as having a quasi two-dimensional lattice of hexagonal structure as a result of weak Van der Waals forces (Kawasaki *et al,* 2009).

Conventional methods of CNT functionalisation include exposure to strong oxidising agents while sonicating the mixture (Banerjee & Wong, 2002). The most common oxidising agent mixture used is a combination of concentrated sulphuric acid (98 %) and nitric acid (55 – 70 %) (3:1 v/v) (Liu *et al.*, 1998; Chen *et al.*, 2001).

The strong oxidation process of acid treatment leads to the formation of perforations along the tube. As a result, the hexagons comprising the tube are cleaved, and the exposed carbons are rapidly functionalised by carboxylation or hydroxylation. While oxidation is widely used to functionalise CNTs, a clear lack of optimisation of the functionalisation process is evident in literature (González-Guerrero *et al.*, 2008), with times of exposure ranging from 1 hour to 72 hours, under varying temperature and acid concentration conditions, and with or without sonication.

According to Chen *et al.* (2001), the capped regions of the CNTs are vulnerable to initial oxidative attack due to the steric strain of the hexagon-heptagon couples, leading to rapid uncapping; leaving exposed pentagonal defects, which are easily carboxylated (Britto *et al.*, 1998). Subsequent to the uncapping of the CNT, perforations occur along the tube, which eventually leads to the breaking of the tube into smaller tubes. Scheme 2.1 illustrates the functionalisation process.

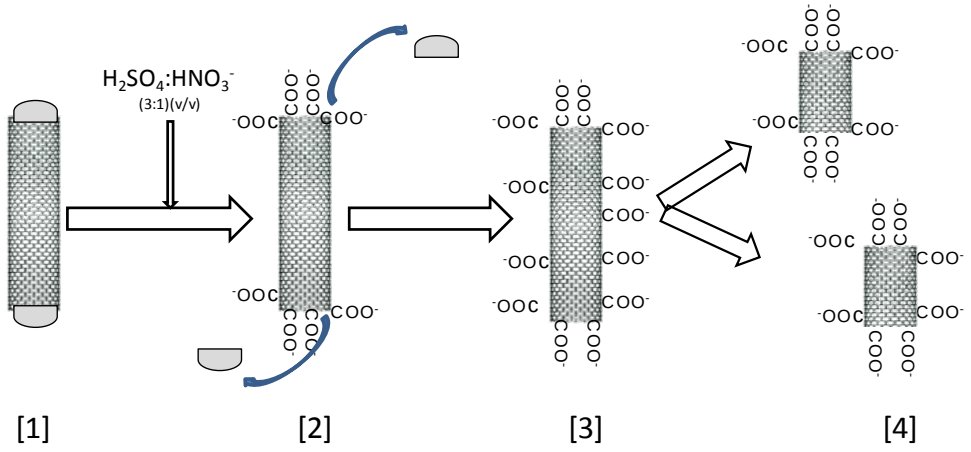

Scheme 2.2 Illustration of the CNT functionalisation process. Capped CNTs (1) are exposed to H_2SO_4:HNO_3 mixture leading to the cleavage of the fullerene caps (2) and subsequent carboxylation of the exposed carbon moieties. Prolonged periods in the acid mixture leads to perforations along the walls of the CNTs and carboxylation at these defects (3), leading to eventual cleavage of the CNTs into smaller functionalised CNTs (4).

Adapted: Liu *et al.* (1998), Chen *et al.* (2001) and Koehne *et al.* (2004).

It is through the addition of functional groups such as carboxyls and hydroxyls to the open ends that CNTs acquire enhanced conductivity (being similar to edge-plane graphite) with resultant exhibition of excellent electrochemical capacity. Apart from the inherent increase in electronic capacity of the functionalised CNTs, functionalisation assists in the dissolution of the CNT bundles with the resultant homogeneous solution of CNTs increasing in solubility in aqueous preparations. Functionalisation of CNTs preparations using acid treatment is known to exfoliate CNTs, removing metal and carbonaceous impurities (Herrera & Resasco, 2003; Zhang *et al.*, 2003; Banks *et al.*, 2005). However, over exposure to acid treatment can lead to the complete consumption of the CNTs, resulting in small carbonaceous fragments that lack the electronic properties of longer CNTs that have only partially been functionalised (Coleman *et al.*, 2006; Banks *et al.*, 2005).

As mentioned previously, unfunctionalised CNTs are described as being semi-conductive at best, whereas functionalised CNTs are known to have metallic and conductive properties. While functionalised CNTs are required in the modification of a GCE for the electrochemical detection of target analytes, some systems do not require functionalisation of CNTs. For instance, field-effect transistors (FETs) in electronics require semi-conducting CNTs. The single dimension of CNTs is not only applicable in composite materials, but is of significant importance when sensors are designed, as this one-dimensional characteristic accommodates the rapid shuttling of charge through the tubes without any scattering of the electrons. It is the electron scattering that typically increases heat produced in conventional conducting materials and as a result of energy dissipation results in increased resistance and subsequent loss of energy. This phenomenon is not noted for CNTs; near negligible energy dissipation occurs in CNTs. This quality allows for the transport of significant magnitudes of current densities in the order of 100 $MA.cm^{-2}$, and is highly sought after in electronics.

Apart from the increase in conductivity, functionalisation is also performed to purify the nanotubes from amorphous carbon and metal catalysts (Dillon *et al.*, 1997, Dujardin *et al.*, 1998) (as previously discussed), improve the aqueous solubility of the CNTs (Banks *et al.*, 2005), to add functional groups that could be used to conjugate biomolecules onto their surface (Allen & Kichambare, 2007), and to open the basal ends for further modification (Banks *et al.*, 2005). Researchers such as Kawasaki *et al,* (2009), have utilised open ended CNTs as means of storing lithium ions for use as a battery, while Xu *et al.* (2008),

have utilised the open ended tubular structure of functionalised CNTs as a drug carrier, the drug of which is released either as a slow release system or in response to a specific stimulus.

Modification of C_{60} fullerenes

While studies are focused on the entrapment of metallic compounds into C_{60} for energy storage, such as for the development of lithium ion batteries, it is the structural morphology and strength that is highly sought after in the construction of electrochemical sensor surfaces. For the purpose of this study C_{60} fullerenes were not modified, but rather the thin film of C_{60} immobilised onto an electrode was electrochemically treated to enhance the properties of the film (Goyal *et al.*, 2007). This is further elaborated on in section 2.4.3.

2.4.3 Choice of Mediator Surface Activation

For SWCNTs- and MWCNTs-modified GCE

Reproducibility of electrochemical responses between electrodes, in addition to increased response, can be obtained through pretreatment of the electrode surface. An initial physical treatment involves the cleaning and sonication of an electrode surface, followed by polishing the surface to a mirror finish. The physical method of treatment allows for more evenly distributed edge and basal planes on the electrode surface, as well as the removal of adsorbed impurities, which effectively increases the active surface area of the electrode. An applied electrochemical treatment can be adopted subsequent to the physical cleaning treatment, which involves cycling of the electrode surface in the presence of an acid or mediator. Cycling in the presence of an acid allows the even distribution of redox species and functional groups on the electrode surface, while cycling in the presence of a mediator (such as catechol) leads to electrodeposition of the mediator onto the electrode surface (under certain conditions such as low solubility). This effectively assists in the transfer of electrons to the electrode during subsequent electrochemical analyses.

Cycling in the presence of a mediator, is a widely used technique in the modification of working electrode surfaces. Mediators such as phthalocyanines (Ozoemena *et al*. 2008), hydrazine (Geraldo *et al.,* 2008) and catechol (Kissinger & Heinemann, 1996) are examples of the common mediators used.

Electrochemical treatment in the presence of catechol has been utilised extensively for the activation of glassy carbon electrode (GCE) surfaces (Engstrom, 1982; Kissinger & Heinemann, 1996). In this thesis the protocol for electrochemical pretreatment by cycling in catechol, as employed by Kissinger & Heinemann, (1996), was adapted for a GCE modified with nanotubes. During electrochemical pretreatment in the presence of catechol, the catechol moieties are included between adjacent nanotubes, allowing for a more rapid electron transfer between the nanotubes and the electrode surface. This treatment is otherwise referred to as *surface activation*, and is elaborated on further in Chapter 4.

The alignment of CNTs on a sensor surface is of additional consideration when constructing a sensor surface. Functionalised single- or multi-walled carbon nanotubes (denoted: *f*SWCNTs or *f*MWCNTs) tend to align in an ordered arrangement, and have been shown by Gooding *et al.* (2007) to exhibit more edge-plane surfaces exposed than randomly dispersed CNTs. This criterion was used by Gooding and co-workers to determine, through observations of the redox behaviour of ferrocyanide at modified electrodes, the alignment of the CNTs (Chou *et al.*, 2005). Using the ferrocyanide model, fast electron kinetics is indicative of vertically aligned CNTs that are highly ordered, while slow electron kinetics is indicative of randomly dispersed CNTs.

For C_{60} Fullerene Films on a GCE

The electrochemical behaviour of a partially-reduced C_{60} fullerene film on a GCE surface has been described by Szűcs (2008), as being a highly efficient electrocatalyst, resulting in an increase in sensitivity through not only lowering redox potentials, but also through increasing the magnitude of the current response. Partially-reduced C_{60} fullerene films are referred to in this text as being the electrochemical inclusion of K^+ (obtained from the bulk solution, as KOH), between pre-adsorbed C_{60} to form K_3C_{60} inclusion bodies (Csiszar *et al.*, 2001). The efficacy of partial reduction is contested by Chou

*et al. (*2005), while other research groups (Goyal *et al.*, 2009) strongly believe in the efficacy of this model. In this study, the approach by Goyal *et al.* (2009) was employed, and its efficacy as an electron mediator assessed. Further elaboration can be found in Chapter 4.4.3.

2.4.4 Choice of a Detection System

The choice of detection system is governed by the target analyte, the complex matrix within which it is found, as well as the desired outcome of the analysis. In the following section, the target analytes that were focused on in this study are introduced, with the desired choice of detection system highlighted.

2.5 Case Studies Using Target Analytes

The target compounds focused on as case studies in this dissertation were all studied as potential solutions to actual demands in the industrial and pharmaceutical industries in South Africa. The target analytes studied were: Wortmannin and Reactive red dye.

Wortmannin is a low volume high value bioproduct that has shown significant promise in the prevention of cancerous tumour growth. The compound 2,4-dimethylaniline is a precursor in many synthesis processes and for the purposes of this study its role in pesticide synthesis as well as in dyes for tannery and textile industries are focused on. Reactive red is a dye with many applications and has been successfully biodegraded using fungal treatment methods. For the purpose of this study its fungal breakdown is monitored through electrochemical detection. Each of these target analytes are introduced in more detail below.

2.5.1 Liquid growth media: Wortmannin electroanalysis and optimisation of semi-continuous monitoring protocol

Wortmannin, a fungal metabolite, has widespread use in molecular signalling research, given its potential as a target for the development of anti-tumour pharmaceutical drugs. In particular,

wortmannin has been shown to be a potent and irreversible inhibitor of phosphoinositide 3-kinase, an enzyme over-expressed in tumour cells.

The first documented report of wortmannin was published by Brian *et al* (1957). These authors had isolated wortmannin from a growth broth of *Penicillium wortmannii*. It was later discovered that wortmannin showed inhibitory effects towards 5'-hydroxyaverantin dehydrogenase, an enzyme produced by aflatoxins. Figure 2.6 shows the chemical structure for wortmannin.

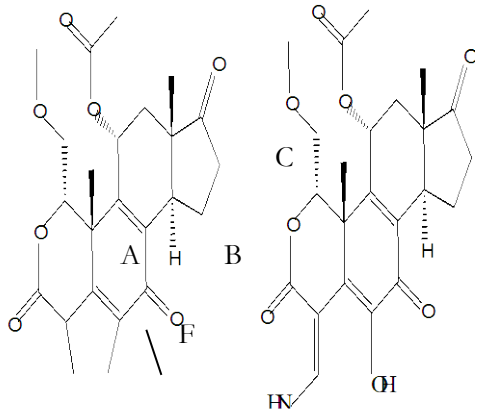

Figure 2.6 Chemical structure of wortmannin (Wipf & Halter, 2005).

(Key): A, B, C = lactone A, B, C rings respectively, F = furan ring.

Aflatoxins are highly toxic secondary metabolites produced by *Aspergillus flavus* and *Aspergillus parasiticus* and are predominantly found on food crops. A significant amount of revenue is lost annually as a consequence of fungal spoilage of food crops. It was due to its capacity to act as a potent and effective agricultural biocide that sparked the original interest in wortmannin. In addition, in an era where pesticide use in biocontrol was receiving much attention, wortmannin was observed as a potential solution to the use of harmful chemical pesticides for the prevention of aflatoxin production. Its mode of action showed significant promise as an alternative to the pesticides that were being over-utilised, the consequence of which was becoming more apparent by their inherent and irreversible mid and long term human health contra-indications. In the 1960s little was known about wortmannin except that it was a potent, alternative and apparently safe biocontrol agent. It was later reported that

wortmannin has a severe hepatotoxic effect and subsequent to this discovery wortmannin use as a biocontrol agent was terminated.

Wortmannin as a potent phosphoinositide 3-kinase inhibitor

More recent interest in wortmannin has however been sparked due to the discovery that it is a potent and specific phosphoinositide 3-kinase (PI 3-k) inhibitor (inhibitory concentration, with an IC_{50} of approximately 5 nM). The family of kinases, including PI 3-k are involved in many signal transduction pathways, which are responsible for the proliferation and maintenance of mammalian cells. It is the over-expression of PI 3-k in tumour cells that leads to their exaggerated proliferation. Wortmannin deregulates this pathway by irreversibly binding to and inhibiting PI 3-k. It is therefore not surprising that wortmannin has been isolated as an important target for cancer chemotherapy.

The potent inhibitory mode of action of wortmannin on PI 3-k is attributed to the electrophilic nature of the strained furan heterocycle, naphtho[1,8-*bc*]furan (marked as F on figure 2.7). The p110 lysine residue of PI 3-k binds specifically and in an irreversible manner to the oxygen moiety of the furan ring resulting in ring opening. However its use as a therapeutic agent has been obstructed by the high toxicity and instability. Regardless of this potential deficit, researchers are searching for mechanisms of introducing wortmannin in specific doses below the toxicity threshold as well as stabilising it. The isolation of wortmannin in high concentrations is difficult since its production is regulated within the fungal system and, current technologies do not allow for the real time continuous monitoring of this compound's biosynthesis to allow for timely harvesting.

Current detection systems for wortmannin

Knowledge of the concentration of wortmannin is especially useful during its laboratory-based biosynthesis (in growth media), or during routine research analyses in tissue culture media. However current diagnostics for wortmannin detection are limited. During recent preclinical evaluations of wortmannin, Holleran *et al.* (2003), had developed a high performance liquid chromatography (HPLC) method for the quantification of wortmannin within complex biological matrices. Although successful,

the protocol employed by Holleran *et al.* (2003), required lengthy and complicated extraction and purification protocols, resulting in low wortmannin yields. The detection protocol also limits the retrieval of the low volume, high value product subsequent to its quantification. This significant drawback in conjunction with the time-consuming sample pretreatment required makes the developed chromatographic technique less than desirable for a continuous monitoring system with little to no sample loss. While the demand and potential shown by wortmannin is on the increase, no improvement on the HPLC protocol of Holleran *et al.* (2003), could be found in literature or in a patent search. A component of this dissertation evaluates and addresses electrochemical techniques as a possible alternative.

Electrochemistry as an alternative technique for the quantitative analysis of wortmannin in growth media

Wortmannin has been cultured under laboratory conditions and grown in liquid growth media that contains essential elements required for the growth of the fungal species. According to M^{c}Cloud *et al.* (1999), wortmannin can be found in an extracellular capacity in the growth liquid medium. No documentation could be obtained describing the electroanalysis of wortmannin or its electroactivity. Since electrochemical techniques are non-destructive, the deciding factor in the detection of wortmannin in growth media would be the possible electrochemical interference effect of concomitant compounds in the growth medium. This study is believed to be a novel account of the qualitative and quantitative electroanalysis of wortmannin.

In addition, given the promise shown by nanomaterial-modified electrodes for the decrease of surface passivation, the potential for the development of an electrode surface that can detect wortmannin in a continuous manner is significant. Given the rapid response time of electrochemistry, feedback on vital aspects of the system can be performed in real time. There may be no need for skilled personnel as the system can potentially be fully automated.

2.5.2 Spent tannery effluent: Azo dye (Reactive red) biodegradation and real-time electrochemical monitoring

Azo dyes (containing –N=N- bonds) such as Reactive red are of the most widely used azo dyes in tannery and textile industries, comprising as much as 50 % of all commercially available dye formulations. What is problematic is the significantly high concentrations of Reactive red that are found in the effluent subsequent to the dyeing process. Dyes are classified as environmentally hazardous materials due to their low biodegradability, high recalcitrance and toxicity. While most dyes can only be biodegraded under anaerobic conditions, and at a slow rate, recent reports have shown that fungal biodegradation of azo dyes under aerobic conditions is relatively quick once a fungal consortium is established. Figure 2.8 shows the chemical structure of Reactive red.

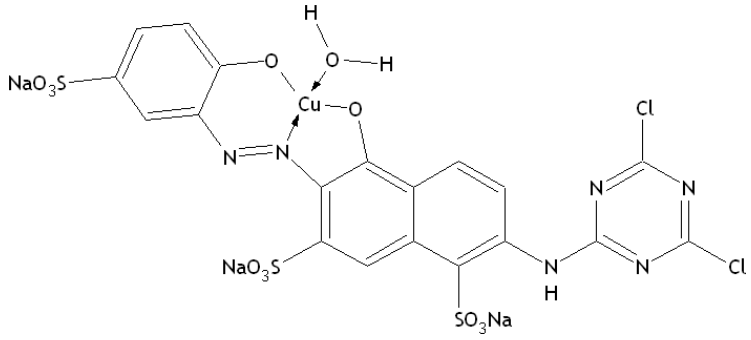

Figure 2.8 Chemical structure of Reactive red.

While the biodegradation of azo dyes by white rot fungi has been recently documented (Novotný *et al.*, 2001; Nillson *et al.*, 2006), its electrochemical detection has yet to be reported on. This case study was chosen since it was based on a bioremediation system that is known to work so the challenge was to monitor the fungal breakdown (and subsequent decrease in Reactive red) electrochemically and to examine the prospect for utilisation thereof as a real time continuous monitoring system. In addition, the versatility of electrodes modified with nanomaterials will be further assessed by testing their utility in real azo dye samples.

2.6 Background to techniques

The techniques predominantly employed in this study are, for the sake of brevity, briefly outlined in the following section. The subsections are: 1) Electrochemical diagnostics (cyclic voltammetry, Osteryoung square wave voltammetry, hydrodynamic voltammetry, amperometry and electrochemical impedance spectroscopy) and 2) Visualisation (atomic force microscopy and high resolution scanning electron microscopy).

2.6.1 Electrochemical diagnostics

Cyclic voltammetry

Cyclic voltammetry (CV) yields valuable information regarding the behavioural kinetics and thermodynamics of analytes within chemical systems (Noel & Vasu, 1990). As characterization of the electrochemical behaviour of the analytes examined in this thesis is an important component of the work conducted, CV analysis is described in some detail below. A typical electrochemical analysis involves the utilisation of a three electrode system, namely a working electrode, WE (can be, but not limited to, glassy carbon, gold, platinum, or a carbon paste), reference electrode, RE [Ag | AgCl, pseudo silver (used in non-aqueous solutions), saturated calomel, normal hydrogen], (Bard & Faulkner, 1980) and an auxiliary electrode, AE (usually a non-reactive substance, typically platinum or titanium wire or coil). These three electrodes are placed equidistant from each other in an electrochemical cell.

Typically the WE (either stationary or rotating) is positioned between the RE and AE to allow for a simple equivalent circuit to be completed between the WE and AE with minimal IR (ohmic) drop (due to solution resistivity), and to prevent polarisation of RE with a resultant equivalent distribution of potential across the electrodes (Bard & Faulkner, 1980; Kissinger & Heinemann, 1996). The significant amount of information that can be obtained from CV has made it the most widespread electrochemical technique used. Data such as the reversibility and formal reduction and oxidation potentials of a target analyte, its kinetics, and behavioural characteristics can be ascertained by using CV. In a typical CV scan (shown in figure 2.9), the potential at the WE is cycled starting at a specified potential where no redox reactions occur, E_i and scanned in either a reduction or oxidation direction at a predetermined scan rate (in $mV.s^{-1}$). The potential is reversed at a specified potential, E_f (switching potential) and conventionally

returned to the original starting potential, E_i. At the potential range at which the target analyte is oxidized or reduced, a significant increase in current occurs, increasing magnitude and peaking at the point where there is an equilibrium between oxidized species and unoxidized sample (for example), decaying to baseline current when the analyte at the diffusion layer at the electrode surface is depleted.

The peak that forms is an indication of the concentration of target analyte in the bulk solution. Its magnitude (in either the reduction direction, I_{pc} or oxidation direction, I_{pa}) is also indicative of the rate of electron transfer during the redox process for reversible systems (Kissinger & Heinemann, 1996).

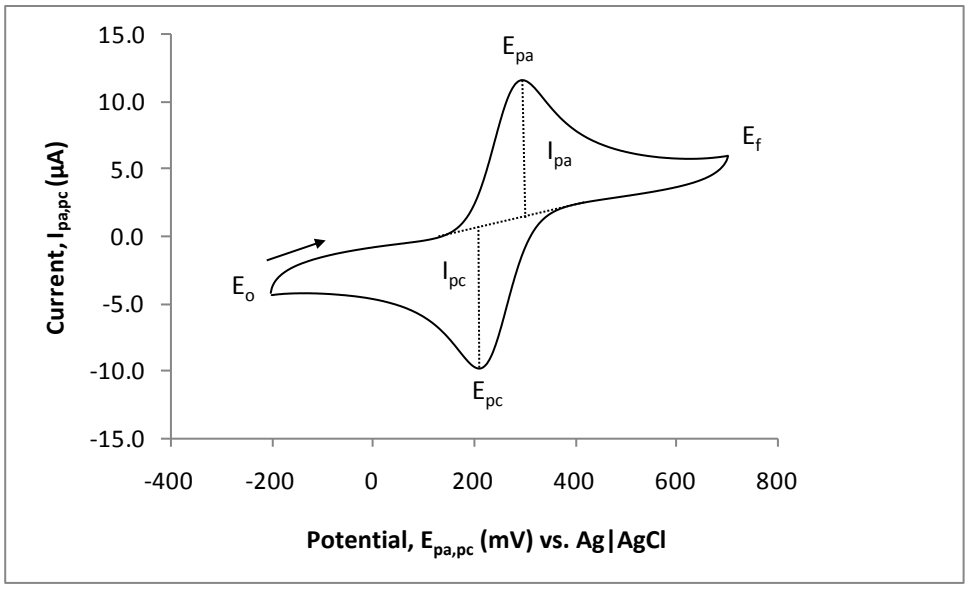

Figure 2.9 Representative cyclic voltammogram showing an example of reversibility. In reversibility E_{pa}-$E_{pc}/2 \leq 59$ mV Legend: E_o: Initial potential, E_f: Final potential, E_{pa}: Anodic potential peak, E_{pc}: Cathodic potential peak, I_{pa}: Anodic current, I_{pc}: Cathodic current. Arrow indicates the initial direction of the scan, while the dotted lines show the peak height.

The peak heights, their position and shape yield a significant amount of information regarding the structure and behaviour of the target analyte as well as which process they typically conform to. Knowing which process the target analyte conforms to is fundamental in understanding the behaviour of the analyte at the electrode surface. For CV, three processes are known to occur, namely reversible, quasi-reversible and irreversible.

An *electrochemically reversible process (ERP)* obeys the Nernstian equation where oxidation and reduction products are equal in current strength due to oxidation and reduction of the analyte of interest being in a state of equilibrium.

The heterogeneous rate constants, k_f and k_r are fast and equal. A typical reversible CV is shown in figure 2.9. Several additional diagnostics are available to assess an analyte's redox reversibility.

For reversible systems, the Nernst equation at 298 K applies:

$$E = E^{\circ} - \frac{0.05916\,V}{n}\log_{10}\quad\frac{[R]}{[O]} \qquad [2.01]$$

Where E = potential of the electrode (vs. the reference electrode)(V) , E° = formal potential (V), n = number of electrons in the cell reaction, [R] and [O] are concentrations of the reduced and oxidised species, respectively (Bard & Faulkner, 1980).

Other diagnostic criteria:

The peak to peak ratio, I_{pa}: I_{pc} is near unity with a peak separation of no more than 59 mV. In addition, I_p is proportional to $\nu^{½}$, where ν is the scan rate in mV.s^{-1}.

An *electrochemically irreversible process (EIP)* is defined as a redox process where the charge transfer step occurs at a slow rate. Essentially only an oxidation or reduction peak is observed, with a weak return peak in some cases, but $I_{pa} \neq I_{pc}$. The heterogeneous rate constants occur at different rates resulting in the oxidation and reduction processes never occurring at equilibrium. Subsequent scans show a decrease in current magnitude as a consequence of redox species adsorbing to the electrode due to an unbalanced redox process. Figure 2.10 shows a CV of an irreversible process.

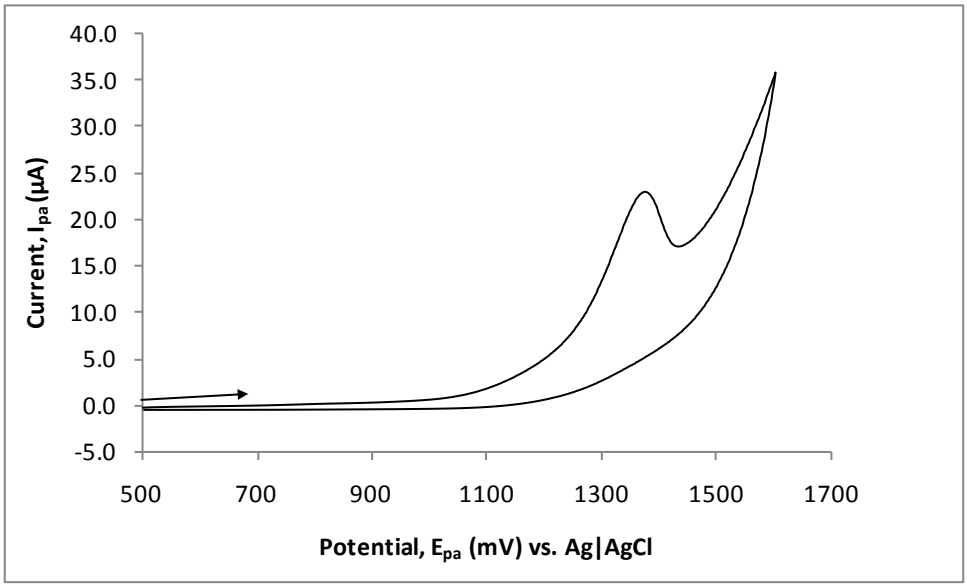

Figure 2.10 Representative cyclic voltammogram showing typical irreversibility.

Given that the concentrations of reactants and products are not equal (as is the case in a reversible processes), the Nernst equation does not apply. The peak current for an irreversible process is therefore given by:

$$I_p = (2.99 \times 10^5)n[(1-\alpha)n]^{1/2}A.c.(Dv)^{1/2} \qquad [2.02]$$

Where I_p= current response, n = number of electrons transferred, α = transfer coefficient (rate of electron transfer), A = surface area of electrode (cm^2), c= concentration of species ($mol.cm^{-3}$), D= diffusion coefficient ($cm.s^{-2}$), v = scan rate ($V.s^{-1}$)

In addition, in irreversible processes, the rate of electron transfer controls the reaction and a shift in peak potential to higher potentials with an increase in scan rate is characteristic.

An *electrochemical quasi-reversible proc*ess *(EQP)* is an intermediate between the reversible and irreversible electrochemical systems with the reaction being controlled by mass transport as well as charge transfer kinetics, the latter being hindered by mass transport. Therefore electrochemical products at the electrode are not in equilibrium with electrochemical reactant in the bulk solution. Typically, $I_{pa} < 1 > I_{pc}$, ΔE_p > 0.059 V.n^{-1} and I_p does not increase linearly with an increase in scan rate (Brown & Large, 1971; Wang, 1994).

Osteryoung square wave voltammetry (OSWV)

The technique of OSWV is an improvement on the established staircase voltammetry (SV) which on its own was an improvement on linear sweep voltammetry (LSV). In LSV, the current response at the WE is measured during a linear scan of an applied potential (vs. time) between the WE and the RE. The resultant peak or trough in the current response is indicative of the oxidation or reduction of the reactive species. With SV, the potential is applied in a stepwise manner, with the resultant current being measured at the end of each stair prior to an increase in the amplitude of the potential. This is done in order to limit the effects of capacitance. In OSWV, a square wave is superimposed on a potential-staircase scan. The magnitude of the current response is measured at $E^{½}$ and plotted as a function of potential; the resultant peaks/troughs are indicative of the oxidation/reduction of the reactive species, respectively (Bard & Faulkner, 1980; Kissinger & Heinemann, 1996).

Hydrodynamic voltammetry

Target analytes within a bulk electrolyte can reach the WE surface through convection, migration or diffusion (Bard & Faulkner, 1980). At a static WE (under the assumption that the bulk solution's effects are negligible), conventionally analytes migrate to the electrode surface by diffusion. In the case of hydrodynamic voltammetry (HV), accelerated analyte transfer is obtained through convection.

Hydrodynamic voltammetry utilises a rotating disk electrode (RDE) as the WE, as compared to the conventional stationary WE employed. The RDE can be rotated at rates between 60 and 10,000 RPM. The purpose of employing a RDE is to replace the typical turbulent flow of the bulk solution with a

laminar flow region which allows for a stagnant Nernst diffusion layer, δ of 0.1 – 0.01 mm thickness near the WE surface. By creating a stagnant Nernst layer it is easier to quantitatively assess more than one electroactive species simultaneously. Another prominent advantage of using HV is that a higher degree of sensitivity can be obtained since the mass transport of redox analyte to the electrode surface is performed more efficiently (Heinemann & Kissinger, 1996).

Laminar flow allows for regeneration of the WE electrode by reduced/oxidised species to be removed from the WE surface, and unreacted redox species to get to the electrode through the convection process. In addition, the interfering effects of capacitative charging current observed at static electrodes are negligible in HV. Convective parameters such as flow rate, angular velocity and rotation speed are useful in determining important parameters such as diffusion,(D) and rate transfer constants ($k_{f,r}$) (Zare *et al.*, 2005; Yadegari *et al.*, 2008). Time is of paramount importance in this system and typically low scan rates are employed to ensure that steady-state conditions are maintained to guarantee the system is restricted to convection mass transport of the analyte to the WE (Bard & Faulkner, 1980).

Amperometry

The direct proportionality between the concentration of the target analyte and the magnitude of resultant current due to a constant potential being maintained between the working and auxiliary electrodes is the basis behind amperometry. Amperometric studies are generally performed in a stirred or flow through bulk solution or at a rotating working electrode (Bard, & Faulkner, 1980). This allows for the homogeneous presentation of fresh analyte to the electrode (since amperometry is performed in real time).

Amperometry can be utilised in two capacities: (i) discontinuous: as a diagnostic to detect a single analyte in a solution with concomitant interferents and (ii) semi-continuous/ continuous: as a flow through analysis to yield data in real time (Bard Faulkner, 1980; Kissinger & Heinemann, 1996).

With respect to (i) amperometric measurement of the activity of redox enzymes is a well established technique since it is highly specific and can therefore be adapted to lower detection limits. The most common application is the blood glucose biosensor, where, for example, the concentration of liberated H_2O_2 from glucose conversion to gluconate by glucose oxidase is measured at a fixed potential. At the applied fixed potential, the target analyte is reduced or oxidised, yielding a measurable increase in current. The magnitude of the current response is proportional to the concentration of the target analyte, and a calibration curve can be established by measuring the current response to standard addition of target analyte to the bulk solution while the predetermined fixed potential is maintained. In (ii) flow injection analyses and flow through cells are on the increase in systems where constant real time information regarding a target analyte is required (Martinez-Calatayud, 1996). This technique has been adopted for gas sensors (such as carbon monoxide), the levels of which are monitored constantly, and also in process biotechnology where the concentration of essential nutrients required for microbial growth are monitored in conjunction with monitoring the product of interest, in real time.

Amperometric detection in standard laboratory samples is very different from complex matrix samples. Kissinger & Heinemann, (1996), stated that amperometric analyses in complex (real) samples without prior cleanup of these samples is not feasible. This is primarily as a result of concomitant analytes fouling the electrode surface which leads to current damping and sensitivity decreases. This is commonly overcome by the addition of a membrane or subsequent cleanup protocols and columns.

Carbon nanotubes have, as a potential solution to the surface passivation issue, shown promise as being capable of regeneration after electrochemical redox reactions have occurred at their surfaces (Lee *et al.*, 2006). This functionality is useful for application in continuous monitoring systems where the replacement of electrodes after each analytical event is not ideal.

Electrochemical impedance spectroscopy (EIS)

Electrochemical impedance spectroscopy (EIS), when used in conjunction with traditional electrochemical techniques (such as cyclic voltammetry), yields invaluable information on the properties of modified layers on electrodes, their porosity, passivation properties as well as probing

electrochemical mechanisms of surface confined species. A conventional resistor, otherwise termed as an ideal resistor, is limited to one circuit element, making it an ideal resistor that does not take into consideration frequency, has in-phase AC current and voltage flowing through it and obeys Ohms law at all current and voltage measurements. Impedance is rather defined by resistance in conjunction with the capacitance of materials, taking into account morphology of the surface. In a Randles' equivalent circuit [(figure 2.11 (A)] an ideal resistor is governed by double layer capacitance, C_{DL} which is replaced by the constant phase element (CPE) when modified surfaces are being assessed. This is done since CPE is a more accurate representation of the resistive and capacitative properties of modified layers. Figure 2.11 (B) shows a standard equivalence circuit for impedance at a modified electrode surface.

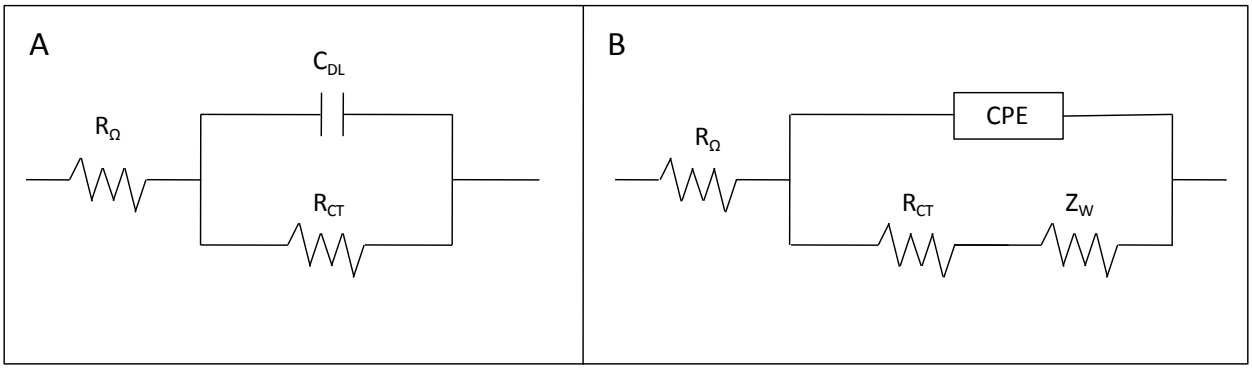

Figure 2.11 (A) and (B) showing the Equivalent circuit used for impedance studies at the thin-film electrode-electrolyte interface. The constant phase element (CPE) (B) is a more accurate representation of actual resistance than the conventional double layer capacitance (figure A) used in Randles' equivalent circuits for ideal resistors. Legend: R_Ω: polarisation resistance, R_{ct}: Charge transfer resistance, Z_W: Warburg impedance. CPE: Constant phase element, C_{DL} Double layer capacitance.

2.6.2 Visualisation techniques

Atomic force microscopy (AFM)

The atomic force microscope is a high resolution visualisation tool capable of resolutions in the nanometer range. The principle of AFM is based on the initial scanning tunnelling microscope but in AFM a cantilever scans the surface of a sample and records topological alterations, making it an ideal tool for 3 - dimensional surface profile imaging.

Two primary modes of operation are available in AFM, namely static (contact) mode and dynamic (non-contact) mode. In contact mode the deflection of the cantilever tip from the sample surface is used to image the topological surface. Typically the force between the cantilever and the sample in contact mode needs to be of a repulsive nature so that the cantilever tip does not alter the surface of the sample. While non-contact mode is generally preferred since it does not touch the sample surface, which allows for the imaging of soft samples, as well as preventing damage to the cantilever tip, contact mode would be opted for if the sample to be visualised has a layer of water on its surface since it penetrates the layer and images the surface below.

The AFM mode used during these studies was non-contact and this technique will be elaborated on. In non-contact (dynamic) mode, the cantilever tip oscillates at a slightly higher frequency than its fundamental resonance (the amplitude would typically be a few nanometers) since van der Waal's forces are at their strongest at an amplitude of no more than 10 nm above the sample surface. The van der Waal's forces decrease the resonant frequency of the oscillating cantilever, and this decrease in frequency is used to adjust the distance between the cantilever tip and the sample surface.

As the tip scans over the surface of the sample, the resonant frequency is altered as the sample to tip distance is changed according to the topology of the sample. At each x, y point on the sample the distance is measured and this is used to image a topographical representation of the sample surface. Figure 2.12 is a graphical representation of the non-contact mode AFM and the frequency analyser feedback loop that maintains constant oscillation of the cantilever.

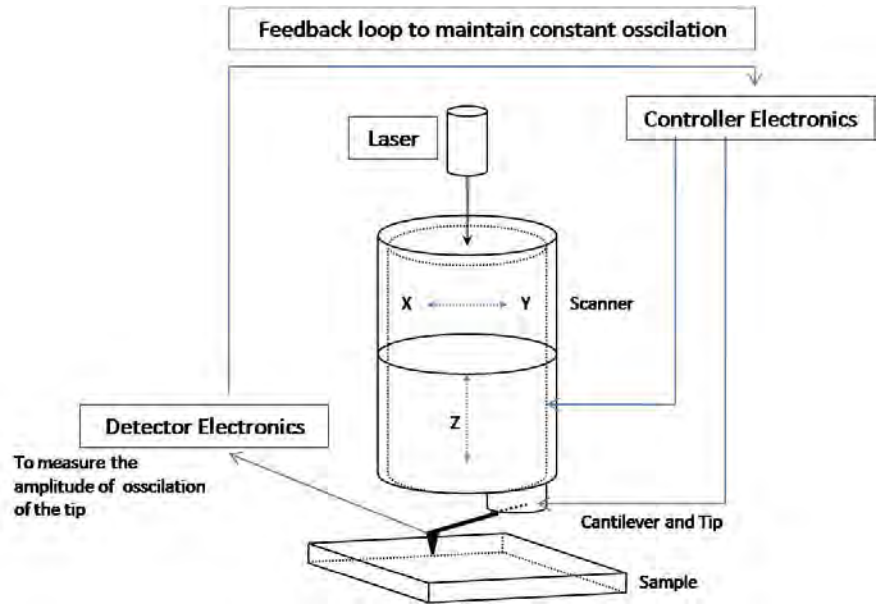

Figure 2.12 Illustration of the setup and feedback mode for a non-contact mode atomic force microscope

High resolution scanning electron microscopy (HRSEM)

The HRSEM utilises a high electron beam thermionically emitted electron gun (zirconium oxide in this instance) to scan a sample surface in a raster mode. The electrons from the beam are focused on a spot on the sample (0.5 nm to 5 nm in diameter) and interact with surface atoms and produce a signal that is converted into an image that represents the distribution of the current from the specimen. Typically HRSEM can be used to obtain information regarding the topographical and compositional features of a sample, all visualised as high resolution images as small as 1 nm. Secondary imaging modes, such as back-scattered electrons (BSE) mode image electrons that are reflected from the sample and is a common additional technique utilised in analytical scanning electron microscopy and is typically used to gain knowledge on the elemental distribution in the sample. Figure 2.13 shows the FEI Nova 230 HRSEM setup used during this study *(Courtesy: Mintek, South Africa).*

Figure 2.13 The FEI Nova 230 High resolution scanning electron microscope setup utilized in this study.

2.7 Significance of this study

This study therefore seeks to assess the efficacy of modifying existing working electrodes with nanomaterials, in order to enhance the performance of the electrodes towards the detection of chosen target analytes. These target analytes represent the industrial/process, pharmaceutical and environmental sectors. Additionally, the modified electrodes were optimised to fulfil the desired predetermined criteria consisting of increased sensitivity, reproducibility and reusability, while considering the portability of the detection system, as well as ease of use. The information reported on in this study would be beneficial to product development institutes given its real-world application.

CHAPTER 3

GENERAL EXPERIMENTAL APPROACH

"The whole of science is nothing more than a refinement of everyday thinking"

– Albert Einstein

General experimental approaches, materials and equations are outlined in this chapter. Detailed accounts of specific experimental protocols are described in the relevant chapter.

3.1 Materials

3.1.1 Reagents

The following materials were purchased from Sigma Aldrich (South Africa): carbon nanotubes [single-walled (as produced, bundle dimensions (diameter x length): 1.2 – 1.5 nm x 2 – 5 µm, 9 % purity); and multi-walled (as produced, 110 – 170 nm diameter, 5 – 9 µm length, 90 % purity)], C_{60} fullerenes (98 % purity), and catechol. $Fe(CN_6)^{3-}$, $Fe(CN_6)^{4-}$, potassium chloride, potassium hydroxide, aluminium oxide (> 10 µm), sodium citrate, sodium acetate, ammonia, potassium dihydrogen orthophosphate, dipotassium hydrogen orthophosphate, hydrogen peroxide as well as reagents used in the preparation of Britton-Robinson buffer (0.1 M acetic acid, 0.1 M boric acid, 0.1 M phosphoric acid (85 % *v/v*) (Britton & Robinson, 1931), were all supplied by Sigma Aldrich, South Africa. Water was distilled using a Millipore system. Nitrogen gas (Instrument grade) was sourced from Afrox South Africa). The following reagents were obtained from SAARCHEM (South Africa): dichloromethane, hexane (HPLC/GC grade > 97 %), hydrochloric acid (30 % *v/v*), sodium hydroxide, nitric acid (55 % *v/v*), dimethylsulphoxide, dimethylformamide, sulphuric acid (0.5 M). Ethanol (> 90% *v/v*) was obtained from Protea Industrial Chemicals, South Africa. The fungal isolate *Pleurotus ostreatus* was received as a gift from Ms. Bronwyn Moore (Rhodes University).

3.1.2 Analytes

Wortmannin (98 % Sigma Aldrich, was isolated from *Penicillium fumiculosum*, freeze dried), Effluent containing Reactive red 120 was obtained from a local Eastern Cape Tannery, and pure Reactive red 120 was obtained from Sigma Aldrich, South Africa.

3.1.3 Electrodes

A typical three electrode system was employed and (unless otherwise stated) a 1 ml glass electrochemical cell was used. The reference electrode used was a Ag | AgCl electrode in saturated 3 M KCl (unless stated otherwise); the auxiliary electrode was a platinum wire and the working electrode was a glassy carbon

(r = 1.5 mm).For hydrodynamic voltammetry studies a glassy carbon rotating disk electrode (r = 1 mm) was used as the working electrode. Electrodes were polished on a Buëhler felt pad.

3.2 Instrumentation

3.2.1 Electrochemical

Cyclic voltammetry (CV) and Electrochemical Impedance Spectroscopy (EIS)

All voltammetric data was collected at an Autolab Potentiostat PGSTAT 30 (Eco Chemie, Utrecht, The Netherlands). Operating programme: General Purpose Electrochemical Systems data processing software (GPES, software version 4.9.007 Eco Chemie). Control of N_2 purging and stirring was maintained using a Metrohm 663 VA stand. pH meter (WTW pH 330I by Wellheim model no: 82362). Sonicator (Elma S10H Elmasonic by Singen. Htw (90W power).

Electrochemical impedance spectroscopy (EIS) was performed using the Frequency Response Analyser (FRA) module and the impedimetric data evaluated with FRA software supplied by Eco Chemie, Utrecht, The Netherlands. UV-Vis spectroscopy was performed using a Powerwave 96-well microtitre plate reader (Bio-TEK instrumentals Inc.).

3.2.2 Visualisation

Atomic Force Microscopy (AFM) operating conditions

Atomic force microscopy (AFM) images were recorded utilizing the non-contact mode in air with a CP-11 Scanning Probe microscope at a scan rate of 0.50 Hz, obtained from Veeco Instruments (Carl Zeiss,

South Africa and Veeco, Germany). Probe: MPP11123, AFM head: CP II. A cut disk from a BAS glassy carbon electrode (GCE) of 0.28 cm^2 was used for immobilizing the catalyst solution, using the same drop-dry method employed for electrochemical analysis.

High Resolution Scanning Electron Microscope (HRSEM)

High resolution scanning electron microscopy was performed using a FEI Nova 230. All visualisations were performed under high vacuum with a high voltage between 1 and 20 kV. A through lens detector (TLD) was initially used to visualise secondary electrons, which was changed to back scatter electron (BSE) detector when immersion mode was used. Specific parameters are listed as a footnote on the HRSEM images.

3.3 Experimental methods

3.3.1 Electrode preparation

Glassy carbon electrode (GCE)

The GCE surface (r = 1.5 mm) was polished on a Buëhler felt pad (Bioanalytical Systems) using alumina powder (< 10 µm, Sigma Aldrich, South Africa) and rinsed with copious $d$$H_2O$. Subsequent to the polishing step the GCE was sonicated in 20 % ethanol for 2 minutes to remove residual alumina, rinsed with $d$$H_2O$ and air dried.

3.3.2 Determination of Electrode Surface Area Using $[Fe(CN)_6]^{3-/4-}$

The true surface area of the GCE was determined experimentally by cyclic voltammetry according to established methods (Bard & Faulkner, 1980). The geometric surface area only accounts for a theoretical and flat surface area, whereas experimental calculation takes into account the topographical variances of the surface. The magnitude of I_{pc}/I_{pa} reversible redox reaction of freshly prepared equimolar (1.0 mM) $K_3[Fe(CN)_6]^{3-/4-}$ in 100 mM KCl was monitored when the scan rate was incrementally increased.

Given the reversibility of the redox process the Randles-Sevcik equation can be employed:

$$I_{pa} = 2.69 \times 10^5 . n^{3/2} . A . C_o . D^{½} v^{½} \qquad [3.01]$$

Where I_{pa} refers to the anodic peak current for $K_3Fe(CN)_6$ (A), n is the number of electrons involved in the reaction (n = 1), D is the diffusion coefficient of $K_3Fe(CN)_6$, = 7.6 x 10^{-6} $cm^2.s^{-1}$, A is the surface area, C_o is the concentration of $K_3Fe(CN)_6$ ($mol.cm^{-3}$)and v is the scan rate ($V.s^{-1}$).

From a curve of I_{pa} vs. $v^{½}$ (Figure 3.1) the slope for I_{pa} vs. $v^{½}$ was determined to be 1 x 10^{-6} (R^2 = 0.9997), with an *apparent* true surface area calculated at, A = 0.0539 cm^2. Given the lowered value for A a theoretical value of 0.07 cm^2 (attributed to a highly polished surface), was adopted.

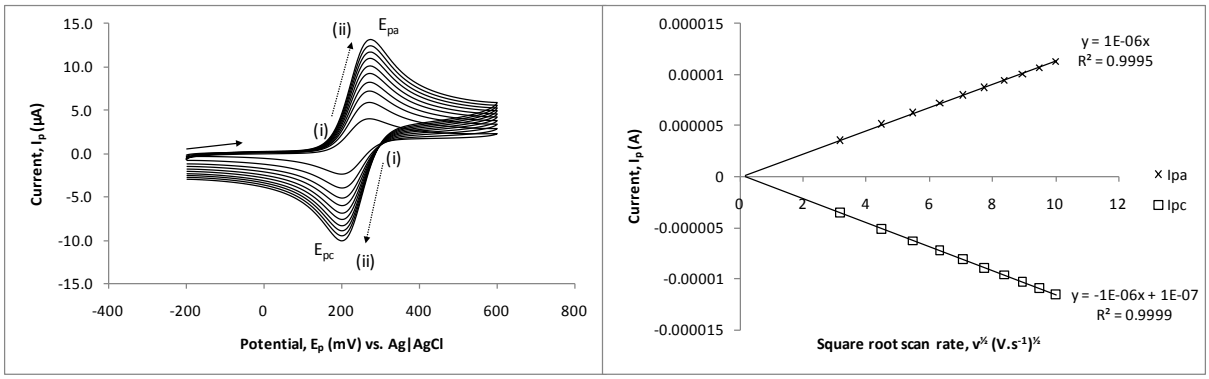

Figure 3.1 Representative CV showing the redox pair for equimolar 1 mM $[Fe(CN)_6]^{3-/4-}$ in 0.1 M KCl at a GCE (vs. Ag|AgCl). Scan rate: 100 $mV.s^{-1}$.

3.4 Electrochemical equations

3.4.1 Reproducibility and standard deviation

The accuracy of the electrochemical scans was determined by calculating the standard deviation, $S.D$ with the scan number being 3 unless otherwise specified. The following equation applies:

$$\% \ S.D = \frac{S.D}{Average \ I_p} \times 100 \qquad [3.02]$$

Where I_p is the current strength of the anodic/ cathodic peak.

Reproducibility, R can therefore be expressed as:

$$R \ (\%) = 100 - \% \ S.D \qquad [3.03]$$

3.4.2 Limit of detection

The limit of detection, LOD is the lowest detectable electrochemical current response that is equivalent to three times the standard deviation, $S.D$ of the baseline of the blank scan (Kissinger & Heinemann 1996). The LOD can be determined from the gradient, m of a linear plot of I_p vs. [concentration of the analyte] (Goyal *et al.*, 2007).

The following equation applies:

$$LOD = \ 3 \ (S.D/m)] \qquad [3.04]$$

3.4.3 Sensitivity

The sensitivity is equivalent to the linear portion of a I_p vs. [analyte] and is expressed as A/M.

3.4.4 Determination of surface coverage, Γ (mol.cm^{-2})

The surface coverage comparison between modified and unmodified (and before and after surface activation) was estimated from the charge (determined as the area under the curve), Q of I_{pa} peaks.

The following equation is used:

$$\Gamma = \frac{Q}{nFA} \qquad [3.05]$$

Where Γ = surface coverage (mol.cm^{-2}), F= Faraday constant = 96485.34 °C.mol^{-1}, A = surface area of the electrode (cm^2) and n = number of electrons involved (Finklea *et al.* 1993, 2000; Ozoemena *et al.* 2006).

CHAPTER 4.

MODIFICATION OF SENSOR SURFACES WITH NANOMATERIALS

"We'd like to make it [nanotubes] in a continuous fiber, roll it on a drum, and go fishing with it."

- Richard E. Smalley

4.1 Introduction

This chapter examines the application of the following materials as electrode modifiers, namely single-walled carbon nanotubes (SWCNTs), multi-walled carbon nanotubes (MWCNTs), and C_{60} fullerenes.

Single-walled and multi-walled carbon nanotubes

4.1.1 The Origin of Carbon Nanotubes' Conductive Properties

The conductive properties of carbon nanotubes have been a topic of interest and debate since their first official documented characterisation by Iijima in 1991. The enhanced conductive properties exhibited by CNTs have been well documented for inclusion in electrochemical sensors with promising outcomes that suggest an ability of the nanotubes to promote electron transfer resulting in enhanced detection sensitivity.

The source of the unique conductive properties of CNTs is an ongoing investigation. A few prominent theories exist in literature that attempt to explain the source of the enhanced conductive properties of these materials.

4.1.2 Carbon Nanotube Functionalisation

In the first instance, it is believed that impurities resulting from CNT synthesis (such as metals) are incorporated into the tubular structure of the CNT and aid the enhanced conductive nature of the tube (Banks *et al.*, 2006; Gooding *et al.*, 2007; Batchelor-McAuley *et al.*, 2008). The electrocatalytic properties of nanotubes have also been attributed to their open ends and defects along the nanotube (Chou *et al.,* 2005; Musameh *et al.*, 2005). Observations reported by Zhang *et al.* (2003), Burghard (2005), Liu & Gao (2005) have shown that only after surface modification of pristine CNTs is performed are the promising enhanced conductor properties apparent. A combination of materials is also possible as has been described by Banks *et al.* (2005) where metallic components have been incorporated into surface-modified nanotubes to increase their conductive properties.

The absence of any electrocatalytic properties unique to CNTs is debated by Compton and co-workers (Banks *et al.*, 2006), who believe that the source of electrocatalytic properties of open-ended CNTs is no different to those observed at an edge plane pyrolytic graphite electrode (EPGE) (Banks *et al.*, 2006).

In similar studies (Banks *et al.*, 2006; Gooding *et al.*, 2007), the favourable electrochemistry of open-ended CNTs was linked to the presence of carboxylic and quinone derivatives situated at the terminal ends of the opened tubes. These are the same functional groups believed to be responsible for the favourable electrochemistry observed at EPGEs (Banks *et al.*, 2006). While the plausibility of the association between the electrocatalytic properties exhibited by open-ended CNTs and EPGEs is apparent, it has been noted that the surface area of CNTs is significantly larger than EPGEs, which allows for greater electron transfer per unit area (Chou *et al.*, 2005).

In general, the carbon nanotubes synthesis process results in low quantities of tubes that are usually capped on both ends by a C_{60} hemisphere (Ajayan, 1999). Many methods exist in literature for the opening of CNTs and adding of functional groups. (These will broadly be referred to in the text as functionalisation). Two overarching approaches to functionalisation exist, namely dry functionalisation (such as exposure to ozone) and wet functionalisation (such as exposure of the capped pristine CNTs to a strong acid or a compilation of strong acids). The most widespread method used is wet functionalisation, and in particular: exposure to strong acids such as nitric acid (HNO_3), sulphuric acid (H_2SO_4), or a combination of both, commonly in a 3:1 (H_2SO_4: HNO_3) ratio. Additionally, the nanotubes functionalisation in acid process can be enhanced by (i) refluxing in HNO_3 (Dujardin *et al.*, 1998; Liu *et al.*, 1998; Shaffer *et al.*, 1998; Hill *et al.*, 2002; Lin *et al.*, 2003; Wang *et al.*, 2005), or (ii) sonication of the nanotubes in HNO_3:H_2SO_4 (1:3 v/v) (Li *et al.*, 2005; Wang *et al.*, 2005).

In this study the preferred wet functionalisation by temperature-controlled sonication of nanotubes in H_2SO_4: HNO_3 (3:1 v/v) was selected and the effect of the length of time of functionalisation on the electroactivity of the nanotubes studied.

Discrepancies for the optimum functionalisation time using the preferred aforementioned functionalisation method are common in literature. For instance, Liu *et al.* (1998) and Gooding *et al.* (2007) suggest that CNTs be functionalised for a maximum of 6 hours while Hou *et al.* (2008) state that the nanotubes should be functionalised for 12 hours. Many authors on the other hand do not report the functionalisation time used. While these discrepancies exist it is clear that exposure of CNTs to acid solutions results in shorter CNTs (Gooding *et al.*, 2007), which terminate in oxygenated moieties (Lee *et al.*, 1997; Chattopadhyay *et al.*, 2003; Strano *et al.*, 2003). The demand for exhaustive studies to be performed on the optimum parameters for wet functionalisation (acid treatment) of CNTs is however emphasised by Chou *et al.* (2005) and Gooding *et al.* (2007).

Many parameters can be considered for the determination of an ideal duration of the functionalisation process. In this study the parameters were decided based on the expected outcome of fabricating a sensor surface with enhanced electrocatalytic abilities resulting in increased current response to target analytes.

Functionalisation process

Functionalisation of CNTs in acids occurs as a multi-step process that is dependent on numerous external factors and parameters that all contribute to the outcome efficacy of functionalisation. While exposure time is of prominent interest in this study, it is noted that other factors such as the concentration of the acid solutions and purity of the starting CNT material (as-produced), whether sonication is used, as well as the CNT solution temperature are of equal importance. It is for instance reported by Banks *et al.* (2005) that an increase in the exothermal conditions of the CNT functionalisation reaction results in CNTs that are markedly shorter than those allowed to functionalise at 25 °C. Accordingly, Banks *et al.* (2005) suggest the addition of ice to the sonicator bath to maintain a temperature below 25 °C to prevent accelerated graphitization (Kastner *et al.*, 1994; Ebbesen, 1997; Jiang *et al.*, 2005) since an increase in the degree of graphitization results in lowered capacitance and electron transport facilitation (Jiang *et al.*, 2005).

The addition of pristine CNTs to strong acid results in the initial cleavage of the C_{60} hemispheres from the terminal ends of the CNTs (Chen *et al.*, 1998; Zhang *et al.*, 2003). The exposed carbon groups are susceptible to chemical alteration, with typical carboxylation and hydroxylation occurring rapidly. With an increased exposure time to the acid, these now functionalised CNTs (*f*CNTs) undergo further randomised cleavage along the carbon nanotube where exposure to the strong acid has created surface defects, the eventual outcome being CNTs that are significantly shorter. Figure 4.1 illustrates the carboxylation and surface defect formation on a carbon nanotube.

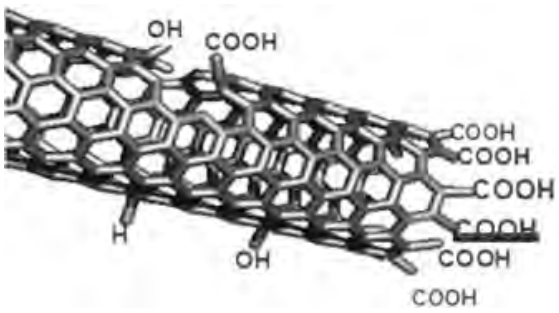

Figure 4.1 Carbon nanotube showing surface defect as a result of overexposure of the tubes to strong acid solutions (Permission to use image obtained from Professor Inaki Mondragon).

The electroactive properties of functionalised nanotubes can be further enhanced by adopting an electrochemical approach once they are immobilised onto a pre-existing electrode surface (such as carbon or gold). An array of electrochemical pretreatment (ECP) protocols for the additional modification of immobilised layers of materials exist that can be applied to the pretreatment of immobilised *f*CNTs. For the sake of clarity, electrochemical pretreatment will here be referred to as activation.

4.1.3 Carbon Nanotube Activation

The electrochemical pretreatment of carbon-based electrodes has been shown to significantly increase the electron-transfer efficiency in redox systems (Musameh *et al.*, 2005). The origins of the acquired electrocatalytic ability through pretreatment (activation) have been attributed to many factors, such as

the inclusion of quinone functional moieties (Engstrom, 1982) as well as the removal of redox species from the electrode surface (Engstrom & Strasser, 1984).

A particular component of this study focused on assessing activation of the surface of functionalised CNTs once immobilised onto an electrode (sensor) surface. Surface activation has been used to enhance the conductive properties of many materials and was assessed for that purpose in these studies.

Many methods of CNTs activation are documented, which include preanodisation by applying a fixed potential to a working electrode for a preselected time (Musameh *et al*., 2005), or the inclusion of transition metals such as Fe, Mn, Ni, Co (Leznoff & Lever, 1996; Kadish *et al.*, 2003; Banks *et al.*, 2004), or phthalocyanine mediators (Ozoemena *et al.*, 2008). Cycling in the presence of KOH (Frackowiak *et al.*, 2002) are alternative activation approaches. For the purpose of this study, activation through cycling in the presence of catechol was employed. The inclusion of catechol onto a *glassy carbon working electrode* is an established technique known to include electrode catalytic efficacy (Kissinger & Heinemann, 1996).

A variety of redox compounds can be used to (i) incorporate between moieties on an electrode surface in order to increase electron transfer efficiency (activation). The success thereof can then be assessed in the 'test' step. Gooding *et al.* (2007) report on the usage of ferromethylamine (FMA) as a model redox active compound to monitor electrode surface activation with dicyclohexylcarbodiimide (DCC). In their study, Gooding *et al.* (2007) showed that no significant electrochemical activity was observed for FMA if the *f*CNTs are not first activated with DCC. The DCC, through covalent attachment, binds the *f*CNTs to FMA.

Catechol inclusion at a GCE involves a cyclic voltammetry activation scan at a high scan rate in a bulk solution containing catechol (referred to here as the activation step), followed by a CV scan in the same catechol solution at a lower scan rate to test the success of the activation step measured by the current response (Kissinger & Heinemann, 1996). (This latter CV scan is referred to further as the test scan in

this chapter). In the test scan the increase in the current response for the redox peaks of catechol are monitored, since theoretically with each activation scan the current response increases until the electrode surface is saturated with catechol moieties, at which point the current response for catechol redox peaks remain constant.

The number of activation scans that are obtained before current response stability is achieved is considered the ideal number of activation scans. While the activation method using catechol is well established for GCE, no literature could be found where it had been used for GCE modified with *f*CNTs. The report on catechol activation of *f*CNTs on a GCE is reported on in this study, and is considered the first account of its application within this capacity.

C_{60} Fullerenes

Fullerenes have received significant attention recently due to their conductive nature, as well as showing a high degree of biocompatibility and potential as drug delivery vectors (Bosi *et al.*, 2003). Of specific interest to this study are their inherent electrocatalytic properties, which offer promising means of reducing overpotential when adsorbed onto a working electrode (Goyal *et al.*, 2007). In particular, the electrochemical behaviour of a partially reduced C_{60} fullerene film on a glassy carbon electrode surface has been described by Szűcs 2008 as being a highly efficient electrocatalyst resulting in an increase in sensitivity through not only lowering redox potentials but also increasing the magnitude of the current response.

4.1.4 Partial reduction of C_{60} thin film

Partially reduced C_{60} fullerene films are referred to in this text as being the electrochemical inclusion of K^+ (obtained from the bulk solution, as KOH) between pre-adsorbed C_{60} to form K_3C_{60} inclusion bodies (Csiszar *et al.*, 2001). The partially reduced GCE-C_{60} system has been described to behave as diodes through their electron accumulating properties (Echegoyen & Echegoyen, 1998). Electrode surfaces modified with C_{60} fullerenes have the added advantage of being stable for long periods as well as

containing a large working potential window (Goyal *et al.*, 2008). The C_{60} loading capacity on a GCE has been studied by Goyal & Singh (2006 a,b), and the approach was adopted in this study.

4.1.5 Techniques

In addition to cyclic voltammetry (CV), Electrochemical Impedance Spectroscopy (EIS) was employed in this study since EIS is frequently utilised to assess the efficacy of the surface modification as well as the electrochemical properties of modified electrodes. In particular, Nyquist plots give information on the resistance, capacitance, and nature of the electrode surface. Bode and magnitude plots yield information on the nature and capacitance of the electrode surface through monitoring changes in phase (Θ) and frequency (*f*) shifts. The electron transfer efficiency (k_{app}) can be determined from data obtained from Nyquist and Bode plots. Visualisation of the electrode surfaces and nanomaterials was performed using high resolution scanning electron microscopy (HRSEM) and topographical features visualised using atomic force microscopy (AFM).

Studies in this chapter are therefore aimed at identifying parameters for efficient functionalisation and activation of both single-walled and multi-walled CNTs with the purpose of applying these to further studies in the succeeding chapters. In addition, C_{60} fullerenes are assessed as potential electrode modifiers for application in real sample analysis of target analytes of relevance to this thesis.

4.2 Objectives

The overall objective of this study was to identify parameters for efficient application of fullerenes and multi- and single-walled CNTs as electrode modifiers for electroanalytical sensor design. In order to achieve the stipulated objectives, the following aims were addressed:

4.2.1 Carbon nanotubes (SW- and MW-):

Determine the optimal functionalisation time for single-walled and multi-walled carbon nanotubes based on predetermined criteria:

- Current response and potential shift for a test analyte, catechol.

- Electrical behaviour as assessed through EIS.

Assess the feasibility of carbon nanotube electrochemical activation with catechol.

4.2.2 C_{60} Fullerenes

Little is known about the electrochemical properties of C_{60} fullerenes (Bae *et al.*, 2010). This section therefore seeks to:

Monitor the electrochemical behaviour of C_{60} fullerenes on a GCE surface.

Assess the electrocatalytic properties of C_{60} modified electrodes.

Determine the ideal loading efficiency of C_{60} on a GCE surface.

4.3 Experimental

Carbon nanotubes (SW- and MW-)

4.3.1 Functionalisation of carbon nanotubes

The protocol for SWCNT functionalisation was adapted from protocols documented by Wang *et al.* (2005). In brief, unfunctionalised multi-walled (90 % purity) and single-walled (9 % starting material) carbon nanotubes (MWCNTs and SWCNTs respectively) were purchased from Sigma Aldrich, South Africa. For each of the MW and SWCNTs, 1 mg was weighed and added to 30 ml 55% HNO_3:H_2SO_4 (1:3 *v/v*), and sonicated in a sonicator bath (Elmasonic S10H). In order to limit perforation of CNTs due to

temperature, ice was added to the sonicator bath at regular intervals to keep the temperature at approximately 15 °C (Banks *et al.*, 2005).

At one hour time intervals, 2 ml of acid-CNT mixture was removed from the reaction vessel and diluted by the addition of 98 ml dH_2O. Aliquots were removed each hour for ten hours and washed in the same way. After the initial wash step, the CNTs were centrifuged at 10,000 x g for five minutes and the supernatant discarded. The process was repeated until the pH of the resuspended CNT pellet was near neutral at which point the CNT mixtures were placed in an oven at 100 °C to dry. Once the functionalised CNTs were dried, the CNTs were weighed and dimethylformamide (DMF) added at a ratio of 10 ml per mg CNT dry weight. An identical procedure was performed on unfunctionalised CNTs for comparative purposes. Prior to use, the sample vials containing CNTs and DMF were sonicated for 2 minutes to disperse the nanotubes and used immediately.

4.3.2 Immobilisation of carbon nanotubes

Physical adsorption of carbon nanotubes onto glassy carbon electrodes through layer-by-layer application: glassy carbon electrodes (GCE) were cleaned as outlined in section 3.3.1 and placed in an oven at 100 °C. When required, the GCE was removed from the oven and 5 µl of the CNT-DMF mixture aliquoted onto its surface and returned to the oven. This was performed until the desired CNT loading was achieved. The CNT-GCE was rinsed with DMF to remove any loosely bound CNTs and rinsed with copious amounts of dH_2O.

4.3.3 Surface activation

For catechol surface activation, the method as described by Kissinger & Heinemann (1996) for GCE surface activation was employed. In brief, 0.45 mM catechol was prepared fresh in 0.1 M H_2SO_4. Surface activation is a two-step process. In the first step, (activation step) a single CV scan from 0 mV to 1780 mV (vs. Ag|AgCl) at 200 $mV.s^{-1}$ was performed which incorporates catechol into the spaces between the CNTs. The second step (test scan) assesses the efficacy of catechol inclusion. An increase in the redox peaks for catechol is indicative of increased catechol incorporation. The catechol test scan parameters

are a CV scan from 800 mV to -150 mV (vs. Ag|AgCl) at 100 $mV.s^{-1}$. This procedure was repeated for each activation step and for each electrode until the catechol test scan showed minimal increase in its redox peaks for the test analyte.

C_{60} Fullerenes:

4.3.4 Preparation of C_{60} modified electrodes

Glassy carbon electrodes were cleaned as described in Chapter 3.3.1 and placed in an oven at 100 °C. Preparation of the C_{60} modified GCE was performed as outlined by Tan *et al.* (2003) and optimised by Goyal & Singh (2006a,b). In brief, a solution of 150 µM C_{60} was prepared in dichloromethane (DCM) and sonicated briefly to disperse the fullerenes. The preheated GCE was removed from the oven and 10 µl (150 µM) preparation of C_{60} aliquoted onto its surface and returned to the oven to dry. The procedure was repeated and the C_{60} loading volume ascertained. The electrodes were rinsed with DCM before performing partial reduction of the C_{60} thin film.

4.3.5 Partial reduction of C_{60}-GCE thin film

Partial reduction of the C_{60} thin film was performed in freshly prepared 1 M KOH, at ambient temperature, as per Goyal & Singh 2006a. A single cyclic voltammetry scan was performed by applying a single reduction potential scan between 0 mV and -1500 mV (vs. Ag|AgCl) at a scan rate of 10 $mV.s^{-1}$. It is important to perform this scan once as over-reduction of the C_{60} thin film results in an insulatory layer (Szűcs, 2008; Goyal *et al.* 2008). Subsequent to the partial reduction, the electrode was rinsed with copious amounts of dH_2O and immediately immersed into 50 mM phosphate buffer (pH 7.0 at 25 °C) which was degassed prior to use with N_2 gas (instrument grade, Afrox, South Africa). Potential cycling was performed between 550 mV and -550 mV at 20 $mV.s^{-1}$ (vs. Ag|AgCl) under a constant N_2 atmosphere until a stable baseline was obtained (≈ 3 scans). The electrode was stored at room temperature until required.

4.3.6 Assessment of partially reduced C_{60}-thin film

Electrochemical impedance spectroscopy (EIS) of the C_{60}-GCE was assessed between 10 kHz and 10 mHz using a 5 mV rms sinusoidal modulation, in a solution of 1 mM $K_3Fe(CN)_6$ and 1 mM $K_4Fe(CN)_6$ with the $E_{½}$ of $[Fe(CN)_6]^{3-/4-}$ using a frequency response analyser (FRA) software. Automatic fitting of the data was performed using a non-linear least squares (NNLS) method (EQUIVCRT programme). Surface coverage was calculated as outlined in Section 3.5.4.

4.3.7 Determination of the loading capacity of C_{60} on GCE

A GCE was cleaned as outlined in Chapter 2. For the loading capacity determination, the protocol of Goyal *et al.* (2008) was employed, in which 10 µl of 150 µM C_{60} in DCM was aliquoted onto a preheated GCE using a pipette and allowed to air dry. The nanomaterial modified electrode (NME) surface was partially reduced as outlined in section 5.2.2, and then immediately immersed into freshly prepared equimolar concentrations of 1 mM $[Fe(CN)_6]^{3-/4-}$ and the surface area determined from the slope of I_{pa} vs. $v^{½}$ determined as outlined in section 3.3.6. In addition, the electrode was cleaned and polished thoroughly (as outlined in chapter 3.3.1). After the electrode was allowed to dry, 20 µl of the 150 µM C_{60} in DCM solution was aliquoted onto the GCE and assessed in a similar manner as before. The procedure was repeated until 60 µl of 150 µM C_{60} in DCM on the GCE was assessed.

4.3.8 Visualisation of carbon nanotubes

Visualisation of carbon nanotubes was performed using atomic force microscopy (AFM) and High resolution scanning electron microscopy (HRSEM). The experimental approach for these techniques was outlined in section 3.2.2.

4.4 Results and Discussion

4.4.1 Single-walled carbon nanotubes

4.4.1.1 Functionalisation and characterisation of single-walled carbon nanotubes

The functionalisation of CNTs is described in section 4.3.1, and the samples taken hourly during the functionalisation process are shown in figure 4.2.

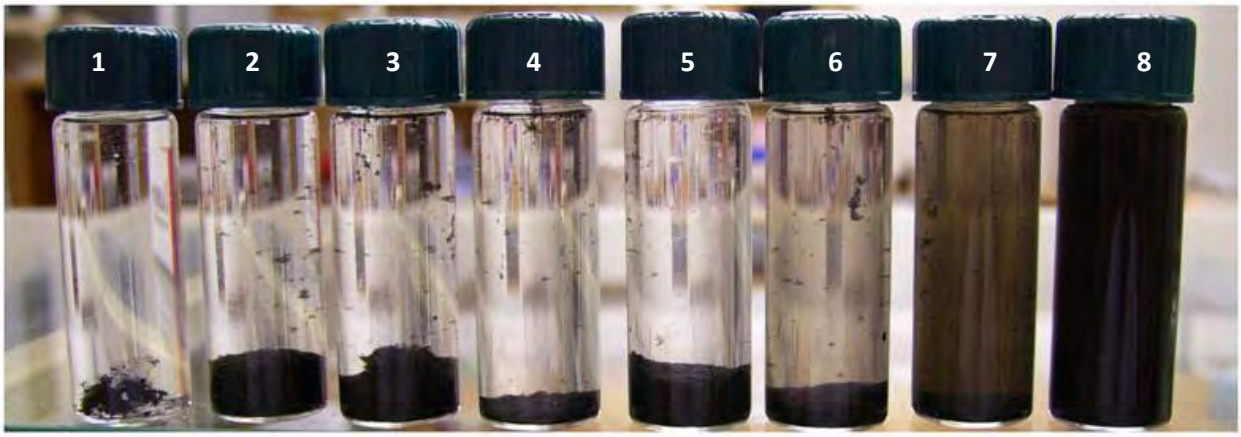

Figure 4.2 Functionalisation of SWCNTs: sample vials showing samples of single-walled carbon nanotubes (each suspended in 4 ml *d*H_2O) taken at each hour and rinsed in *d*H_2O. On the far left is the vial following 1 hour treatment, whereas the far right hand side is the sample at 8 hours. Note: each sample is 5 ml total volume and was aliquoted from the same reaction vessel at hourly intervals. Discrepancies in observed volumes of precipitated nanotubes could be attributed to variances in density between the different functionalisation times.

After 1 hour exposure of SWCNT to the acid mixture, the SWCNTs were observed to precipitate in a highly aggregated cluster [observed as (1) in figure 4.2]. With increased acid exposure, the SWCNTs tend to disassociate and remain in solution for longer. A suspension of SWCNTs was noted after 6 hours, and at 8 hours, a more soluble suspension of SWCNTs was observed. The functionalisation process has been described by Zhang *et al.* (2003) and Banks *et al.* (2005) to result in the addition of carboxyl groups initially at the terminal ends of the tubes following cleavage of the C_{60} fullerene hemispheres, and then along the length of the tube walls at site defects created by the acid treatment. Tsai *et al.* (2006) attribute the reduction in aggregates to a decrease in Van der Waals' interactions between adjacent SWCNTs as a consequence of an increase in the number of carboxyl groups on the SWCNT walls. Sano *et*

al. 2001 further state that CNTs typically aggregate in aqueous solutions or polar solvents, but through functionalisation, CNTs tend to remain dispersed for longer. This behaviour was observed to occur and in particular after 6 hours of functionalisation. The increase in dispersion in aqueous solutions is plausible since the addition of functionalised groups onto the terminal ends of nanotubes increases the hydrophilicity of the tubes and subsequently increasing their solubility. However, the walls of the tubes remain highly hydrophobic. The *f*SWCNTs shown at 8 hours functionalisation (figure 4.2) remain suspended in solution for long periods in comparison to less functionalised CNTs since the breaking of the tube walls (which occurs with prolonged exposure to the acid treatment process) results in the addition of oxygenated species to the perforations, therefore increasing the tube's overall hydrophilicity (Gooding, 2005).

Functionalised SWCNTs as visualised under immersion mode using HRSEM are shown. Figure 4.3 (A-B) show the morphological characteristics of unfunctionalised SWCNTs (A), and SWCNTs functionalised for 4 hours (B).

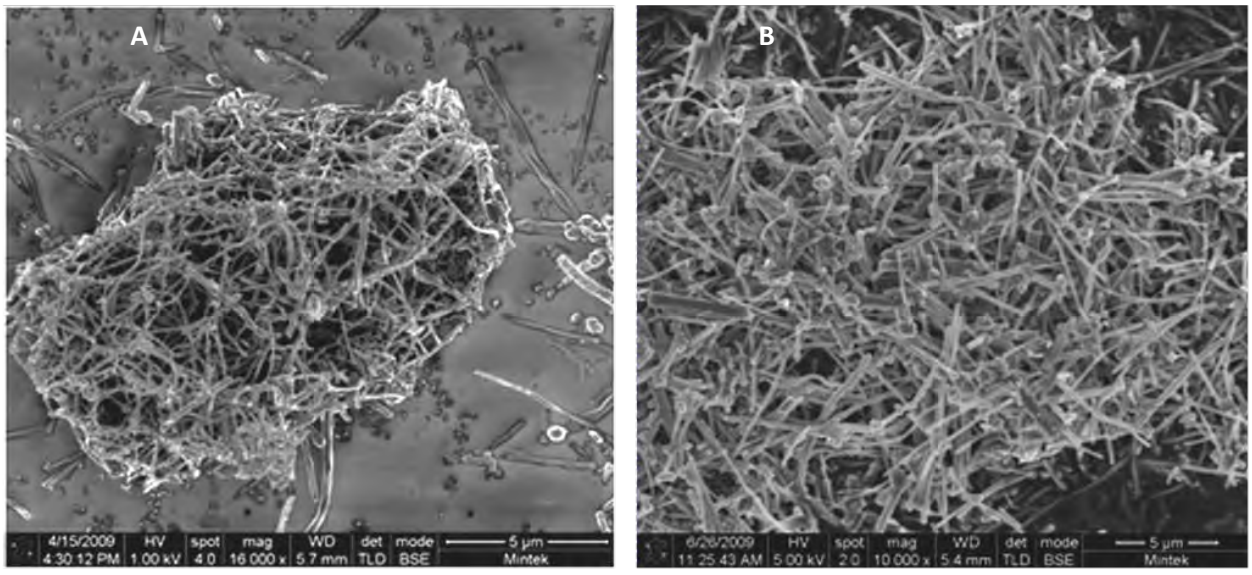

Figure 4.3 (A) HRSEM images of unfunctionalised SWCNTs tend to aggregate partly due to their hydrophobic properties. (B) shows SWCNTs functionalised for 4 hours. The nanotubes tend to become less aggregated and are cleaved into shorter fragments. The operational parameters for HRSEM are shown in the respective figure legends.

In figure 4.4 (A) a nanotube of more than 300 µm length is shown after 4 hours acid treatment, and damage to a nanotube after extensive acid treatment (< 6 hours) is shown in figure 4.4 (B).

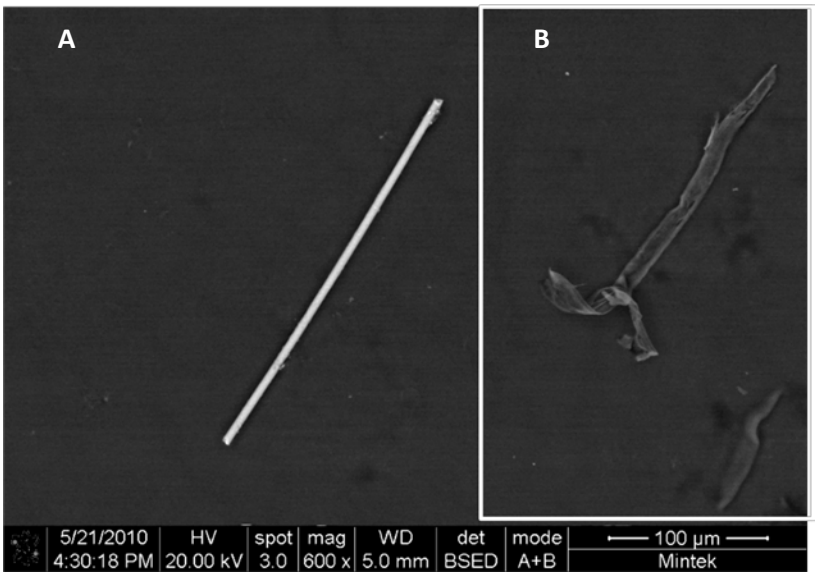

Figure 4.4 (A) HRSEM image of a single SWCNT at 4 hours acid functionalisation, with extensive damage shown at longer functionalisation times (< 6 hours). The operational parameters for HRSEM are shown on the figure legend.

Yuan *et al.* (2010) discovered that while long nanotubes do exhibit a high degree of tensile strength, nanotubes that are micrometers in length are poor conductors due to interactions predominantly occurring at the terminal ends (due to their functionalisation at these areas). This results in poor electron transfer due to electron inaccessibility to the inner pore. Additionally the length of the tube is mainly hydrophobic in nature, which further hinders efficient electron transport. Yuan *et al.* (2010) had established that shorter SWCNTs facilitate the transport of electrons.

In figure 4.3 (A) the HRSEM image shows aggregated SWCNTs that have not been functionalised. After 4 hours functionalisation the nanotubes tend to be cleaved into shorter fragments and begin to dissociate from each other due to an increased hydrophilicity, figure 4.3 (B). Gooding *et al.* (2007) reported similar observations using transmission electron microscopy.

Figures 4.5 (A – B) show the effects of acid functionalisation on the terminal ends of nanotubes. Unfunctionalised SWCNTs are capped with a C_{60} hemisphere at each end (Ajayan, 1999; Zhang *et al.*, 2003; Tsai *et al.*, 2006), as is visible in figure 4.5 (A). Acid treatment tends to cleave off the C_{60} hemispheres leaving exposed open nanotubes, figure 4.5 (B) (Ajayan, 1999; Zhang *et al.*, 2003; Tsai *et al.*, 2006). While the cleavage effect of acid treatment can be clearly seen in figure 4.5 (B), the diameter of 500 nm for these particular visualised tubes are not typical, and should therefore in this context only be viewed as representative tubes to illustrate the acid treatment effect on the tubes.

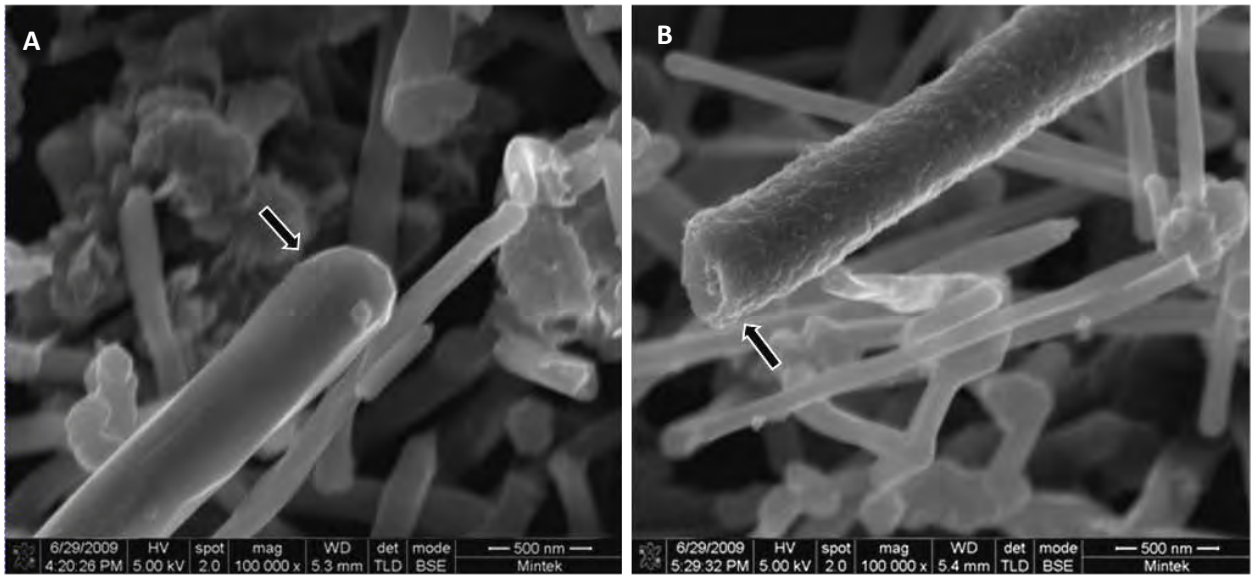

Figure 4.5 (A) Representative HRSEM images of SWCNTs prior to functionalisation showing the intact C_{60} hemisphere (shown with the arrow). After acid treatment, (B) the C_{60} hemispheres are cleaved off the terminal ends of the SWCNTs resulting in open ended nanotubes (4 hours treatment) that are rapidly carboxylated. (In figure 4.3 (B) the surface roughness of the nanotube is attributed to the addition of surface defects during the acid treatment. The operational parameters for HRSEM are shown in the respective figure legends.

Zhang *et al.* (2003) suggest that SWCNTs are, in the presence of H_2SO_4:HNO_3 (3:1 v/v), shortened as a result of a 2-step process: (i) a defect generating step and (ii) a defect consuming step. In (i) the single graphene sheet comprising SWCNTs is attacked by NO_2^+ (derived from HNO_3 in the presence of H_2SO_4) with the outcome being the addition of oxygen containing functional groups to susceptible areas of the nanotubes (i.e. the terminal ends and areas along the nanotube wall). The subsequent defect consuming step (ii) is responsible for the cleavage of nanotubes at the pre-oxidised areas in conjunction with the

addition of carboxyl groups to the terminal ends as a result of continuous oxidation in the presence of the strong acids.

In comparison to the aggregated unfunctionalised SWCNTs in figure 4.3 (A) the difference in the solution homogeneity as a result of 6 hours acid treatment is distinct, as observed in figure 4.6 (A).

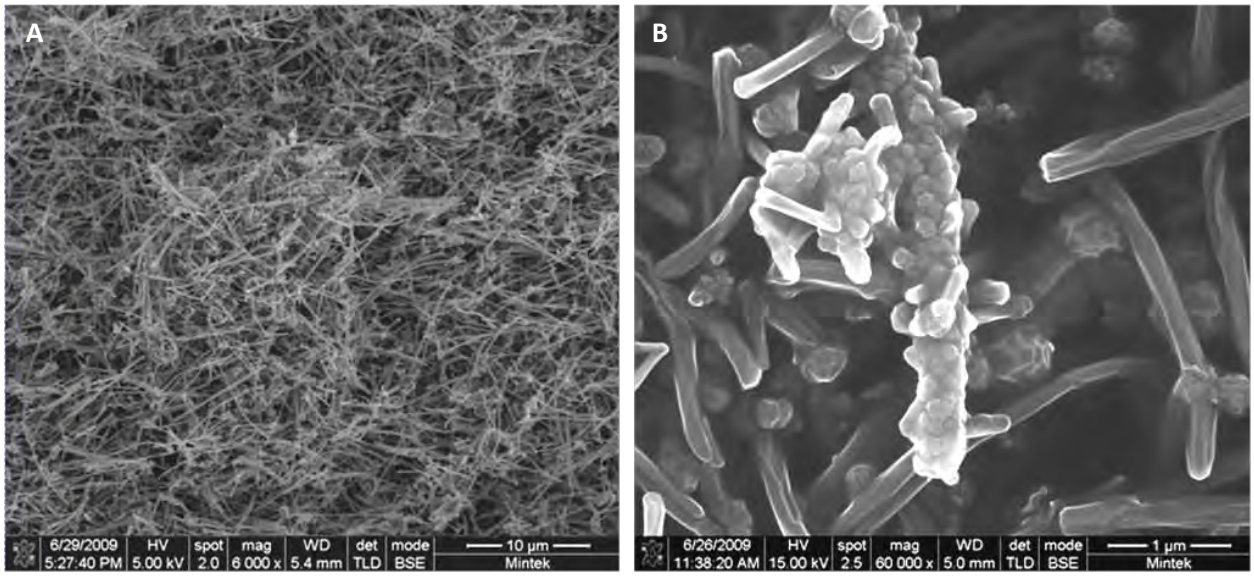

Figure 4.6 (A) HRSEM images showing a homogeneous suspension of functionalised SWCNTs (6 hours acid treatment) of shorter length. (B): Highly functionalised SWCNTs (9 hours acid treatment). The HRSEM operational parameters are shown in the respective figure legends.

Of interest is the nodular formation of C_{60} hemispheres on the wall surface of a highly functionalised SWCNT (9 hours exposure to acid), as observed in figure 4.6 (B) which suggests a high degree of surface functionalisation. Goyanes *et al.* (2007) describe the effect of prolonged exposure of nanotubes to an acid medium as complete functionalisation of the tubes occurring due to disruptions of the bond symmetry of the tubes, resulting in an amplified selectivity with adjacent carbon atoms becoming more reactive. This analogy could explain the nodes observed on highly functionalised nanotubes. The morphology shown in figure 4.6 (B) was visualised for the sample treated for 9 hours with acid. It was also observed at 9 hours acid treatment that the SWCNT walls were damaged as can be seen in the background of figure 4.6 (B) together with smaller pieces of carbonaceous material. Goyanes *et al.*

(2007) report on the complete destruction of the nanotube structure due to prolonged exposure to H_2SO_4:HNO_3 (3:1 v/v).

The increase in CNT solubility in polar solvents (as described earlier) has been utilised as a means of immobilising *f*CNTs onto electrode surfaces (Banks *et al*., 2006). Such organic dispersants as dimethylformamide (DMF) are typically used to add *f*CNTs to electrode surfaces since the combination of even distribution in the solvent in conjunction with the volatility of the solvent allows for the rapid formation of an evenly distributed layer on the electrode surface (Wang *et al.*, 2005; Gooding, 2005).

Perforations along the CNT walls has been linked to increased hydrophilicy of the tube (with subsequent increase in solubility), as well as increased conductive properties (Gooding *et al.*, 2007) as a result of the inclusion of electroactive moieties at these defective sites. Additionally, the presence of electroactive sites along the length of the *f*CNT is advantageous since it increases the possibility of more efficient electron transfer per unit area (Heng *et al.*, 2005).

4.4.1.2 Activation of GCE surface with catechol

This section examined the effect of activation of an unmodified glassy carbon electrode (GCE) surface and a GCE modified with *f*SWCNTs (of either 1, 4 or 9 hours functionalisation), by incorporating catechol, as per the approach of Kissinger & Heinemann (1996).

The electrocatalytic properties of catechol are well documented for application in modified electrode surfaces and for this purpose were utilised in the electrochemical activation of the electrode surface modified with *f*SWCNTs.

Figure 4.7 shows CVs comparing the current response at an unmodified GCE (solid line, inset) and at a GCE modified with *f*SWCNTs (6 hours, dotted line) for the detection of 1 x 10^{-3} M $[Fe(CN)_6]^{3-/4-}$ in 0.1 M KCl.

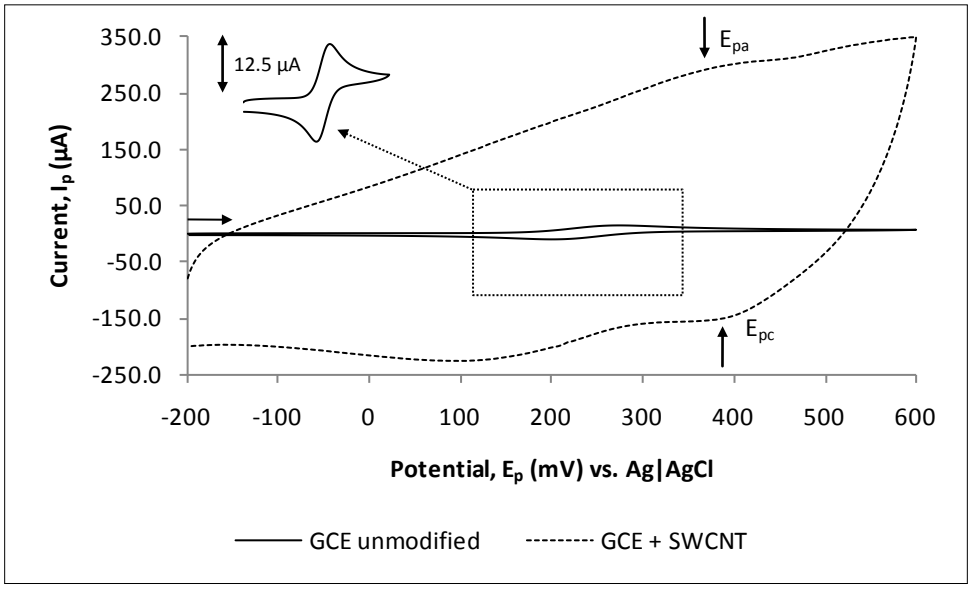

Figure 4.7 Comparative cyclic voltammograms of the redox activity of 1 mM $[Fe(CN)_6]^{3-}$and 1 mM $[Fe(CN)_6]^{4-}$ in 0.1 M KCl at GCE modified with *f*SWCNTs (6 hours) before activation (dotted line). The solid line shows the electrochemical response of $[Fe(CN)_6]^{3-/4-}$ at an unmodified GCE. Scan rate: 100 mV.s^{-1} vs. Ag|AgCl. *Key*: (E_{pa}) anodic and (E_{pc}) return cathodic scans.

While the current response at a modified electrode is markedly greater, the large background (Faradaic) current afforded by the nanotubes results in the masking of the redox peaks for $[Fe(CN)_6]^{3-/4-}$. Chen *et al.* (2008) ascribe this behaviour to an increase in surface area afforded by the nanotubes. The increased rectangular shape of the CV is indicative of an increase in capacitative behaviour.

Rectangular-shaped CVs over a range of scan rates are indicative of the electrode surface exhibiting desirable double layer capacitor properties (Chen *et al.*, 2002). In figure 4.8 the formation of a more rectangular-shaped CV occurs with increased scan rates, suggesting the possibility that the GCE modified with *f*SWCNTs (4 hours) exhibits optimum double layer capacitative properties between the nanotube/solution and nanotube/electrode interfaces.

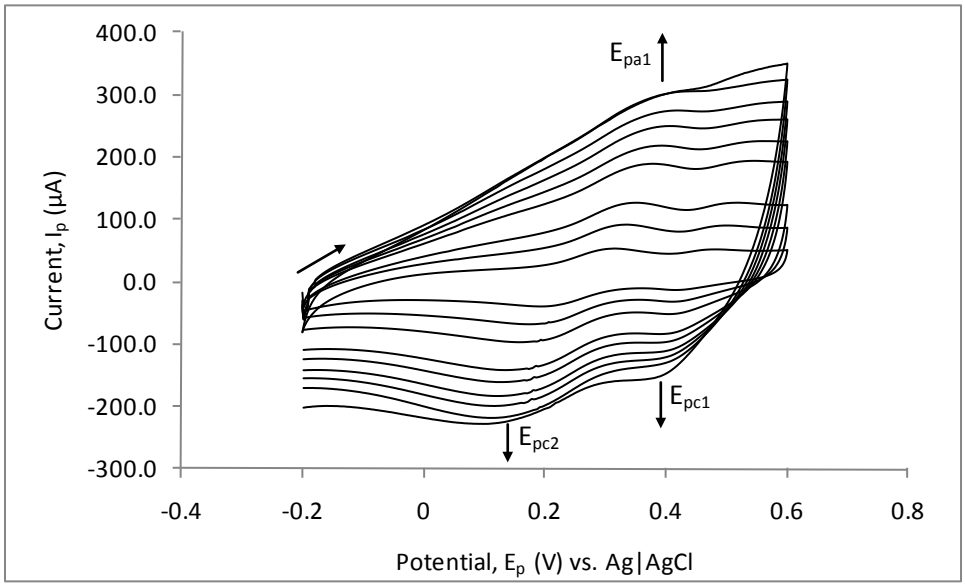

Figure 4.8 Cyclic voltammograms of the redox activity of 1 mM $[Fe(CN)_6]^{3-}$ and 1 mM $[Fe(CN)_6]^{4-}$ in 0.1 M KCl at GCE modified with *f*SWCNTs (4 hours) at increased scan rates from 5 $mV.s^{-1}$ – 100 $mV.s^{-1}$ vs. Ag|AgCl. *Key:* E_{pa1}: primary oxidation peak, E_{pc1}, E_{pc2}: primary and secondary reduction peaks, respectively.

In order to compare with CVs at *f*SWCNT-modified GCE, test scans showing the reversible redox pair for catechol at an unmodified GCE are shown in figure 4.9. A slight increase in the redox current response was noted after the first activation scan (i), after which the increase is nominal (ii) which could be attributed to less catechol being incorporated.

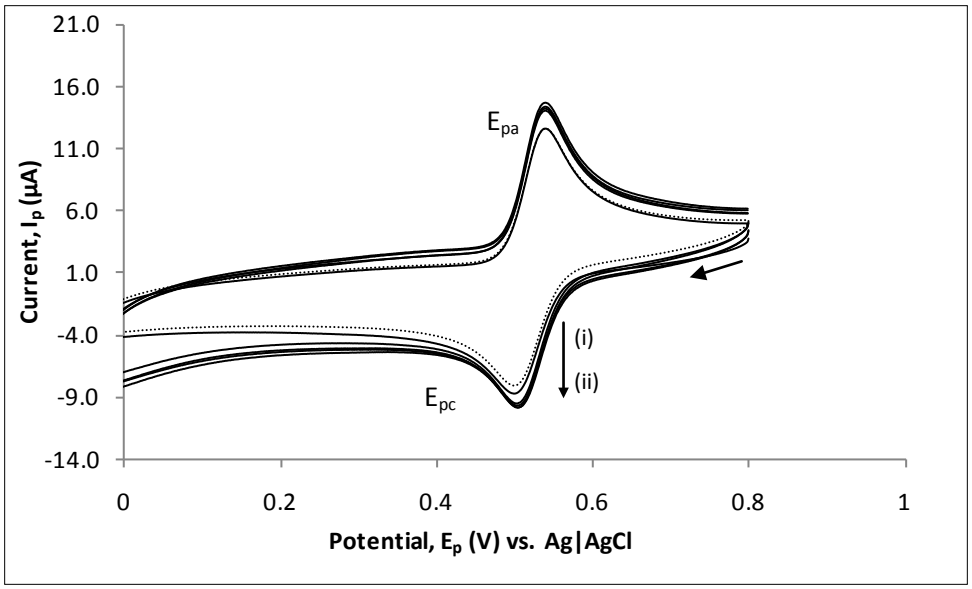

Figure 4.9 Cyclic voltammograms showing the test scans at an unmodified glassy carbon electrode in 0.45 mM catechol in 0.1 M H_2SO_4. Key: (i) (dotted line) is the first activation scan, with an increase in activation scan numbers (ii). Scan rate: 0.20 $V.s^{-1}$ vs. Ag|AgCl.

Figure 4.10 is an example of CVs obtained during the catechol test scans at a surface-activated *f*SWCNTs-modified GCE. Twin peaks were observed for the forward cathodic scan (E_{pc1}, E_{pc2}) as well as for the reverse anodic scan (E_{pa1}, E_{pa2}). When compared to an unmodified GCE (dotted line, i) E_{pa1} and E_{pc1} correlate with the redox pair for catechol, with E_{pc2} and E_{pa2} resulting from modification of the GCE with SWCNT. When the GCE is not activated by cycling in catechol a low current response for the redox peaks of catechol was observed. Both sets of peaks ($E_{pc1,2}$, $E_{pa1,2}$) do not increase significantly after 4 activation scans, suggesting surface saturation with catechol.

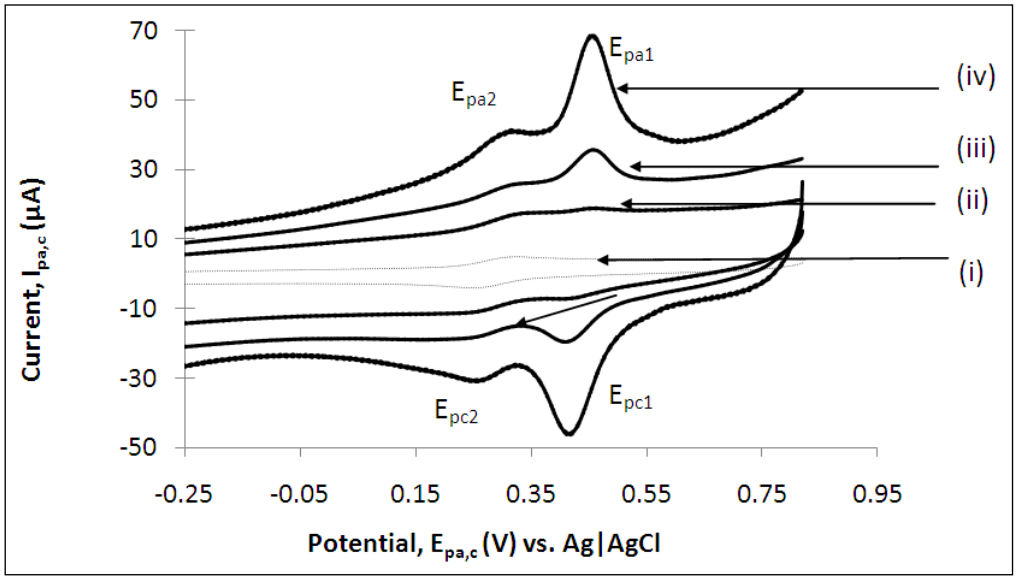

Figure 4.10 Test cyclic voltammogram scans of functionalised (4 hours) SWCNT-modified GCE after each electrochemical surface activation scan by using 0.45 mM catechol in 0.1 M H_2SO_4. Scan rate: 0.20 $V.s^{-1}$ vs. Ag|AgCl. *Key*: (ii)-(iv) test scans 1 to 3 respectively, dotted line (i): unmodified GCE (after 3 activation scans). E_{pc1}, E_{pa1}: catechol redox pair, E_{pc2}, E_{pa2}: SWCNT redox peak. Test scan 4 is similar to test scan 3 and was omitted for the sake of clarity.

Similar peaks (E_{pa2} and E_{pc2} on figure 4.10) were observed by Chen *et al.* (2008) for SWCNTs, and were ascribed by these authors to the presence of electroactive surface functional groups. Additionally, these peaks have been described to possibly result from metallic impurities that exist from the nanotube synthesis process (Skunik *et al.*, 2008). In addition, Skunik *et al.* (2008) do not discount the plausibility of the peaks resulting from surface electroactive groups at the open ends of the tubes. Barisci *et al.* (2000) attribute broad peak pairs in the aforementioned region to the interfacial redox activity of carboxyl or chinone moieties.

Surface activation at an unmodified GCE (figure 4.9) resulted in a 1.5 µA increase in current response over 3 activation scans. In comparison, the GCE modified with *f*SWCNTs acid functionalised for 4 hours (figure 4.10) resulted in a 37 µA increase in the current response for the catechol redox pair over 3 scans. Additionally, at an unmodified GCE, the forward cathodic peak for catechol was observed at a potential of 0.55 V which shifted to 0.45 V at the electrode modified with *f*SWCNTs (4 hours), suggesting a desired electrocatalytic behaviour of the nanotube modified layer. A negligible increase in current

response after 3 scans was noted, which could be attributed to the saturation of the electrode surface with catechol.

In order to further elucidate the properties of the surface interaction and conductive properties of the modified electrode surface, electrochemical impedance spectroscopy (EIS) was performed.

4.4.1.3 Assessment of modified electrodes by electrochemical impedance spectroscopy

The impedance data in this section is represented as a set of complex plane plots, specifically: Nyquist (Z_{REAL} vs. Z_{IMAG}) and Bode (log f vs. Θ) plots. These plots had been obtained by the application of a Randles' equivalent circuit where the double layer capacitance was replaced with a constant phase element, CPE (Q) since the latter is a more accurate representation of actual (real) resistance (Retter & Lohse, 2002). In particular, the interfacial capacitance, C_{calc} can be used to compare capacitative behaviour between the various modified electrode surfaces, as calculated using equation 4.03 (Hsu & Mansfeld, 2001).

$$C_{calc} = (Y_o R_{ct})^{1/\alpha} / R_{ct} \qquad [4.03]$$

The equivalent circuit used for all impedance studies to fit the EIS data is the Randles' equivalent circuit of mixed kinetic and diffusion control shown in scheme 4.1, and exhibited the characteristic semi-circles at high frequencies and a straight line at low frequencies corresponding to kinetic and diffusion processes, respectively.

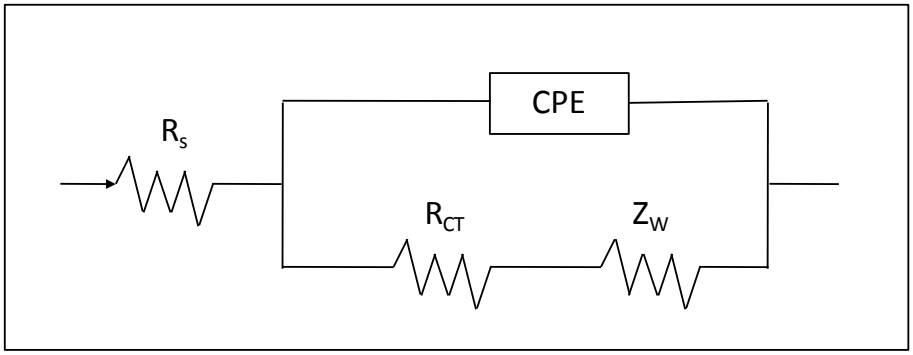

Scheme 4.1 The equivalent circuit used for impedance studies at the thin-film electrode-electrolyte interface. The constant phase element (CPE, Q) is a more accurate representation of actual resistance than the conventional double layer capacitance used in Randles' equivalent circuits for ideal resistors. *Legend*: R_{ct}: Charge transfer resistance, R_s: Solution resistance, Z_W: Warburg impedance. CPE: Constant phase element, Q.

The *f*SWCNT physically adsorbed onto the GCE was activated by cycling in 0.45 mM catechol, and the change in impedance, Z after each activation cycle assessed using EIS. The effect of activation of a GCE modified with *f*SWCNTs (4 hours) is shown in figure 4.11 (A – B).

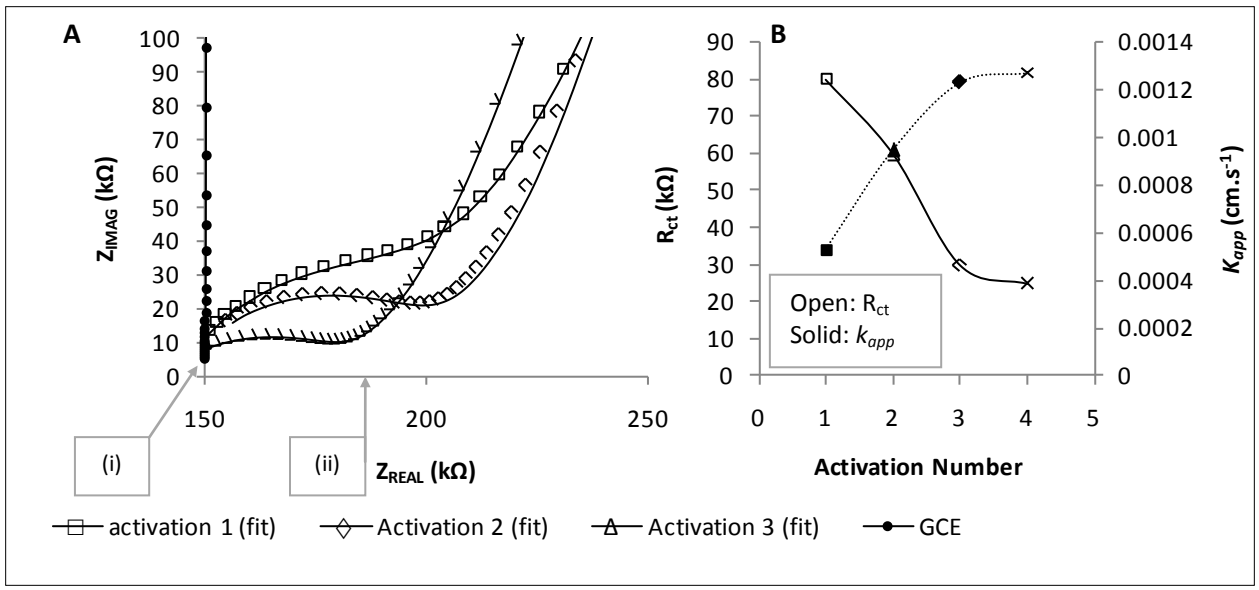

Figure 4.11 (A) Representative Nyquist plot and line graph (B) showing the decrease in charge transfer resistance (R_{ct}) of a GCE modified with *f*SWCNTs (4 hours) with each activation scan in 0.45 mM catechol. *Key*: (i) x-axis intercept 1 = solution resistance, R_s, (ii) x-axis intercept 2 = polarisation resistance R_Ω. Solid lines in (A) indicate fitted data.

Two well-defined areas can be observed from Nyquist plots. At high frequency regions [(i) on figure 4.11 (A)], the capacitative behaviour can be determined. At lower frequency regions [(ii) on figure 4.11 (A)], information regarding the interfacial processes affecting the electrode or modification layers can be obtained (Wang *et al.*, 2005). In figure 4.11 (A), at the high frequency region, a straight line that is near perpendicular to the real impedance (Z_{REAL}, Z') was observed for the unactivated GCE, that intersects the Z' axis at Z' = R_Ω =150 kΩ. An angle for this line, δ_f of less than 90° was obtained, which is attributed to surface contamination and roughness of the solid electrode (Chen *et al.*, 2002; Geraldo *et al.*, 2008). According to Retter & Lohse (2002), a straight line obtained for the impedance at a solid electrode, with the straight line intersecting the Z' axis at Z' = R_Ω is a characteristic observation.

The diameter of the semi-arcs for activation cycles 1 through 3 are shown in figure 4.11 (A) to decrease with each activation cycle, indicative of a possible decrease in the charge transfer resistance of the modified layer due to increased conductivity. The diameter of the semi-arc is equivalent to the charge transfer resistance, R_{ct} which is expressed as:

$$R_{ct} = (R_\Omega - R_s) \qquad [4.01]$$

Where R_s is the solution resistance (x-intercept at high frequency, Ω), R_Ω is the polarisation resistance (x-intercept at the low frequency, Ω), denoted as (i) and (ii) respectively on figure 4.11 (A).

The apparent electron transfer rate, k_{app} (cm.s^{-1}), as shown in figure 4.11 (B), is the rate of electron transfer across the electrode layer, and was derived from the following equation:

$$k_{app} = \frac{R.T}{F^2 A.C.R_{ct}} \qquad [4.02]$$

Where R = Universal gas constant (J.mol^{-1}.K^{-1}), T = temperature (K), F = Faradays constant (C.mol^{-1}), C = concentration of [Fe(CN)6]$^{3-/4-}$ 1 x10^{-6} mol.cm^{-3}, R_{ct}= charge transfer resistance (Ω) (Sabatani & Rubinstein, 1987).

An increase in the ease of electron flow is indicated by a larger value for k_{app}. In figure 4.11 (B) k_{app} was observed to increase from 0.5 x 10^{-3} cm.s^{-1} to 1.3 x 10^{-3} cm.s^{-1} between the first and third activation scans. In comparison, R_{ct} decreased from 80 kΩ to 30 kΩ. A decrease in R_{ct} in conjunction with an increase in k_{app} indicates a rapid transfer of electrons to the electrode surface, potentially afforded by an ease of electron passage due to a decrease in the resistance of the layer.

The conductivity of the catechol modified layer could be attributed to the applied catechol surface activation of the electrode surface, since the aforementioned increase in conductivity was not observed prior to surface activation. Further evidence of an increase in surface conductivity was shown through an increased current response for the redox pair of catechol at both a modified and unmodified GCE surface.

4.4.1.4 Comparison of the effect of activation on SWCNTs functionalised at different times

A GCE was modified (through physical adsorption) with each of the SWCNT samples functionalised for between 1 and 9 hours. Each functionalisation time, consisting of 1 hour intervals, was assessed separately and compared. Additionally, activation and subsequent test scans in the presence of catechol were performed as prescribed by Kissinger & Heinemann (1996) for a GCE.

Figure 4.12 (A) shows representative CVs of the redox behaviour of catechol at an unmodified GCE and compared to GCE modified with SWCNTs that had been functionalised for 1, 4 and 6 hours, respectively. For the sake of brevity, only the cyclic voltammograms of a GCE modified with *f*SWCNTs of 1, 4 and 6

hours are shown. Figure 4.12 (B) is a summary of the range of *f*SWCNTs tested and their current responses for each of the activation steps (1 to 3).

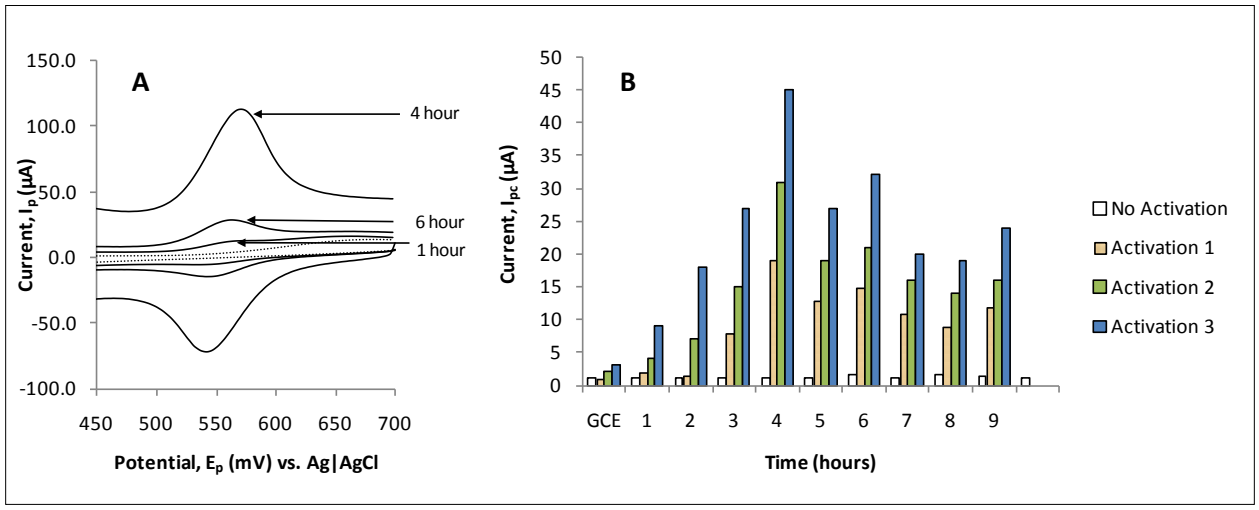

Figure 4.12 (A) The increase in the current magnitude for the forward cathodic scan for the reduction of catechol during the test scan, for each of the time intervals of SWCNT acid functionalisation (1, 4 and 6 hours, respectively). Dotted line is the GCE. (B) Bar graph represents a summary of cathodic current response, I_{pc} (µA) for the test scan for 0.45 mM catechol (prepared in 0.1 M H_2SO_4) forward reduction peak for each sample of *f*SWCNTs as compared to a GCE, after each activation cycle. Activation cycle: 0 mV to 1780 mV (vs. Ag|AgCl) at 200 mV.s^{-1}. Test cycle: 800 mV to -150 mV (vs. Ag|AgCl) at 100 mV.s^{-1}. S.d = 3. Error bars were omitted for clarity were all within the 95 % confidence interval.

According to Kissinger & Heinemann (1996), catechol is a highly effective electron transfer mediator that readily integrates between materials immobilised onto an electrode surface. This allows for more efficient electron transfer between nanotubes in this instance, as well as between the nanotubes and the electrode surface. This is thus evident as the linear increase in current with activation cycle, which was observed at each surface examined, figure 4.12 (B).

The increased current response noted for *f*SWCNTs (4 hours), figure 4.12(B) could be as a result of the acid functionalisation process, where carboxylation of the terminal ends of the nanotubes results in an increased conductivity and active surface area. The marked decrease after 4 hours could be attributed

to the fragmentation of nanotubes resulting in a loss of the intrinsic conductive properties of the nanotubes. Jiang *et al.* 2005 had discovered that extensive graphitisation of nanotubes resulted in a decrease in capacitance and conductance. Interestingly, an increase in current response was observed for nanotubes functionalised for 9 hours, figure 4.12(B), which could be attributed to an increased surface area of nanotube sections afforded by the acid fragmentation and functionalisation process.

The resultant current response from electrochemical activation was affected by the number of activation cycles performed, as well as the duration of nanotube functionalisation. With respect to the electrochemical activation cycles performed, it was noted that the current response for the catechol test scan increased with consecutive scans, regardless of the form of *f*SWCNTs used. Interestingly, the current response for the test catechol scan showed a marked decrease after 3 consecutive electrochemical activation scans. This decrease could be attributed to many factors, notwithstanding electrode surface saturation with catechol resulting in current damping. In addition to the number of activation scans, the form of *f*SWCNTs was noted to have an effect on the electron transfer efficiency of the modified electrode surface, apparent from the additional peaks denoted as E_{pc1} and E_{pa1} on figure 4.10. In figure 4.12 (B) it can be seen that at an unmodified GCE surface the current response for the test catechol scan was low in comparison to a GCE surface modified with nanotubes. Of particular interest is the difference in current response for the different times used for SWCNT-functionalisation. A near-linear increase in current response was noted for nanotubes functionalised between 1 and 4 hours, with a maxima observed at 4 hours functionalisation. A marked decrease was observed for 5 hours, with an increase at 6 hours and a further decrease between 7 and 9 hours functionalisation.

In order to further elucidate the electrical properties of the modified electrodes, electrochemical impedance spectroscopy (EIS) was performed. In particular, the capacitative and resistive behaviour of modified electrodes was ascertained by applying Nyquist plots (Z_{REAL} versus $Z_{IMAGINARY}$) and monitoring the change in capacitance (CPE, Q_{calc}) and indicators of resistance (R_{ct}, R_{Ω}). Nyquist plots for GCE modified with *f*SWCNTs (1, 4, 6, and 8 hours) are shown in figure 4.13.

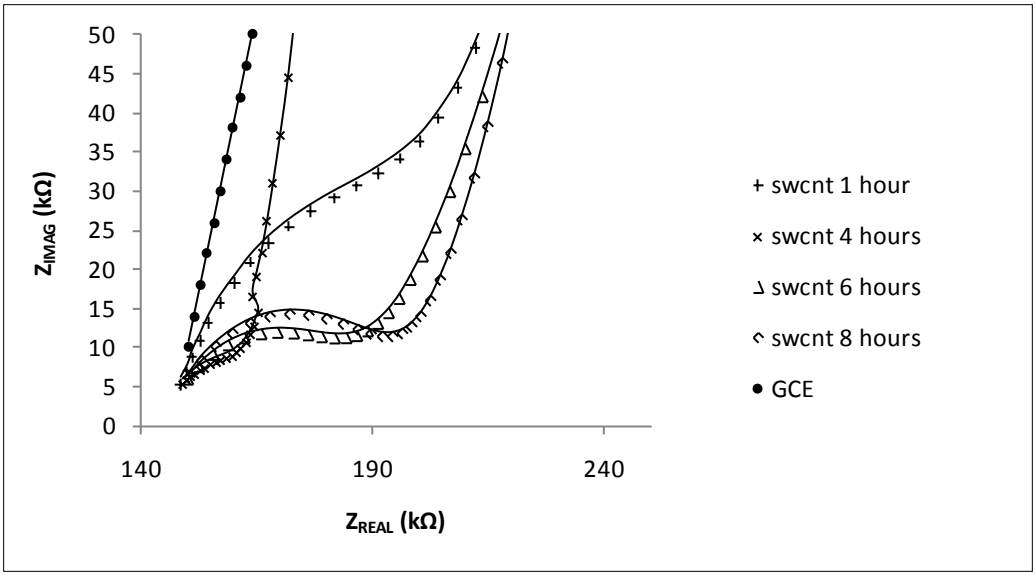

Figure 4.13 Nyquist plots of SWCNT samples taken at 1, 4, 6 and 8 hours, all adsorbed onto a GCE, and compared to an unmodified GCE after 3 activation scans. Lines indicated fitted data.

An unmodified GCE exhibited a characteristic straight line with an angle, δ_f of less than 90°, which is attributed to surface contamination and roughness of the solid electrode (Geraldo *et al.*, 2008). A GCE modified with SWCNTs that had been functionalised for 1 hour showed a large semi-arc, with a smaller arc observed for 4 hours functionalised SWCNTs, increasing with each of 6 and 8 hours functionalisation, respectively. The smaller arc at 4 hours SWCNTs functionalisation indicates an easier electron passage to the electrode. A more hindered electron passage was observed as larger semi-arcs when the functionalisation time was increased, suggesting that with an increase in functionalisation beyond 4 hours a dominant contribution of resistance, R_{ct} occurs either at the SWCNT-electrode or the SWCNT-solution interface (Pillay & Ozoemena, 2009) therefore hindering efficient flow of electrons. This result is congruent with that observed in figure 4.12 (B), providing a rational basis for the increase in current from *f*SWCNT-modified electrodes at 1 hour to that at 4 hours, followed by a decrease at 6 hours.

Electrochemical activation of nanotubes immobilised onto an electrode surface and in the presence of KOH was shown by Frackowiak *et al.* 2002 to increase electron transfer kinetics across the modified layer, and was attributed by the authors to the intercalation of potassium ions between nanotubes affectively creating a micro- and mesoporous network conducive to the promotion of effective redox

processes to the electrode surface. Additionally Frackowiak *et al.* (2002) describe the process of electrochemical activation to be very efficient for producing the aforementioned pores, without damaging the tubular integrity of the nanotubes.

Figure 4.14 compares the values for R_{ct} before and after activation in the presence of catechol for each of an unmodified GCE, and GCE modified with each of SWCNTs functionalised for either 1, 4, or 8 hours.

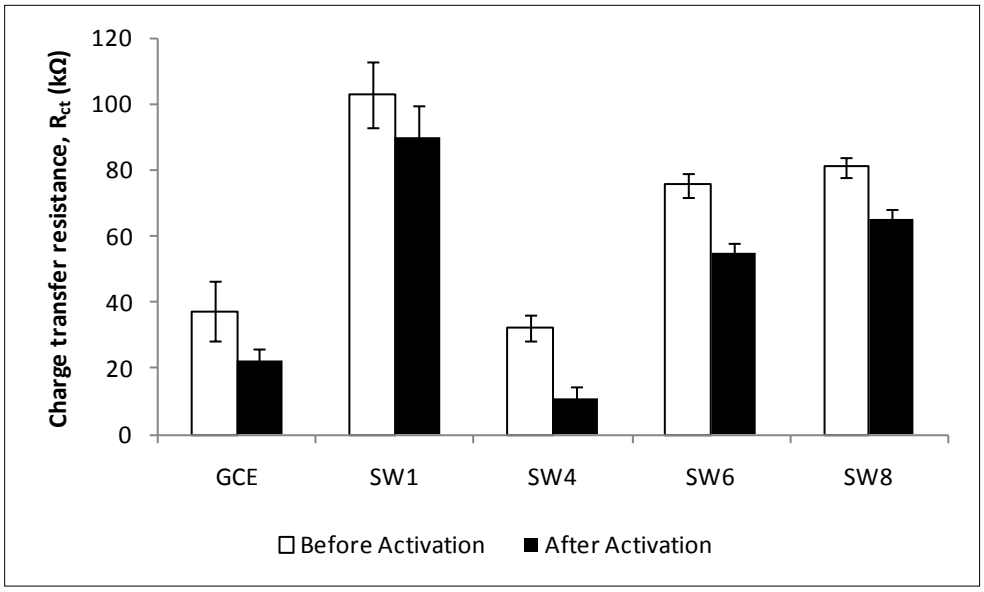

Figure 4.14 Comparison of charge transfer resistance (Rct) at functionalised (fSWCNT) before and after surface activation with catechol. Key: SW indicates functionalised single-walled carbon nanotubes. The number denotes the hours of functionalisation.

At an unmodified GCE the ohmic charge transfer resistance of 39.90 kΩ was obtained (figure 4.14), which decreased to 24.60 Ω after three activation scans in the presence of catechol. Interestingly, at a GCE modified with SWCNTs functionalised for 1 hour (before activation) the R_{ct} was observed to be 104.20 kΩ, which is significantly higher than at an unmodified GCE. After three activation scans the R_{ct} for *f*SWCNTs, (1 hour) was shown to decrease to 91.30 kΩ.

When a GCE was modified with *f*SWCNTs (4 hours) the initial R_{ct} was found to be 33.60 kΩ, which is marginally lower than an unmodified GCE. After three activation scans a marked decrease in R_{ct} to 14.60 kΩ was obtained. Similar decreases in R_{ct} from before performing activation to after three activation scans were observed for *f*SWCNTs (6 and 8 hours, respectively), with the R_{ct} increasing with increasing functionalisation time.

A higher R_{ct} for each *f*SWCNT-modified electrode before the activation scans could be attributed to the addition of the nanotube layer onto the electrode surface, acting as an insulator, which retards the movement of electrons through the layer to the electrode. In all instances, the R_{ct} was observed to decrease after applying three electrochemical activation scans, suggesting a facilitated electron passage afforded by the integration of catechol moieties between adjacent functionalised nanotubes as well as the electrode surface (Barsoukov & Macdonald, 2005). This creates an interconnected meso- and microporous cage-like network, which is key to efficient electron transport facilitation through enhanced charge accumulation (Frackowiak *et al.*, 2002).

The highest R_{ct} was recorded for a GCE modified with SWCNTs functionalised for 1 hour. The lower amount of functional groups added at this interval results in nanotubes that are highly aggregated and predominantly hydrophobic in nature, which decreases the wettability of the nanotube layer in direct contact with the electrolyte solution. Additionally, the nanotubes' active surface area is smaller due to the convolution of the aggregates, with large areas between adjacent aggregates of nanotubes, which may increase the resistance of the layer. These structural attributes retard the efficient flow of electrons (Frackowiak *et al.*, 2002; Jiang *et al.*, 2005; Chen *et al.*, 2008).

The lowest R_{ct} was recorded for *f*SWCNTs (4 hours functionalisation, with 6 and 8 hours yielding only slightly greater R_{ct} values (figure 4.14). A decreased in R_{ct} values is associated with an increase in surface functional groups as a direct result of acid functionalisation (Chen *et al.*, 2008). The greatest difference between R_{ct} determined before and after activation was observed for *f*SWCNTs (4 hours and 6 hours).

The microporosity of nanotubes is significantly increased with electrochemical activation (Frackowiak *et al.*, 2002), and with the increased surface area of nanotubes afforded by the acid functionalisation process, a greater network of micro- and mesopores is formed which markedly enhances the charge accumulation and subsequent current response efficiency, which can explain the decreased resistance observed for SWCNTs functionalised for greater than 4 hours.

Gooding *et al.* (2007) describe the interactions that occur between the walls of unfunctionalised (hydrophobic) nanotubes and the functionalised groups (hydrophilic) added along the walls of adjacent nanotubes at defects introduced by the acid treatment process, a phenomenon observed for SWCNTs functionalised for 4 hours, figure 4.3 (B).

Islands of nanotubes with exposed hydrophobic areas will result in lowered capacitance due to lowered surface area and electron transfer (Skunik *et al* 2008). This observation could account for the rapid rise in Z_{IMAG} at lower frequencies as observed in figure 4.11, since this behaviour is similar to what was observed at an unmodified electrode. A small amount of energy can however be stored in aggregates due to hydrophilic regions introduced through acid functionalisation (Skunik *et al.*, 2008), resulting in the lowered impedance observed for SWCNTs functionalised for 4 hours (figures 4.13 and 4.14).

The creation of defects along the walls of functionalised nanotubes allows for pore formation, which leads to increased capacitance due to network formation with catechol moieties. The capacitance of a modified layer can be determined from Nyquist and Bode magnitude plots. The constant phase element (CPE, C_{calc}), is accepted as a realistic indication of the capacitative behaviour of surfaces. Otherwise referred to as electrochemical capacitance, CPE depends on the pore structure and surface functional groups of the electrode surface or added layer (Chen *et al.*, 2008). Skunik *et al.* (2008) have described higher capacitances to occur at nanotubes with greater surface defects.

Bode plots of the unmodified GCE as compared to *f*SWCNTs (1, 4, 6 and 8 hours) are shown in figure 4.15, with well-defined symmetrical peaks observed for the unmodified GCE and each of the 4 *f*SWCNTs modifications assessed. The phase angle (Θ), frequency (Hz), capacitance factor and interfacial capacitance (C_{calc}) (as calculated using equation 4.03) are tabulated in table 4.1.

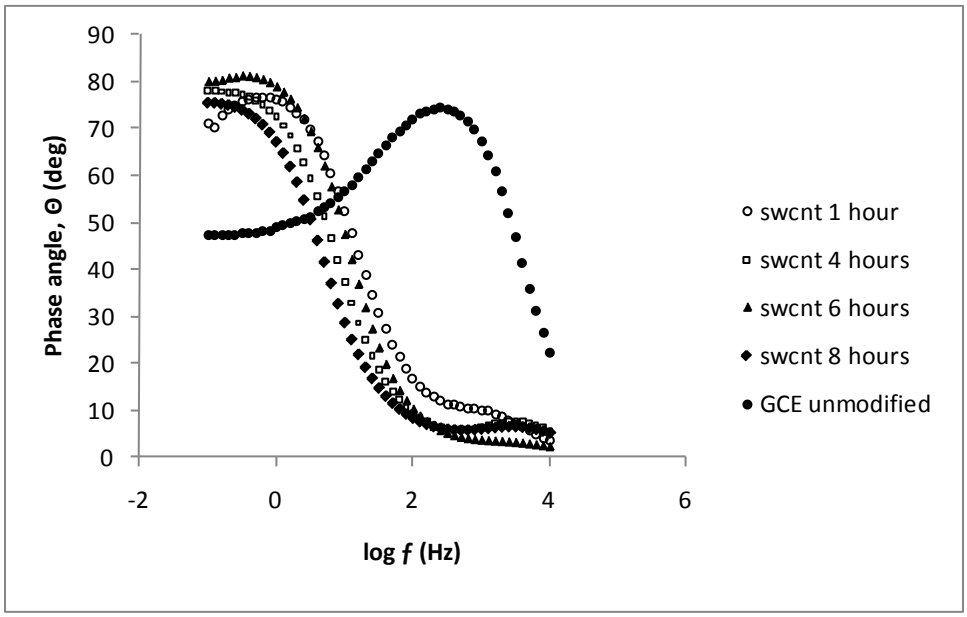

Figure 4.15 Bode plots for GCE modified with SWCNTs, functionalised by acid treatment for 1, 4, 6, and 8 hours respectively as compared to an unmodified GCE.

The phase angle and frequency values obtained from the Bode plots in figure 4.15 are tabulated (table 4.1) in addition to the capacitance factor obtained from the gradient of the magnitude plots.

Table 4.1 Comparison of phase angle shift, frequency drift, and the change in capacitance factor between various SWCNT electrode modifications and an unmodified GCE.

ELECTRODE	PHASE ANGLE, Θ (DEG)	FREQUENCY, f (Hz)	CAPACITANCE FACTOR† (R^2)	INTERFACIAL CAPACITANCE, C_{calc} (μF)
GCE_{UNMOD}	75	246.04	-0.530 (0.9999)	241.54
GCE_{ACT}	67	394.50	-0.540 (0.9998)	296.47
$SW1_{UNACT}$	76	2.36	-0.902 (0.9998)	30.16
$SW1_{ACT}$	78	1.02	-0.900 (0.9997)	36.90
$SW4_{UNACT}$	76	11.23	-0.867 (0.9998)	14.36
$SW4_{ACT}$	78	9.85	-0.893 (0.9998)	13.15
$SW6_{UNACT}$	78	0.91	-0.939 (0.9998)	25.87
$SW6_{ACT}$	80	0.48	-0.933 (0.9999)	27.96
$SW8_{UNACT}$	72	8.21	-0.931 (0.9999)	37.59
$SW8_{ACT}$	75	7.58	-0.863 (0.9998)	40.38

† Obtained from the slope of magnitude plots, a value of -1 is indicative of an ideal capacitor whereas a value of 0 is an ideal resistor.

‡ Q Obtained from a Nyquist plot (figure 4.13), C_{calc} calculated using equation 4.03.

Information regarding frequency shifts can be obtained from Bode plots. A phase angle, Θ of 67° at 394.50 Hz for an unmodified GCE (as shown in table 4.1), corresponds to the relaxation phase of a typical GCE/solution interface (Geraldo *et al.*, 2008).

Phase angles near 90° in conjunction with capacitance factors near -1 suggest ideal pseudocapacitative properties. A shift in the peak optima from between 72° and 75° for each of the electrode modifications before activation, to between 75° and 80° after activation indicates that the $[(FeCN)_6]^{3-/4-}$ redox processes occur at the modified layer rather than at the electrode surface (Pillay & Ozoemena, 2009).

Additionally, estimated slopes of the magnitude plots tabulated in table 4.1 are near -1 after modification suggesting an acquisition of near ideal capacitor properties (Ozoemena *et al.*, 2007). The lower C_{calc} observed for each of the *f*SWCNTs modified electrodes, as compared to the unmodified GCE implies that the added *f*SWCNTs were incapable of large capacitance storage, attributed largely to a greater R_{ct}.

Interestingly, a significantly larger increase in the slope for activated *f*SWCNTs functionalised for 4 hours was observed in contrast to what was observed at other surfaces. This observation could explain the proportionately larger current response obtained for *f*SWCNTs (4 hours), as indicated in figure 4.12 (B), following activation. Increased graphitisation (8 hours functionalisation) however, tends to result in lowered ideal capacitor behaviour, regardless of a perceived increase in pseudocapacitance afforded by the increased surface area of highly functionalised nanotubes.

4.4.1.5 Effect of SWCNT functionalisation time and activation on the apparent rate of electron transfer, k_{app}

The efficacy of electron transport can be assessed through the rate of apparent electron transfer, k_{app} using the experimentally determined values for R_{ct} (figure 4.14), the apparent rate of electron transfer,

k_{app} (cm.s^{-1}) can be calculated using Equation 4.02. Figure 4.16 illustrates the relationship between k_{app} (cm.s^{-1}) and acid functionalisation time.

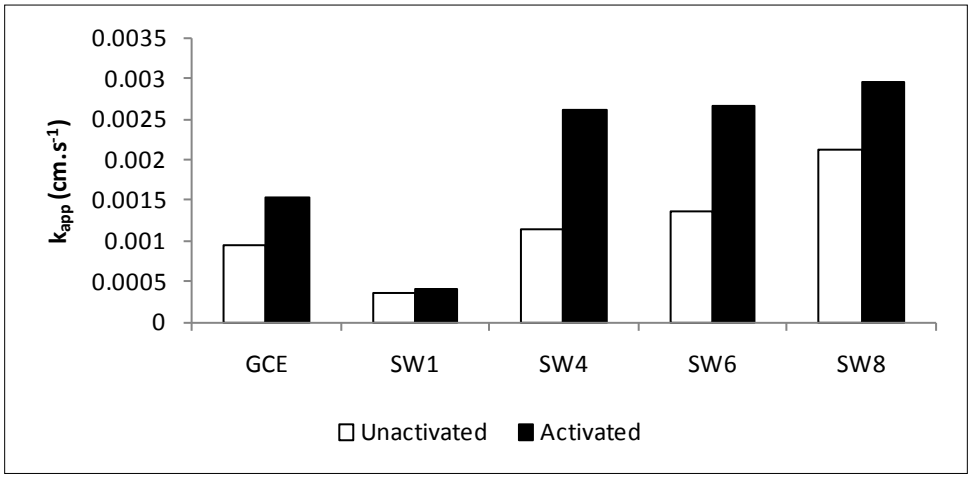

Figure 4.16 The change in electron transfer rate, k_{app} before and after activation scans for SWCNTs functionalised for 1 hour (SW1), 4 hours (SW4), 6 hours (SW6), and 8 hours (SW8). *Key:* Δ k_{app} (%) indicates the difference between activated and unactivated electrode surfaces for the rate of electron transfer.

In figure 4.16 a marked increase in the rate of electron transport was observed for before and after electrochemical activation for each of the functionalised nanotube electrodes, corresponding to a decrease in R_{ct} as shown in figure 4.14.

A GCE modified with SWCNTs functionalised for 1 hour exhibited the lowest increase in k_{app}, which implies that the modified layer hinders redox processes to the electrode surface. This is further shown by the greater R_{ct} shown in figure 4.14 for *f*SWCNTs (1 hour). However a marked capacitance for *f*SWCNTs as shown in table 4.1 suggests the layer is capable of energy storage. It is well established that hydrophobic groups do not contribute to the capacitance of nanotubes (Chen *et al* 2008) which implies that discrepancies in surface coverage homogeneity, as observed for nanotubes functionalised for 1 hour, results in the surface layer behaving differently depending on its coverage and wettability (Frackowiak *et al.*, 2002; Jiang *et al*., 2005; Chen *et al.*, 2008; Skunik *et al.*, 2008).

4.4.1.6 Summary

With reference to figure 4.11 (A, B), activation of the *f*SWCNTs-modified electrode surfaces in the presence of catechol had shown the greatest decrease in R_{ct} for *f*SWCNTs functionalised for 4 hours, from 80 kΩ to 30 kΩ between the first and third scans, respectively. Additionally a corresponding increase in k_{app} from 5 x 10^{-4} Ω.cm^{-1} to 12 x10^{-4} Ω.cm^{-1} was noted for the aforementioned scans. Interestingly, when compared to figure 4.12 (A, B), a corresponding increase in current response was observed for each modified surface from scan 1 to 3, regardless of the functionalised state of the nanotubes added to the electrode surface. This indicates a feasible possibility that an ease of passage of electrons to the electrode surface is afforded by activation of the modified surfaces in the presence of catechol. A near linear increase in current response was observed for SWCNTs functionalised from 1 – 4 hours [figure 4.12 (B)]; however this trend was not observed for SWCNTs functionalised for longer than 4 hours. The reason for the non-linear nature of current response increase after 4 hours functionalisation was further explored and supported through EIS studies, where R_{ct} was observed to increase after 4 hours functionalisation (figure 4.14), which offers a plausible explanation for the erratic current response obtained for SWCNTs functionalised for a longer duration. Interestingly, 6 hours functionalisation exhibited a sharp increase in current response [figure 4.11 (B)] and a corresponding increase in k_{app}, suggesting a greater efficiency in electron transport to the electrode surface (with resultant increases in Faradaic current), influenced by increased capacitance and lowered resistance due to increased functional groups, hydrophilicity, surface area (Zhou *et al.*, 2004) and surface homogeneity afforded by an enhanced homogeneous meso- and microporous network (Frackowiak *et al.*, 2002; Jiang *et al.*, 2005; Musameh *et al.*, 2005; Jurewicz *et al.*, 2006; Wang *et al.*, 2005; Chen *et al.*, 2008; Skunik *et al.*, 2008; Jang *et al.*, 2009; Yuan *et al.*, 2010). This is further evidenced by the visual structural difference between unfunctionalised and acid functionalised SWCNTs [figure 4.3 (A, B)].

In this instance, a minimum of 4 hours functionalisation with a maximum of 6 hours is recommended since a decline in structural integrity of the SWCNTs was observed after 6 hours functionalisation, attributed to damage incurred by the SWCNTs as a result of the acid treatment. Furthermore the inclusion of catechol in the "activation" of the SWCNT has been justified through increased current response, lowered R_{ct} and increased k_{app}.

4.4.2 Multi-walled carbon nanotubes

4.4.2.1 Functionalisation and characterisation of multi-walled carbon nanotubes

The functionalisation of multi-walled carbon nanotubes (*f*MWCNTs) was performed by employing the same approach as described for the functionalisation of SWCNTs (section 4.3.2). Figure 4.17 shows the washing step for *f*MWCNTs samples taken at each hour.

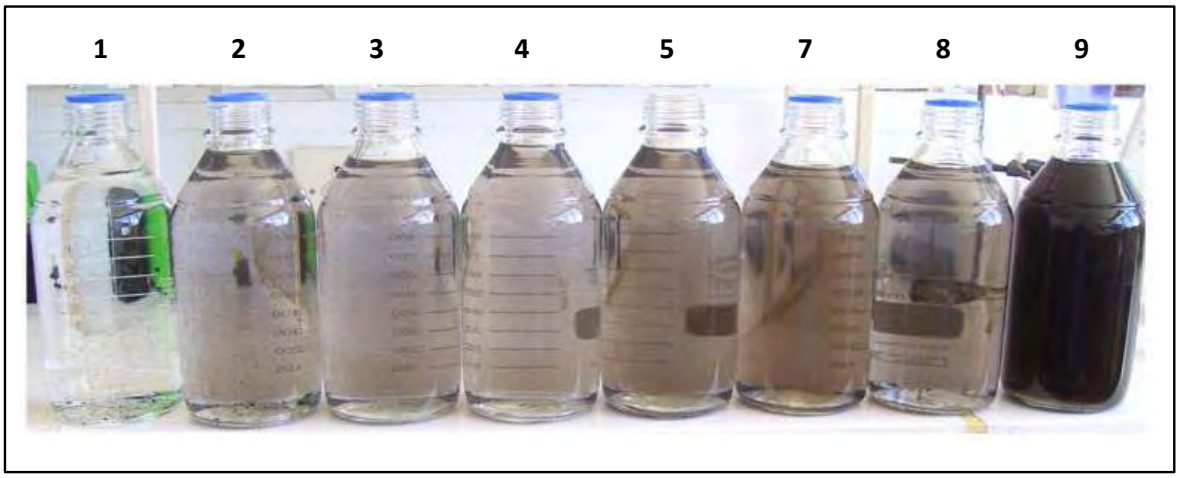

Figure 4.17 Functionalisation and cleaning of MWCNTs: Schott bottles showing the rinsing of samples of multi-walled carbon nanotubes taken at each hour of the functionalisation process and in *d*H_2O. The numbers denote the length of time of acid treatment in hours.

After 1 hour the *f*MWCNTs were observed to precipitate as aggregates, while after 9 hours a homogeneous suspension of *f*MWCNTs was clear, similar to that observed for the *f*SWCNTs.

Visualisation of the *f*MWCNTs was performed using atomic force microscopy (AFM) as well as high resolution scanning microscopy (HRSEM). Figures 4.18 (A – C) are AFM images and their corresponding topographical representations showing the morphologies of *f*MWCNTs at 1 hour, 4 hours and 9 hours of functionalisation.

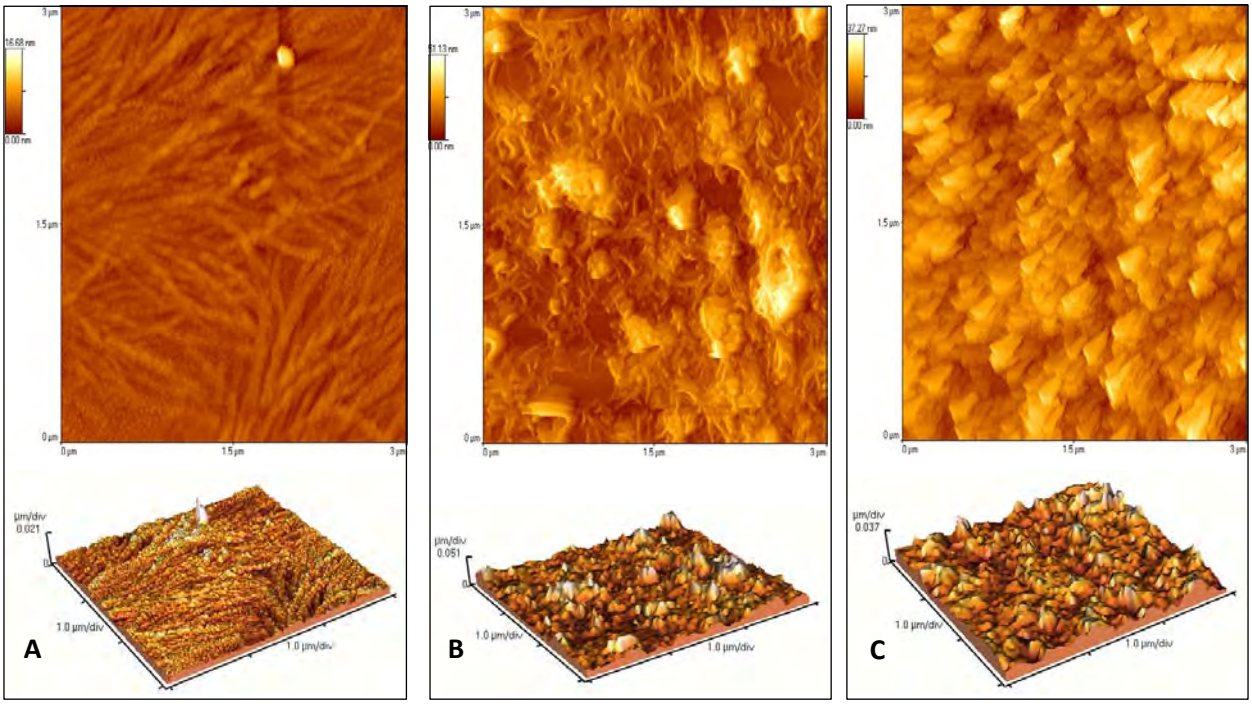

Figure 4.18 (A – C) AMF images of MWCNT drop dried onto a glassy carbon electrode, at various stages of nanotube functionalisation through acid treatment. *Key:* A) = MWCNT after 1 hour, B) = 4 hours and C) = 9 hours.

Long tubes were observed for nanotubes that were exposed to acid treatment for 1 hour, figure 4.18 (A). Similar observations have been reported by Goyanes *et al.* (2007) and Lamprecht *et al.* (2009) for short functionalisation times. After 4 hours of functionalisation, figure 4.18 (B) the length of the nanotubes was observed to decrease as a result of perforation along the walls of the tubes due to acid treatment. A heterogeneous mixture of shorter and longer nanotubes was observed which could be attributed to non-uniform rates of functionalisation and subsequent tube perforation. Additionally the nanotubes tend to aggregate which has been described by Bhushan (2004) to be due to the preference of a mixture of nanotubes to associate with each other to form bundles. This is due to the hydrophobic terminal ends reacting with the hydrophobic walls of adjacent tubes. While this is not ideal for the formation of uniform monolayers, theoretical calculations have shown that the aggregated nanotubes increase the efficiency of molecular binding through the formation of pores within the aggregates (Bhushan, 2004) which makes this form of nanotube a consideration for biosensor construction. After 9 hours of functionalisation, figure 4.18 (C) a homogeneous solution of nanotubes of similar lengths was observed and interestingly the nanotubes aligned in a uniform manner on the surface. Alignment of

nanotubes in this manner has been described by Bhushan (2004) to occur due to van der Waals interactions between adjacent nanotubes, resulting in self-assembly like behaviour.

Figure 4.19 (A –C) compare the HRSEM morphologies of *f*MWCNTs at 4 hours functionalisation. In Figure 4.19 (A) varying lengths of *f*MWCNTs were observed, the tube depicted by the arrow being at least 9 µm in length. In Figure 4.19 (B), the capped MWCNTs (white arrow) are clearly distinguishable from the uncapped (black arrows) *f*MWCNTs that occur during the functionalisation process. Additionally in figure 4.19 (B) the terminal C_{60} hemispheres had been observed to have been removed from the nanotubes, to reveal hollow tubular nanostructures. In figure 4.19 (C) the effect of prolonged exposure to the strong acid medium utilised in the functionalisation process resulted in defects occurring along the walls of the tubes, which lead to the tubes perforating and breaking into smaller tube fragments.

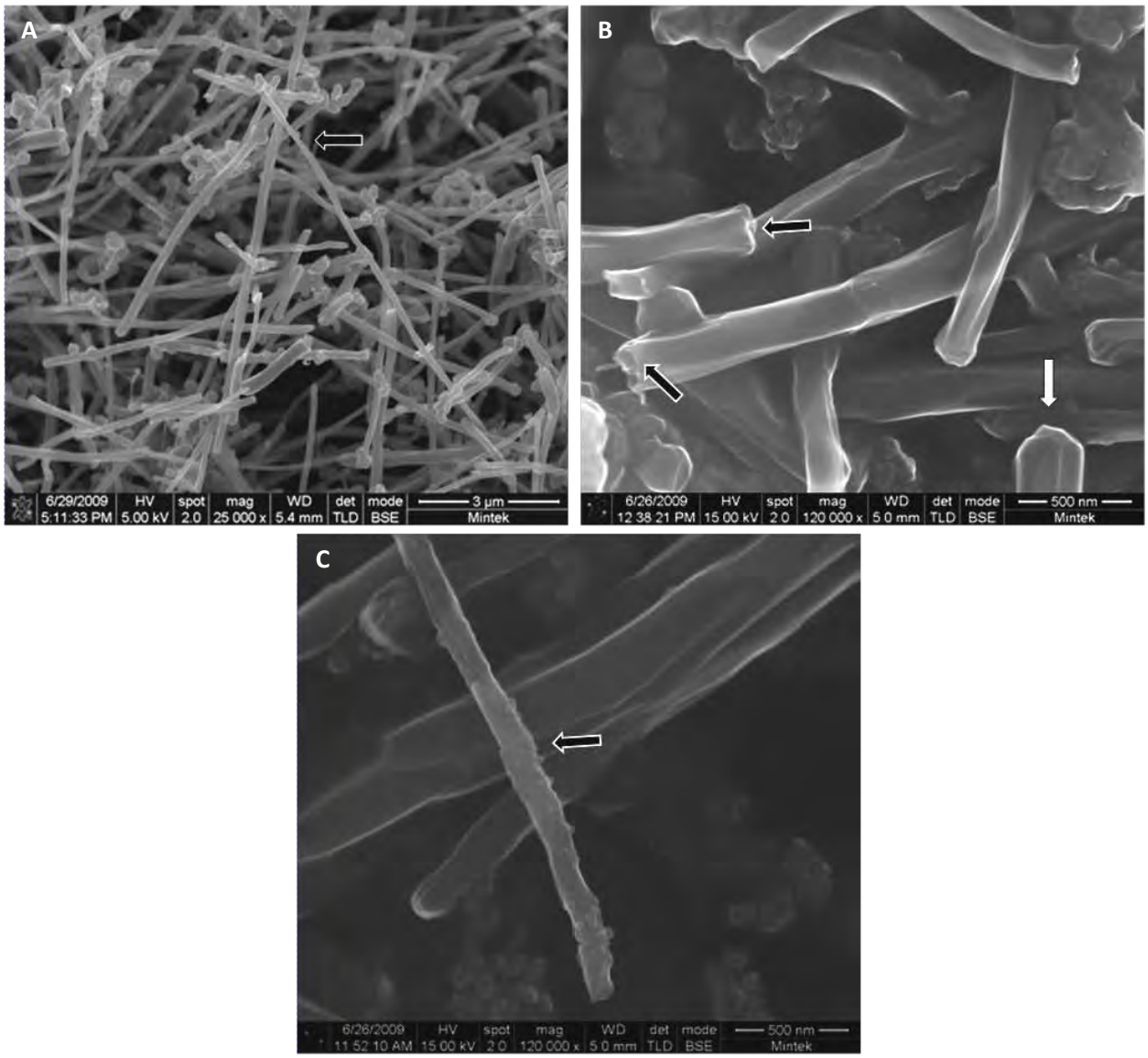

Figure 4.19 (A – C) HRSEM images of MWCNTs at 4 hours functionalisation. In (A) the long capped MWCNTs are clear in a heterogeneous mixture of MWCNTs. In (B) the hemispherical C_{60} cap is observed as indicated by the white arrow, while those MWCNTs where the cap has been cleaved off exposing hollow tubes are shown by the black arrows. In (C) the effects of prolonged exposure to the acid medium during functionalisation leads to wall rupture and eventual perforation with resultant shorter nanotubes.

Figure 4.20 (A – C) visually compares the effect of functionalisation on MWCNTs at 1 hour (A), at 4 hours (B) and at 9 hours (C).

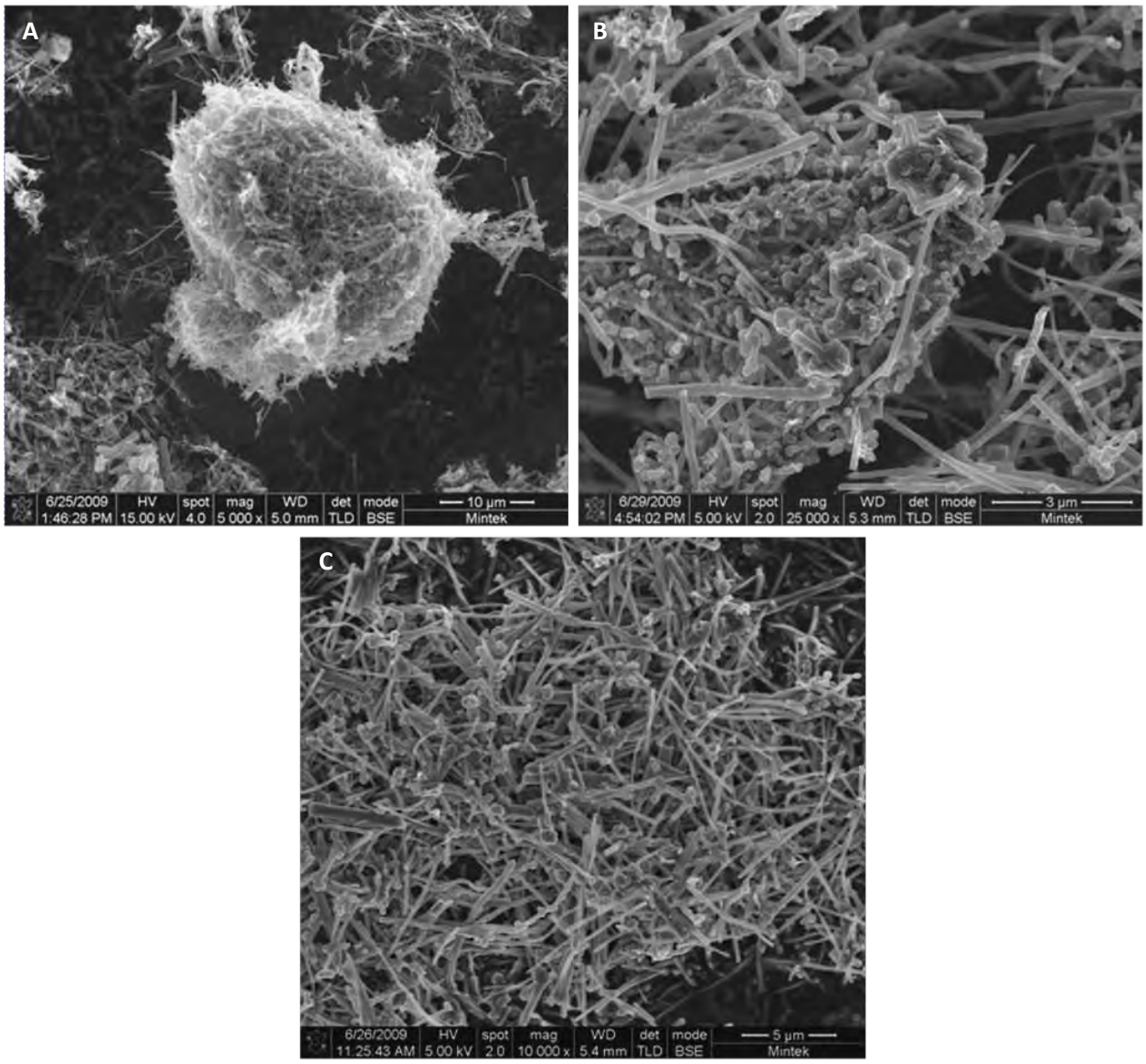

Figure 4.20 (A – C) HRSEM images of MWCNTs functionalisation at 1 hour (A), at 4 hours (B) and at 9 hours (C).

At 1 hour of functionalisation the aggregation of the MWCNTs is clearly observed in figure 4.20 (A), while after 4 hours the MWCNTs are observed to become shorter and dissociate (B) until a

homogeneous mixture of highly functionalised MWCNTs of similar lengths was observed, as is clear in figure 4.20 (C).

4.4.2.2 Activation of immobilised fMWCNTs using catechol as the mediator and test analyte

The reactive areas of functionalised carbon nanotubes have been reported to occur in the tubes, in the interstitial spaces between tubes, on the outer surface of a bundle (with shorter functionalisation times) and most prominently on the grooves formed between adjacent tubes (with longer functionalisation times) (Zhao *et al*., 2002). Groove spaces, interstitial spaces and pores are preferred binding sites over surface adsorption, due to higher binding affinities (Zhao *et al.*, 2002). Where the functionalisation time of the nanotubes is long, fewer bundles tend to form, however greater uniformity is achieved (figure 4.20 C). Groove spaces can be far apart and in order to assist in the transport of electrons across this area functionalised nanotubes are typically activated (Froudakis, 2001). Activation with a hydroxyl-containing moiety potentially enhances the adsorption of hydrogen, because of the charge transfer from the alkali molecule to the nanotube. This leads to the polarisation of H_2 molecules with resultant induction of dipole interactions (Froudakis, 2001).Figure 4.21 is an example of test CVs in catechol obtained after each of the activation scans at a modified GCE. In this case the GCE was modified with *f*MWCNTs (4 hours).

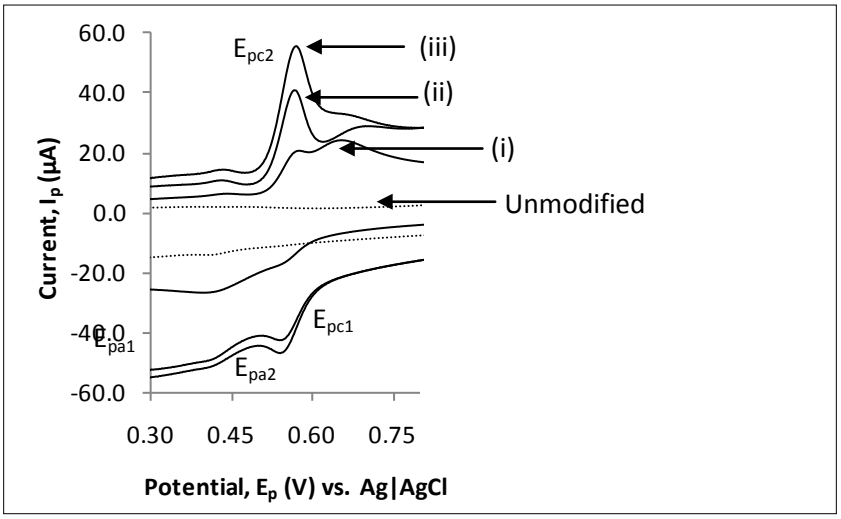

Figure 4.21 Representative figure showing test cyclic voltammogram scans of functionalised (4 hours) MWCNT-modified GCE after each electrochemical surface activation scan by using 0.45 mM catechol in 0.1 M H_2SO_4. Scan rate: 200 $mV.s^{-1}$ vs. Ag|AgCl. *Key*: (i)-(iii) test scans 1 to 3 respectively. E_{pa1} E_{pc2}: catechol redox pair, E_{pa2}, E_{pc1}: MWCNT redox peak. Test scan 4 is similar to test scan 3 and was omitted for the sake of clarity.

The test scans following each activation scan are shown in figure (4.21 i – iii). A pronounced reduction peak is observed on the forward cathodic scan with an associated weaker peak on the shoulder. On the return anodic scan, a weaker associated pair is evident. The forward cathodic peak is observed to increase in current response with subsequent activation scans (i - iii). After 3 activation scans, the increase in current response for the prominent forward cathodic peak was minimal. A decrease in the cathodic potential was observed for catechol at the *f*MWCNT-modified electrode compared to the unmodified GCE.

4.4.2.3 Comparison of the effect of activation on MWCNTs functionalised at different times

Figure 4.22 (A) shows representative CVs of the redox behaviour of catechol at an unmodified GCE and compared to GCE modified with *f*MWCNTs following acid functionalisation at 1, 4, 7 and 9 hours, respectively. Figure 4.22 (B) shows a summary of the range of *f*MWCNTs tested and their current responses for each test scan performed after each of the activation steps (1 to 3).

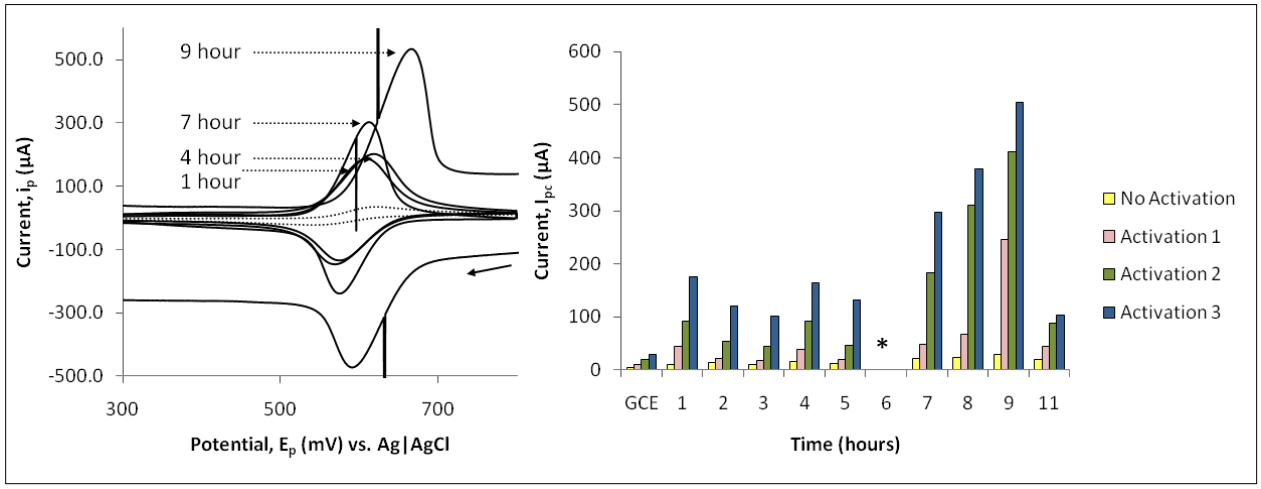

Figure 4.22 (A) Comparison of the test cyclic voltammogram scans at an unmodified glassy carbon electrode with functionalised MWCNT-modified GCE of one, 4, 7 and 9 hours after four activation cycles. The dotted line is the catechol test scan on an unmodified activated GCE. CVs were scanned in the presence of 0.45 mM catechol in 0.1 M H_2SO_4. Scan rate: 100 $mV.s^{-1}$ vs. Ag|AgCl. Figure (B): Bar graph summary of cathodic current response, I_{pc} (µA) for the test scan for 0.45 mM catechol at the range of MWCNT modified surfaces constructed. Time (hours) indicates length of acid functionalisation of MWCNTs. * no data available.

No observable trend is apparent at shorter functionalisation times, as observed in figure 4.22 (B). however, with an increase in functionalisation time a peak in current response was observed at 9 hours, which tapers off with prolonged functionalisation times, as observed at 11 hours functionalisation time, figure 4.22 (B). The significance of these values was further explored through EIS.

4.4.2.4 Assessment of modified electrodes by electrochemical impedance spectroscopy

The resultant change in impedance, Z after each activation cycle of MWCNT modified GCE in catechol assessed using EIS is represented in the Nyquist plot (Figure 4.23) for an unmodified GCE as compared to GCEs modified with MWCNTs functionalised for 1 hour, 4 hours and 9 hours, respectively.

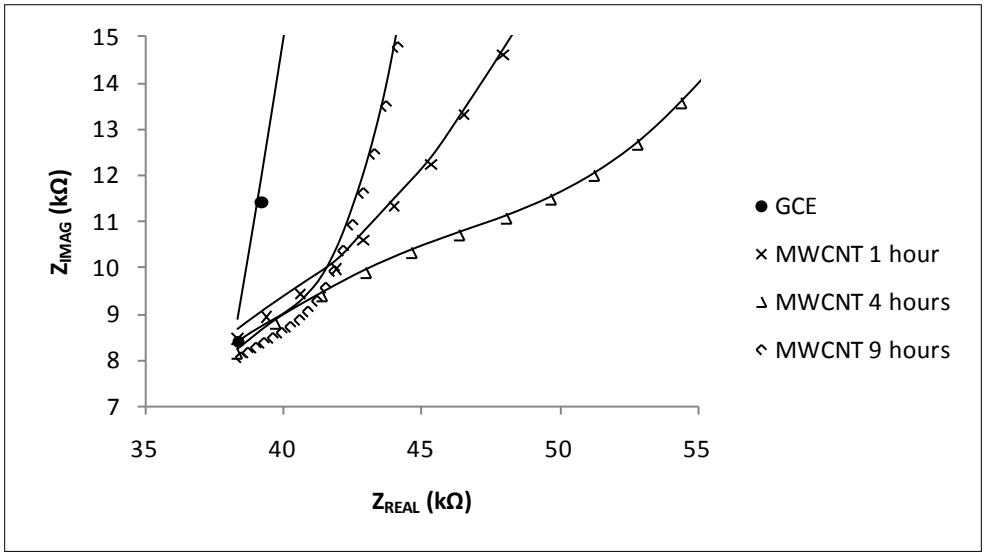

Figure 4.23 Nyquist plot showing the plane plots for GCE modified with functionalised MWCNTs (1, 4 and 9 hours), as compared to an unmodified GCE after activation.

In figure 4.23 a straight line (intersecting the Z' axis at Z' = R_s with an angle, δ_f of less than 90°) is observed for an unmodified GCE, which is indicative of a solid unmodified electrode surface. At higher frequencies, the electrode reaction is controlled by kinetics, and at this region the charge transfer resistance, R_{ct} is expected to be indicative of the inhibition or facilitation of electron transfer by the adsorbed species (Geraldo *et al.*, 2008). The relationship between R_{ct} and k_{app} is shown in equation 4.02.

Figure 4.24 compares the values for R_{ct} (determined from Fig 4.23) before and after activation in the presence of catechol, for an unmodified GCE, and a GCE modified with MWCNTs of 1, 4 or 9 hours, respectively.

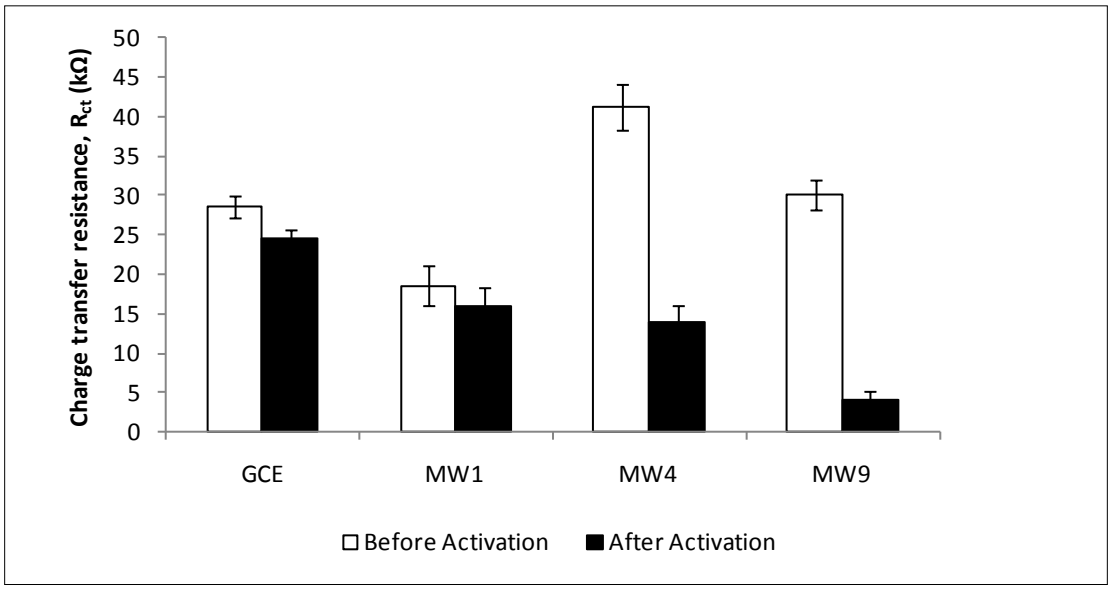

Figure 4.24 Change in charge transfer resistance before and after activation scans with 4 and 9 referring to the length of time of acid functionalisation.

Comparisons between R_{ct} before and after activation showed a marked improvement on the transfer of electrons to the electrode surface, as exhibited by a decrease in R_{ct} for each nanotube functionalisation time assessed after activation. Before activation, the R_{ct} was calculated to be (in descending order): MW 4 > GCE > MW 9 > MW 1. After activation, the order of R_{ct} was determined to be (in descending order): GCE > MW 1 > MW 1 4 MW 9. The lower R_{ct} for MW 9 was observed to be the greatest improvement on the R_{ct} after activation. This suggests that a more comprehensive mesoporous network formed between the functionalised nanotubes and catechol, resulting in greater electron transfer efficiency. In the case of MW 1, the starting R_{ct} was low before activation with only a slight improvement observed after activation. This implies that a network may have formed between the impurities found in low functionalised nanotube preparation.

A lowered concentration of carboxyl groups on the MWCNTs is described by Zhang *et al.* (2003) to be the main contributing factor to their high insolubility index and subsequent tendency to interact with adjacent nanotubes as opposed to the surrounding medium. As a result, the heterogeneity of the nanotube clusters would elicit a greater R_{ct} as compared to a more homogeneous mixture of functionalised nanotubes obtained at higher functionalisation times, with the result being slower electron transfer kinetics. With MW 4, the initial R_{ct} was high, which greatly improved after activation. The high starting R_{ct} could be due to the hydrophobic nanotubes forming heterogeneous clusters as an imperfect film on the GCE surface therefore preventing the flow of electrons efficiently, while after activation a decrease in R_{ct} could indicate an activation of the unmodified areas of the GCE surface, since similar observations were made at an unmodified GCE. This observation is further evidenced by the increase in current response in figure 4.22 (B) noted after activation for each of the functionalisation times, and in particular MW 4. Bode plots of the unmodified GCE as compared to *f*MWCNTs (1, 4 and 9 hours) are shown in figure 4.25, with the well-defined symmetrical peaks for the unmodified GCE and each of the 3 *f*MWCNTs modifications assessed. The phase angle (Θ), frequency (Hz), capacitance factor and CPE (Q) are tabulated in table 4.2.

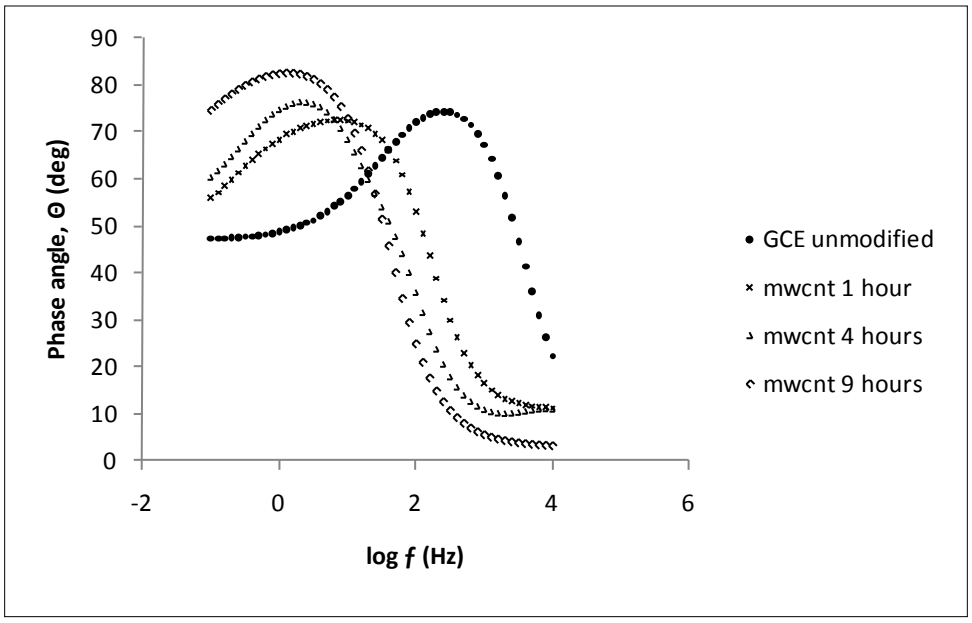

Figure 4.25 Bode plots for a GCE modified with *f*MWCNT 1, 4 and 9 hours, as compared to an unmodified GCE after activation.

The phase angle and frequency values obtained from the Bode plots in figure 4.25 are tabulated (table 4.2) in addition to the capacitance factor obtained from the gradient of the magnitude plots.

Table 4.2 Summary of the phase angle shift, frequency drift and the change in capacitance factor between various MWCNT electrode modifications and an unmodified GCE.

ELECTRODE	PHASE ANGLE, Θ (DEG)	FREQUENCY, *f* (Hz)	CAPACITANCE FACTOR† (R^2)	INTERFACIAL CAPACITANCE, C_{calc} (CPE) (μF)
GCE_{UNMOD}	75	246.04	-0.530 (0.9999)	241.54
GCE_{ACT}	67	394.50	-0.540 (0.9998)	296.47
$MW1_{UNACT}$	70	5.13	-0.780 (0.9998)	138.17
$MW1_{ACT}$	74	10.00	-0.784 (0.9997)	208.29
$MW4_{UNACT}$	70	1.02	-0.812 (0.9999)	176.57
$MW4_{ACT}$	76	2.04	-0.867 (0.9997)	282.60
$MW9_{UNACT}$	75	1.55	-0.860 (0.9998)	250.17
$MW9_{ACT}$	85	0.81	-0.935 (0.9999)	374.66

† Obtained from the slope of magnitude plots, a value of -1 is indicative of an ideal capacitor.

‡Obtained from a Nyquist plot (figure 4.23), C_{calc} calculated using equation 4.03.

Two distinct observations regarding the constant phase element (CPE, C_{calc}) of the electrodes compared can be drawn from table 4.2. In the first instance the C_{calc} was noted to increase for each electrode after being exposed to the activation process for each of the electrodes assessed. Secondly, the C_{calc} was observed to increase in proportion to the duration of the acid functionalisation, with *f*MWCNTs that had been functionalised for 9 hours exhibiting the greatest C_{calc} of 374.66 μF (after activation). Similar observations were made for functionalised SWCNTs, where increased activation was theorized to result

in the formation of a mesoporous cage-like structure that aided in electron transfer to the electrode surface, resulting in increased C_{calc} values. In figure 4.25 the phase angle, Θ for an unmodified GCE (after activation) of ~ 67 °at 394.50 Hz was obtained, which is indicative of the relaxation phase that is within the range previously recorded for a GCE-solution interface (Geraldo *et al* 2008). A shift in the peaks to lower frequencies was observed to occur for each of the nanomaterial-modified electrodes, after activation, with *f*MWCNTs (1 hour) exhibiting the smallest shift, while *f*MWCNTs (9 hours) the largest. A shift to lower frequencies is evidence of the redox reactions for $[Fe(CN)_6]^{3-/4-}$ occurring at the modified surface, rather than at the unmodified GCE surface (Ozoemena *et al.*, 2008; Geraldo *et al.*, 2008). The greatest Θ was observed, in ascending order, as: MW1 < GCE < MW4 < MW9. A Θ value of 85° obtained after activation for MW9, in conjunction with a capacitance factor of -0.935, is near the theoretical value of 90° and -1, respectively, as described for an ideal capacitor (Ozoemena *et al.*, 2008; Geraldo *et al.*, 2008).

4.4.2.5 Determination of apparent rate of electron transfer, k_{app}

Using the experimentally-determined values for R_{ct} (figure 4.24), the k_{app} can be determined using equation 4.02. The relationship between k_{app} and functionalisation time is shown in figure 4.26.

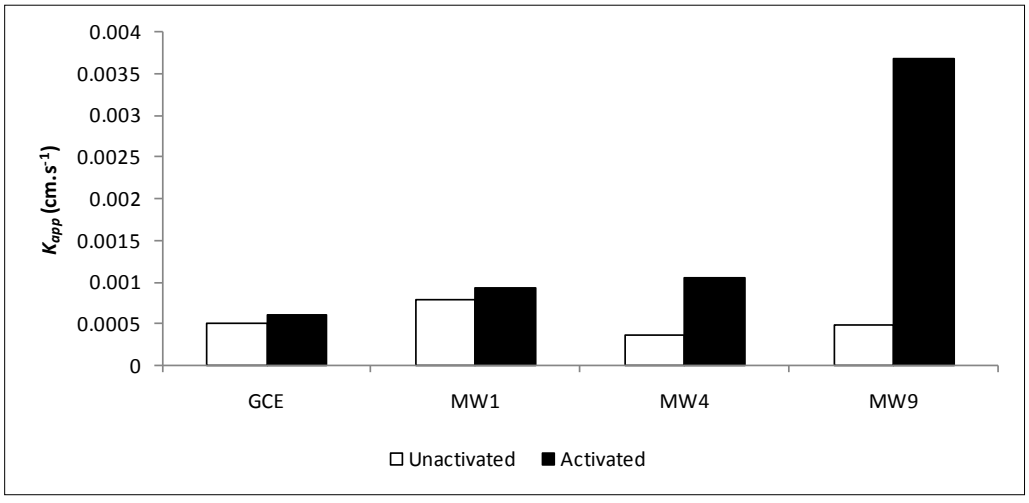

Figure 4.26 The k_{app} value before and after activation scans for *f*MWCNTs. MW refers to MWCNT modified surface, with1, 4 and 9 referring to the length of time of acid functionalisation.

In each of the electrode surfaces assessed (unmodified, MW 1, 4 and 9 respectively) the k_{app} was observed to increase after activation, suggesting that the inclusion of catechol between nanotubes and electrode surface moieties enhances electron transfer to the electrode regardless of the presence or modified version of nanotubes on the electrode surface. The initial k_{app} was observed to be, in ascending order: MW4 < GCE ~ MW 9 < MW 1 while after activation the k_{app} was observed to be (in ascending order): GCE < MW 1 < MW 4 < MW 9. The low k_{app} observed for MW 4 coincides with the lower current response (figure 4.22) (compared to MW1) observed earlier, further suggesting that the clusters of nanotubes on the GCE surface visualised (figure 4.18) do tend to hinder the flow of electrons to the electrode surface. At 4 hours functionalisation, it was observed in both the *f*SWCNTs and *f*MWCNTs that there is a mixture of functionalised and unfunctionalised nanotubes, which results in the counter-intuitive observations reported. However, as the functionalisation time is increased, so the uniformity of the functionalisation and electrode response increases.

The increased k_{app} for MW 9 further corroborates the increased current response observed earlier, as well as the lower R_{ct} observed in figure 4.24. This relationship is further evidence of the enhanced properties afforded by functionalisation of nanotubes, as reported on by Frackowiak *et al.* (2002), Jiang *et al.* (2005), Musameh *et al.* (2005), Jurewicz *et al.* (2006), Wang *et al.* (2005), Chen *et al.* (2008), Skunik *et al.* (2008), Jang *et al.* (2009) and Yuan *et al.* (2010) and shows a distinct role for functionalisation time and activation in enhancing those properties as observed for SWCNT.

4.4.2.6 Summary

Based on fig 4.22, this study showed in general an increase in current for catechol after activation with catechol supporting its application in sensor design with *f*MWCNTs. This enhancement in current response was observed for all lengths of functionalisation times studied. The trend was however not immediately apparent for the length of acid treatment. Compared to an unmodified GCE, modification with *f*MWCNTs at all functionalisation times increased current response with a peak at 9 hrs, followed by a decrease at 11 hours. EIS supported the current trends in terms of decreased R_{ct} for each activation scan, with the lowest R_{ct} recorded for 9 hours functionalisation time.

The aggregated *f*MWCNTs that had formed islands observed at 4 hours acid functionalisation before activation, figure 4.18 (B), in conjunction with the unmodified electrode surface (pores), afford independent resistances resulting in high R_{ct} values (40.10 kΩ at k_{app} = 0.40 x 10^{-3} cm.s^{-1}). The relatively large R_{ct} value for unactivated *f*MWCNTs (9 hours) (k_{app} = 0.45 x 10^{-3} cm.s^{-1}) can be explained by the ordered alignment of the nanotubes as observed using AFM, figure 4.18 (C) where the *f*MWCNTs (9 hours) are noted to be orientated in an organised conformation. According to Nkosi & Ozoemena (2008), electron transport across nanotubes aligned in a flat conformation is considered to be retarded by the need for electrons to transfer from one nanotube to the next. This elucidation could explain the high R_{ct}, at MW9 which consequently decreases significantly after 3 activation scans as a result of the inclusion of catechol between the aligned nanotubes which behave as electron mediators that shuttle the electrons with less resistance (lower R_{ct}, 4.8 kΩ) and at a more rapid rate (higher k_{app}, 1.7 x 10^{-3} cm.s^{-1}). This explains the high current observed for catechol as in figure 4.21 at 9 hours functionalisation time. In this instance, 9 hours of functionalisation tends to be ideal, while a longer duration of functionalisation as observed for 11 hours with the sharp decrease in current is not recommended, given the extent of damage the acid treatment causes on the structural integrity of the tubes.

4.4.3 C_{60} Fullerenes

4.4.3.1 Characterisation of C_{60} Fullerenes

The deposition of C_{60} fullerenes onto a glassy carbon electrode (GCE) has commonly been performed through a preparation of C_{60} in toluene or dichloromethane (DCM) cast onto a clean GCE surface with the solvent allowed to evaporate. This technique is referred to by Xiao *et al.* (2009) as solvation casting. In this study DCM was opted for based on observations reported by Goyal *et al.* (2009) and Xiao *et al.* (2009) where it had been elucidated that C_{60} DCM provides a more uniform dispersion with a more concentrated size distribution of C_{60} once cast. In their visual studies of cast C_{60} on GCE surfaces Xiao *et al* 2009 discovered that C_{60} in toluene agglomerates on the GCE surface in rod-like formations, whereas in the presence of DCM the more characteristic spherical form of C_{60} was observed.

Visual confirmation of the dissolution of C_{60} fullerenes in DCM was achieved through AFM, as shown in figure 4.27. The spherical morphology and homogeneous dispersion of the C_{60} fullerenes is clearly visible in figure 4.27 (A).

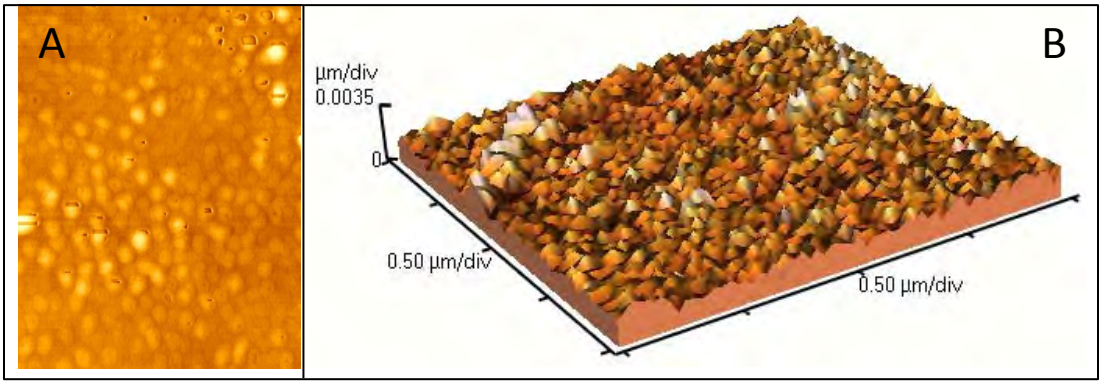

Figure 4.27 (A - B) AFM images showing the circular structure of a homogeneous dispersion of C_{60} fullerenes. The radius of spherical C_{60} is 0.56 nm with a surface area of 1 nm^2 (Szűcs 1996).

Figures 4.28 (A – D) show HRSEM images of C_{60} fullerene agglomerates in DCM.

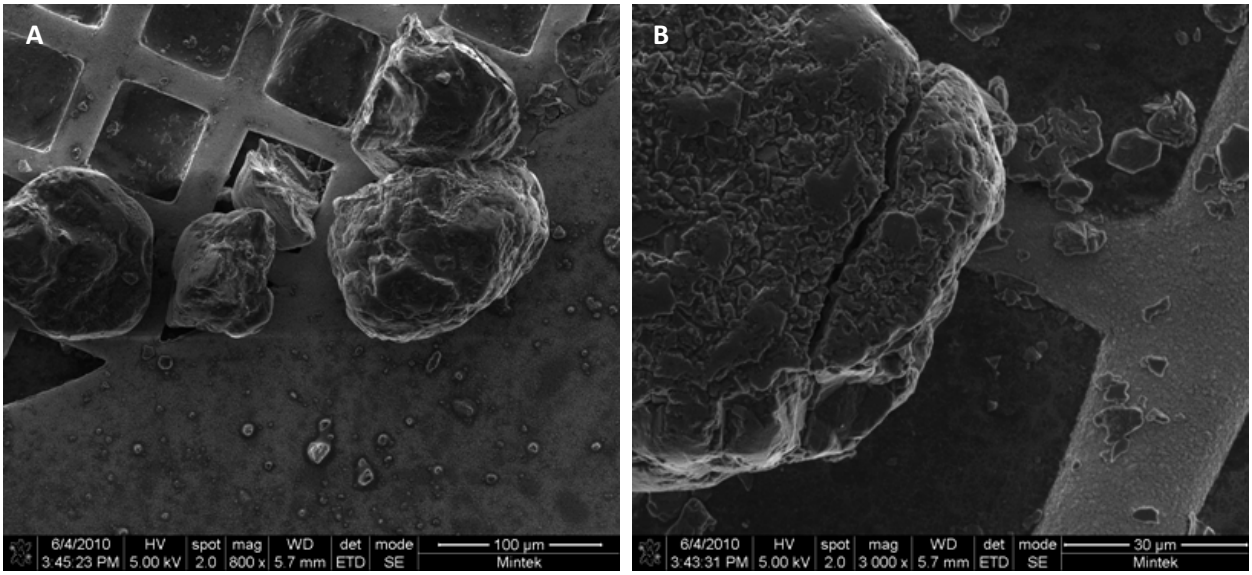

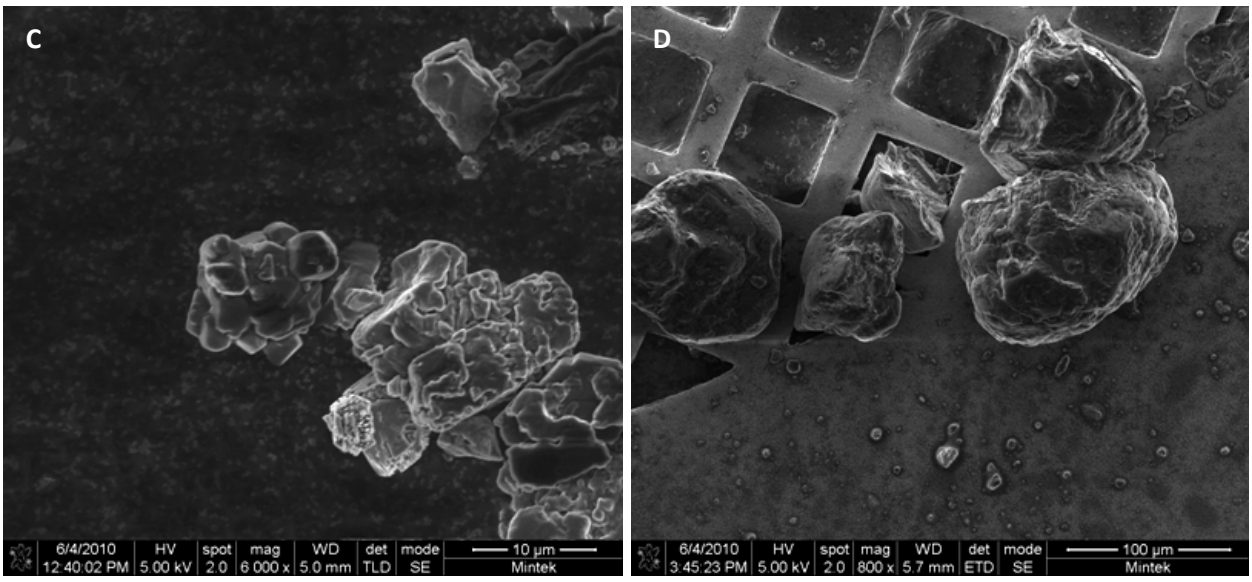

Figure 4.28 (A – D) HRSEM images of C_{60} fullerene clusters. Each of A – D exhibit large aggregations of fullerenes. HRSEM parameters are shown on the figures.

Stephens (1993) described C_{60} fullerenes to typically exist in large clusters, which tend to precipitate out of solvents. In figure 4.28 (A - D) the large aggregates of C_{60} can be observed to occur even after sonication, consisting of complex layers of fullerene aggregates. Interestingly, Drake & Cassar (2006) have attributed this behaviour to be typical of C_{60} fullerenes and have described the aggregate formation to be as a result of high affinities between the single C_{60} fullerenes resulting in the formation of concentric layers of fullerenes analogous to the layers of an onion.

4.4.3.2 Partial reduction of the C_{60} fullerene film

Many authors report on the need to activate C_{60} thin films deposited onto electrode surfaces, that are subsequently applied to the electroanalytical detection of target analytes (Sherigara *et al.*, 2003; Tan *et al.*, 2003; D'Souza *et al.*, 2005; Goyal *et al.*, 2008; Zhou *et al.*, 2008). The activation (otherwise referred to as partial reduction) of the C_{60}-GCE thin film comprises a single reduction sweep of the modified electrode in an aqueous supporting electrolyte containing excess cations (K^+ and Na^+). The electrochemical reduction of the cast C_{60} film was performed in 1.0 M KOH although the use of NaCl or NaOH has been reported (Szűcs, 2008; Xiao *et al.*, 2009). For the purposes of this study, the protocol as used by Goyal *et al.* (2007) for the partial reduction in 1.0 M KOH of C_{60} film on a GCE protocol was

adopted since this approach has become the benchmark standard (Goyal *et al.*, 2007; Xiao *et al.*, 2009). A single CV scan was performed by scanning from 0 mV to -1500 mV (vs. Ag|AgCl) at a scan rate of 10 $mV.s^{-1}$. Figure 4.29 shows the CV recorded for partial reduction of C_{60}-GCE thin film.

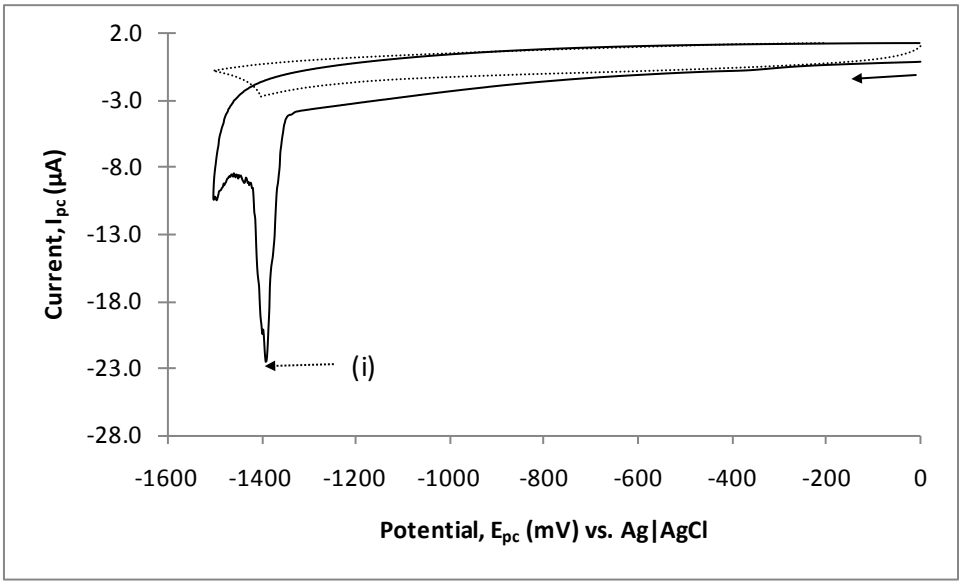

Figure 4.29 Partial reduction of the C_{60}-GCE thin film in 1 M KOH supporting electrolyte at a scan rate of 10 $mV.s^{-1}$ (vs. Ag|AgCl). Dotted line represents the blank of an unmodified glassy carbon electrode in 1 M KOH. *Key*: (i) prominent reduction peak observed during partial reduction.

A sharp single cathodic peak was observed at -1400 mV (vs. Ag|AgCl) as shown by (i) on figure 4.29. This observation is in agreement with literature (Szűcs, 2008; Goyal *et al.*, 2009; Xiao *et al.*, 2009). Ward-Jones *et al.* (2008) attribute a single peak observed during the partial reduction of C_{60} cast films solvated in DCM to gamma distributions of relatively uniform size, and prominently of 1 mean value, which results in a single peak. In the presence of toluene, the size distribution is more erratic, resulting in 3 peaks being observed.

No peaks were observed on the return anodic scan indicating that no re-oxidation of the reduced C_{60} occurs. It was also noted that if a second reduction scan is performed, a significant decrease in the current response of the cathodic peak occurs. As a consequence, the reduced C_{60} thin film becomes

insulatory, which is confirmed through similar observations documented by Csiszár *et al.* (2001), Barazzouk *et al.* (2002). This activity has been reported to be attributed to the ions within the supporting electrolyte not being able to transfer to the electrode surface due to the compactness of the associated K^+ and C_{60} moieties within the reduced layer.

The prominence of the cathodic peak is attributed by Szűcs *et al.* (2008) to be as a result of the inclusion of cations into the reduced C_{60} film, aptly known as the cation insertion model. This has been described by Xiao *et al.* (2009) to be the most feasible explanation to date with the most supporting experimental evidence. In order to determine the efficacy of the C_{60} film partial reduction, the redox probe, $[Fe(CN)_6]^{3-/4-}$ was employed in an attempt to clarify the nature and presence of C_{60} on the GCE surface. A single scan of 1 mM $[Fe(CN)_6]^{3-/4-}$ was performed at 0.100 $V.s^{-1}$ for a C_{60}-modifed GCE before and after partial reduction, as outlined previously (section 4.3.3). Figure 4.30 is a representation of the effect of partial reduction on the current strength and potential before and after surface activation.

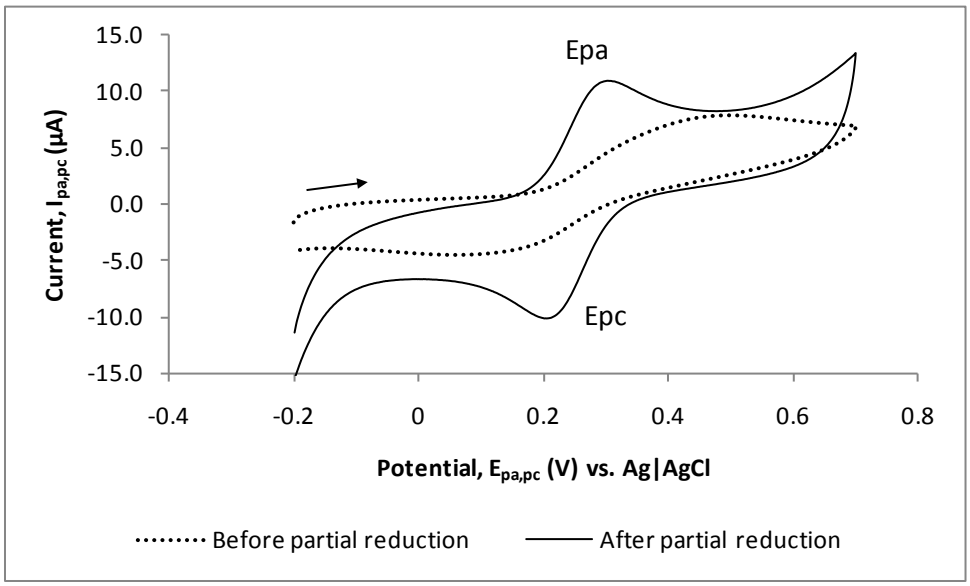

Figure 4.30 Representative cyclic voltammogram showing the effect of partial reduction on the enhancement of current signal at a C_{60} modified GCE using a $[Fe(CN)6]^{3-/4-}$ redox probe cycled in 0.1 M KOH.

The amplified redox peaks for $[Fe(CN)_6]^{3-/4-}$ at a partially reduced C_{60} layer as compared to a C_{60} layer that had not been partially reduced (as graphically represented in figure 4.30), indicates higher electrocatalytic activity of the modified electrode towards the redox activity of $[Fe(CN)_6]^{3-/4-}$. This is observed through a shift in the peak potential for E_{pa} to less positive potentials, with a subsequent increase in the current strength and peak resolution. All these attributes suggest increased electrocatalysis as a result of the partial reduction of the C_{60} thin layer on the GCE surface.

4.4.3.3 Assessment of electrocatalytic nature of C_{60}-modified electrodes

The electrocatalytic nature of the C_{60}-modified GCE was assessed by electrochemical impedance spectroscopy (EIS) as well as cyclic voltammetry (CV). Figure 4.30 shows the Nyquist plots for the C_{60}-modifed GCE before and after partial reduction of the thin film, as compared to an unmodified GCE EIS data was fitted using the circuit model shown in scheme 4.1.

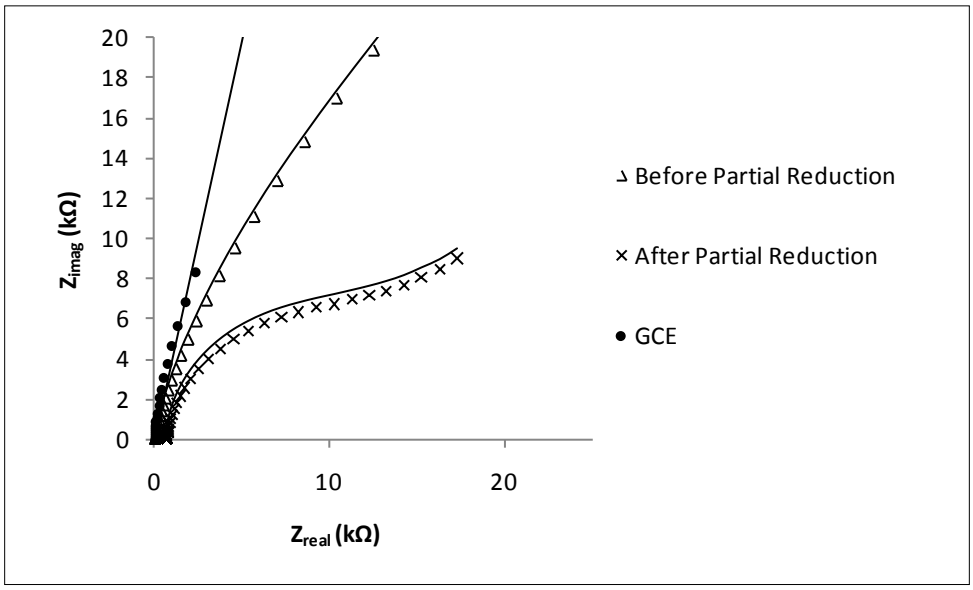

Figure 4.31 Nyquist plots for the C_{60}-modified GCE before and after partial reduction, as compared to an unmodified GCE.

From the Nyquist plot (figure 4.31) it is apparent that prior to partial reduction, a C_{60}-modifed GCE yields a line of near linearity for a solid unmodified electrode surface (intersecting the Z' axis at Z' = R_Ω with an angle, δ_f of less than 90°).

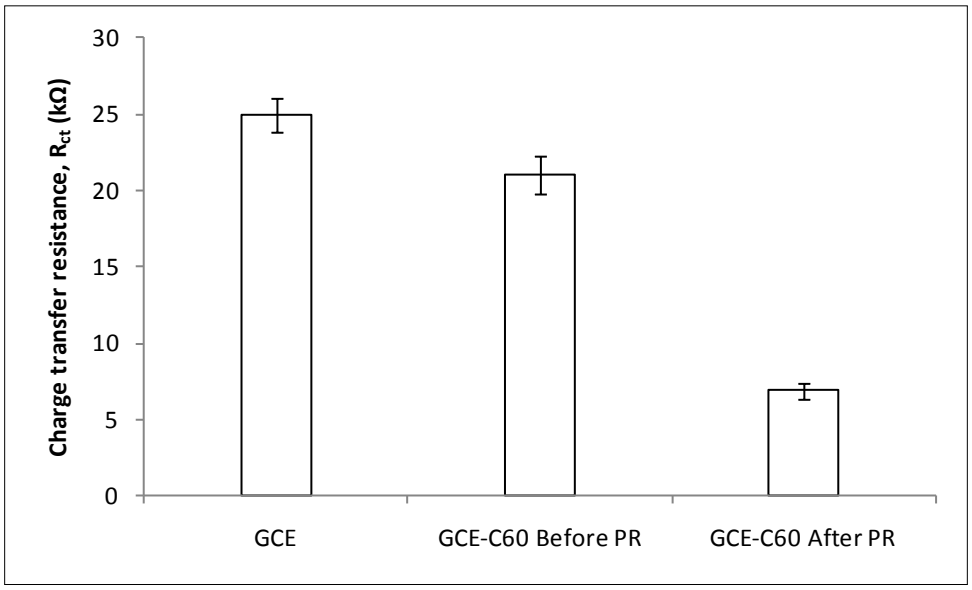

Figure 4.32 Comparison of the resistance between unmodified GCE, and C_{60}-modified GCE (before and after partial reduction), using electrochemical impedance spectroscopy. n= 3 +/- S.D.

The charge transfer resistance (R_{ct}) is observed to decrease significantly when a C_{60} film is cast onto the GCE which further decreases after partial reduction, proposing the possible mediation of electron passage as a result of the modified film.

Bode plots of the unmodified GCE as compared to a GCE modified with C_{60}, before and after partial reduction, are shown in figure 4.33.

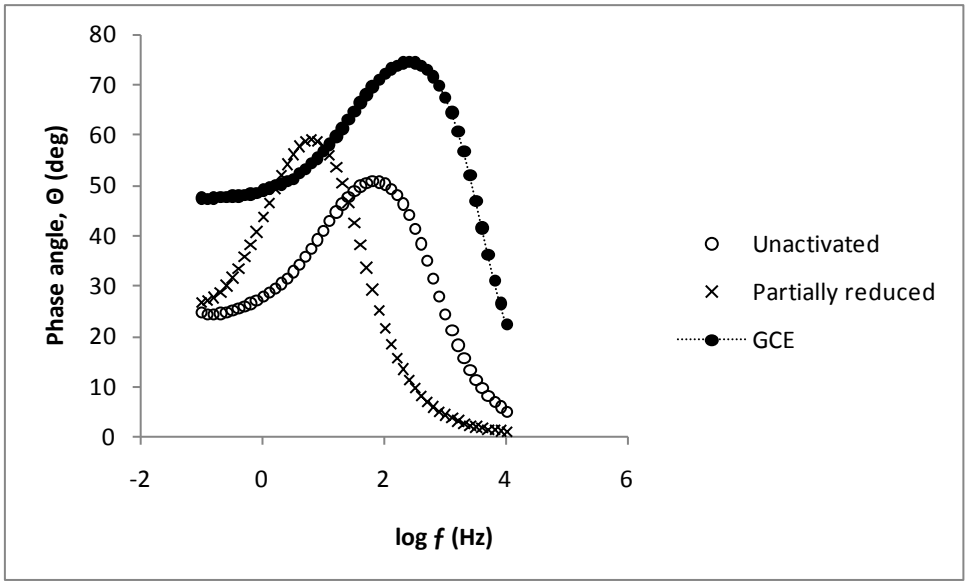

Figure 4.33 Bode plots for the C_{60}-modified GCE before and after partial reduction, as compared to an unmodified GCE.

Table 4.3 summarises the phase angle Θ, frequency, *f*, capacitance factor and constant phase element, Q obtained from the Bode and magnitude plots.

Table 4.3 Comparison of phase angle shift, frequency drift and capacitance factor between an unmodified GCE, a GCE modified with a C_{60} thin film, before and after partial reduction of its surface.

ELECTRODE	PHASE ANGLE, Θ (DEG)	FREQUENCY, *f* (Hz)	CAPACITANCE FACTOR‡ †(R^2)	INTERFACIAL CAPACITANCE, C_{ALC} (μF)
GCE_{UNMOD}	67 (± 2.062)	394.50 (± 4.983)	-0.540 †(0.9998)	241.54 (± 9.26)
$C_{60\text{-}UNACT}$	50 (± 1.291)	100.17 (± 2.281)	-0.622 †(0.9997)	77.62 (± 2.31)
$C_{60\text{-}ACT}$	60 (± 3.304)	6.34 (± 0.292)	-0.700 †(0.9999)	90.37 (± 1.95)

‡Gradient of magnitude plot (log Z' vs. log *f*), C_{60}-ACT: GCE modified with 40 μl of 150 μM C_{60} and partially reduced, brackets: standard deviation, s.d (n = 3).

For a GCE surface with a partially reduced (activated) layer of C_{60} fullerenes (referred to as $C_{60\text{-ACT}}$ in table 4.3), a typical symmetrical peak is observed with a phase shift of 60° at 6.34 Hz. This is indicative of a process where the electron transfer occurs between the electrode surface and the solution at the electrode-solution interface. In addition, the gradient of the magnitude plot (not shown) is -0.700 (R^2 = 0.9999), characteristic of a surface that behaves more like an ideal capacitor since the value is nearer 1. In comparison, at an unmodified GCE the capacitance factor was observed to be -0.540 signifying a surface that behaves neither in an ideal capacitative or resistive manner (Geraldo *et al.*, 2008).

At a GCE modified with 40 µl of 150 µM, prior to partial reduction (referred to as $C_{60\text{-UNACT}}$ in table 4.3) in the presence of 1.0 M KOH, a lowered phase angle of 50° was observed, with a frequency of 100.17 Hz. This suggests that the modified layer hindered the transfer of electrons to the electrode surface. The capacitance factor was observed to increase minimally from the unmodified GCE, which implies a low degree of energy storage. After partial reduction, a phase shift to 60° was observed with a marked lowered frequency. Additionally the capacitance factor increased slightly while the C_{calc} was noted to increase to 90.37 µF upon activation, which is lower than that observed at an unmodified GCE (241.54 µF) and at GCE modified with C_{60} before partial reduction (77.62 µF). This increase between a partially reduced and unreduced surface suggests the partially reduced surface is capable of improved energy storage through electron transfer to the GCE surface more efficiently. This behaviour is further evidenced by the aforementioned observed increase in capacitance factor.

4.4.3.4 Apparent electron transfer rate k_{app} determination

The apparent electron transfer rate, k_{app} ($cm.s^{-1}$) was calculated using equation 4.02. Figure 4.34 shows bar graphs for k_{app} as compared to R_{ct} values.

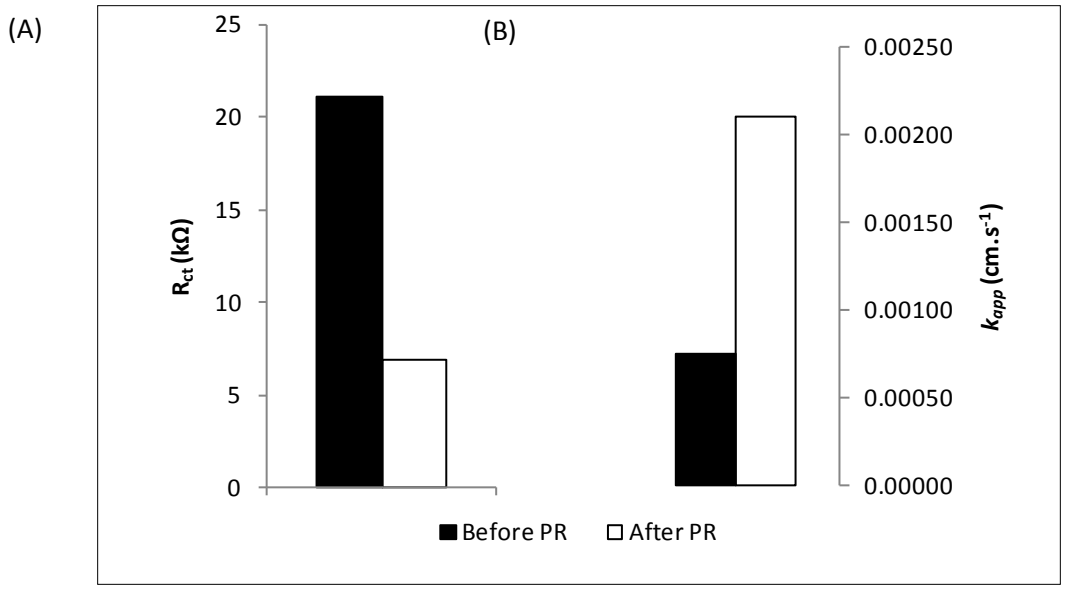

Figure 4.34 (A) The change in charge transfer resistance (R_{ct}) before and after partial reduction (PR) while (B) shows the k_{app} value before and after partial reduction, for GCE modified with C_{60}. *Key*: Solid bars: before partial reduction, clear bars: after partial reduction.

In Figure 4.34 (A) the R_{ct} for the C_{60} modified layer before partial reduction is significantly higher than after partial reduction, while the k_{app} value increases with partial reduction. This behaviour is indicative of an increase in the electron transfer efficiency facilitated by the partial reduction of the C_{60} layer.

4.4.3.5 Determination of the ideal loading capacity of C_{60} on GCE

The loading of C_{60} onto a cleaned and polished GCE was performed as outlined in 3.3.1.

Xiao *et al.* (2009) highlights the importance of the aliquot procedure for C_{60} onto an electrode surface, as first published by Szűcs, 2008. It was suggested by the aforementioned authors that smaller aliquots need to be repeatedly added to the electrode surface successively until the desired amount is deposited onto the electrode surface. This is to minimise the deposition of C_{60} onto the insulating Teflon mantle of the electrode that would otherwise occur with a single aliquot. The overarching outcome of this approach is an increased surface area (Szücs, 2008; Xiao *et al.*, 2009).

For the purposes of this study, the redox probe, 1 x 10^{-3} M $[Fe(CN)_6]^{3-/4-}$ in 0.1 M KCl, was used to assess the efficacy of electron transfer across the modified layer. Figure 4.35 (A) shows the CV obtained for the redox probe as obtained after each 10 µl C_{60} aliquot modification and partial reduction of the GCE.

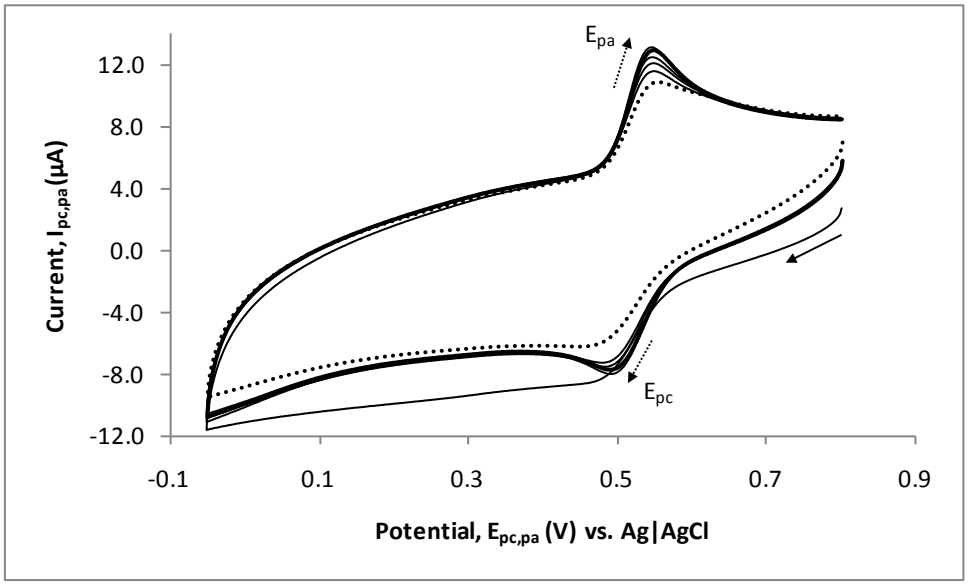

Figure 4.35 (A) Cyclic voltammograms showing the electrocatalytic activity of equimolar(1 x 10^{-3} M) $[Fe(CN)_6]^{3-/4-}$ in 1.0 M KOH, for layer-by-layer C_{60}-thin film modification of GCE. Scan rate 100 mV.s^{-1}.

Figure 4.36 (B) is an enlargement of figure 4.35 (A), highlighting the change in the magnitude of the current response with each C_{60} 10 µl aliquot for the forward and reverse scans, respectively.

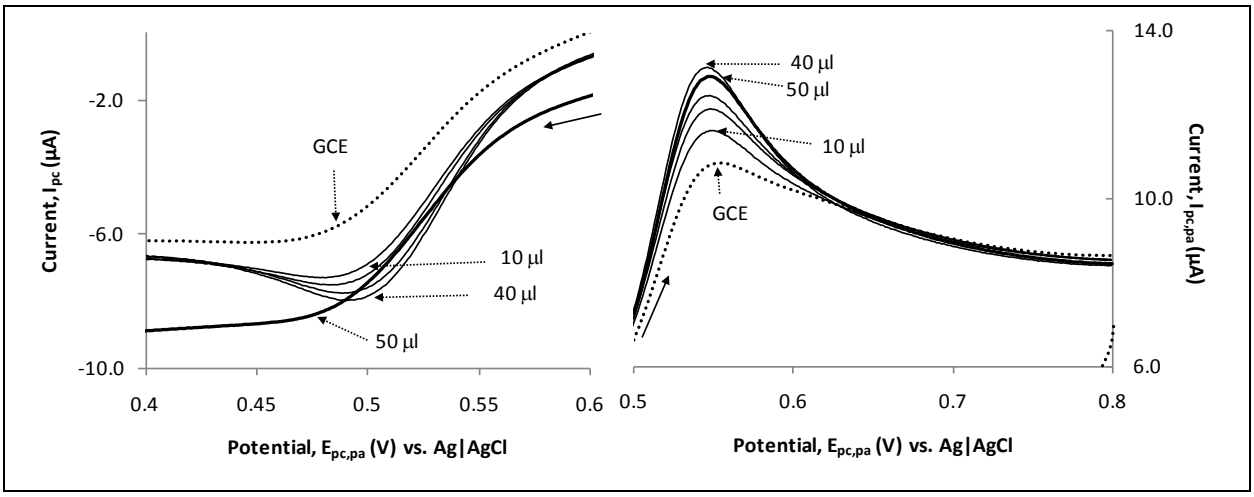

Figure 4.36 (B) Cyclic voltammograms highlighting the electrocatalytic activity of equimolar $[Fe(CN)_6]^{3-/4-}$ for layer-by-layer C_{60}-thin film modification of GCE. Solid arrows indicate the direction of the scan.

A clean GCE modified with 10 µl C_{60} and partially reduced is observed to significantly increase the current response for the detection of the redox probe, $[Fe(CN)_6]^{3-/4-}$ as compared to an unmodified GCE. When the electrode was cleaned and 20 µl C_{60} added and partially reduced, the current response for $[Fe(CN)_6]^{3-/4-}$ was observed to be greater than that observed for the electrode modified with 10 µl C_{60}.Continuation in GCE modification in this manner showed that the maximum current response for $[Fe(CN)_6]^{3-/4-}$ was obtained for a GCE that was modified with 40 µl C_{60} and partially reduced. At 50 µl, the current response was observed to decrease. The use therefore of 40 µl of 150 µM C_{60} in DCM concurs with the findings of Goyal *et al.* (2007).

The surface coverage, was calculated for each electrode modified with C_{60} in order to ascertain the amount of C_{60} bound to the GCE. Figure 4.37 is a summary of the surface coverage values obtained for the cathodic and anodic scans.

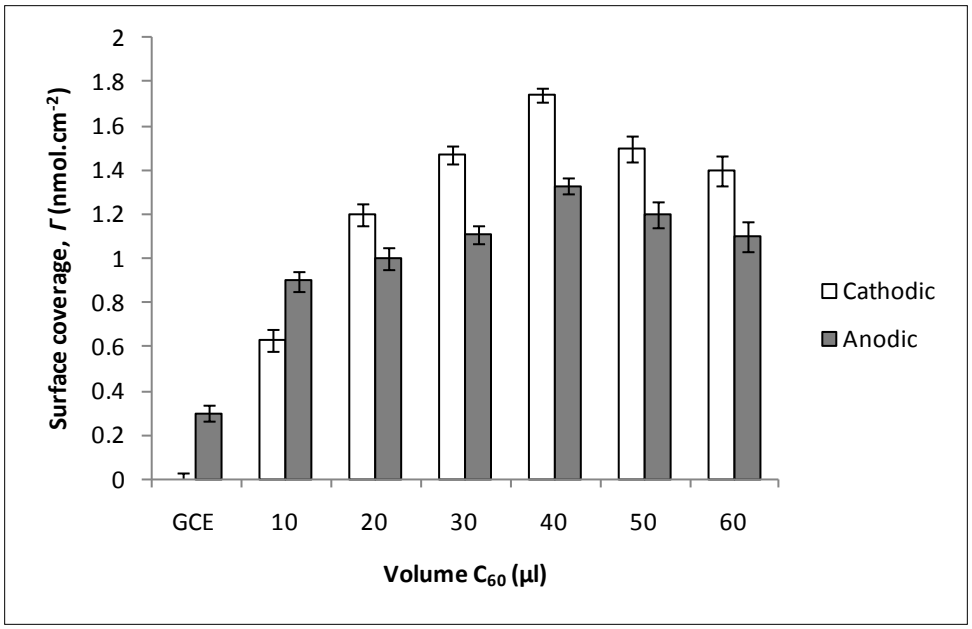

Figure 4.37 Summary of surface coverage, values according to equation 3.05 (section 3.6.4), before and after partial reduction, for the layer-by-layer C_{60}-thin film modification of GCE.

In figure 4.37 the amount of C_{60} bound on the forward cathodic scan is observed to increase in a linear manner from 10 µl to 40 µl C_{60}, with subsequent decrease in surface coverage from 50 µl C_{60}. The reverse anodic scans are observed to follow a similar trend. This parallels results for electrocatalytic activity with the highest current observed at 40 µl C_{60}, equivalent to the greatest surface coverage.

Partially reduced C_{60} fullerene films have been reported to exhibit a high degree of electronic conductivity due to their highly electroactive and increased surface area, resulting in increased sensitivity attributed to a lowered peak potential and an amplified current magnitude. In addition, C_{60} has been shown to be biocompatible, of use (Csiszár *et al.*, 2001; Bosi *et al.*, 2003) potentially in the development of drug delivery systems (Bosi *et al.*, 2003).

The cathodic peak noted in figure 4.28 for the reduction of the C_{60} thin film at -1400 mV (vs. Ag|AgCl) is well-documented (Jehoulet *et al.*, 1992; Compton *et al.*, 1993; D'Souza *et al.*, 2005). According to Goyal *et al.* (2007) the mechanism shown in scheme 4.2 occurs during partial reduction:

$$C_{60} \xrightarrow{e^-} KC_{60} \xrightarrow{e^-} K_2C_{60} \xrightarrow{e^-} K_3C_{60}$$

Scheme 4.2 The 3 e^- partial reduction process (Goyal *et al.*, 2007).

Zhou *et al.* (1992) have shown using scanning tunnelling microscopy (STM) that the C_{60} film undergoes structural alterations during partial reduction in the presence of cations such as K^+, Na^+ and Tetra-*n*-butylammonium (TBA^+). The utilisation of partially reduced C_{60} on GCE has been adopted for the detection of trace levels of biologically important compounds including nandrolone (Goyal *et al.*, 2007) and salbutamol (Goyal *et al.*, 2008). During the electrochemical partial reduction of C_{60} films, cations are incorporated between C_{60} moieties (Carlisle *et al.*, 1996), creating a network through which highly efficient electron passage can occur. Goyal *et al.* (2007) report that the reduction of C_{60} involves approximately 3 electrons per C_{60} molecule, resulting in the formation of K_3C_{60}. During the multi-step conversion two transient species, KC_{60} and K_2C_{60} are non-conductive ion exchangers that facilitate the formation of K_3C_{60}.

In figure 4.30 prior to the partial reduction, low current response was noted for the redox probe (as illustrated by the dotted line). However, after a single partial reduction scan, the current strength for the redox probe is observed to increase significantly (as shown by the solid line in figure 4.30) with a corresponding decrease in the formal potential, E°', suggestive of electrocatalytic behaviour. What is of interest is that prior to partial reduction, no peaks for the redox probe should in theory be observed given the insulatory nature of the film. The slight redox response has been described by Szűcs, (2008) to be due to non-uniform C_{60} fullerene coverage of the electrode surface resulting in islands of fullerene and pits of unmodified electrode surface. The observed current response is as a result of direct interaction with the unmodified electrode surface (pits) and not via the fullerene layer (islands).

A Nyquist plot (figure 4.31) for the C_{60} modified GCE before partial reduction of the modified layer results in a typical semi-arc at higher frequencies and a straight line at lower frequencies. A straight line at higher frequencies could be attributed to an interaction directly with the unmodified GCE surface through pores on the surface of the electrode since similar behaviour had been noted previously at an

unmodified GCE surface. After partial reduction the semi-arc was noted to decrease in diameter due to a decrease in R_{ct}, suggesting enhanced electron facilitation. At lower frequencies, the straight line is not as prominent after partial reduction. The latter could be attributed to the entrapment of K^+ between C_{60} during the partial reduction, forming an inclusion complex, K_3C_{60} (Csiszar *et al.*, 2001).

Thin films of C_{60} on a GCE have been reported by Szűcs, (2008) to form a barrier on the electrode surface that behaves as a semi-conductor at best. Additionally, the same authors state that partial reduction of the C_{60} layer results in a conductive C_{60} layer that is electrocatalytic in nature. Kachoosangi *et al*. (2006) attributed the electrocatalytic capacity of C_{60} to graphite impurities rather than to the C_{60} since Banks *et al.* (2005) suggested that 1 – 5 % impurity content was sufficient to affect the voltammetric response. In response, Goyal *et al.* (2007) showed with high purity C_{60} fullerenes (>99.5 %) that the apparent electrocatalytic effects were still notably present. Additionally, Goyal *et al.* (2008) specifically observed that coexisting impurities did not show any electrocatalytic properties when assessed alone.

Some of the prominent disadvantages of using fullerene films are the instability and sensitivity of the fullerene films to ambient conditions. In particular, the films readily react with oxygen and water (Kalsberg & Thorp 1991; Haddon, 1992). Only very porous fullerene films can be formed on the electrode surface (as observed in figure 4.28), so the underlying electrode is also involved in the reaction (Kalsberg & Thorp, 1991; Haddon, 1992). These disadvantages potentially render the utilisation of C_{60} films highly unfeasible as sensor surfaces. Szűcs, (2008) had overcome the aforementioned drawbacks by electrochemically partially reducing the C_{60} films in 1 M NaOH, and observed that the reduced films were compact, as well as being stable in aqueous solutions and in the presence of oxygen.

In an earlier report, Xiao *et al.* (2009) suggest that the lack of a return corresponding anodic peak in partial reduction of the C_{60} thin film is evidence of an EC mechanism where a fast electrochemical step is followed by a slow chemical step. The irreversibility of the cathodic peak (in partial reduction), in addition to a significant decrease in the current response for the cathodic peak in the second scan indicates atypical mediator behaviour, which contends its electrocatalytic advantage (Griese *et al.*, 2008).

The improvement in electrocatalytic properties of the GCE after casting of the C_{60} film cannot be doubted, however whether these properties are solely as a result of the C_{60} film is still not without contention. Banks *et al.* (2005) argue that the apparent source of electrocatalytic behaviour of the C_{60} thin film is due to direct interaction with the underlying GCE electrode surface. While this could be possible due to the large uncovered areas afforded by C_{60} aggregation, what is without doubt is the increase in capacitance (CPE, Q_{calc}), apparent electron transfer rate (k_{app}), as well as a decrease in the charge transfer resistance (R_{ct}) observed after partial reduction of the C_{60} thin film, all indicative of electrocatalysis.

4.5 Overall Summary and Conclusions

This study shows the need for careful consideration of parameters otherwise considered trivial in the treatment duration and protocol of carbon nanotubes, and that merely monitoring current response is not sufficient. Impedance and visualisation are key to explaining the modification of electrode surfaces. In this study ideal parameters to utilise when functionalising and activating carbon nanotubes were identified. These parameters were tested by monitoring current response and the impedance of the nanotube- modified electrodes. Secondly, visualisation of the modified nanotubes was performed using HRSEM and AFM (MWCNT), and structural differences noted. Using HRSEM, the uncapping of nanotubes during acid functionalisation was clearly visible. The aggregation of nanotubes at lower functionalisation times was also observed using HRSEM and AFM. This study also shows for the first time the effect of catechol inclusion in carbon nanotubes with substantial enhancements in current response, decreases in R_{ct} and increases in k_{app}. To exemplify the role of both catechol activation and the role of length of time in acid functionalisation of carbon nanotubes, a 490 % increase in current response for the catechol test scan following activation was observed for *f*MWCNT modified surfaces at 9 hours functionalisation time relative to the unactivated unmodified GCE.

4.5.1 Single-walled carbon nanotubes

Table 4.4 summarises parameters that were identified in this study as being ideal for the modification of carbon nanotubes and subsequent modification of the glassy carbon electrode. The general trend for each of SWCNTs, MWCNTs and C_{60} showed that after their respective activation procedures the

performance of the modified electrodes was enhanced. The performance of the electrodes are therefore subsequently compared in the following tables after activation.

Table 4.4 Summary of the outcomes for SWCNT functionalisation and modified electrode surface activation. The recommended time intervals to use are listed.

TEST PARAMETER	OUTCOME†	RECOMMENDED‡
Ideal number of catechol activation cycles	3 – 4	3 (since 4 gave similar results)
Catechol test scan (based on current response)	4 > 6 > 8 > 1 > GCE	6 (4 was disregarded)
C_{calc}	GCE > 8 > 1 > 6 > 4 > GCE	8
R_{ct}	4 > GCE > 6 > 8 > 1	8, 6
k_{app}	8 > 6 > 4 > GCE > 1	8, 6

†In descending order from most ideal to least ideal.

‡Chosen based on representation of the range from most optimal to least optimal.

Functionalisation of SWCNTs was achieved by acid treatment of as produced SWCNTs. In this preliminary study the effects of prolonged exposure of SWCNTs to a strong acid environment were shown, with the rationale being that this parameter is not standardised in literature. For the purposes of this study it was observed that the effect of acid exposure significantly alters the morphological appearance of SWCNTs, which is as a result of the walls of the SWCNTs being functionalised. In accordance, the conductivity of the *f*SWCNTs layer is affected. Electrochemical treatment of a GCE modified with *f*SWCNTs increased the conductivity as well as decreased the resistance of the modified layer which is considered to be as a result of catechol moieties being incorporated within the adsorbed layer, interlinking the functionalised nanotubes and consequently mediating efficient electron transfer.

In table 4.4 it is evident that on average the modified GCE performed more efficiently when the SWCNTs were exposed to acid treatment for 4 - 8 hours and that the SWCNTs should be functionalised for a minimum of 4 hours to achieve satisfactory electrode performance. These were used in subsequent studies involving *f*SWCNTs. Recently Gooding *et al*. (2007) published their observation regarding acid treatment of SWCNTs and found that 6 hours exposure produced nanotubes comprising promising electrocatalytic properties, which corroborates the observations made in this study.

4.5.2 Multi-walled nanotubes

The ideal parameters obtained for the modification of MWCNTs in order to obtain a high degree of conductivity and low resistance are summarised in table 4.5.

Table 4.5 Summary of the outcomes for MWCNT functionalisation and activation. The recommended time intervals to use are listed.

TEST PARAMETER	**OUTCOME†**	**RECOMMENDED**
Ideal number of catechol activation cycles	3 – 4	3
Catechol test scan (I) (after activation)	9 > 1 > 4 > GCE	9
C_{calc}	9 > GCE > 4 > 1	9
R_{ct}	9 > 4 > 1 > GCE	9
k_{app}	9 > 1 > 4 > GCE	9

†In descending order from most ideal to least ideal.

Functionalisation of MWCNTs was achieved in an identical manner to that of SWCNTs by exposure of the nanotubes to a strong acid solution for a period of time. Additionally the *f*SWCNTs-modified GCE surface was activated through electrochemical cycling in catechol. In table 4.5 the various parameters that were assessed to determine the performance of the modified layer are summarised. It is evident from the table that MWCNTs should be acid treated (functionalised) for at least 4 hours, but that optimal operating conditions are obtained with *f*MWCNTs that had been exposed to acid for 9 hours, which is clear from the lower resistance (R_{ct}), and faster rate of electron transfer (k_{app}). For the purpose of subsequent studies MWCNTs that had been acid treated for 9 hours were used at this surface.

4.5.3 C_{60} fullerenes

For studies on the conductance and resistance of C_{60} fullerene modified electrodes, the effect of partial reduction of a physically adsorbed layer of C_{60} on a GCE, in the presence of 1.0 M KOH was evaluated. Additionally, the ideal loading capacity of C_{60} on a GCE was assessed. The findings of this particular study of an ideal loading capacity of 40 µl of 150 µM C_{60} on a 3 mm diameter GCE and a single reduction scan concurred with those observations published by Szűcs *et al.* (2008) and l by Goyal *et al*. (2008), and were adopted for subsequent studies involving C_{60} fullerenes.

4.5.4 Overall comparison of the optimal performances between single-walled and multi-walled nanotubes, and C_{60} fullerenes

Figures 4.38 (A – D) summarise and compare the performance of the nanomaterials with respect to the prominent parameters assessed in this study.

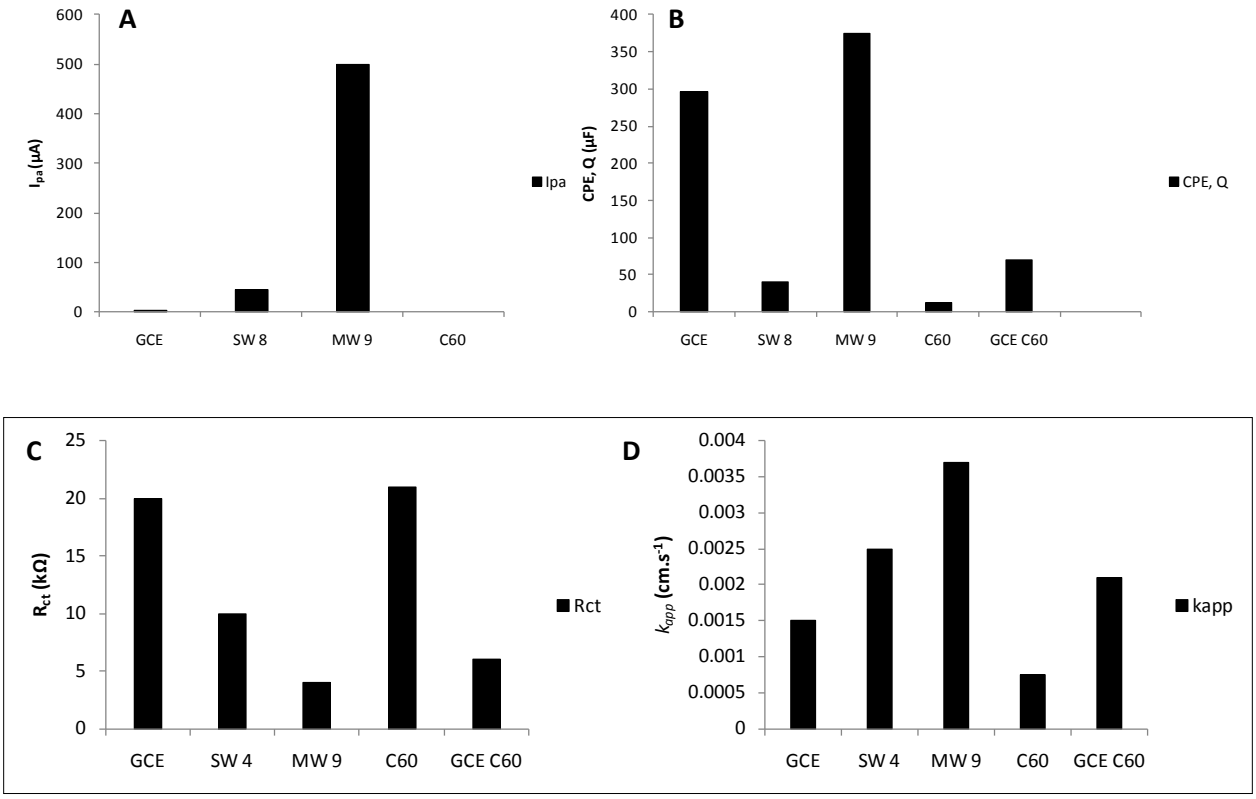

Figure 4.38 Comparisons of the current response, I_{pa} (A), constant phase element, Q (B), charge transfer resistance, R_{ct} (C) and apparent electron transfer rate, k_{app} (D), between an unmodified GCE, *f*SWCNTs functionalised for each of 4 and 6 hours, *f*MWCNTs functionalised for 9 hours; as well as a GCE modified with C_{60} after partial reduction. GCE C_{60} refers to the GCE used in the C_{60} studies prior to modification with C_{60}. The current response, I_{pa} (A) can only be compared between the carbon nanotube-modified electrodes since catechol was detected for these and not for C_{60} fullerenes.

In figures 4.38 (A, B and D) *f*MWCNTs exhibited the greatest increases in current response (A), capacitance (B) and charge, while GCE-C_{60} was low in all the aforementioned figures. Additionally, the GCE-C_{60} before partial reduction exhibited the greatest R_{ct}, indicating that the decrease in current response, C_{calc} and k_{app} for GCE-C_{60} was attributed to the modified layer exhibiting increased insulatory behaviour. In comparison to *f*MWCNTs, GCE-C_{60} and fSWCNTs showed a low current response and k_{app}. When comparing the relative percentage increase in C_{calc}, k_{app} before activation and after, (in the case of *f*SWCNTs and *f*MWCNTs), and partial reduction (for GCE-C_{60}), it can be observed that, (as shown in figure 4.39) *f*MWCNTs exhibit the greatest increase in k_{app} at 750 %, with 330 % at *f*SWCNTs, in comparison to 195 % at an unmodified GCE. Additionally, *f*MWCNTs showed the lowest Rct which indicates the electrode is behaving more as a conductor than an insulator. In comparison, a GCE modified with C_{60}

shows high levels of insulatory behaviour, as evidenced by the greater R_{ct}. interestingly C_{calc} was similar for each of the electrode surfaces modified with *f*CNTs, as compared to an unmodified GCE proving that the additional layer does not inhibit the transport of electrons to the electrode surface. In contrast, GCE-C_{60} showed marked increases in insulatory behaviour, which could be attributable to the morphological aggregation observed earlier in the HRSEM studies.

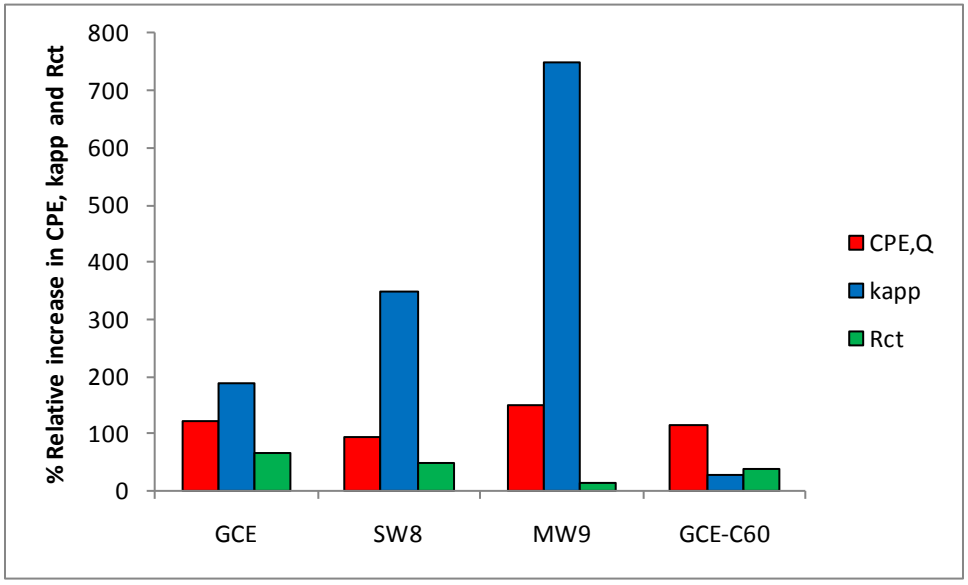

Figure 4.39 Percentage comparisons of I_p, C_{calc}, k_{app} and R_{ct} between the activated and unactivated surfaces for functionalised SWCNTs (4 and 6 hours), and MWCNTs (9 hours), as well as the comparison with partial reduction of GCE-C_{60} surface.

In summary, *f*MWCNTs functionalised for 9 hours exhibited the greatest improvement following surface activation, in addition to the greatest current response, and would be recommended for subsequent electrode modification studies if sensitivity is of importance.

CHAPTER 5

ELECTROANALYSIS OF WORTMANNIN

"*When I am working on a problem, I never think about beauty…..but when I have finished, if the solution is not beautiful, I know it is wrong*"

– Richard Buckminster Fuller

5.1 Introduction

Wortmannin is a secondary metabolite of pharmaceutical importance that was first isolated from *Penicillium wortmanni* in 1957, by Brian and co-workers (Brian *et al.*, 1957). The steroidal furanoid is classified with structurally similar furanoids such as viridin (Hanson, 1995), viridiol and wortmannalone (Wipf & Halter, 2005). Figure 5.1 shows the chemical structure of wortmannin.

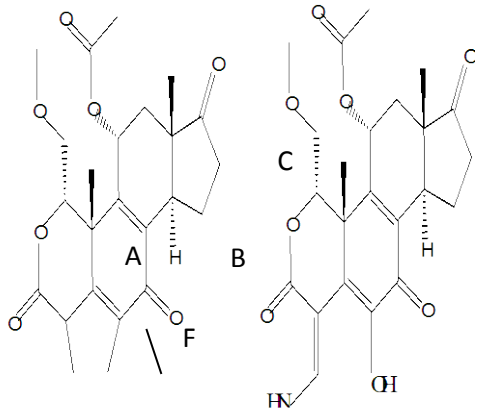

Figure 5.1 Chemical structure of wortmannin (Wipf & Halter, 2005).

Key: A, B, C = lactone A, B, C rings respectively, F = furan ring.

Wortmannin is comprised of an electrophilic strained naphtha[1,8-*bc*]furan heterocycle (F on figure 5.1) that is flanked by carbonyl groups (figure 5.1) (Wipf & Halter, 2005). The carbonyl groups are electron withdrawing in nature, which further increases the electrophilicity of the α-carbon of the furan. Wortmannin binds with high affinity via its tricyclic furan heterocycle (denoted F on figure 5.1) (Wipf & Halter 2005) to the ATP-binding domain on the p110 catalytic subunit of PI3-k (Yuan *et al.* 2007). This non-covalent interaction is sufficient for the inhibition of kinase activity (Wymann *et al.* 2003; Creemer *et al.*, 1996; Yuan *et al.*, 2007), with an IC_{50} value of as low as 10 nM (Yuan *et al.*, 2007). It is however the subsequent covalent modification of a lysine (LYS-802) residue (situated in the catalytic subunit of PI-3K) that leads to the irreversible formation of a wortmannin-PI-3K adduct (Wipf & Halter, 2005).

Wortmannin detection has been met with some challenges, which has subsequently largely been limited to traditional laboratory-based methodologies, specifically high performance liquid chromatography that is often coupled to additional detection techniques such as mass spectrometry

(HPLC-MS) (Holleran *et al.*, 2003). While these techniques are highly sensitive, disadvantages such as a prerequisite for extensive sample pretreatment and cleanup to limit the interferent effect of co-existing compounds, as well as equipment operation being localized and necessitated by proficient personnel in a laboratory, make this technique an undesirable option for rapid and portable detection systems. Indirect methods of detecting wortmannin have been more commonly employed, the popular methods being based on phosphoinositide 3-kinase (PI3-k) inhibition assays. While these assays are highly specific, response times are not rapid and the reliability of the technique working on the first attempt is low.

In this study the utilisation of electrochemistry as a prospective alternative to the established wortmannin detection and quantification techniques was investigated. Electrochemical methods are attractive due to the high degree of specificity and sensitivity they offer, which can be achieved under rapid response times with little to no sample pretreatment required. Additionally, electrochemical methods have successfully been integrated into portable hand-held devices with a simplified and user friendly interface.

The fundamental analysis of the electrochemical behaviour of wortmannin was of primary interest in this section. To the best of our knowledge, this was the first report of the electrochemical detection and characterisation of wortmannin. The electroanalysis of wortmannin is of necessity for the development of an analytical method based on using electrochemistry for the continuous detection and monitoring of wortmannin.

5.2 Objectives

The overarching aim of this chapter was to ascertain the voltammetric behavioural characteristics of wortmannin. In order to develop a successful analytical protocol for wortmannin detection under an array of variable conditions, the following objectives needed to be addressed:

Assess the effects of chemical parameters on the electrochemical behaviour of wortmannin. This was achieved by the evaluation of the effects of:

(a) The ideal supporting electrolyte and its ionic strength for electrochemical analyses of wortmannin,

(b) The pH of the bulk solution on wortmannin electrochemistry.

Ascertain the electrochemical characteristics of wortmannin.

Determine the quantitative capacity for the electrochemical detection of wortmannin. This objective included the evaluation of:

(a) Calibration curves setup for wortmannin quantification.

(b) Limits of detection and quantification.

5.3 Experimental

Key conditions and parameters required for the fundamental electroanalysis reported on here were classified as being either: (i) electrochemical or (ii) operational in nature. The type, ionic strength and pH of the supporting electrolyte were considered to be relevant. Operational parameters comprise physical and mechanical conditions of the electrochemical system. The effect of scan rate, mechanical agitation and continuous scanning on the electroanalysis of wortmannin were identified as important factors. All electrochemical analyses were performed using a polished glassy carbon electrode (r = 1.5 mm), with all hydrodynamic voltammetry performed at a rotating disk carbon electrode (r = 1 mm).

5.3.1 Initial electrochemical characterisation of wortmannin

Wortmannin was received in lyophilised powder form (98 % purity) from Sigma Aldrich, South Africa. The desired wortmannin stability and stock concentration was obtained by preparing stock solutions of wortmannin in 20 % ethanol (to a final concentration of 2.33×10^{-6} mol.cm^{-3}), and stored at 4 °C until required. All electrochemical analyses were performed using aliquots from the stock solution.

5.3.2 Determination of ideal electrochemical conditions

5.3.2.1 Effect of supporting electrolyte type and ionic strength

Table 5.1 summarises the supporting electrolytes assessed in this study, as well as their ionic strengths and pH range.

Table 5.1 Supporting electrolytes assessed in the optimisation of wortmannin electroanalysis.

Supporting Electrolyte	**Ionic strength range (M)**	**pH buffering range (at 25 °C ± 3°C)**
Sodium citrate	0.05 – 0.20	1.0 – 5.0
Britton-Robinson	0.05 – 0.20	2.0 – 12.0
Sodium acetate	0.05 – 0.20	3.0 – 6.0
Ammonia	0.05 – 0.20	9.0- 12.0
Potassium phosphate	0.05 – 0.20	5.5 – 8.5

*All ionic strength concentrations were assessed in 0.05 M increments.

**pH was assessed in 1 pH value increments.

5.3.2.2 Effect of pH of the bulk solution

Wortmannin from a stock solution was added to electrochemical cells each containing 0.2 M BR buffer of different pH values between 2.0 and 10.0 to a final concentration of 1.50×10^{-8} mol.cm^{-3}, at room temperature. All electrochemical cells were degassed with N_2 prior to usage.

5.3.3 Determination of ideal operational parameters

5.3.3.1 Electrochemical surface passivation

The GCE was scanned continuously without cleaning the electrode surface. Surface passivation of the GCE was measured as a decrease in current response with subsequent scans.

5.3.3.2 Effect of scan rate on wortmannin

Scan rate studies were performed using stock wortmannin in 0.2 M BR buffer (pH 4.0) in the scan rate range 5 to 260 $mV.s^{-1}$ (Wang, 2005), at a potential window between 0 and -1500 mV (vs. Ag|AgCl), at a polished GCE. The potential shift and current magnitude for E_{pc1} and E_{pc2} were assessed.

5.3.4 Determination of diffusion coefficient, total number of electrons, αna

For ease of reference, relevant data treatment and equations to determine relevant parameters for wortmannin electrode processes are indicated in the Results & Discussion section.

5.4 Results and Discussion

5.4.1 Initial electrochemical characterisation of wortmannin

Figure 5.2 (A) is a representative CV showing the observed wortmannin redox behaviour. The voltammetric analysis of pure wortmannin in 0.2 M Britton-Robinson buffer (pH 4.0) yields a single irreversible cathodic peak, E_{pc1} between 850 and 1000 mV (depending on pH) suggesting a following rapid homogenous chemical reaction. The effects of pH on the peak potential are outlined in section 5.4.2.2. On the return anodic scan a broad anodic peak, E_{pa1} was observed between 200 and 300 mV. The presence of E_{pa1} was only observed following the initial reduction of wortmannin, E_{pc1}. Studies conducted under stirred conditions [(Figure 5.2 {B)] revealed an additional reduction peak, related to E_{pa1}. This second reduction wave suggests an ECE mechanism for wortmannin redox behaviour at these scan rates in which the product of the chemical reaction following reduction (E_{pc1}) was oxidised (E_{pa1}) and then reduced yielding E_{pc1b} (Figure 5.2 b). Evidence of such behaviour has been reported in the literature (Nigoić *et al.*, 2001).

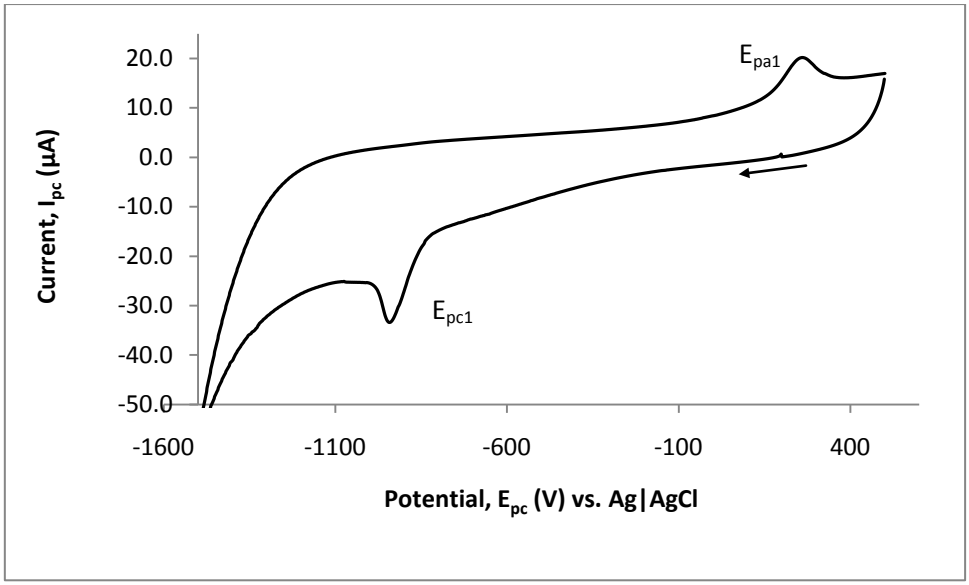

Figure 5.2 (A) Cyclic voltammogram showing the reduction of 4.21 x 10^{-7} mol.cm^{-3} wortmannin at an unmodified glassy carbon electrode in 0.2 M Britton-Robinson buffer pH 4.0, vs. Ag|AgCl. Scan rate: 100 mV.s^{-1}. *Key:* E_{pc1} = prominent reduction peak for wortmannin, E_{pa1} = weak anodic peak.

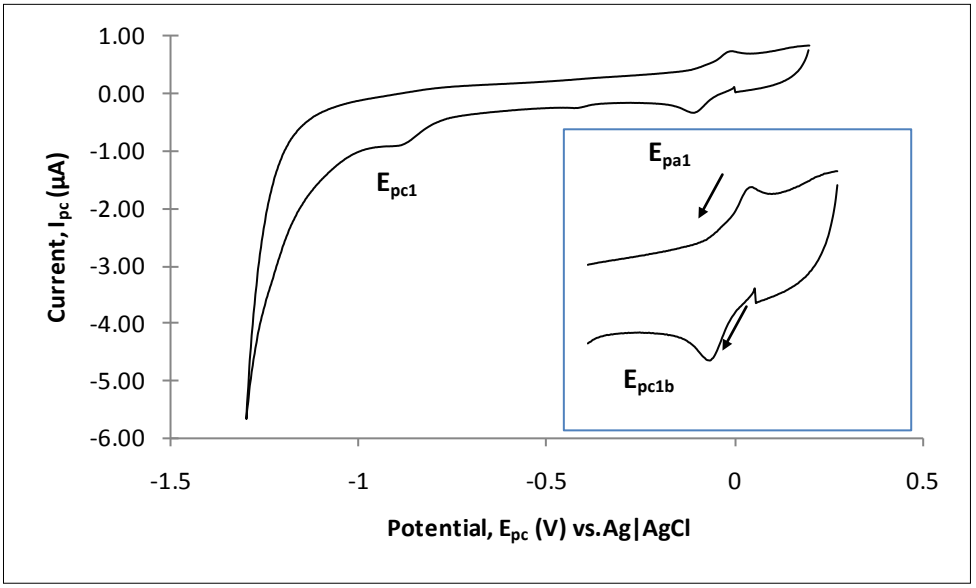

Figure 5.2 (B): (a)Cyclic voltammogram showing the reduction of 2.0 x 10^{-9} mol.cm^{-3} wortmannin at a GCE in 0.2 M Britton-Robinson buffer pH 4.0, vs. Ag|AgCl. *Inset*: showing reversible couple obtained. Scan rate: 100 mV.s-1.

5.4.2 Identification of ideal electrochemical conditions

5.4.2.1 Effect of supporting electrolyte and ionic strength

The effect of a supporting electrolyte on the detection of wortmannin was assessed in two ways: (i) the effect on the current response magnitude, and (ii) the effect on potential. Britton-Robinson buffer is a common supporting electrolyte used since it has a broad buffering capacity (pH 2.0 – 12) and numerous reports of its ideal electrochemical supporting electrolyte capacity have been documented (Britton & Robinson, 1931, Ibrahim *et al.*, 2001). Each buffer assessed in this study was compared to BR buffer within their particular buffering range. Typical buffers used in biological storage and handling of wortmannin were assessed. The buffers compared were: sodium citrate, sodium acetate, ammonia and potassium phosphate. The pH buffering range and ionic strength for each buffer is referred to in table 5.1. Figure 5.3 (A) compares the effect of the supporting electrolyte on the potential window and (B) the current magnitude for the primary reduction peak for wortmannin, E_{pc1} in figure 5.2.

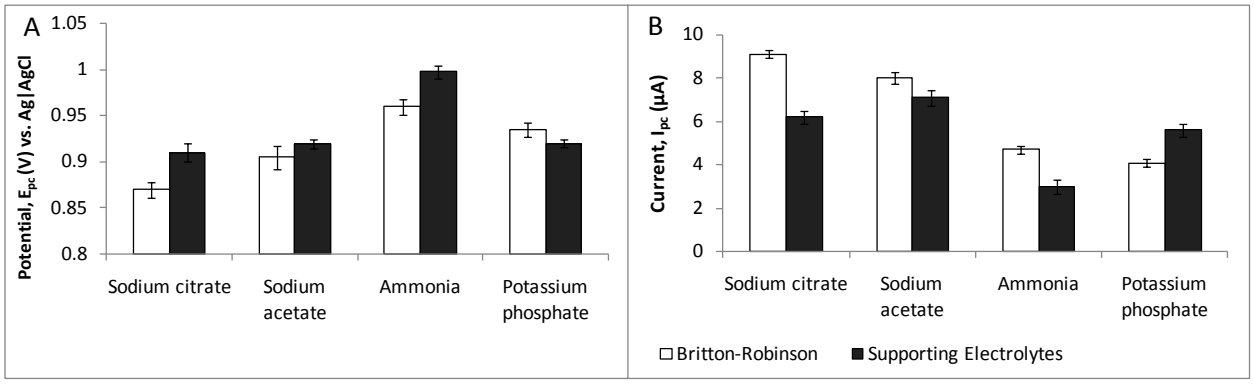

Figure 5.3 Comparison of the normalised (A) potential shift and (B) current strength for 1.5 x 10^{-7} mol.cm^{-3} wortmannin, average over the pH buffering ranges (at 1 pH value increments): sodium citrate: 1.0 – 5.0, sodium acetate: 3.0 – 6.0, ammonia: 9.0 – 12.0, potassium phosphate: 5.5 – 8.5 and BR buffer: 2.0 – 12.0. Error bars show the standard deviation of 3 scans.

The pH of a supporting electrolyte affects the potential at which a redox reaction occurs. Typically, reduction reactions tend to occur at more negative potentials under more alkaline conditions. In figure 5.3 (A) the effect of supporting electrolyte on the redox reaction for E_{pc1} as compared to BR buffer of the same pH is shown. The lowest potential was observed when sodium citrate was used, while the highest potential was observed for ammonia buffer. The use of BR buffer exhibited a

lowered potential in comparison to the alternative buffers, except in the case of potassium phosphate buffer, where a lower potential for E_{pc1} was obtained.

In figure 5.3 (B) the magnitude of the current response was observed to increase in proportion to an increase in the acidity of the bulk solution. Accordingly, the highest current response was observed in BR buffer (pH 4.0) and the lowest in ammonia buffer (pH 9.0). The low current response in ammonia buffer (pH 9.0) could be attributed to the wortmannin structural changes that are described by Holleran *et al.* (2003) to occur under alkaline conditions, and further elaborated on in chapter 6.

Due to the lowered potential and higher current magnitudes exhibited for wortmannin reduction, as well as its application over a broad pH range, BR buffer was opted for as the ideal supporting electrolyte for the electroanalysis of wortmannin and was subsequently utilised.

5.4.2.2 Effect of pH of the bulk solution

Figure 5.4 (A) shows cyclic voltammograms for wortmannin recorded at pH increments of 0.5 or 1.0 pH value between pH 2.0 and 10.0 in 0.2 M BR buffer, with the line graph shown in figure 5.4 (B). The greatest amplitude in current response was observed under acidic conditions. A near linear decrease in current magnitude was observed with an increase in bulk solution alkalinity. A secondary reduction peak was observed to form with an increase in alkalinity suggestive of a possible structural alteration of the parent wortmannin compound under alkaline conditions. The hydrolysis of wortmannin under neutral to alkaline conditions has been described by Holleran *et al*. (2003) and Wipf & Halter, (2005), and is further investigated in chapter 6.

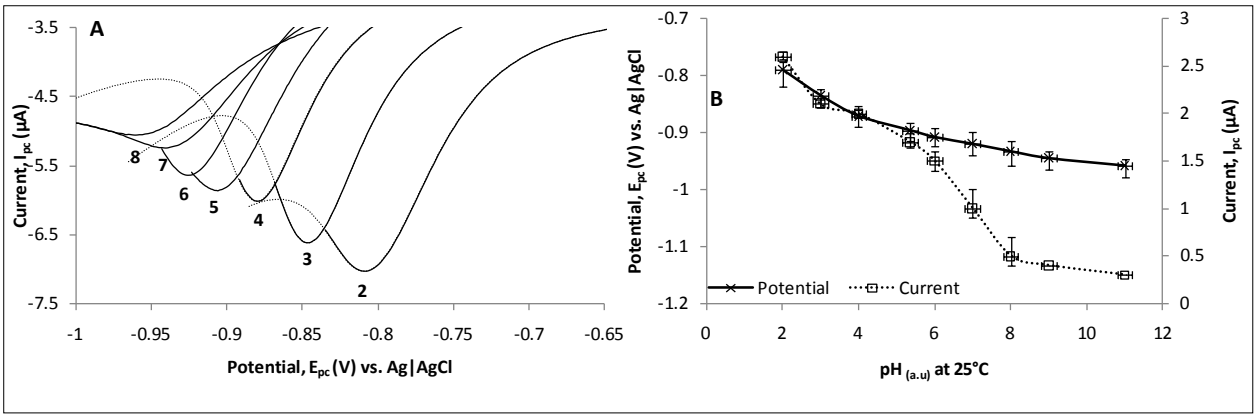

Figure 5.4 (A) Representative cyclic voltammograms and, (B) the corresponding line graphs showing the effect of pH on the reduction (E_{pc1}) of 1.5 x 10^{-8} mol.cm^{-3} wortmannin at a glassy carbon electrode in 0.2 M Britton-Robinson buffer, vs. Ag|AgCl. Scan rate: 100 $mV.s^{-1}$. *(Key)*: numbers in (A) indicate pH value.

The relationship between pH and potential shift can assist in the determination of the redox process and the number of electrons involved (D'Souza *et al*., 2005; Yadegari *et al*., 2008). In figure 5.4 (B) a distinctive shift in potential to more negative values occurs with an increase in solution alkalinity; however, this appeared to occur in three phases. Under acidic conditions (pH 2-4) a $\delta E_p.pH^{-1}$ of 45 $mV.pH^{-1}$ was observed which decreased to 15 $mV.pH^{-1}$ (pH 4 - 6) and to 10 $mV.pH^{-1}$. Inflection points at pH 4 and pH 9 may be associated with two pKa values. A shift of 45 $mV.pH^{-1}$ is indicative of a system where $4e^-/3H^+$ are involved in an irreversible reaction. Similar descriptions were made by El-Samanody *et al*, 2001 for the electro-reduction of osmium complexes. The decrease of $\delta E_p.pH^{-1}$ to 10 $mV.pH^{-1}$ with increasing alkalinity of the bulk solution suggests less efficient electron transfer within the bulk solution (Bard & Faulkner, 1980; Kissinger & Heinemann, 1996), as well as possible secondary reduction reactions occurring.

5.4.3 Electrochemical behaviour of wortmannin

5.4.3.1 Electrochemical surface passivation

The effect of a series of reduction CVs performed without cleaning the electrode between scans is shown in figure 5.5 (A) while the line graph in figure (B) shows the relationship between the decrease in the primary cathodic wave for wortmannin reduction, E_{pc1} and the corresponding increase in a secondary cathodic wave, $E_{pc2,}$ observed as a post-peak.

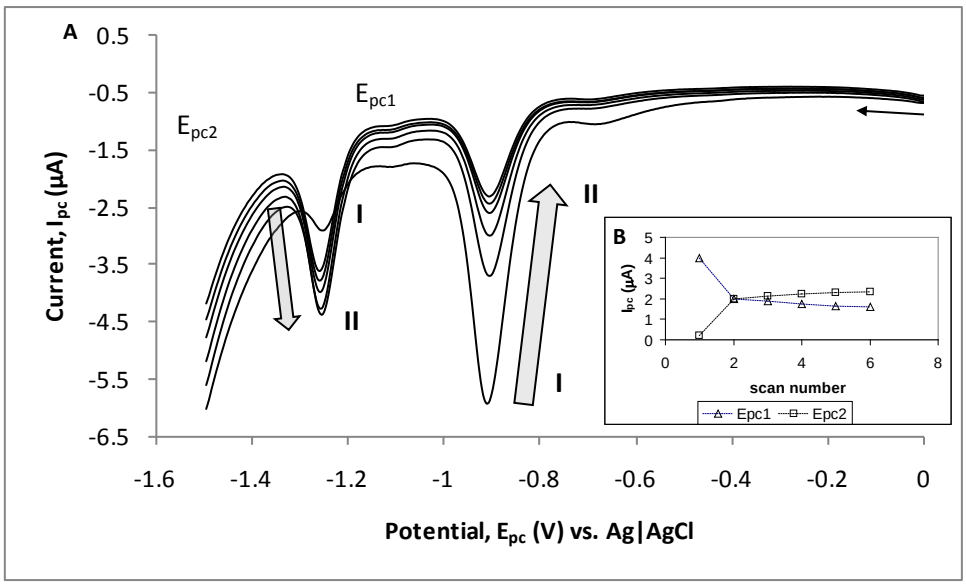

Figure 5.5 (A) Consecutive cyclic voltammetry scans of 4.21 x 10^{-7} mol.cm^{-3} wortmannin showing the effects of surface passivation on the magnitude of the current response (I_{pc}) at a GCE. The inset (B) shows the line graph of I_{pc} vs. scan number for the primary (E_{pc1}) and secondary (E_{pc3}) reduction peaks. *Parameters:* 0.2 M Britton-Robinson buffer pH 4.0, Scan rate: 50 mV.s^{-1}. *Key:* E_{pc1} = prominent primary reduction peak for wortmannin, E_{pc2} = secondary reduction peak for wortmannin, (I) = scan 1, (II) = scan 6.

The current response for E_{pc1} was observed to decrease with subsequent scans, associated with the depletion of diffused wortmannin, while E_{pc2} was noted to increase. The decrease in E_{pc1} also implies a lowered active electrode surface, which could be attributed to the adsorption of wortmannin moieties onto the electrode. Similar behaviour has been reported for adsorbed species (Abdel-Hamid, 1988). An increase in E_{pc2} then suggests the reduction of increasingly adsorbed wortmannin. E_{pc2} cannot be attributed to the reduction of products of the first wortmannin reduction (E_{pc1}) since this second reduction wave (E_{pc2}) is not observed as a pre-peak, rather as a post-peak (Bard & Faulkner, 1980). The nature of E_{pc2} can thus be attributed to reduction of adsorbed wortmannin, its reduction potential being more negative than that of the reduction of diffused wortmannin (E_{pc1}) as it is stabilised by its interaction with the electrode surface. Reduction of wortmannin under diffusion control then occurs at either the free surface or through adsorbed wortmannin (Bard & Faulkner, 1980).

The current of E_{pc1} was observed to return to ~ 90 % of the magnitude of the first scan following agitation of the bulk solution for 5 minutes, followed by 2 minutes equilibration while E_{pc2} was decreased to near baseline levels, ostensibly associated with the desorption of the adsorbed wortmannin moieties associated with this reduction wave.

5.4.3.2 Effect of scan rate on wortmannin mass transport

The effect of scan rate on the reduction peak for wortmannin, E_{pc1} was assessed through CVs of wortmannin in a quiescent solution of 0.2 M BR buffer (pH 4.0), by employing a scan rate range from 5 $mV.s^{-1}$ to 200 $mV.s^{-1}$. Figure 5.6 shows the CVs for the scan rate range 5 $mV.s^{-1}$ to 50 $mV.s^{-1}$.

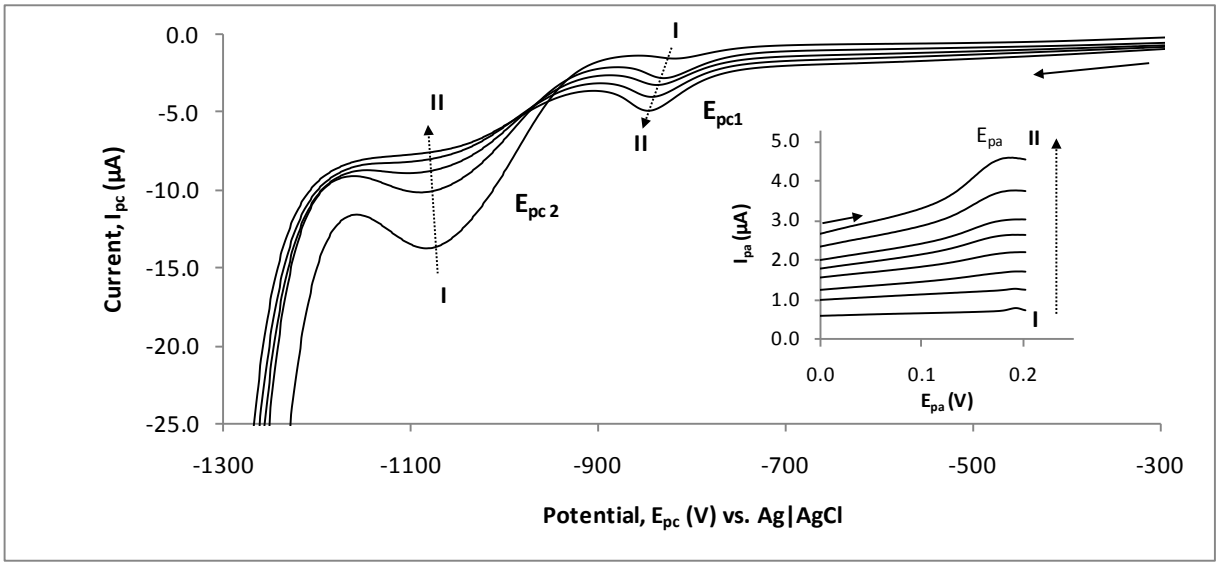

Figure 5.6 Cyclic voltammograms showing the effect of low scan rates on the current strength and cathodic peak potential (E_{pc1}) for 2.1 x 10^{-7} $mol.cm^{-3}$ wortmannin reduction at a glassy carbon electrode in 0.2 M Britton-Robinson buffer (pH 4.0), vs. Ag|AgCl. Scan rate range: 5 $mV.s^{-1}$ (I) – 50 $mV.s^{-1}$ (II). *(Inset)*: Complementary cyclic voltammograms for the return anodic peak (E_{pa}) for wortmannin.

In contrast to what was previously observed at 100 $mV.s^{-1}$, at lower scan rates (5 $mV.s^{-1}$ to 50 $mV.s^{-1}$) (figure 5.6) E_{pc2} was prominent, with E_{pc1} being near negligible at 5 $mV.s^{-1}$. As the scan rate was increased to 50 $mV.s^{-1}$, E_{pc2} was observed to decrease (indicating that this was not a diffusion controlled process) and with a corresponding increase in the current magnitude for E_{pc1}. This dependence of E_{pc2} on scan rate suggests a time dependent adsorption and following reduction at slow scan rates. That this wave predominates at low scan rates is also further evidence that the reduction at E_{pc2} is not as a result of the reduction of electroactive products formed following E_{pc1}.

Figure 5.7 shows CVs for scan rates between 60 mV.s^{-1} and 110 mV.s^{-1}. In contrast to the lower scan rates (figure 5.6) the preferential reduction of E_{pc1} was observed to occur, with E_{pc2} not occurring at scan rates above 110 mV.s^{-1} on the first scan.

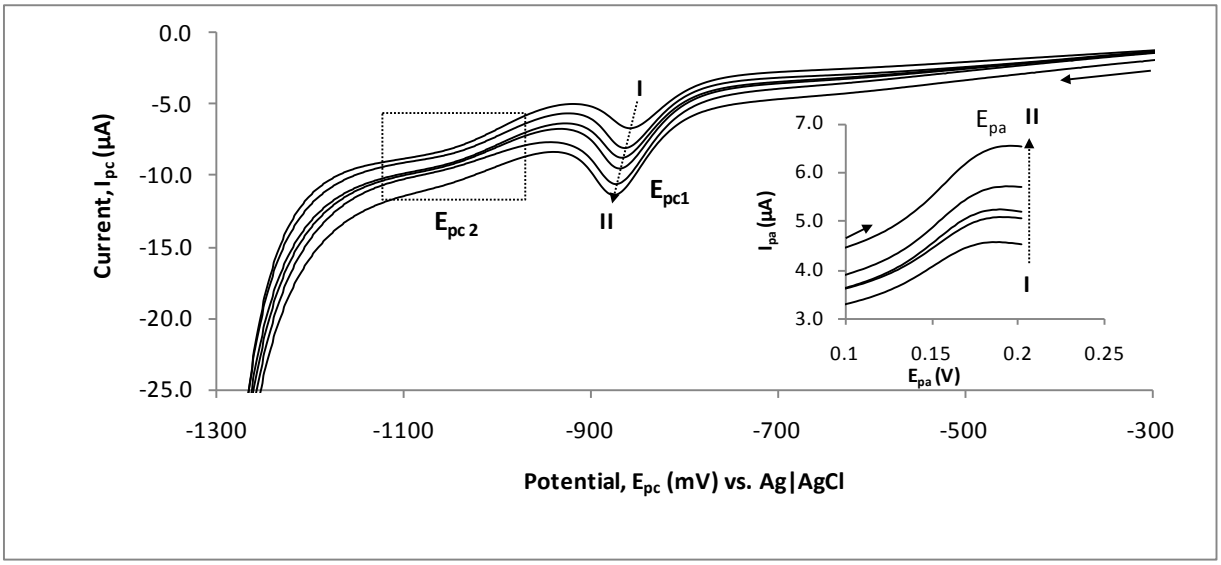

Figure 5.7 Cyclic voltammograms showing the effect of scan rate on the cathodic peak potential ($E_{pc1,2}$) for 2.1 x 10^{-7} mol.cm^{-3} wortmannin reduction at a glassy carbon electrode in 0.2 M Britton-Robinson buffer pH 4.0 vs. Ag|AgCl. Scan rate range: 60 – 110 mV.s^{-1}. *(Inset)*: Complementary cyclic voltammograms for the return anodic peak (E_{pa}) for wortmannin.

Figure 5.7 shows a plot of current (I_{pc}) and scan rate ($v^{½}$) for the reduction of wortmannin. At scan rates not exceeding 100 mV.s^{-1}, a linear relationship (R^2 = 0.9958) was observed between I_{pc} and $v^{½}$ (figure 5.8), which is indicative of an electrode process that is diffusion-controlled (Bard & Faulkner, 1980). With scan rates greater than 100 mV.s^{-1}, a non-linear increase in I_{pc} was observed, which suggests the occurrence of a process governed by kinetics.

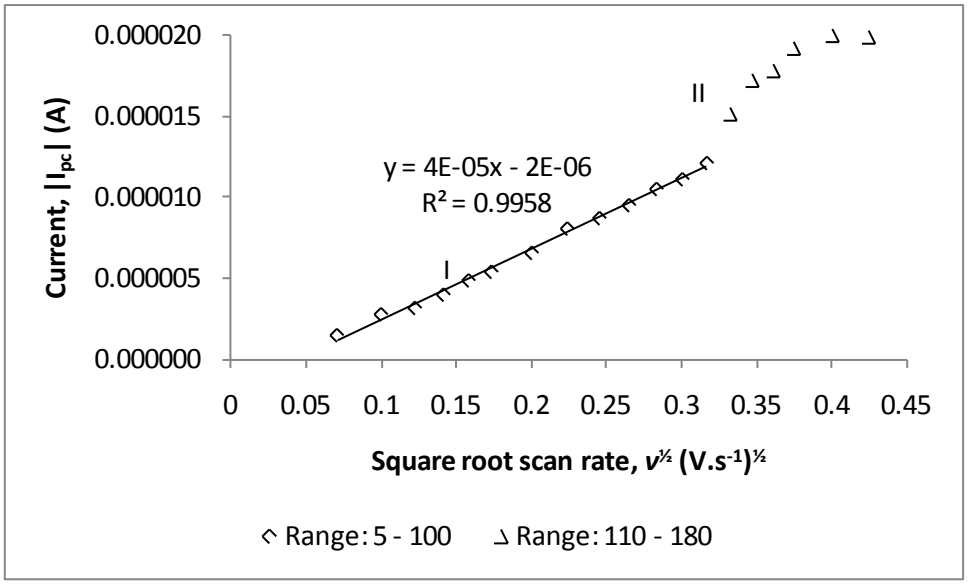

Figure 5.8 The relationship between current response, I_{pc1} and the square root of scan rate, $v^{½}$ for the reduction of 2.1 x 10^{-7} mol.cm^{-3} wortmannin at an unmodified glassy carbon electrode in 0.2 M Britton – Robinson buffer pH 4.0, vs. Ag|AgCl. (*Key*): scan rate range 0.005 V.s^{-1} – 0.100 V.s^{-1} (R^2 = 0.9950); II = 0.110 V.s^{-1} – 0.180 V.s^{-1}. Error bars omitted for clarity, n = 3.

According to Bard & Faulkner, (1980), the slope of a plot of log I_{pc} (µA) vs. log *v* (mV.s^{-1}) (figure 5.9) yields information on the type of mass transport processes occurring at the electrode surface.

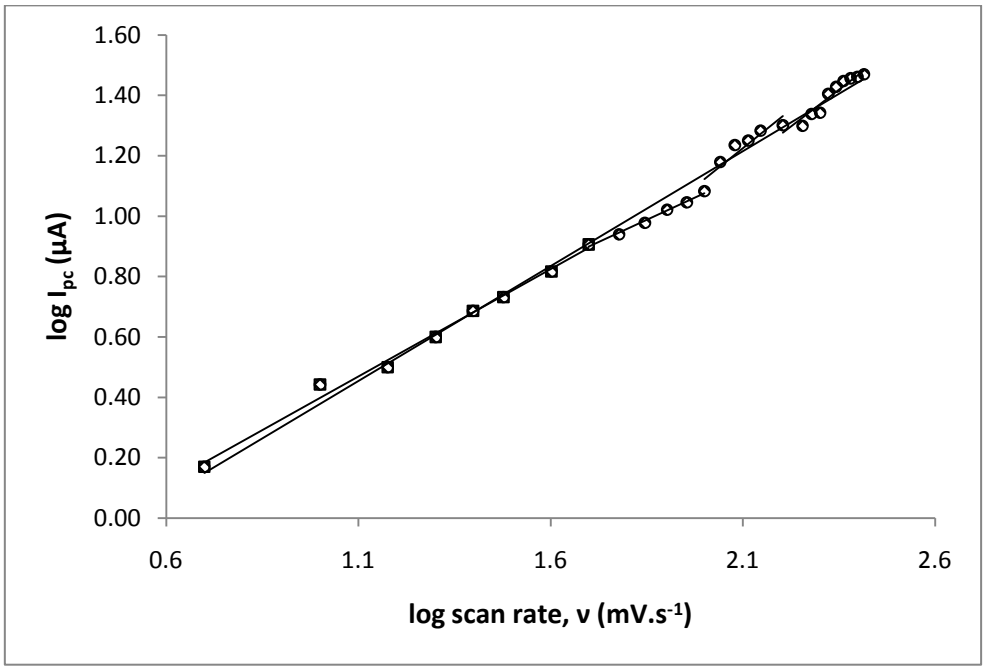

Figure 5.9 The relationship between log scan rate, *v* and log current response, I_{pc1} for the reduction of 2.1 x 10^{-7} mol.cm^{-3} wortmannin at an unmodified glassy carbon electrode in 0.2 M Britton – Robinson buffer pH 4.0, vs. Ag|AgCl. (Key): scan rate range 5 mV.s^{-1} – 260 mV.s^{-1}.

A linear relationship between log I_{pc} and log *v* with a gradient near the value of 0.50 describes a system, which is purely diffusion-controlled (Bard & Faulkner, 1980). In figure 5.9 various areas of linearity were observed at increasing scan rates. Table 5.2 summarises gradients obtained at the different areas of linearity.

Table 5.2 Summarising the gradients of log *v* versus log I_{pc1}

Scan rate range ($mV.s^{-1}$)	Gradient	Correlation coefficient, R^2
5 – 50	0.708	0.9918
50 – 100	0.590	0.9907
100 – 160	1.023	0.8766
160 – 260	0.976	0.9214

At lower scan rates (5 – 50 $mV.s^{-1}$) the gradient was observed to be greater than 0.50 (Table 5.2). A value of 0.71 suggests a system controlled by adsorption and diffusion, reinforcing observations of a post-wave following reduction of wortmannin, and attributed to reduction of adsorbed wortmannin moieties. Between 50 and 100 $mV.s^{-1}$ a gradient of 0.59 was obtained, which is near the theoretical value of ~ 0.50 used to describe systems largely controlled by diffusion (Zare *et al.*, 2005) but with adsorptive behaviour. At scan rates greater than 100 $mV.s^{-1}$, the gradient was observed to be near 1 suggesting the electrochemical process is not controlled by diffusion but rather by kinetics (Zare *et al.*, 2005), corresponding to lack of linearity in this scan rate range in plots of the square root of the scan rate versus current (figure 5.8).

This result suggests that the electrochemical processes for wortmannin are complex and differ depending on the scan rate and that three different behavioural patterns are observed governed by adsorption and diffusion at low scan rates, largely diffusion (with adsorption) at intermediate scan rate ranges and by kinetics at higher scan rate ranges. The complex nature therefore means that it becomes difficult to separate influences of adsorption and diffusion particularly within the scan range of 50 $mV.s^{-1}$ to 100 $mV.s^{-1}$. Studies were largely conducted within this scan rate region.

A plot of current response, I_{pc} vs concentration of wortmannin (figure 5.10) that is linear is further evidence of a largely diffusion-controlled process (Nicholson & Shain, 1964), at 100 mV.s^{-1} within the intermediate (50 – 100 mV.s^{-1} scan range). Figure 5.10 shows the relationship between wortmannin concentration and current response.

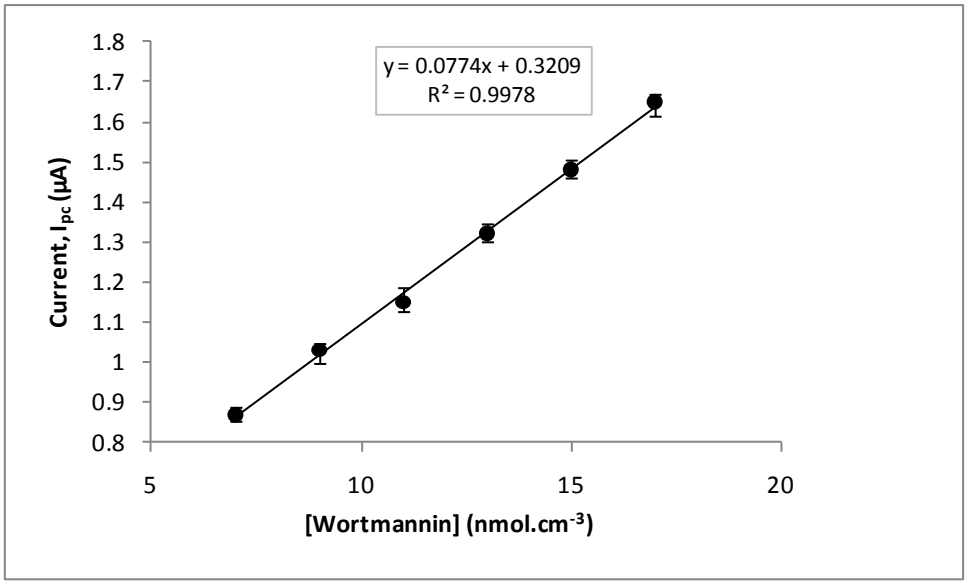

Figure 5.10 Standard curve of wortmannin concentration versus current in 0.2 M BR buffer (pH 4.0) at an unmodified GCE. Each scan was performed in triplicate with identical operational parameters maintained. Scan rate: 100 mV.s^{-1}.

5.4.3.3 Elucidation of the wortmannin reduction mechanism

Plots of current function ($I_{pc}.v^{-½}$ versus scan rate) provide useful insight into electrode mechanisms. Decreases in $I_{pc}.v^{-½}$ for irreversible reactions with scan rate suggests the occurrence of a chemical step following the electron transfer, via an ECE electrode reaction (Abdel-Hamid, 1998; Nigoić *et al.*, 2001). For E_{pc1}, Fig 5.11 shows this dependence on scan rate. Between 5 to 50 mV.s^{-1} an increase in current function is observed indicative of adsorption processes. From 50 mV.s^{-1} to 100 mV.s^{-1} a decrease is observed in the current function associated with an ECE mechanism. Beyond 100 mV.s^{-1}, in the kinetically controlled region the trend is unclear. For E_{pc2}, a reduction in the current function with scan rate between 5 and 50 mV.s^{-1} was also observed (data not shown).

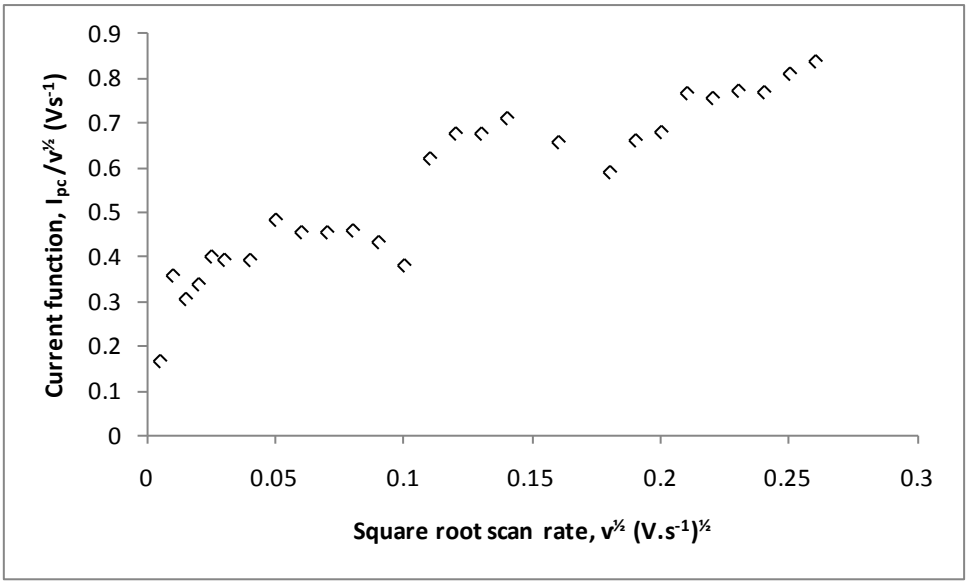

Figure 5.11 Plot of current function ($I_{pc}/v^{½}$) versus scan rate, v for E_{pc1} of 2.1 x 10^{-7} mol.cm^{-3} wortmannin at a glassy carbon electrode, in 0.2 M Britton-Robinson buffer (pH 4.0).

Further support for a chemical step following electron transfer is observed in figure 5.12 where, according to Nicholson & Shain, 1964, a plot of the scan rate, v versus potential function for wortmannin reduction (E_{pc1}), $E_{pc}/v^{½}$ would be observed as hyperbole-shaped. The linearity observed in a plot of potential versus log scan rate, figure 5.13 (R^2 = 0.9934) is also consistent with an EC mechanism (Brown & Large, 1971) and also provides further support for an irreversible reduction.

The results thus indicate an ECE mechanism for diffusion controlled wortmannin in scan rates between 50 and 100mV.s^{-1}.

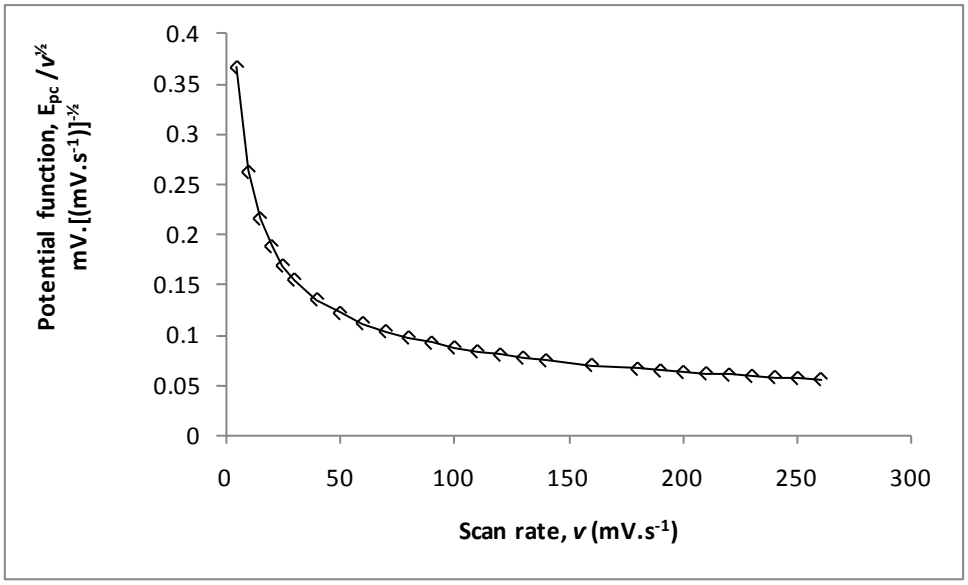

Figure 5.12 Plot of scan rate (v) versus potential function ($E_{pc}/v^{½}$) for the reduction of 2.1 x 10^{-7} mol.cm^{-3} wortmannin at a glassy carbon electrode, in 0.2 M Britton-Robinson buffer (pH 4.0).

5.4.3.4 Determination of charge transfer coefficient and number of electrons in the rate limiting step

Several methods can be utilized to determine these parameters as described further.

A line plot of log scan rate, *v* (mV.s^{-1}) vs. potential, E_{pc1} (mV) yields the Tafel slope (*b*) (Figure 5.13).

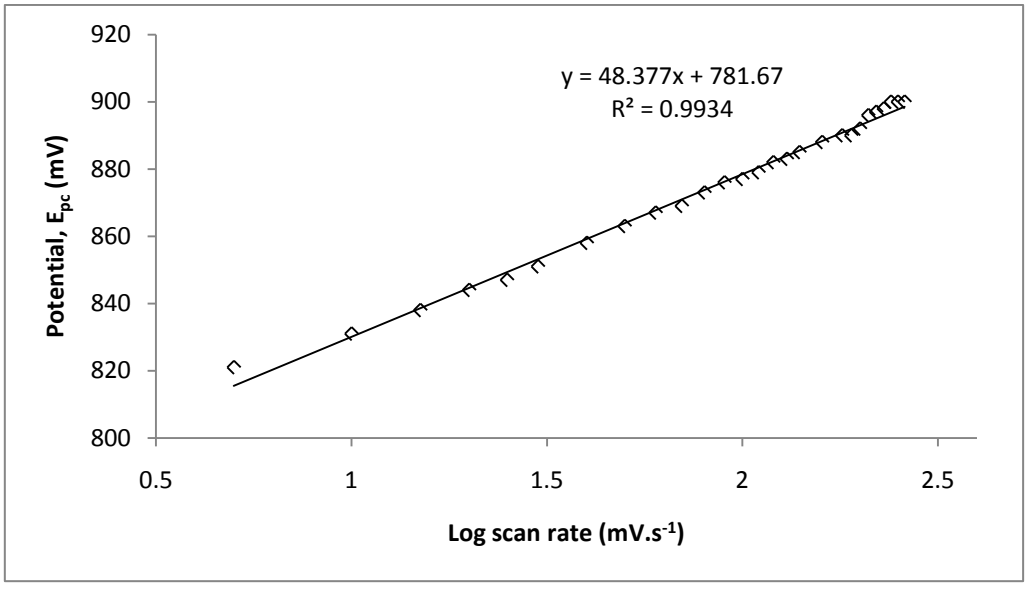

Figure 5.13 The log of scan rate, *v* versus potential, E_{pc1} for 2.1 x 10^{-7} mol.cm^{-3} wortmannin. Scan rate range: 5 to 260 mV.s^{-1}, in 0.2 M Britton-Robinson buffer (pH 4.0).

The Tafel slope (*b*) can be expressed as:

$$b = 2\left(\frac{\delta E_{pc1}}{\delta log v}\right) \qquad [5.01]$$

Where $\left(\frac{\delta E_{pc1}}{\delta log v}\right)$ is the slope of E_{pc} (mV) vs. log *v* (mV.s^{-1})

The value calculated for b using equation [5.01] can be used to determine the transfer coefficient, α according to the method of Laviron (1979).

$$b = 2.303\ \frac{R\,T}{F\alpha n_a} \qquad [5.02]$$

Where $2.303\ \frac{RT}{F}$= 59.1 mV

Such that:

$$b = \frac{59.1}{\alpha n_a}$$

By employing equation 5.01, and incorporating a slope of 48.38 obtained for figure 5,13, the Tafel slope, b was determined to be 96.75 mV.dec^{-1} for the scan rate region 5 to 260 mV.s^{-1}. A tafel slope of 96.50 mV.dec^{-1} was obtained for the scan rate region 50 to 100 mV.s^{-1} (suggesting a one electron reduction in the rate limiting step) (Mazloum-Ardakania *et al.*, 2010). A lowered value of 83.90 mV.dec^{-1} was obtained for the potential region of 5 to 50 mV.s^{-1} while the tafel slope increased above 100 mV.dec^{-1} at scan rates above 160 mV.s^{-1}.

The transfer coefficient was determined by employing equation [5.02]. With a calculated (*b*) of 96.75, a value of 0.61 was obtained for αn_a. A value for α of 0.61 is determined if 1 electron is transferred in the RDS. If 2 electrons are inferred to be involved in the RDS, a value of 0.31 for α is obtained. However, since for irreversible systems α is often assumed to be 0.5, a value of 0.61 is assumed.

Using this derived value for αn_a the diffusion coefficient, *D* was determined experimentally via the relevant derivation of the Randles-Sevcik equation:

$$I_{pc} = 2.98 \times 10^5 n_t (\propto n_a)^{½} A D^{½} C v^{½} \ (at\ 298K) \qquad [5.03]$$

Where $\frac{Ipc}{v½}$ =- slope of a plot if current versus the square route of the scan rate for wortmannin detection, n_t= total number of electrons, A is the theoretical surface area, 0.0707 cm2, C is the concentration of wortmannin (in mol.cm-3), 2.10 x10-7 mol.cm-3; and the rest of the variables have their usual meanings.

The diffusion coefficient, D was determined using the slope from figure 5.8 $\frac{I_{pc}}{v^{½}}$ = 4.32 × 10^{-5}, assuming an n_t = 4 (based on figure 5.4) and αn_a = 0.61

Solving equation [5.03]: for D = 1.67 x 10^{-5} $cm^2.s^{-1}$

This value for *D* is however unrealistic considering that wortmannin is a bulky molecule. It is theorized that the contribution of adsorption has overestimated the diffusion coefficient and by inference underestimated the value for αn_a via the calculated methods above. Alternative derivations for αn_a were thus examined.

Laviron's equation has been utilised in the literature for irreversible reductions associated with adsorptive behaviour.

$$E_p = E_0 + \frac{RT}{\alpha nF}\left[ln\left\{\frac{RTk_s}{\alpha nF}\right\} - lnv\right] \qquad [5.04]$$

Where, α = the charge transfer co-efficient, n_a – the number of electrons transferred in the RDS, k_s – the electron transfer rate constant, v - the scan rate, E^0 – the formal reduction potential and F – Faraday's constant.

A linear plot of E_p vs. ln*v* yields the αn_a value from its slope and k_s from its intercept. The E^0 value is extrapolated from the intercept of a plot of E_p vs. *v*. (Laviron, 1979; Chandra *et al*., 2008).

The intercept of a plot of E_p (V) vs. *v* ($V.s^{-1}$) of E_{pc1} (Figure 5.14) yields an intercept of 0.8311 = E^0 value.

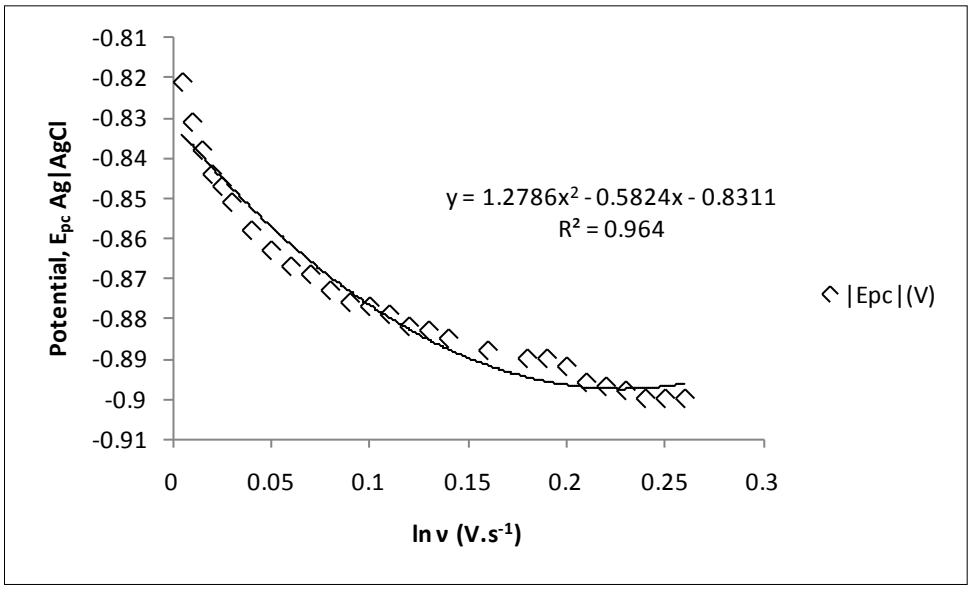

Figure 5.14. Slope of a plot of lnv, V ($V.s^{-1}$) versus E_{pc} (V) for E_{pc1}.of wortmannin reduction.

Solving equation 5.04 yields:

$$-\frac{RT}{\alpha n_a F} = slope\ (of\ a\ plot\ of\ E_{pc} vs.\ lnv) \qquad [5.05]$$

The slope of a plot of E_{pc} vs. lnv = -0.0207 (Figure 5.15). Solving for equation 5.05 yields αn_a = 1.2405. This is suggestive of α = 0.62 if n_a = 2.

To probe this value for αn_a , we examined an alternative and simpler method for determining αn_a via the following equation (Bard & Faulkner, 1980):

$$E_p - E_{\frac{p}{2}} = \frac{47.7}{\alpha n_a} \qquad [5.06]$$

Where E_p = peak potential (mV) and $E_{p/2}$ = potential at which current is at half its peak value

For example, at pH 3: E_{pc} = -0.8441, $E_p^{½}$ =-0.8093. This yields αn_a = 1.37, which is more closely aligned with the value determined in Equation 5.05. This then suggests that adsorptive behaviour has influenced the accurate determination of the Tafel slope derived value for αn_a and indicates 2 electrons are involved in the RLS for wortmannin with α = 0.62.

A value for α of approximately 0.50, indicates the reaction - activated transition state can either form reactants or products. A value nearer 1 for α implies that the reaction equilibrium would favour the formation of products, while nearer 0 favours reactant formation and is typically not dependent on the applied potential (Laviron, 1979). The calculated value of 0.62 for α suggests an equilibrium shift that is more in favour of product formation. Subsequently, a more profound barrier to activation exists, and higher energy levels are required to reduce the wortmannin species, resulting in a slower electron process. This behaviour is typical of irreversible systems (Bockris *et al.*, 2000). The linearity observed in figure 5.13 is a further indicator of irreversibility (Caro *et al.*, 2002), since with increasing scan rates the potential was observed to shift in a characteristic manner to higher potentials.

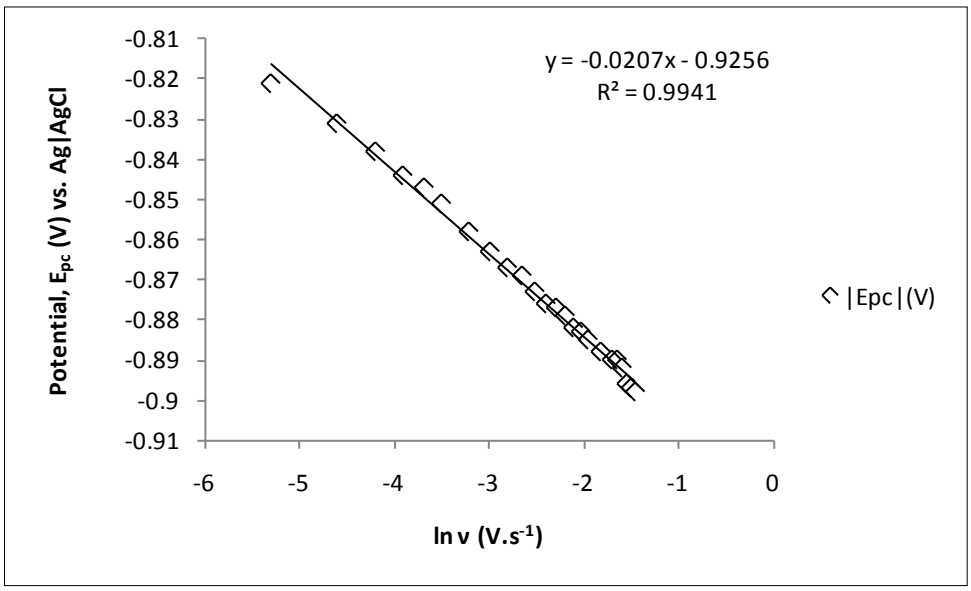

Figure 5.15. Slope of a plot of lnv ($V.s^{-1}$) versus Epc1 (V) for wortmannin reduction.

Resolving equation 5.04, where ln v = 0 yields:

$$k_s = \frac{\alpha n_a F}{RT} e^{\frac{\alpha nF}{RT}(E_p - E_o)} \qquad [5.07]$$

Solving for k_s using values for E^0 = 0.8311 and αn_a = 0.62 determined above yields a value of 0.50 cm.sec^{-1}.

If $k_s = k_o$, and the values of αn_a are known, the diffusion coefficient can be determined from the following relation between E_p and scan rate (for irreversible diffusion controlled reactions, Bard & Faulkner, 1980) where R, T and F have their conventional meanings.

$$E_p = E_o' + \left(\frac{RT}{\alpha n_a F}\right)\left[0.780 + ln\left(\frac{D_R^{½}}{k_o}\right) + \ln\left(\frac{\alpha n_a F v}{RT}\right)½\right] \qquad [5.08]$$

Resolving this equation, yields a plot of E_p versus ln v, where if ln v is set to 0, yields an equation for D where intercept = - 0.9256 (Figure 5.15)

$$D^{½} = k_o e^{\left(\frac{\alpha nF}{RT}[Intercept - E_o'] - 0.780 - ½ln(\alpha n_a F) + ½ln(RT)\right)} \qquad [5.09]$$

A value for *D* of 1.19 x 10^{-7} cm^2.s^{-1} was obtained which represents a more realistic value for D than that determined via the Randles-Sevcik equation. This determination for the value of D is potentially more plausible given that it is not dependent on assumptions made for n_t.

The determination of *D* via the Randles –Sevcik equation was reliant on the assumption of n_t = 4 for wortmannin based on the slope of E_{pc1} versus pH within the pH range 2 to 4. It was of interest to probe this value using an alternative set of experiments. Hydrodynamic voltammetry at a rotating

disk electrode (RDE) for the reduction of 2.33 x 10^{-8} mol.cm^{-3} wortmannin in 0.2M BR buffer (pH 4.0) was recorded at an increasing angular frequency of rotation $\omega^{½}$, figure 5.16.

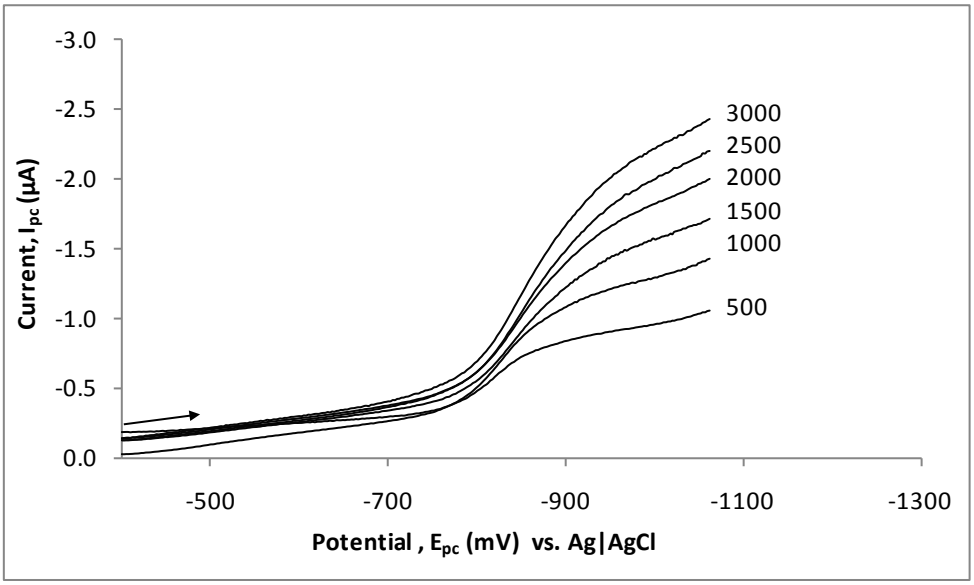

Figure 5.16 Hydrodynamic linear sweep voltammetry curves for the reduction of 2.33 x 10^{-8} mol.cm^{-3} wortmannin at a glassy carbon rotating disk electrode in 0.2 M Britton-Robinson buffer pH 4.0, vs. Ag|AgCl, at different rotation speeds between 500 RPM and 3000 RPM. Scan rate = 60 mV.s^{-1}.

A plot of I_{pc} versus $\omega^{½}$ (figure 5.17), otherwise known as the Levich plot (Zare *et al.*, 2007) was used to derive the n_t value by employing the Levich equation, [5.10] (Zare *et al.*, 2007) and utilising values of αn_a =1.204 and D = 1.19 x 10^{-7} cm^2.s^{-1}.

$$I_{pc} = 0.620nFAD\omega^{½}Cv^{-} \qquad [5.10]$$

Where $\frac{Ipc}{\omega ½}$ = slope of the Levich plot, 9.89 x 10-8, n is n_t the total number of electrons F is Faraday's constant, 96485.34 C.mol^{-1}, A is the determined electrode surface area (cm^2), ω is the angular frequency of rotation (rad.s^{-1}), C is the concentration of wortmannin in the bulk solution, 2.33 x 10^{-8} mol.cm^{-3}, and v is the kinematic viscosity, 0.01 cm^2.s^{-1} for H_20 at STP.

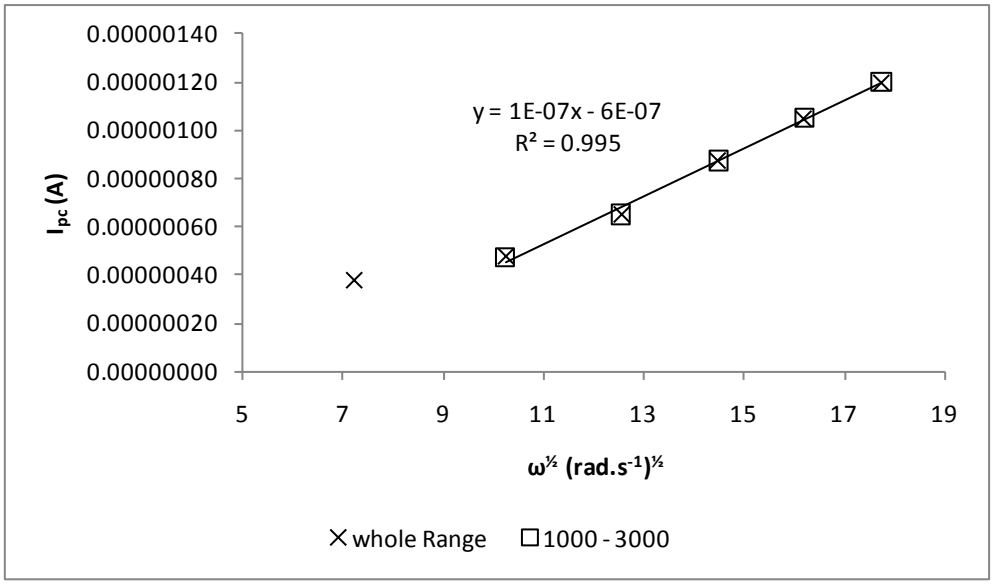

Figure 5.17 Levich plot of 2.33 x 10^{-8} mol.cm^{-3} wortmannin reduction, E_{pc1}, at a rotating disk electrode (0.1 cm radius) in 0.2 M Britton-Robinson buffer (pH 4.0).

With a slope value of 1 x 10^{-7}, an n_t = 4.33 ~ 4 for wortmannin reduction was obtained, aligned with the value determined based on the slope of potential versus pH.

5.5 Summary and Conclusions

The electrochemical analysis of wortmannin is complicated by mixed adsorption and diffusion processes, dependent on scan rate. Wortmannin reduction exhibited a single irreversible cathodic peak, E_{pc1} at scan rates greater than 60 mV.s^{-1} in a region which was shown to be governed largely by diffusion, but complicated by adsorption. When scan rates less than 60 mV.s^{-1} were applied, a cathodic peak (E_{pc2}) more electronegative than E_{pc1} (post peak) was preferentially reduced over E_{pc1} and associated with the reduction of adsorbed wortmannin. This waveform was observed at higher scan rates only upon a second scan suggesting that the adsorption is time dependent. At scan rates in excess of 100 mV.s^{-1} the process was largely kinetically - controlled.

Plots of current function versus scan rate further highlighted the scan rate dependence on these processes. For E_{pc1} an ECE mechanism was theorized based on the decrease in slope of this plot between only 50 – 100 mV.s^{-1}. For E_{pc2} between 0 and 50 mV.s^{-1} a similar decrease in the slope of the current function was suggestive of an ECE mechanism for adsorbed wortmannin reduction.

Considering this, and the irreversibility of the reduction wave, a rapid chemical step following reduction of wortmannin is suggested.

At scan rates of 100 mV.s^{-1} under stirred conditions, a quasi- reversible couple was observed with E_{pc} -100 mV suggestive of the oxidation and following reduction of an electrochemically active chemical product. Based on analyses of the plot of potential versus pH and the determination of the n_t via hydrodynamic voltammetry, 4 electrons were determined to be involved in the reduction of wortmannin. Separate analyses of the determination of αn_a yielded a value close to 1.2, suggestive of 2 electrons being involved in the RLS, with an α value of 0.62.

The value determined for D for this scan rate region using the Randles-Sevcik equation yielded a value within the order of 10^{-5} cm^2.s^{-1}. Considering that wortmannin is a bulky molecule, its diffusion coefficient is expected to be slower. However, as discussed, the electrochemical analyses of wortmannin is compounded by the fact that mixed diffusion – adsorption occurs at scan rates above 60 mV.s^{-1}. As such, it is plausible that the diffusion coefficients determined are overestimated owing to the complications of adsorption of wortmannin moieties. As such an alternative determination was utilised yielding a more realistic value of 1.19 x 10^{-7} cm^2.s^{-1} for D.

CHAPTER 6

PERFORMANCE OF SENSORS MODIFIED WITH NANOMATERIALS FOR WORTMANNIN DETECTION

"Foresight has been quite successful in promoting the concept of nanotechnology and in making it a serious area of scientific research. Its real work is yet to come, as it leads the public in grappling with the huge social transformations that nanotechnology will impose on every living human being"

– John Gillmore

6.1 Introduction

Wortmannin has shown convincing evidence of lowering excessive cellular proliferation by being able to bind to an array of tumour causative agents. In particular, wortmannin binds with greatest affinity *in vitro* to phosphoinositide 3-kinase (PI 3-k). The lack of discrimination between healthy and transformed cells by wortmannin however, is currently a research challenge. Of interest to this work is the stability of wortmannin in biological media such as tissue culture media (TCM) due to the prevailing alkaline conditions (Holleran *et al.*, 2003; 2004).

In their follow up study Holleran *et al.* (2004) further their research on wortmannin detection in biological media using liquid chromatography coupled to mass spectrometry (LC-MS). While these authors were able to obtain quantitative detection levels of 23.34×10^{-9} mol.cm^{-3}, these values could only be obtained after extensive sample pretreatment which involved long incubation intervals and stringent extraction and purification protocols (Holleran *et al.,* 2003; Yuan *et al.,* 2007).

A further demand for the application of an electrochemical detection and quantification method for wortmannin exists in the monitoring of its biosynthesis. Wortmannin, a high value product, is produced in low concentrations as a secondary metabolite by fungal species such as *Penicillium duclauxi, Penicillium wortmannii*, *Fusarium oxysporum,* and *Talaromyces wortmannii* (M^{c}Cloud *et al.,* 1999). Secondary metabolites are typically produced when microorganisms are placed under environmental stress (such as non-favourable temperatures or pH), or the low availability of essential nutrients. Wortmannin produced at laboratory scale is performed in bioreactors, such as the continuously stirred tank reactor (CSTR) used by M^{c}Cloud *et al.* (1999).

In order to achieve maximum wortmannin production within a bioreactor, the nutrients and conditions need to be carefully monitored in real time and optimised accordingly. For instance, M^{c}Cloud *et al*. (1999) emphasise the importance of maintaining a glucose concentration of between 0.5 and 4.0 mg.l^{-1}, and dissolved oxygen levels near 100 % in a CSTR, while maintaining low shear forces. Nutrients and physiological conditions within a CSTR can be monitored using probes that can be used for the continuous monitoring (dissolved oxygen probe), or semi-continuous detection (such

as a flow injection system for glucose). While many parameters can be monitored in real time, this has yet to be achieved for the monitoring of wortmannin biosynthesis.

The demand for a suitable quantitative method for wortmannin, as a means of monitoring its fate, is emphasised by Holleran *et al.* (2003). The HPLC approach employed by the aforementioned authors and Yuan *et al*. (2007), while highly sensitive, is not rapid and requires extensive sample pretreatment. The electrochemical approach suggested in this chapter is not to be considered as an alternative to the established HPLC technique, but rather to be integrated as an initial diagnostic to quantify total wortmannin within a bioreactor system, the quality and state of which would subsequently be determined using HPLC.

Hydrolysis of wortmannin was observed by Holleran *et al.* (2003) (using HPLC) to occur in TCM (pH 7.4), and subsequently confirmed by Yuan *et al*. (2007), who (also using HPLC) observed a half life of wortmannin of 0.99 min in TCM (pH 7.4). Accordingly, it has become common practice to replace TCM containing wortmannin every 4 hours, a general laboratory practice first proposed by Kimura *et al.* in 1994. The cause of wortmannin hydrolysis in biological systems had been suggested by Yuan *et al*. (2007) to be attributed to two prominent processes: (i) a rapid opening of the furan ring, initiated through nucleophilic attack at the C20 position of the furan ring, and (ii) a slow hydrolytic opening of the lactone A ring. Hydrolysis of the lactone A ring has been described by Holleran *et al*. (2003), and is shown in scheme 6.1. The prevalence of either or both of these processes was explored further in this study.

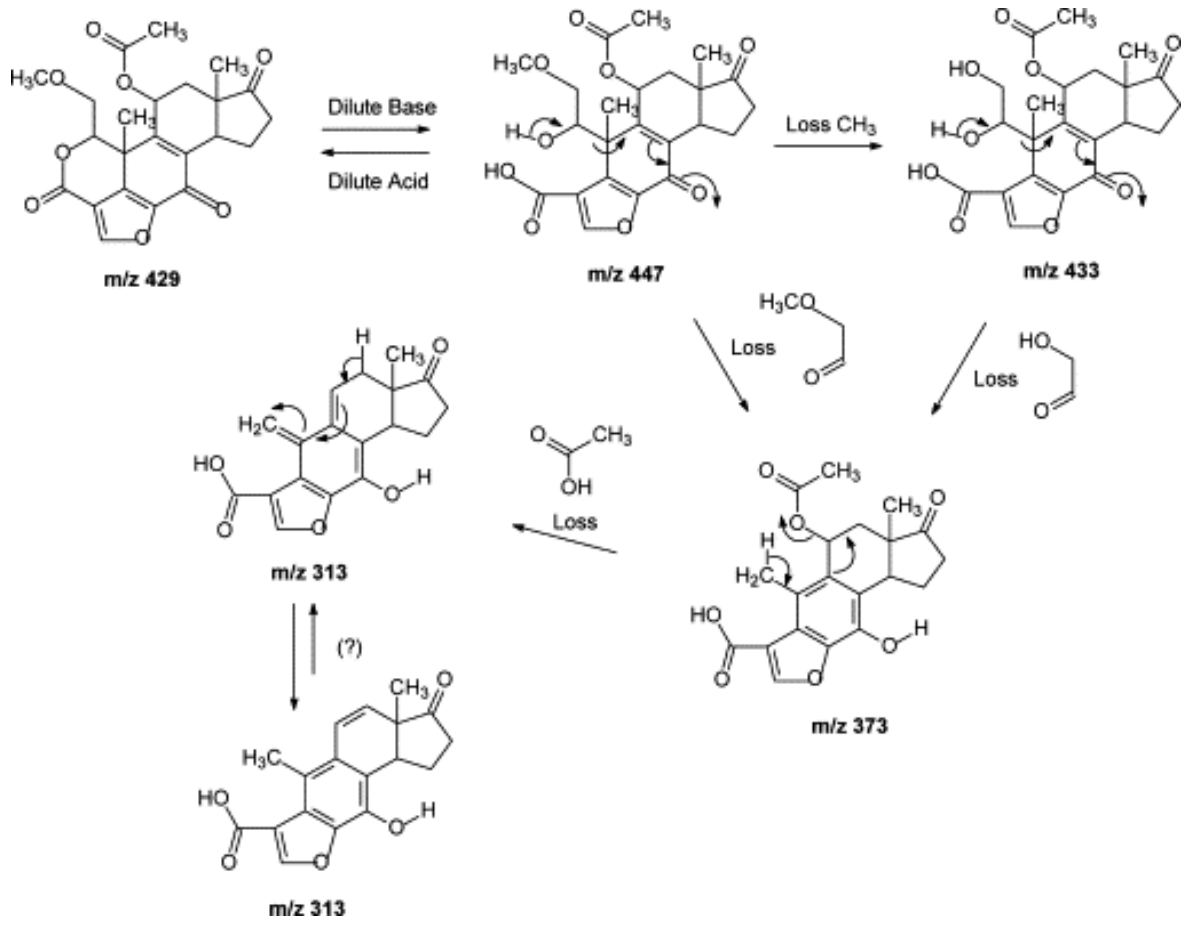

Scheme 6.1 Proposed breakdown pathway of wortmannin under alkaline pH conditions, as elucidated by Holleran *et al*. (2003).

A rapid loss of wortmannin under physiological conditions was described by Yuan *et al.* (2007), who subsequently noted that wortmannin maintained its anti-proliferative activity towards PI-3k. Interestingly, Wipf & Halter 2005, suggest that lactone A hydrolysis is followed by the elimination of methoxyaldehyde, resulting in aromatisation of the lactone B ring and subsequent loss of PI3-k inhibition.

The ability to quantify target analytes in a rapid manner with little to no sample pretreatment is the prevalent characteristic of electrochemical systems employed here. Additionally, the ability to enhance surface detection capabilities and surface reusability through the incorporation of nanomaterials, as described in Chapter 4 is of particular interest.

Carbon nanotubes incorporated onto an electrode surface have been shown by Bhushan, 2004 to lower the adsorption of redox species onto the electrode surface, which results in the possibility to re-use the electrode. This is particularly useful for application in flow through sensors in continuous monitoring systems. In this study the electrochemical performance of the NMEs discussed in chapter 4 were assessed for the detection of wortmannin. In particular, multi-walled carbon nanotubes functionalised for 9 hours (*f*MWCNTs), single-walled carbon nanotubes functionalised for 6 hours (*f*SWCNTs) and partially reduced C_{60}, all immobilised onto a GCE were compared to studies at an unmodified GCE.

The stability of wortmannin under alkaline conditions was monitored electrochemically by employing the NME that showed the most suitable performance and stability. Additionally, the effect of lysine on the redox behaviour of wortmannin was assessed. Furthermore, interference exhibited by oxygen, glucose, ascorbic acid and uric acid that typically co-exist in growth media used for wortmannin biosynthesis was examined.

6.2 Objectives

The objective of this study was to assess the performance of the nanomaterial modified electrodes for the detection of wortmannin in real samples, and to provide insight into the fate of wortmannin under alkaline conditions, as well as the electrochemical behaviour of wortmannin in the presence of lysine. In order to address this objective, the following aims were addressed:

Compare the electrochemical performance for wortmannin at an unmodified electrode (GCE) and the different NMEs (*f*MWCNTs, *f*SWCNTs, C_{60}).

Electrochemically monitor wortmannin stability under alkaline conditions.

Determine the effect of common interferents found in growth media, in particular, ascorbic acid, uric acid, glucose and lysine, on the efficacy of wortmannin detection by testing in real samples.

Evaluate wortmannin detection efficiency in a model biological mediator (foetal calf serum).

6.3 Experimental

6.3.1 Evaluation of NMEs for wortmannin detection.

6.3.1.1 Assessing NME for wortmannin detection

Before assessing the performance of wortmannin in real samples, the most suitable nanomaterial formulation to use needed to be addressed. This was ascertained in two ways:

(1) Compare wortmannin detection for each NME as compared to a GCE,

(2) Compare linear ranges for wortmannin quantification through standard curves (in 0.2 M Britton - Robinson buffer (pH 4.0) as determined in chapter 4).

Comparative studies were performed using the chemical modification parameters previously determined for the detection of catechol (chapter 4). For the sake of brevity the electrodes were used in the comparative evaluation of wortmannin are listed in Table 6.1

Table 6.1 Electrodes used in the evaluation of sensor performance.

ELECTRODE/ NANOMATERIAL	DESCRIPTION
GCE	Unmodified, cleaned
GCE-SWCNTs	4 hours functionalisation*
GCE-MWCNTs	9 hours functionalisation*
GCE-C_{60}	Partial reduction in KOH

*Functionalisation time interval in H_2SO_4:HNO_3 (3:1). All functionalised nanotube electrodes were subjected to an electrochemical activation consisting of 4 scans in catechol, as outlined in section 4.3.3.

A standard consisting of 2.33 x 10^{-6} mol.cm^{-3} wortmannin was prepared as previously reported (Chapter 2) and degassed using N_2 (Instrument grade, Afrox, South Africa). Each electrode prepared

was treated under identical conditions, with consistent operational parameters maintained for each. Calibration curves were set up for each of the electrodes in 0.2 M Britton - Robinson buffer as the supporting electrolyte in the pH range 4.0 – 8.0 (at 25 °C), in the range of 7.10 x 10^{-9} mol.cm^{-3} to 17.06 x 10^{-9} mol.cm^{-3} wortmannin.

6.3.2 Evaluation of selected interferents for wortmannin detection

6.3.2.1 Effect of dO_2 in wortmannin detection

The effect of dissolved oxygen (dO_2) on the current response for the primary reduction peak, E_{pc1} for wortmannin was assessed by OSWV.

6.3.2.2 Co-existing molecules in wortmannin biosynthesis

Each electrode was assessed by employing chronoamperometry at a fixed potential of -0.87 V, for the detection of wortmannin in 0.2 M Britton – Robinson buffer (pH 4.0) in the presence of compounds typically found in the growth medium fed into a bioreactor. Equimolar concentrations of 1.20 x 10^{-9} mol.cm^{-3} uric acid (UA), ascorbic acid (AA), and glucose (GLU) were assessed. The linearity of the detection response of wortmannin was then determined in this synthetic growth medium.

6.3.3 Detection of wortmannin in biological media

6.3.3.1 Detection of wortmannin in foetal calf serum

Foetal calf serum (FCS) stock was prepared in 0.2 M BR buffer (pH 4.0) (50:50 *v/v*) and deaerated with N_2 for 5 minutes prior to electrochemical assessment. The electrochemical behaviour of wortmannin in FCS was assessed by OSWV over time.

6.6.3.2 Detection of wortmannin in presence of lysine

Lysine (20 µM) was prepared fresh in 0.2 M BR buffer (pH 6.0),and the detection of wortmannin electrochemically was assessed through CV.

6.3.4 Effect of alkaline conditions on wortmannin detection

CV of wortmannin was performed in BR buffer (pH 8.0).

6.4 Results and Discussion

6.4.1 Evaluation of NMEs for wortmannin detection

6.4.1.1 Assessing NME for wortmannin detection

Figure 6.1 (A, B) shows the aggregation of unfunctionalised SWCNTs (A) and MWCNTs (B) immobilised on a GCE surface. Figures 6.1 (C, D) show a GCE surface modified with functionalised (C) *f*SWCNTs (6 hours) and (D) *f*MWCNTs (9 hours). In figure 6.1 (A, B) the typical aggregation of unfunctionalised nanotubes can be seen, while the more uniform length resulting from acid functionalisation can be seen in figures 6.1 (C, D). In figures 6.1 (C, D), the terminal ends of the tubes were observed to migrate toward each other, suggesting a greater affinity between the functionalised terminal ends of the tubes. The lower concentration of *f*SWCNTs in (A) could be attributed to lower starting concentrations of nanotubes, as well as the more rapid destruction of the tubular structure given its single-wall nature.

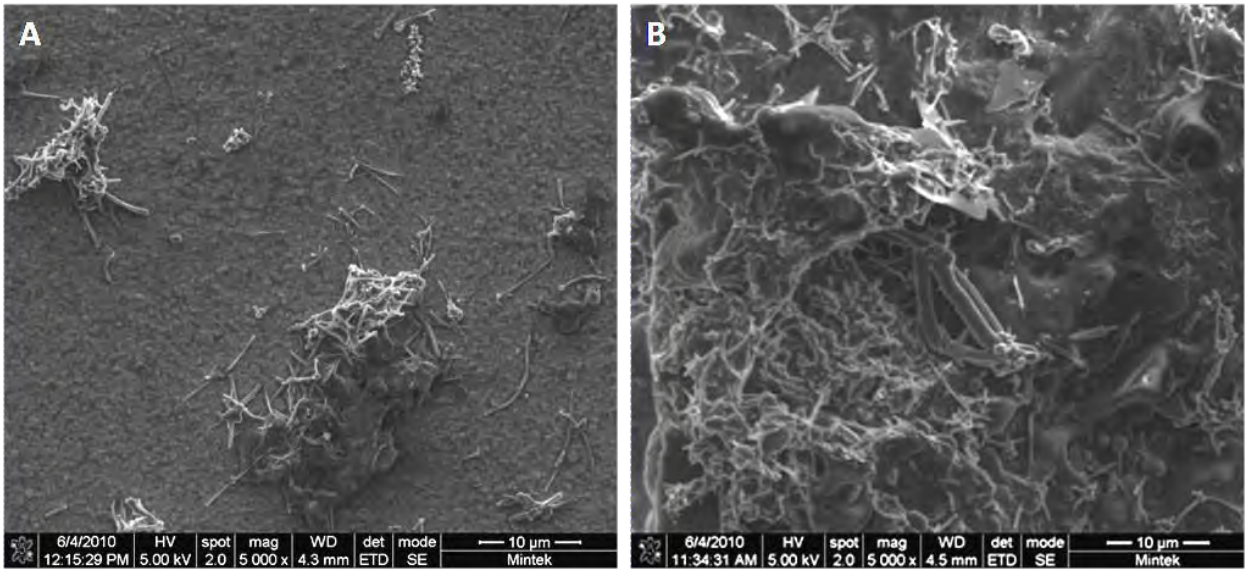

Figure 6.1 (A, B) HRSEM images of GCE surface modified with unfunctionalised (A) SWCNTs and (B) MWCNTs. Operating parameters are shown on the figure.

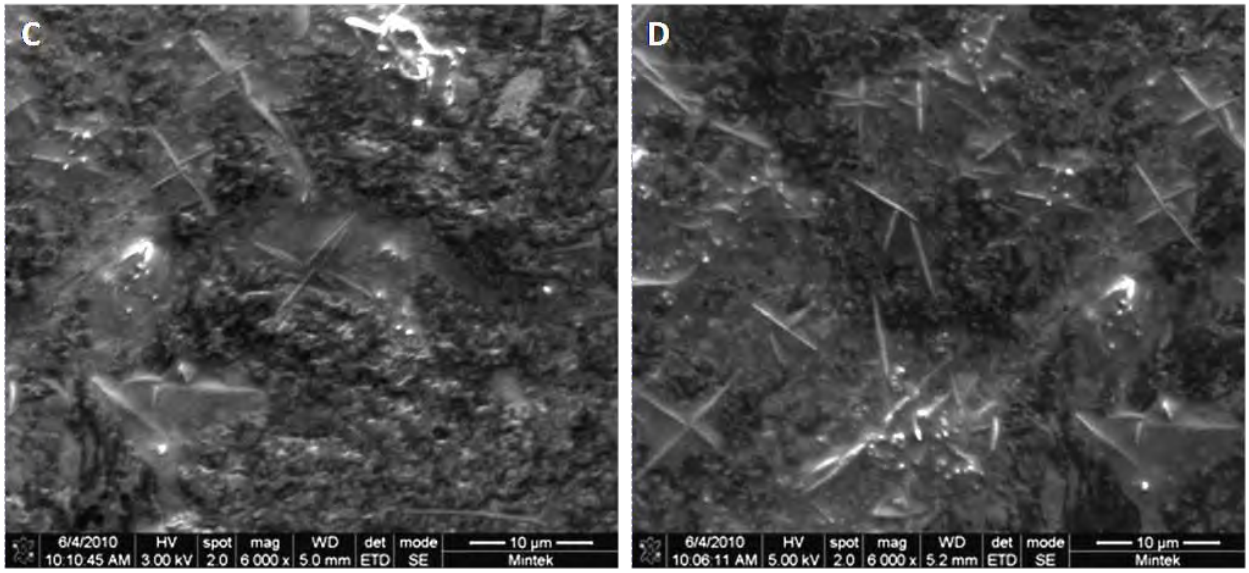

Figure 6.1 (C, D) HRSEM images of GCE surface modified with functionalised (A) *f*SWCNTs (6 hours) and (B) *f*MWCNTs (9 hours). Operating parameters are shown on the figure.

Figure 6.2 shows comparative OSWVs for the primary cathodic peak, E_{pc1} resulting from wortmannin reduction at different nanomaterial modified electrodes (NMEs) under pH 4.0 conditions while Figure 6.3 examines the same but at pH 6.0.

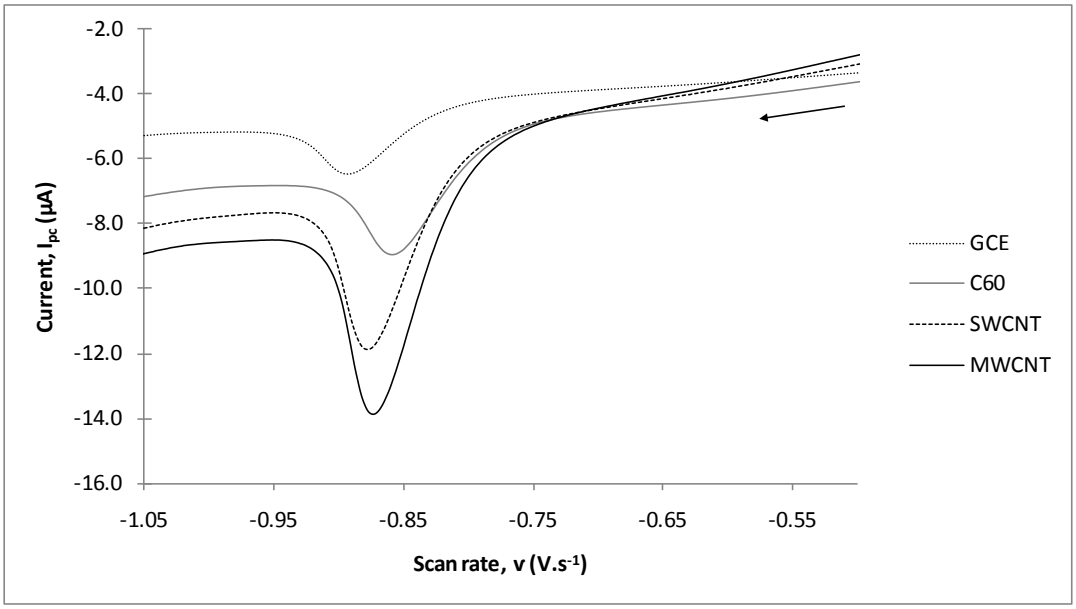

Figure 6.2 Osteryoung square wave voltammograms comparing the detection of 17 x10^{-9} mol.cm^{-3} wortmannin at different NMEs, as compared to an unmodified GCE. Supporting electrolyte: 0.2 M BR buffer (pH 4.0), Scan rate: 0.10 V.s^{-1}, vs. Ag|AgCl. *Key:* GCE: Unmodified glassy carbon electrode, SWCNT: Glassy carbon electrode

modified with single-walled carbon nanotubes, MWCNT: GCE modified with multi-walled carbon nanotubes, C_{60}: GCE modified with C_{60} fullerenes.

At pH 4.0 (Figure 6.2), an unmodified GCE yielded the lowest current response with a reduction potential near 0.90 V. The GCE modified with C_{60} produced a slight increase in current response but with the most significant decrease in reduction potential, suggesting a high degree of electrocatalysis occurring. The GCEs that were modified with *f*SWCNTs (6 hours functionalisation) and *f*MWCNTs (9 hours functionalisation) respectively yielded the highest current response, with improved reduction potentials for wortmannin, further suggesting probable electrocatalytic capacity of the functionalised nanotubes.

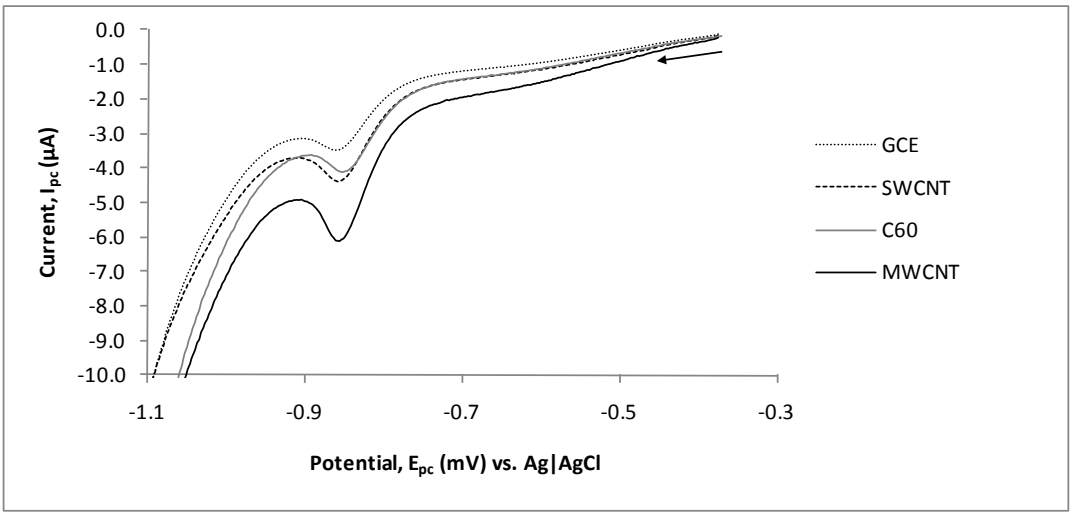

Figure 6.3 Osteryoung square wave voltammograms comparing the detection of 17 $x10^{-9}$ $mol.cm^{-3}$ wortmannin at different NMEs, as compared to an unmodified GCE. Supporting electrolyte: 0.2 M BR buffer (pH 6.0), Scan rate: 0.10 $V.s^{-1}$, vs. Ag|AgCl. *Key:* GCE: Unmodified glassy carbon electrode, SWCNT: Glassy carbon electrode modified with single-walled carbon nanotubes, MWCNT: GCE modified with multi-walled carbon nanotubes, C_{60}: GCE modified with C_{60} fullerenes.

An overall lowering of the cathodic currents for wortmannin was observed at pH 6.0 (Figure 6,3) compared to similar studies at pH 4.0 (Figure 6.2). This could be attributed in part to the effects of bulk pH on the current response and peak potential for wortmannin reduction where a decrease in current response is observed with increasing alkalinity (Chapter 5). At pH 6, all NMEs except for *f*SWCNTs showed an increase in current response as compared to an unmodified GCE, with a slight decrease in the peak potential. A GCE modified with C_{60} exhibited the lowest increase in current response of the NMEs with the most improved (lowered) peak potential, while *f*MWCNTs (9 hours

functionalisation) yielded the greatest increase in current response but with minimal lowering of the peak potential. Table 6.2 summarises the current responses and reduction potentials at each of the NMEs for the two bulk solution pH values.

Table 6.2 Summary of the comparative current response and potential for the cathodic reduction of 17 x10^{-9} mol.cm^{-3} wortmannin at pH 4.0 and 6.0.

	Current, $\|I_{pc}\|$ (μA)		**Potential, E_{pc} (V)**	
	pH 4.0	**pH 6.0**	**pH 4.0**	**pH 6.0**
GCE (unmodified)	2.24 (4.23)	1.43 (5.02)	-0.897 ± 0.009	-0.881 ± 0.012
GCE-C_{60}	3.53 (2.14)	1.74 (2.67)	-0.856 ± 0.003	-0.846 ± 0.007
GCE-SWCNT	5.38 (3.93)	1.28 (4.88)	-0.875 ± 0.012	-0.853 ± 0.011
GCE-MWCNT	6.71 (4.12)	2.63 (4.05)	-0.870 ± 0.013	-0.851 ± 0.014

Values in brackets (for current) are the relative % standard deviation (determined using equation 3.02), and E_{pc} values are shift in potential (in V). All scans were performed in triplicate and under identical operating conditions.

An increased current response for a GCE modified with *f*MWCNTs as compared to the other NMEs listed in table 6.2 was obtained for wortmannin at pH 4.0 and pH 6.0. The *f*MWCNTs' greater surface area, in addition to characteristic electrocatalytic properties, could explain the enhanced sensitivity. The electrocatalytic capacity of *f*MWCNTs was further evidenced through a lowered peak potential. A GCE modified with C_{60} exhibited lowered peak potentials in comparison to the rest of the NMEs (table 6.2), but with a lower current response. The HRSEM images reported on earlier [figure 4.28 (A - D)] showed that C_{60} tend to form aggregates with GCE surface exposed. It is likely that the lower current response was due to redox activity occurring directly with the bare electrode surface as well as with the C_{60} aggregates. Current responses for *f*SWCNTs was lower than the *f*MWCNTs NME, but greater than that for the GCE and C_{60} NME at pH 4.0. The lower current response for *f*SWCNTs could be attributed to a low concentration of nanotubes on the electrode surface as a result of a low concentration of starting material (comparing figure 6.1 C and D), as well as a greater extent of damage to the nanotubes due to acid treatment.

Figure 6.4 (A – D) shows OSWVs generated for the construction of calibration curves at each of the NMEs evaluated in this study, as compared to an unmodified GCE.

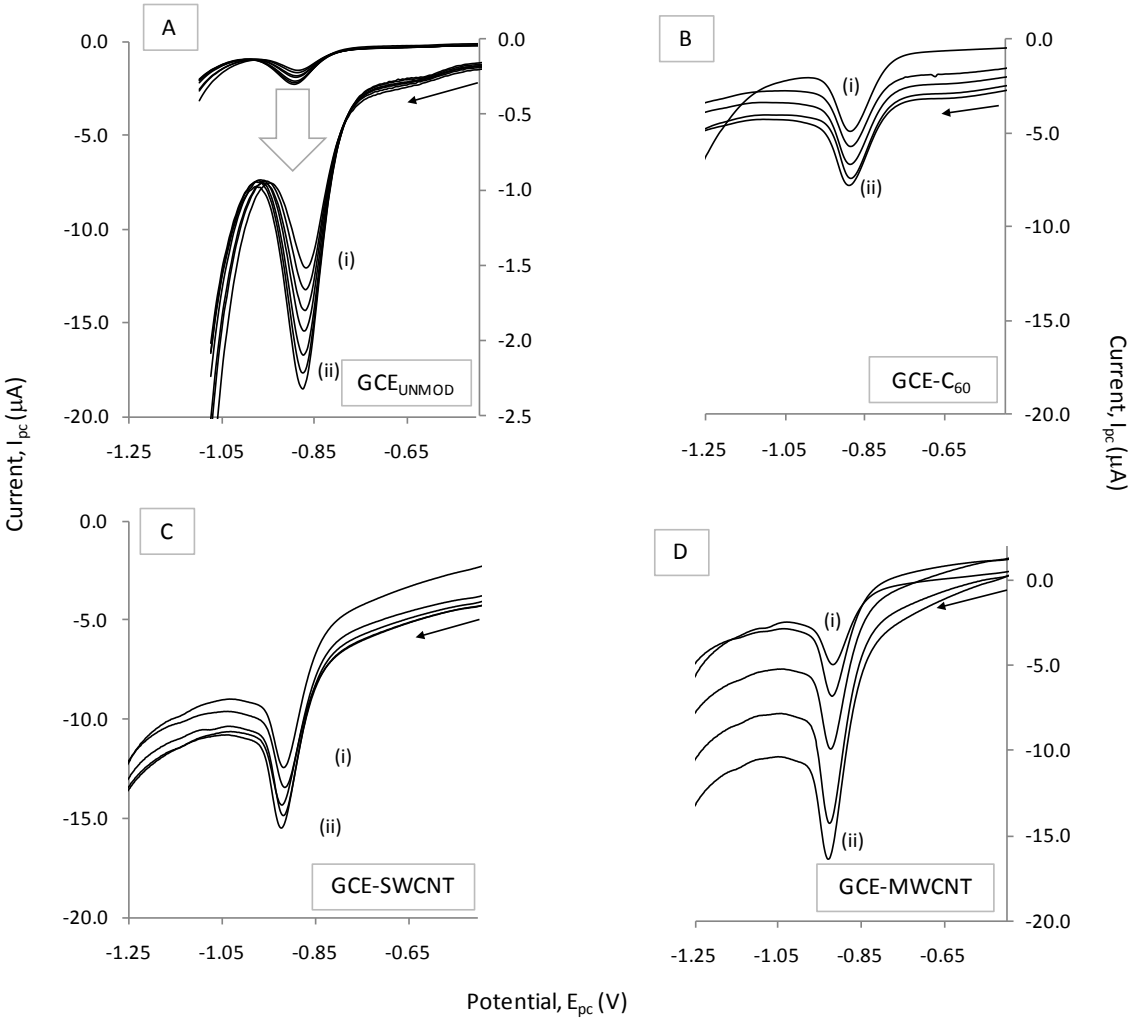

Figure 6.4 (A – D) Calibration of osteryoung squarewave voltammogram curves for the cathodic peak of wortmannin reduction at the nanomaterial modified electrodes, as compared to an unmodified GCE, by addition of wortmannin to 0.2 M BR buffer (pH 4.0). Representative OSWV plots: A) unmodified GCE, B) is at a GCE modified with C_{60}, C) is at a GCE modified with *f*SWCNTs and D) is at a GCE modified with *f*MWCNTs. All scans were performed in triplicate with identical operational parameters maintained for each. *Key*: (i) is the current response for 7.20 x10^{-9} mol.cm^{-3} wortmannin, and (ii) is the current response for 15.10 x 10^{-9} mol.cm^{-3} wortmannin (17.06 x 10^{-9} mol.cm^{-3} for GCE). Scan rate: 0.10 V.s^{-1}. (Note, for Figure 6.4 A, the lower set of curves are a magnification of the set above representing actual waveforms for wortmannin reduction at a GCE).

Figure 6.5 shows the corresponding line graphs representing the calibration curves generated at each NME as compared to an unmodified GCE.

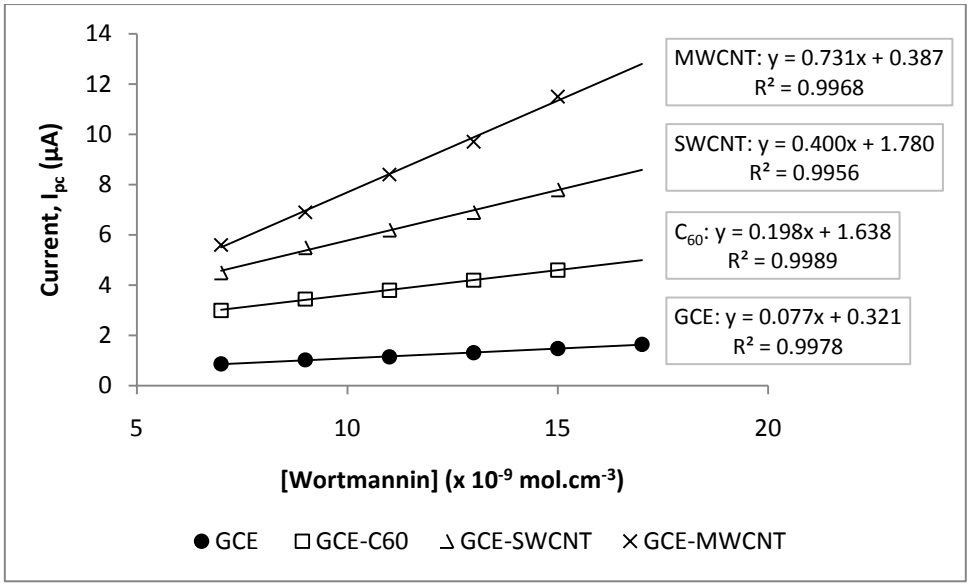

Figure 6.5 Calibration line curves obtained from the OSWVs of the standard addition of wortmannin to 0.2 M BR buffer (pH 4.0) for the nanomaterial modified electrodes as compared to an unmodified GCE. Each scan was performed in triplicate with identical operational parameters maintained.

In figure 6.5 the highest sensitivity for the detection of wortmannin was observed by using *f*MWCNTs (0.731 µA/nmol.cm^{-3}) with *f*SWCNTs yielding the second greatest sensitivity and C_{60} the least in comparison to an unmodified GCE. Further correlation to the aforementioned sensitivity was obtained through the determination of the respective limits of detection (LOD), calculated using equation 3.04. Table 6.3 summarises these findings.

Table 6.3 Limits of detection comparison between an unmodified glassy carbon electrode, and the various nanomaterial-modified electrodes assessed.

ELECTRODE	LIMIT OF DETECTION (nmol.cm^{-3})
GCE	5.667
GCE-C_{60}	0.560
GCE-*f*SWCNTs	0.128
GCE-*f*MWCNTs	0.102
HPLC (Holleran *et al.*, 2003)*	0.233

*Literature comparative using HPLC (Holleran *et al.,* 2003).

In table 6.3 it can be seen that the voltammetric assessment of the limits of detection at an unmodified GCE (5.667 nmol.cm^{-3}) and GCE-C60 (0.560 nmol.cm^{-3}) are greater than that obtained in literature using HPLC (0.233 nmol.cm^{-3}). However when *f*SWCNTs were added to the electrode surface, the LOD dropped to lower detection levels comparing favourably with literature (0.128 mol.cm^{-3}), with a marked decrease observed for *f*MWCNTs (0.102 mol.cm^{-3}). This observation shows evidence that the addition of nanomaterials, in particular *f*SWCNTs and *f*MWCNTs to an electrode surface increases the sensitivity of the detection of wortmannin, of relevance to the detection of trace levels of wortmannin during its biosynthesis.

The criteria for the choice of NME used in subsequent studies was based on the performance of the NMEs (as discussed in 6.4.1, 6.4.2) as well as the specific application. In diagnostics reproducibility in conjunction with competitive sensitivity is vital. GCE-*f*MWCNTs were utilized further for studies where sensitivity was considered a key component. For studies where error was likely to be a factor, for example in analysis of wortmannin in biological media such as foetal calf serum, GCE modified with C_{60} was used since it exhibited the lowest relative percentage error in current response as well as cathodic potential (Table 6.2) of all the surfaces examined.

6.4.2 Evaluation of selected interferents for wortmannin detection

6.4.2.1 Effect of dO_2 in wortmannin detection

The effect of dissolved oxygen (dO_2) on the magnitude of the current response for wortmannin reduction is shown in figure 6.7.

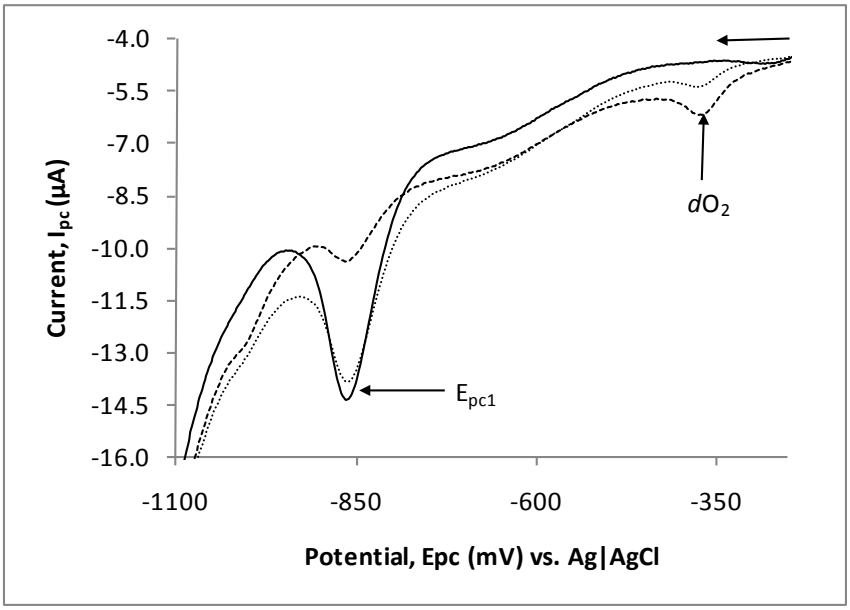

Figure 6.6 Osteryoung square wave voltammograms of 7.50 x 10^{-9} mol.cm^{-3} wortmannin (E_{pc1}) in the presence (dashed line) and absence (solid line) of dissolved oxygen (dO_2). The dotted line shows the effect of deaeration of the bulk solution for 120 seconds. The solid line represents deaeration for 300 seconds. Working electrode: GCE modified with C_{60}, supporting electrolyte: 0.2 M BR buffer (pH 4.0) scan rate: 0.10 V.s^{-1}.

Under conditions where the bulk solution had not been deaerated prior to analyses, the current response for wortmannin was significantly affected, with a resultant low current magnitude. Deaeration for 120 seconds resulted in a significant increase in the current response, with 300 seconds resulting in a well defined peak with high current response for wortmannin reduction and the absence of a cathodic wave attributed to reduction of dissolved oxygen.

6.4.2.2 Co-existing molecules in wortmannin biosynthesis

This section evaluates the efficacy of using a NME modified GCE to monitor wortmannin under semi-continuous conditions. A GCE modified with *f*MWCNTs (functionalised for 9 hours) was chosen as the NME to evaluate in this section, due to sensitivity and observed electrode surface regeneration properties (chapter 4). While real growth media could not be utilised due to intellectual property constraints, typical components of fungal growth media were assessed instead. Specifically the effects of uric acid, ascorbic acid, and glucose were assessed as potential interferents.

Figure 6.8 shows an amperometric scan to assess the effect of interferents on the detection of wortmannin. A recovery test for wortmannin was also performed by spiking with 7.50 x 10^{-9} mol.cm^{-3} wortmannin (ii) and comparing the current response with the initial current response (i) for wortmannin, as shown in figure 6.8.

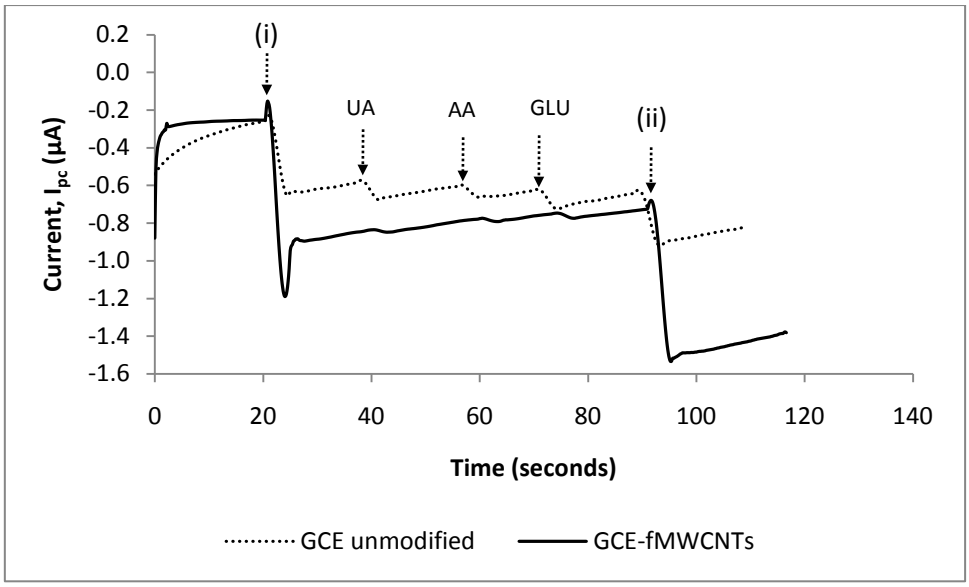

Figure 6.7 Amperometric interference tests at a fixed applied potential of -0.87 V, comparing the effects of common interferents present in growth medium (pH 6.0) on the detection of 7.50 x 10^{-9} mol.cm^{-3} wortmannin at an unmodified GCE (dotted line) and GCE-*f*MWCNTs (solid line). *Key*: (i) initial wortmannin spike, (ii) second wortmannin spike, UA: uric acid, AA: ascorbic acid, GLU: glucose.

Initial CVs performed on the reduction of wortmannin in the presence of UA, AA and GLU had exhibited interference from UA predominantly. Amperometry was used as an alternative since a fixed potential could be applied. In figure 6.8 the result of amperometry for the reduction of wortmannin is shown. At (i) 7.50 x 10^{-9} mol.cm^{-3} wortmannin addition (at GCE-*f*MWCNT) resulted in an increased current response that at (ii) exhibits 92.86 % of the original current response strength at (i), as opposed to 77.78 % at an unmodified GCE. The effects of interferents are low for GCE-*f*MWCNTs as compared to an unmodified GCE. Table 6.4 summarises the recovery test and the effects of interferents on wortmannin reduction.

Table 6.4 Comparison of the recovery test and effect of interferents on the detection of wortmannin at GCE_{UNMOD} and GCE-*f*MWCNTs.

	GCE_{UNMOD}	**GCE-*f*MWCNTs**
Initial I_{pc} (μA)	0.45	0.70
Final I_{pc} (μA)	0.35	0.65
% Recovery	77.78 %	92.86 %
Interferent **[% Relative Interference]***		
Uric acid (μA)	0.12 [27.1 %]	0.05 [7.0 %]
Ascorbic acid (μA)	0.10 [22.4 %]	0.05 [7.0 %]
Glucose (μA)	0.12 [27.2 %]	0.06 [8.6 %]

* Relative to current response at (i), initial I_{pc}

At an unmodified GCE the interfering effects of UA, AA and GLU were marked at 27.1 %, 22.4 % and 27.2 %, respectively. In contrast, at a GCE-*f*MWCNTs percentages for UA, AA and GLU were estimated at 7.0 %, 7.0 % and 8.6 %, respectively. Additionally, recovery tests showed that wortmannin recovery at an unmodified GCE could be performed with 77.8 % efficacy, while at GCE-*f*MWCNTs this was higher at 92.9 %, with an increase in current response (sensitivity) when comparing the unmodified GCE and the GCE-*f*MWCNTs. These observations further suggest that the addition of *f*MWCNTs to an electrode surface increase the degree of sensitivity as a result of increased surface area and the inherent electrocatalytic properties of the nanotubes, decrease passivation effects caused by adsorbed species therefore increasing recovery levels, as well as lowering the interferent effects of co-existing analytes. The decreased interferent effects could be attributed to the porosity of the increased surface area of the nanotubes in conjunction with repulsion afforded by the net negative charge on the nanotubes (for negatively charged species at this surface). The interferent effects of the co-existing analytes assessed (UA, AA and GLU) were not negligible however. The plausibility of using amperometry as an alternative method of wortmannin quantification in complex matrices is addressed in the subsequent section.

A calibration curve using amperometry and GCE-*f*MWCNTs (functionalised for 9 hours) was constructed for application to the quantification of wortmannin in growth media (GM):BR (50:50 *v/v*). Figure 6.9 (A, B) show the amperometric scan and the corresponding line curve.

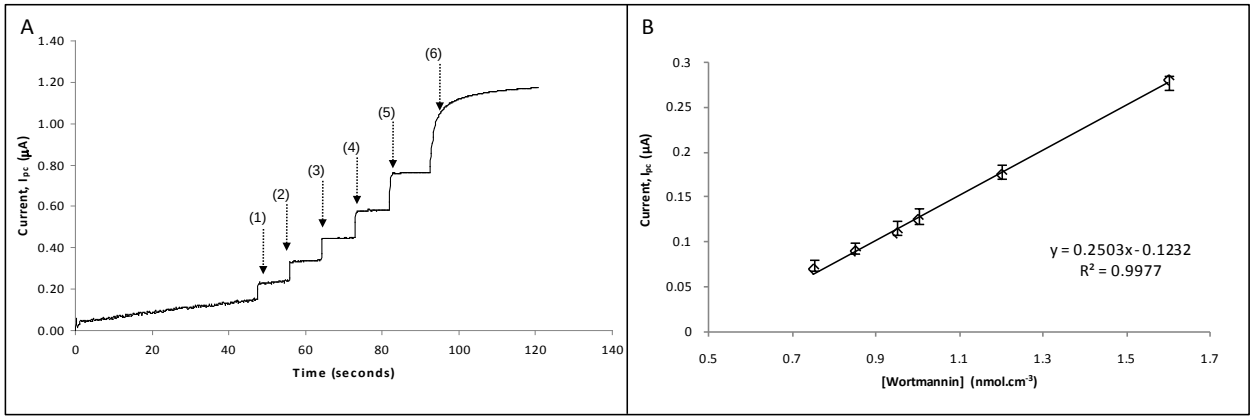

Figure 6.8 (A) Amperometric calibration curve at a fixed potential of 0.875 V, for 0.75 x 10^{-9} mol.cm^{-3} – 1.62 x 10^{-9} mol.cm^{-3} wortmannin using a GCE-*f*MWCNTs (functionalised for 9 hours) as the working electrode, (B) is the corresponding line curve, R^2 = 0.9977.

Addition of wortmannin to GM:BR (50:50 *v/v*) exhibited a linear response with a correlation coefficient, R^2 of 0.9977, and sensitivity, (0.2503 μA/mol.cm^{-3}). Additionally, the linear observation further ascertains the regeneration capacity of *f*MWCNTs since a high degree of linearity was observed between additions without cleaning the electrode surface.

6.4.3 Detection of wortmannin in biological media

6.4.3.1 Wortmannin detection in foetal calf serum (FCS)

In laboratory diagnostics wortmannin is typically solubilised in foetal calf serum (FCS) due to the similarity in composition to human serum (Yuan *et al.,* 2007). Subsequently, the electrochemical behaviour of wortmannin in FCS was assessed.

Preliminary studies conducted had shown that wortmannin detection in 100 % FCS produced lowered current responses compared to that in 0.2M BR buffer. Optimisation of the ratio of FCS to 0.2 M BR buffer (pH 7.4) resulted in a 50:50 (*v/v*) ratio producing comparative current response

magnitudes to that observed in BR buffer. Figure 6.6 shows OSWVs comparing the reduction of wortmannin in 0.2 M BR buffer (pH 7.4) as compared to FCS:BR (50:50 *v/v*) (pH 7.4).

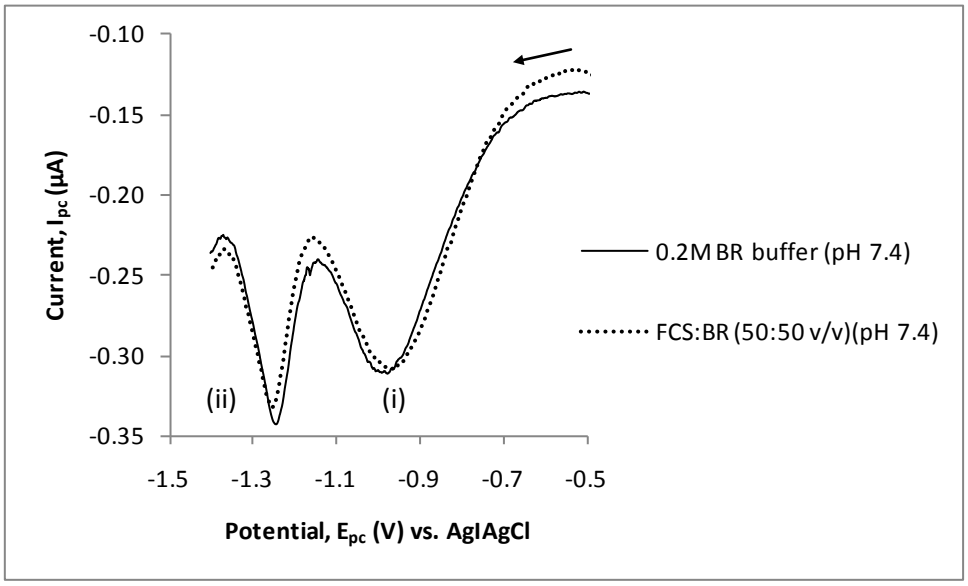

Figure 6.9 Osteryoung squarewave voltammograms comparing the detection of 2.50 x 10^{-9} mol.cm^{-3} wortmannin in 0.2 M BR buffer (pH 7.4) with foetal calf serum:BR buffer (50:50 *v/v*) (pH 7.4) spiked with an equivalent concentration of wortmannin. Working electrode: GCE modified with C_{60}. *Key*:: (i) primary reduction peak, E_{pc1},(ii) secondary reduction peak, E_{pc2}. Scan rate: 0.10 V.s^{-1}.

Spiking of BR:FCS with wortmannin exhibited the formation of a peak pair (i, ii) on Figure 6.6. Interestingly, at the same pH in BR buffer, a similar peak pair was observed, whereas under more acidic conditions, only a single peak was observed (i), suggesting that the secondary peak (ii) to likely be associated with pH-dependant degradation of the compound (as examined further below).

6.4.3.2 Detection of wortmannin in growth media and role of lysine

It is well documented that wortmannin interacts specifically and irreversibly with the lysine residue of PI-3k. This occurrence is as a result of the nucleophilic attack of lysine on the furan ring at the C20 position (Wipf & Halter 2005). Scheme 6.2 shows the strained furan heterocycle that is susceptible to nucleophilic addition by the lysine residue of PI-3K.

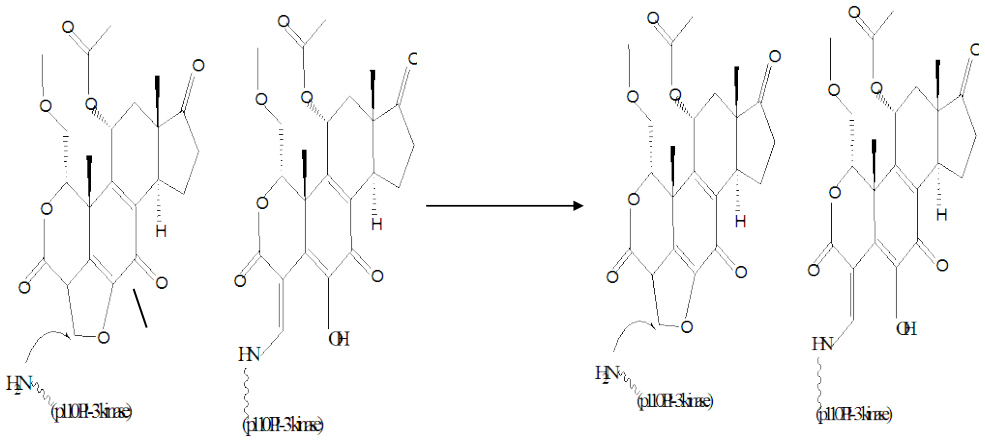

Scheme 6.2 Nucleophilic addition of lysine residue of PI-3K to wortmannin (Wipf & Halter, 2005; Yuan *et al.,* 2007).

The electrochemical behaviour of wortmannin in the presence of lysine would assist in a better understanding of the binding mechanism, as well as identify the electrochemically active areas of the wortmannin molecule. Figure 6.10 shows OSWVs for the reduction of wortmannin in the presence of lysine.

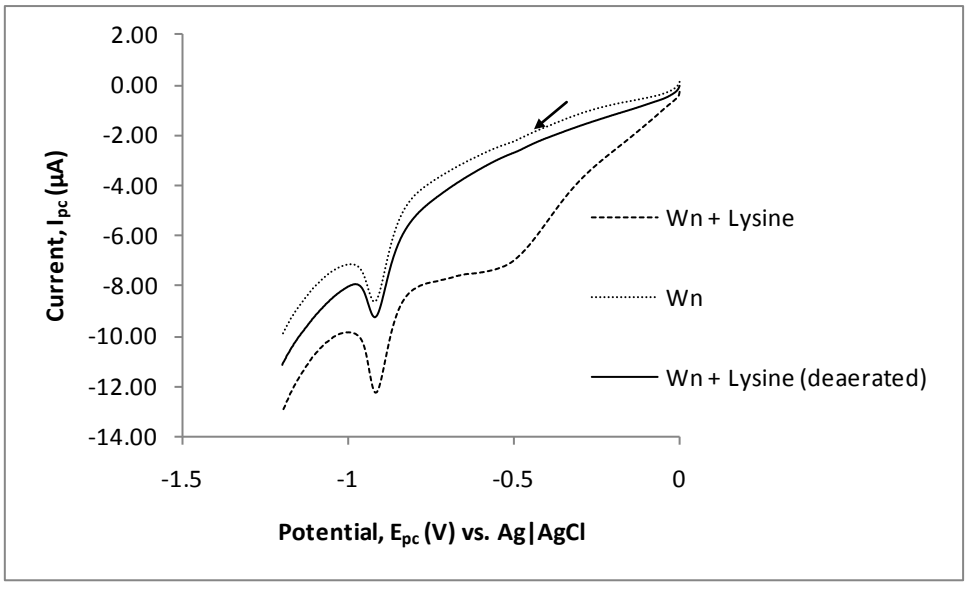

Figure 6.10 Osteryoung squarewave voltammograms of 7.50 x 10^{-9} mol.cm^{-3} wortmannin (E_{pc1}) in the presence (solid line) and absence (dotted line) of 20 µM lysine. The dashed line shows the effect of deaeration of the bulk solution (in presence of lysine) for 120 seconds. Working electrode: GCE modified with C_{60}, scan rate: 0.10 V.s^{-1}.

The furan ring can be cleaved by a variety of nucleophiles, with more rapid ring opening occurring in the presence of amines and thiols, resulting in orange coloured diosphenols (Wipf & Halter, 2005). The potent and specific inhibition of PI 3-k by wortmannin is achieved through its targeted binding in an irreversible covalent manner to the epsilon amine group of the p110 lysine, found in the active site pocket of PI 3-k (Isosaki 2004; Yuan *et al.*, 2007).

Wortmannin binds covalently to phosphoinositide 3-kinase (PI 3-k) in an irreversible manner via the terminal lysine amino acid (Wipf & Halter, 2005). In figure 6.10 it is clear that in the presence of lysine the current response magnitude for wortmannin reduction is unaffected. This implies that the electrochemical reduction of wortmannin does not occur at the furan ring, since this is the preferred site of nucleophilic attack by the lysine residue (Wipf & Halter, 2005; Yuan *et al.,* 2007).

Confirming earlier studies (Figure 6.7) dO_2 exhibits a marked interfering effect on the reduction of wortmannin (dashed line, figure 6.10), and it is therefore recommended that deaeration of the sample is performed prior to electrochemical assessment of wortmannin.

6.4.4 Electrochemical monitoring of wortmannin degradation under alkaline conditions

A stock solution of wortmannin was added to 0.2 M BR buffer (pH 8.0) that had been deaerated with N_2. The bulk solution containing wortmannin was observed to immediately turn from colourless to yellow once wortmannin had been added. Figure 6.11 shows the yellow formation in vials containing 0.2M BR buffer bulk solutions of increasing alkalinity.

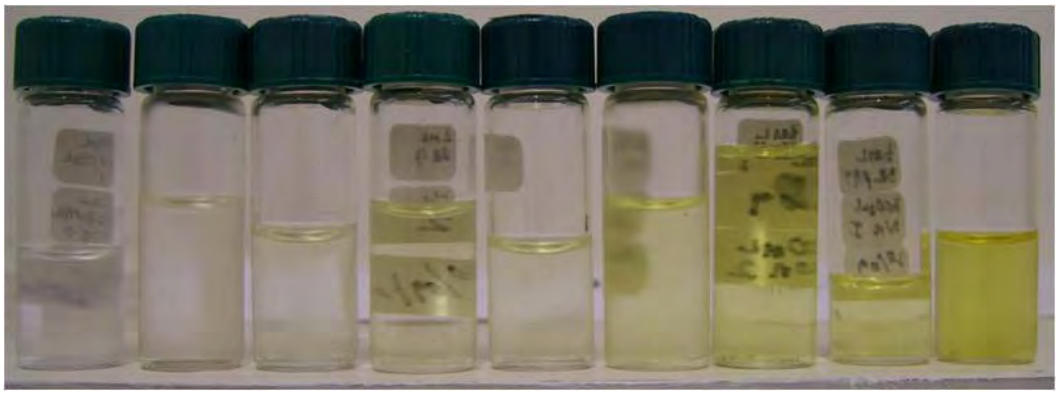

Figure 6.11 Vials containing 0.2 M BR buffer of increasing alkalinity to illustrate the formation of a yellow coloured product with increasing alkalinity. From left: pH 2.0 – 10.0 increasing at 1 pH increment per vial.

In their report, Wipf & Halter 2005 describe the rapid formation of deep yellow coloured diosphenols when amines and thiols are added to wortmannin as a result of nucleophilic addition in the presence of amino acids. Similar observations were made by Isosaki 2004 who attributed the colour change to the opening of the strained furan heterocycle (scheme 6.2) due to resultant nucleophilic attack susceptibility in the presence of amines and thiols.

Under alkaline conditions wortmannin has been reported to undergo furan ring opening at pH 7.4 (Wipf & Halter, 2005), while others have reported on the alkalinity induced lactone A hydrolysis (Holleran *et al*., 2003; Yuan *et al*., 2007in a pathway as proposed by Holleran *et al*. (2003) shown in scheme 6.1. It is likely that both mechanisms may occur as a result of increased alkalinity and associated lowered stability of wortmannin (Wipf & Halter, 2005).

The rapid furan ring opening was suggested by Wipf & Halter (2005) to result from the electrophilic character of the strained tricyclic furan moiety (naphtho[1,8-bc]furan) flanked on either side by carbonyl groups. These electron withdrawing carbonyl groups increase the electrophilicity of the α-carbon of the furan ring at the C20 position. A high degree of strain of the tricyclic heterocycle culminates in a susceptible furan ring that is highly reactive.

Absorption spectra of wortmannin in the range 200 nm – 700 nm are shown in figure 6.12 at pH 5.8 (A) and at pH 8.0 (B). In figure 6.12 (A) three distinctive peaks (i – iii) were observed at pH 5.0. In

figure 6.12 B) peaks ii-iii are shifted and decreased in intensity, with an additional peak observed at 408 nm. Isosaki 2004 had observed similar peaks in their studies at pH 7.4 with the peak at 408 nm attributed to furan ring opening by amino acids. While this is plausible, the ring opening may have been due to the effects of pH on the stability of wortmannin, given that experiments were conducted at a pH of 7.4.

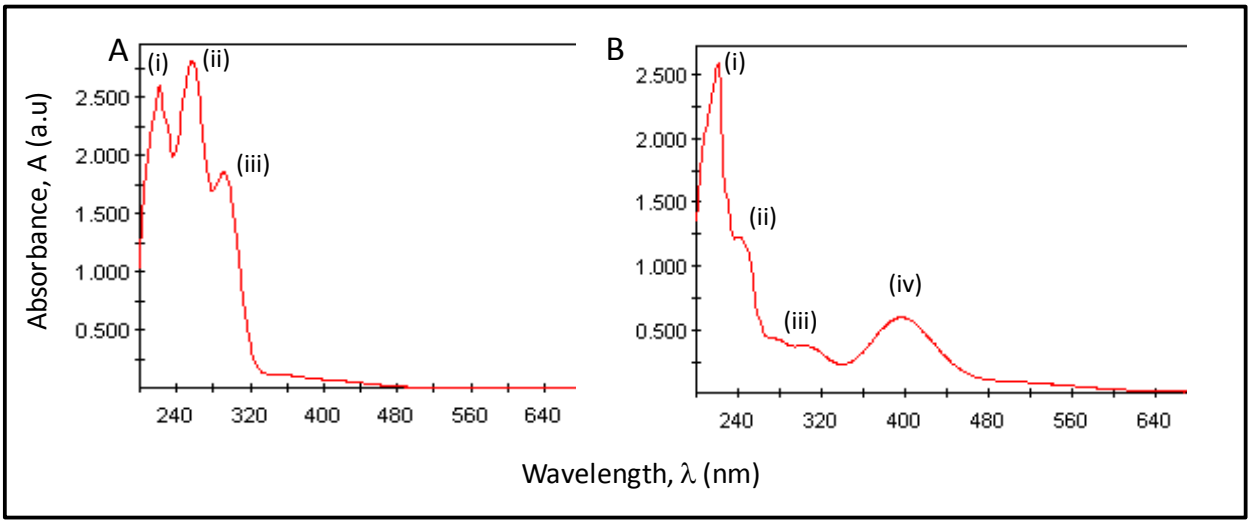

Figure 6.12 (A, B) Absorption spectra for wortmannin at (A) pH 5.8 and (B) pH 8.0. *Key*: (i – iii): wortmannin parent peaks, (iv): wortmannin hydrolysis daughter peak.

In other spectroscopic studies, lactone A hydrolysis was observed to result in the formation of a quinone at the lactone B ring, with spectroscopic studies revealing that the quinone yielded 3 distinctive peaks at 242 nm (strong K band), and at 281 and 434 nm, respectively (weak R bands).

In an attempt to understand the stability and electrochemical behaviour of wortmannin under alkaline conditions, the optimised electrochemical parameters (chapter 5) were applied at an unmodified GCE with a bulk solution of 0.2 M BR buffer (pH 8.0). Figure 6.13 shows a representative cathodic section of a CV scan performed under pH 8.0 conditions.

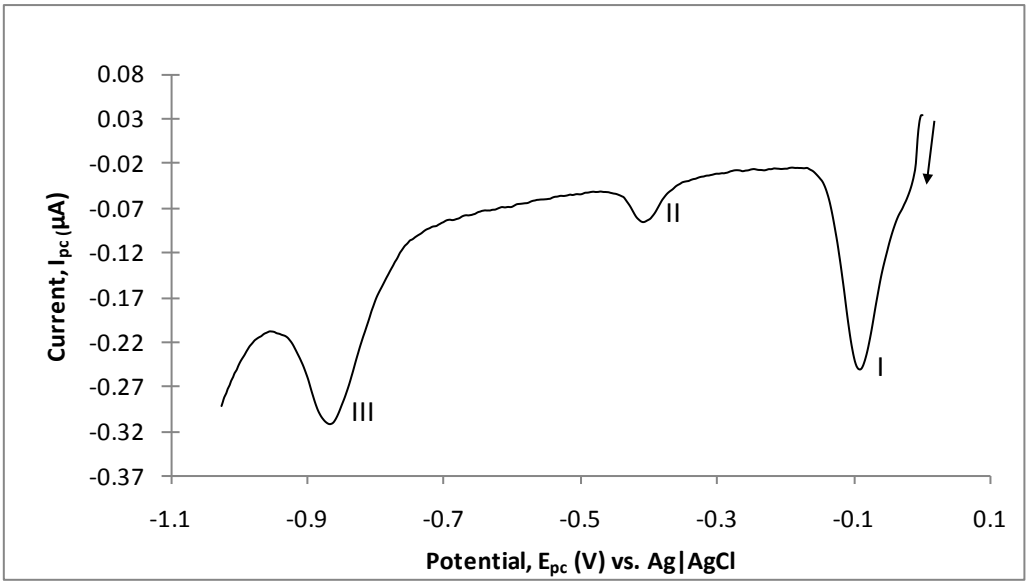

Figure 6.13 Representative convoluted Osteryoung squarewave voltammogram of the initial cathodic scan for 17 x 10^{-9} mol.cm^{-3} wortmannin reduction in 0.2 M BR buffer (pH 8.0). *Key:* I – III: cathodic peaks observed under alkaline conditions. Scan rate: 0.10 V.s^{-1}.

A reduction scan was performed within 2 minutes of spiking deaerated 0.2 M BR buffer (pH 8.0) with wortmannin. In figure 6.13 the prominent wortmannin cathodic peak (III on figure 6.13) was observed. However under alkaline conditions additional peaks were observed to form (I and II on figure 6.13), corresponding to a decrease in the parent peak for wortmannin (III on figure 6.13). With time peaks II and III disappeared with peak I remaining. This observation suggests that the alkaline conditions potentially hydrolyse wortmannin to yield electrochemically active intermediates and final hydrolysis products.

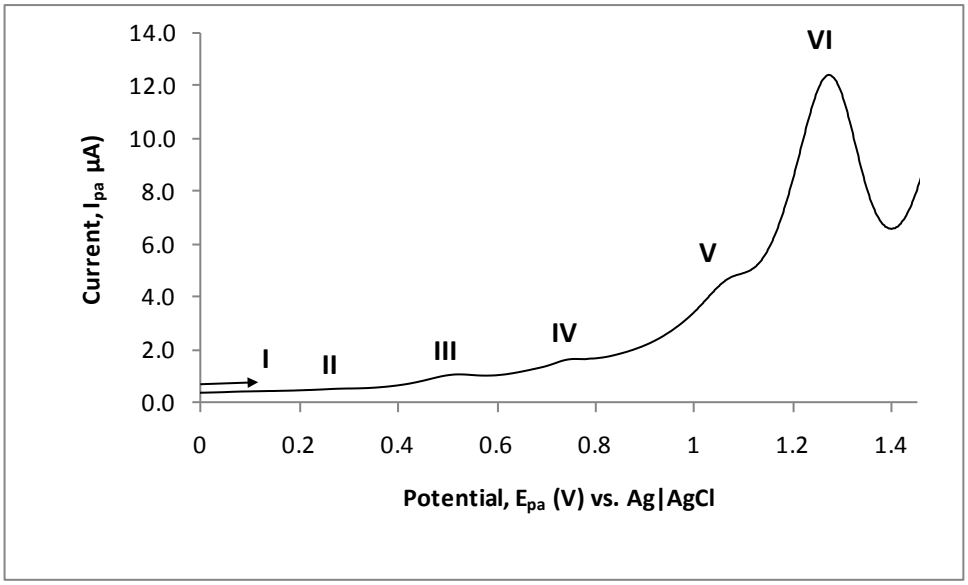

Figure 6.14 Representative Osteryoung sqarewave voltammogram of the anodic scan for 17 x 10^{-9} mol.cm^{-3} wortmannin breakdown in 0.2 M BR buffer pH 8.0. *Key:* I – VI: anodic peaks observed under alkaline conditions. Scan rate: 0.10 V.s^{-1}.

Anodic scans for wortmannin characterisation (chapter 5) showed no peaks at pH 4.0. However, an anodic scan performed at pH (8.0) showed the presence of 6 anodic peaks (I – VI on figure 6.14), the most prominent being oxidised at 1.28 V further confirming the detection of electrochemically active hydrolysis products.

Assignation of the waveforms to particular hydrolysis products is problematical by the lack of confirmation in the literature as to the particular functional groups hydrolysed as result of pH. This can only be confirmed through voltammetric analysis of pure compounds of the intermediates proposed to form by previous authors (Holleran *et al.*, 2003; Wipf & Halter, 2005).

In their postulation of the role of lactone A hydrolysis, Holleran *et al.* (2003) showed that lactone A ring cleavage was rapid and could be reversed within 5 minutes of initial cleavage if the pH of the bulk solution is returned to acidic conditions. This was assessed in this study and shown to occur but not with absolute regeneration of the initial wortmannin current strength.

However, changes in the colour of wortmannin upon increasing alkalinity support Wipf & Halter (2005), and Yuan *et al.* (2007), in their attribution of furan ring opening under alkaline conditions.

In chapter 5 it was proposed that the primary reduction of wortmannin occurs at the C7 position of wortmannin (figure 6.18). Studies reported on in section 6.4.3.1 (ii) showed the effect of lysine on the reduction peak for wortmannin. It is reported in literature that lysine binds specifically to the furan ring and leads to its cleavage and subsequent irreversible binding to the lysine amino acid. Accordingly, electrochemical studies on the effect of lysine binding to the furan ring resulted in the prominent wortmannin reduction peak (at – 0.90 V) remaining unaltered. The nucleophilic addition of lysine residues to wortmannin resulting in furan ring opening is well characterized in the literature (Scheme 6.1). Following this Scheme 6.1, C7 is unaffected by the ring opening in this particular mechanism, lending some support to the attribution of the electroreduction of C7 to the prominent cathodic reduction peak for wortmannin.

In scheme 6.1 it is illustrated that alkaline induced lactone A ring cleavage is initiated at the O2 position and results in the transport of electrons across the adjacent lactone ring leading to an oxidised C7, and C=O being converted to C-OH. This observation could explain the disappearance of the primary reduction peak for wortmannin between -0.90 V and -1.10 V (if attributed to C7) and the formation of electrochemically active intermediates with reduction waves close to 0.0 V often associated with the reduction of phenolic moieties. These studies therefore support alkaline induced lactone A hydrolysis but do not discount concomitant furan ring hydrolysis.

To summarise, spectroscopic studies lend support to furan ring opening as observed by previous authors, while electrochemical studies conducted lend support to lactone A hydrolysis. With access to pure intermediate compounds (outside the scope of this study) further such voltammetric studies seem poised to resolve these ongoing studies into wortmannin instability.

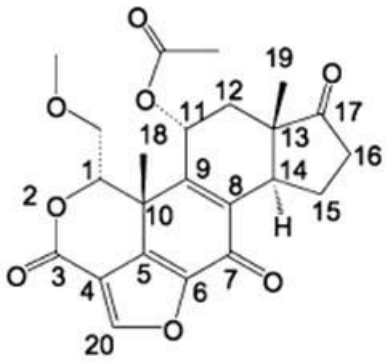

Figure 6.15 Chemical structure of wortmannin with atom position numbers included (Yuan *et al.* 2007).

6.5 Summary and Conclusions

This study successfully showed the feasibility of NME for enhancing the detection of wortmannin with a recorded LOD of 0.102 nmol.cm^{-3} comparing favourably with reported LOD via HPLC of 0.233 nmol.cm^{-3}. In descending order (from greatest sensitivity to lowest sensitivity) the following was observed: *f*MWCNTs > *f*SWCNTs > HPLC* (Holleran *et al.,* 2003) > GCE-C_{60} > GCE. Of specific relevance to the application of NME for wortmannin studies in biological media, limited interference was observed for synthetic growth medium containing uric acid, ascorbic acid and glucose when *f*MWCNTs were added to the GCE surface. These findings strongly suggest that *f*MWCNTs reduce the effects of common interferents on the electrochemical detection of wortmannin, as well as reducing the passivation effect of electrode surfaces commonly observed due to the adsorption of compounds onto the electrode surface. Dissolved oxygen was found to interfere with the reduction peak of wortmannin, and it is recommended that samples be either deaerated prior to analyses, or that amperometric methods are employed to overcome the effects of O_2. Further quantification by employing amperometry showed that a calibration curve can be constructed with a correlation coefficient, R^2 of 0.9977.

The electrochemical detection of wortmannin in this instance therefore compares favourably with published findings of Holleran *et al.* (2003), and also show promise for the development of a continuous monitoring system for the detection of wortmannin biosynthesis in a growth medium, in real time.

An additional prospect of this diagnostic system is in the ability to gain knowledge on the behaviour of wortmannin under physiological conditions (such as pH). Furthermore the detection of wortmannin was not compromised by studies in matrices such as foetal calf serum frequently used in biological studies. The prospect of real time monitoring of wortmannin behaviour as exemplified through the detection of electrochemically active intermediates and products following alkaline induced hydrolysis serves as a valuable basis for future such mechanistic and behavioural studies in biological media. The feasibility thereof is enhanced owing to the lack of sample pretreatment and passivation of the NME surface observed in these studies.

CHAPTER 7

PERFORMANCE ASSESSMENT OF NMEs FOR THE ELECTROCHEMICAL DETECTION OF REACTIVE RED

"Every industry that involves manufactured items will be impacted by nanotechnology research. Everything can be made in some way better – stronger, lighter, cheaper, easier to recycle – if it's manufactured at the nanometer scale"

– Stan Williams, Director of Quantum Science Research.

7.1 Introduction

The class of Reactive dyes are a major and diverse group dominating the more than 100,000 commercially available dyes (Robinson *et al.*, 2001; Forgacs *et al.*, 2004), and consist of the azo, phthalocyanine and anthraquinone dye groups (Forgacs *et al.*, 2004).

The extensive use of these Reactive dyes in textile industries is as a result of their diverse and brilliant colour shades, ease of use and application, low energy use, good high wet profiles, stability in light (resistance to UV) and resistance to microbial degradation (Wesenberg *et al.*, 2003). While these are significant advantages, most Reactive dyes are known carcinogens (Platzek *et al.*, 1999), mutagens (Erkurt *et al.*, 2007), and are recalcitrant and toxic within the environment (Hao *et al.*, 2000; Forgacs *et al.*, 2004). In addition, the wet processing of textiles consumes significantly large amounts of water. The chemical structure of Reactive red, which is of significance in this study, is shown in figure 7.1.

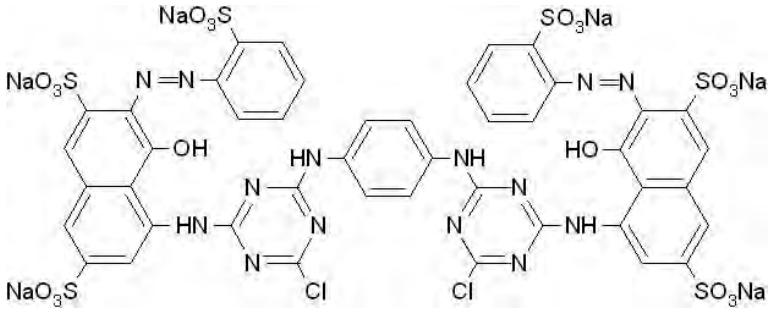

Figure 7.1 Chemical structure of Reactive red 120 dye.

The wastewater effluent generated from reactive dyes used in the textile industry, with consideration to the volume (over 700,000 tons worldwide annually) (Robinson *et al.*, 2001), as well as effluent composition, is rated as being the most significant pollutant within the industrial sector as a whole (Vandevivere *et al.*, 1998), contributing more than 40 % of the total wastewater from industry (Agarwal, 2001).

Figure 7.2 Discharge of untreated effluent containing reactive red into rivers in (A) the Kaliakor district of Bangladesh. (*Permission to use obtained from Dr. Jeremy Knapp*) and (B) Roxian, Guangxi China (*Permission to use obtained from Jeffrey Hays*).

The treatment of textile effluent can be categorised into physico-chemical and biological methods (Hao *et al.*, 2000; Robinson *et al.*, 2001; Forgacs *et al.*, 2004). Physico-chemical methods, including electrochemical, oxidation and coagulation-flocculation are expensive due to high energy consumption rates, and form large quantities of sludge and potentially toxic by-products.

The conventional and current domestic wastewater treatment technologies have shown little efficacy in the treatment of dye effluent. This is attributed to the chemical stability of the dyes (Wesenberg *et al.*, 2003; Forgacs *et al.*, 2004) and the susceptibility of the bacterial growth to the effects of co-existing effluent interferents (surfactants and dispersants). Of significant interest are figures reported on by Shaul *et al* (1991), on the verification that of the 18 major azo dyes, 11 were untreated downstream of the aerobic activated sludge process, biosorption of 4 dyes onto the flocculants were observed, while only 3 were partially degraded.

While these figures were reported on nearly 2 decades ago, the activated sludge system has remained relatively unchanged since 1991. Under anaerobic conditions the azo dyes are biodegraded to amine moieties by azo-reductases. These amine moieties have been reported to be more carcinogenic and mutagenic than the parent compound (Chung & Stevens, 1993).

The use of lignolytic (white-rot) fungi to degrade azo dyes aerobically has proven to be a cost effective and efficient alternative to the conventional degradation methods (Borchert & Libra, 2001; Kapdan & Kargi, 2002; Wesenberg *et al.*, 2003). This is in part as a result of the non-discriminate degradation of an array of dyes by a group of catalytic free-radical enzymes that are produced by lignolytic fungi and secreted in an extracellular manner (Abadulla *et al.*, 2000; Hou *et al.*, 2004). As an added advantage, lignolytic fungi generally do not require acclimatization or preconditioning to the dye and can degrade the xenobionts to untraceable levels or in the case of certain dyes, can achieve complete elimination (Bumpus & Aust, 1987).

While their modes of action are well documented and are not of primary concern in this study, the three principal lignolytic enzymes that have been implicated in numerous documented reports on the degradation of azo dyes are: manganese-dependent peroxidase (MnP, E.C. 1.11.1.13), laccase (phenol oxidase)(LAC, E.C. 1.10.3.2) and lignin peroxidase (LiP, E.C. 1.11.1.14). White-rot fungi produce either only one of these enzymes or a combination of the three (Novotný *et al.*, 2001) in response to the xenobionts.

In this study the lignolytic fungi, *Pleurotus ostreatus* was chosen to biodegrade the Reactive red dye, since, in addition to being isolated relatively easily, its capacity to degrade azo dyes is well-documented in literature (Vyas & Molitoris, 1995; Novotný *et al.*, 2001; Hou *et al.*, 2004; Palmieri *et al.*, 2004; Nilsson *et al.*, 2006).

A specific relationship is apparent between the efficacy of the lignolytic enzymes to decolourise the dye medium and the activity of the enzyme (Padgornik *et al.*, 1999; Ozsoy *et al.*, 2005). In addition, the specific activity of the lignolytic enzymes is increased in proportion to the dye concentration (Erkurt *et al.*, 2007). However, measurement of the enzyme activity within the growth medium is not a true representation of dye biodegradation since the enzyme may be secreted locally within the fungal mat or bioballs, and will therefore not be detected in the liquid growth medium, leading to inaccurate azo dye concentration determinations.

Apart from the extraction of the dye from the growth medium followed by the quantification of the dye, no method has been documented that can accurately achieve this in the growth medium

without extracting the dye. Secondly, while reactive red does exhibit a UV-VIS spectroscopic spectrum, the opaque nature of fungal biomass in the growth medium makes its application non-feasible for monitoring in growth media.

The biodegradation of Reactive red by *Pleurotus ostreatus* is thus well-documented and understood and despite its limitations its fate typically monitored via spectroscopic means (Carliell *et al.*, 1995; Forgacs *et al.*, 2004). This study is the first known account of the electrochemical monitoring of Reactive red biodegradation.

7.2 Objectives

The overarching aim of this study was to ascertain the performance of an electrochemical sensor surface modified with nanomaterials for the detection of Reactive red in effluent and to examine the same for monitoring electrochemically the biodegradation thereof by a fungal isolate, *Pleurotus ostreatus* in a semi-batch mode aerobic reactor.

In order to achieve this aim, the following specific objectives were addressed (all in actual effluent):

Electrochemical characterisation of Reactive red in effluent at an unmodified GCE.

Evaluation of GCE-NME as compared to GCE (unmodified) for the electrochemical detection of Reactive red in effluent.

Decolourisation and biodegradation of Reactive red by employing the use of *Pleurotus ostreatus* in a semi-continuous batch mode reactor.

Monitoring of the biodegradation electrochemically of Reactive red at 12 hour intervals by employing the optimised nanomaterial-modified electrode surface.

Compare spectroscopic and voltammetric methods for monitoring the rate of Reactive red biodegradation .

7.3 Experimental

7.3.1 Initial characterisation of Reactive red at an unmodified GCE

Effluent known to contain Reactive red was obtained from a local textile industry and was used as received. The initial concentration of Reactive red was unknown since the effluent was obtained from holding vessels filled in a batch mode with spent Reactive red effluent.

For initial characterisation purposes (to confirm the identity of the observed redox peaks), the dye effluent was spiked with purchased Reactive red 120 (Sigma Aldrich, 50 % purity).

For this purpose all electrochemical analyses, unless otherwise specified, were performed directly in the effluent. Cyclic voltammetry was employed for initial characterisation of the redox behaviour of Reactive red at an unmodified GCE. Briefly, a clean GCE was placed in 100 % industrial effluent bulk solution and a broad potential window scanned in the anodic direction from 0 V to 1.4 V and the cathodic direction from 0 V to -1.5 V (vs. Ag|AgCl) at a scan rate of 0.1 $V.s^{-1}$.

7.3.2 Sensitivity comparison between GCE and nanomaterial modified electrodes

By applying OSWV, the current response for the prominent anodic peak (E_{pa1}) of Reactive red was assessed at an unmodified GCE and at the GCE-NMEs (MWCNTs and C_{60} fullerenes). Electrodes were prepared as described in chapter 4. Each NME was assessed under identical conditions and operating parameters, with a potential window scanned in the anodic direction between 0 V and 1.4 V at a scan rate of 0.1 $V.s^{-1}$. The NME that exhibited the highest relative sensitivity with the greatest reproducibility was adopted for further performance assessment through its incorporation into the monitoring of the biodegradation of Reactive red in real samples. The linearity of the current response was evaluated by measurement of current at several dilutions of Reactive Red containing effluent. Standards of the effluent were prepared by serial dilution with dH_2O. Each standard was assessed separately and in triplicate.

7.3.4 Enrichment of - and toxicity threshold determination for *P. ostreatus*

A pure culture of *Pleurotus ostreatus* was obtained as a gift from Ms. Bronwyn Moore (Rhodes University), and incubated on solid potato dextrose (PDA) agar at 25 °C until a fungal mat covered the surface of the agar plate. Cubes measuring 1 cm^3 were cut out of the agar plates containing the fungal mat and inoculated onto PDA plates containing concentrations of Reactive red effluent from 0 to 100 % at 10 % increments and incubated at 25 °C. The diameter of the mycelial growth halo was measured at 12 hour intervals until the negative control (0 %) plate was covered with a fungal mat.

A 1 cm^3 cube of agar containing *P. ostreatus* was inoculated aseptically into a conical flask containing pre-sterilised enrichment liquid growth medium, with composition: 20 $g.l^{-1}$ malt extract broth enriched with 10 $g.l^{-1}$ glucose and 2 $g.l^{-1}$ yeast extract. The flask was agitated at 120 RPM and 25 °C on a gyrator shaker (Labcon, South Africa). Samples of the inoculum were taken aseptically at 12 hour intervals and placed on preweighed dry filter papers (Whatman) and dried at 100 °C. When the fungal inoculum sample was dry it was weighed and the mass recorded. This procedure was continued until the mass/concentration of the fungal inoculum reached 50 $g.l^{-1}$. The enrichment liquid medium containing the fungal inoculum was continuously agitated to allow for aeration until required for inoculation into the semi-continuous batch mode reactor.

7.3.5 Setup and inoculation of the semi-continuous batch reactor with *P. ostreatus*

The effluent containing Reactive red was autoclaved at 121 °C, sealed and maintained under sterile conditions at 25 °C. Once the effluent had cooled, the conical flask was inoculated with 50 $g.l^{-1}$ fungal biomass under sterile conditions and resealed. Aerobic conditions were maintained through the flask supply being fed with a constant flow of air passing through a 0.2 µm Whatman filter. Ambient temperature (25 °C) was maintained by a controlled environment room. Scheme 7.1 is a representation of the semi-continuous batch mode reactor setup used.

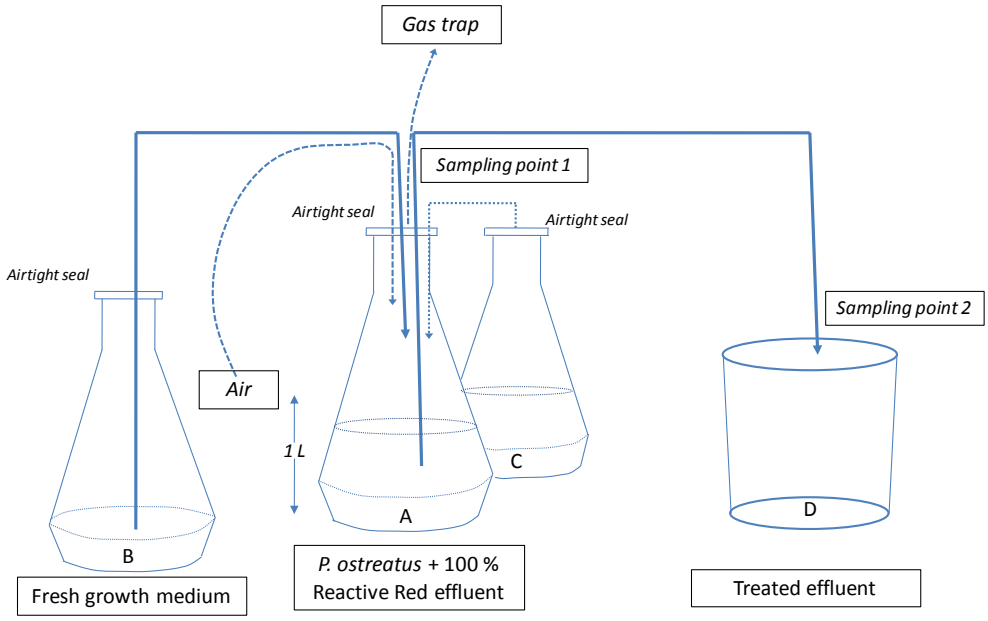

Scheme 7.1 Design of the semi-continuous batch reactor mode setup used for the monitoring of the biodegradation of Reactive red by *Pleurotus ostreatus*. In batch mode the batch reactor (A) containing 1L 100% Reactive red effluent was inoculated with *P. ostreatus* and sealed until decolourisation occurred and a biodegradation profile was established. Once near 100 % biodegradation had occurred, the batch system was converted to a semi-batch system by simultaneous slow feeding with fresh growth medium (B) and 100 % untreated effluent (C) while the treated effluent was collected in (D). Samples were taken at the sampling point 1 (influent) and 2 (effluent).

The growth of *P. ostreatus*, its enzyme production and dye biodegradation are highly dependent on the culture conditions of which pH, the dye class and initial concentration, dissolved oxygen requirements, resistance to shear forces (usually from impellers in continuously stirred tank bioreactors) as well as the media composition are the most important (Vyas & Molitoris, 1995; Novotný *et al.*, 2001; Nilsson *et al.*, 2006). In order to minimise the effect of shear forces on the fungal growth and subsequent production of the necessary enzymes, aeration was achieved through gentle bubbling of air through an airstone.

7.3.6 Electrochemical monitoring of Reactive red biodegradation using modified electrodes

A glassy carbon electrode modified with NMEs, as discussed in Chapter 4 was used for the quantitative assessment of the biodegradation efficacy of Reactive red by *P. ostreatus.* Square wave voltammetry was employed as the electrochemical technique. Each sample was assessed under identical operating conditions of an applied potential window of -0.3 V to 1.2 V at a scan rate of 0.1

$V.s^{-1}$. Additionally, spectroscopy scan profiles were setup as a qualitative comparison. Prior to the spectroscopic scans, the samples were centrifuged at 5,000 x g for 5 minutes to remove the fungal biomass (pellet). The supernatant was analysed on a 96-well microtitre plate using a Powerwave spectrometer. The spectroscopic scan was set at 1 nm increments from 200 nm to 650 nm. All scans were performed in triplicate.

7.4 Results and Discussion

7.4.1 Initial electrochemical identification

Figure 7.3 shows a cyclic voltammogram (CV) for the oxidation of Reactive red as detected in 50 % (*v/v*) effluent.

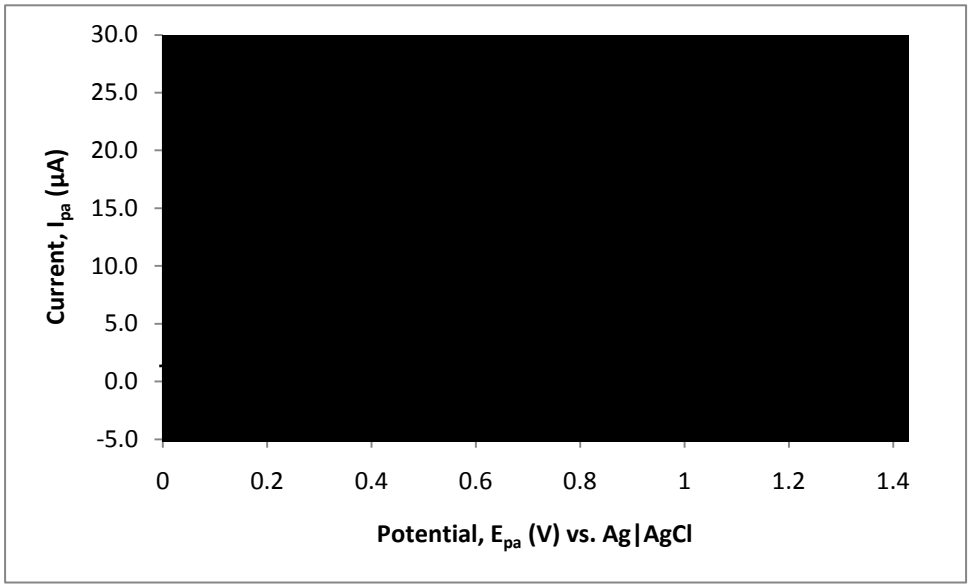

Figure 7.3 Representative cyclic voltammogram for the anodic scan of Reactive red in 50 % industrial effluent. The anodic pair, E_{pa1} and E_{pa2} were observed during the oxidation scan at an unmodified GCE, at a potential window between 0.0 V and 1.4 V (vs. Ag|AgCl) at a scan rate of 0.1 $V.s^{-1}$. (pH of effluent = 4.2)

During the oxidation scan, a distinct pair of anodic peaks ($E_{pa1,2}$) were observed between 0.75 V and 0.90 V at an unmodified GCE, with the secondary anodic peak, E_{pa2} being prominent with a smaller shoulder peak, E_{pa1}. Figure 7.4 shows the cathodic scan for this sample in 100 % effluent at an unmodified GCE.

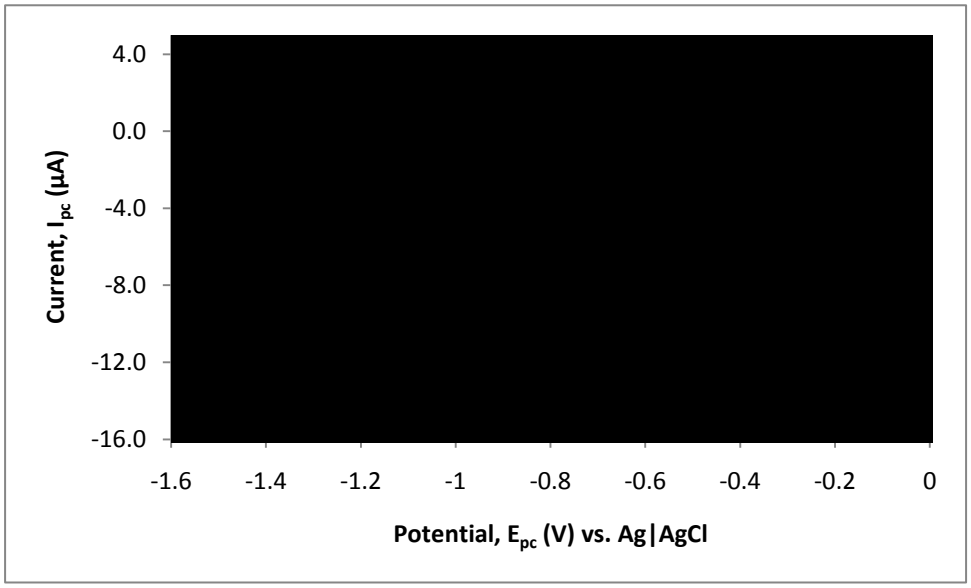

Figure 7.4 Representative cyclic voltammogram for the cathodic scan of Reactive red in 100 % industrial effluent. The cathodic pair, E_{pa1} and E_{pa2} were observed during the oxidation scan at an unmodified GCE, at a potential window between 0.0 V and - 1.5 V (vs. Ag|AgCl) at a scan rate of 0.1 $V.s^{-1}$.

For confirmation of the identity of the anodic pair ($E_{pa1,2}$ on Figure 7.5 B) effluent containing Reactive red was spiked with 0.5 $nmol.cm^{-3}$ Reactive red 120 (Sigma Aldrich) and Osteryoung square wave voltammetry performed. The anodic peaks observed in Figure 7.3 were shown to increase after spiking of the sample with pure Reactive red 120. The resultant OSWVs are shown in figure 7.5.

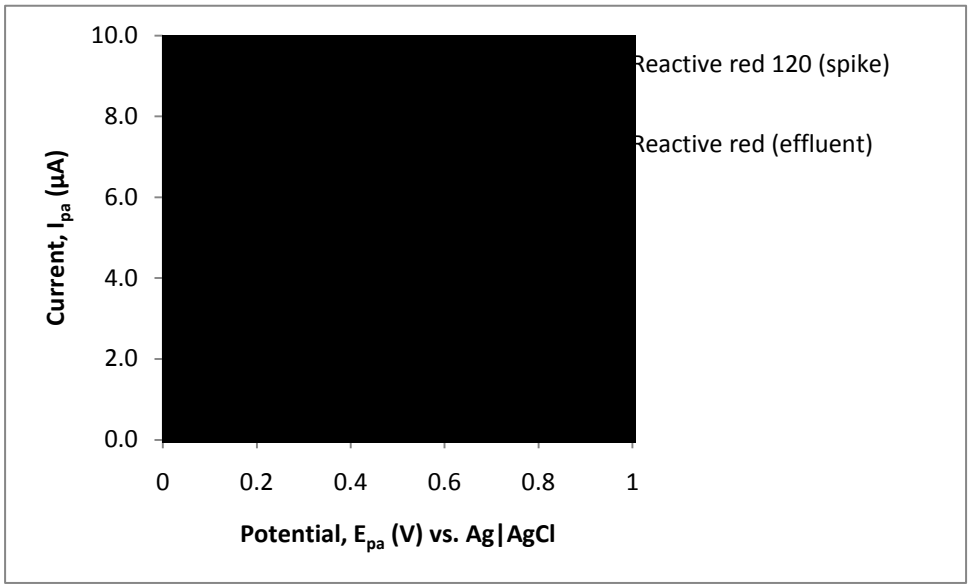

Figure 7.5 Osteryoung squarewave voltammograms comparing the anodic response at an unmodified GCE for effluent containing Reactive red, before (solid line) and after (dotted line) spiking with a 0.75 $nmol.cm^{-3}$ Reactive red 120. Scan rate: 0.1 $V.s^{-1}$.

In figure 7.5 Reactive red 120 spiking of the effluent containing Reactive red resulted in the overlay of a prominent anodic peak pair (dotted line). The shoulder peak of the spiked sample was small and near negligible. The potential of the spiked sample was similar to that of the anodic pair obtained from the effluent containing Reactive red.

7.4.2 The effect of scan rate on current response

The effect of scan rate on the anodic peak pair for Reactive red in the effluent was assessed through CVs of the effluent in a quiescent solution at different scan rates between 0.05 $V.s^{-1}$ and 0.12 $V.s^{-1}$. Figure 7.6 (A, B) are the CVs and line graph, respectively for the scan rate studies.

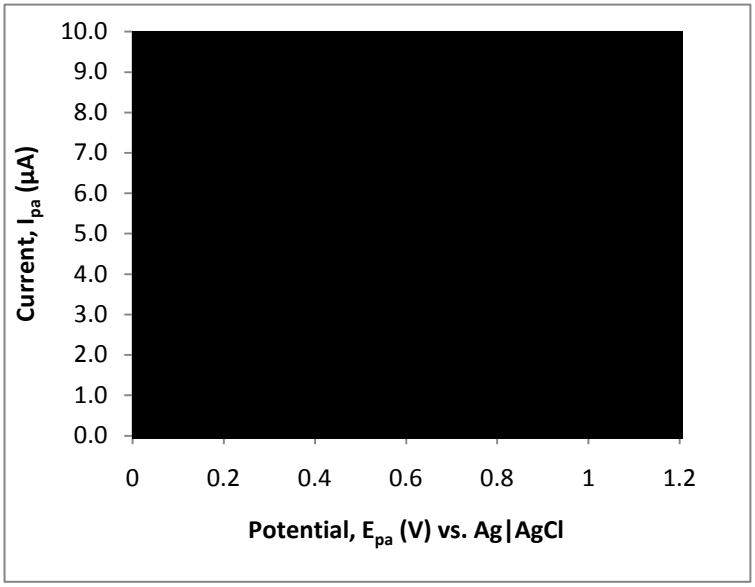

Figure 7.6 (A) Cyclic voltammograms of Reactive red (100 % effluent) at a range of scan rates between 0.05 $V.s^{-1}$ and 0.12 $V.s^{-1}$.

The line graph for figure 7.6 (A) is shown in figure 7.6 (B) below:

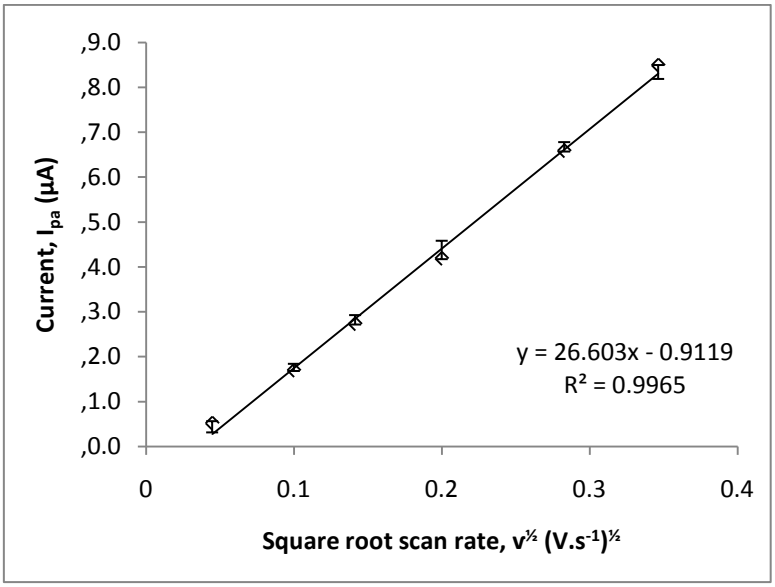

Figure 7.6 (B) Linear plot of current, I_{pa} (µA) vs. square root of scan rate, $v^{½}$ $(V.s^{-1})^{½}$.

From figure 7.6 (A, B) it is clear that a linear response results from the plot of I_{pa} (µA) $v^{½}$ $(V.s^{-1})^{½}$, which indicates that in a quiescent solution, the transport of Reactive red to the electrode surface is diffusion-controlled.

7.4.3 Generation of calibration curves using NMEs for Reactive red in effluent

Calibration curves were generated for Reactive red in effluent by employing OSWV and comparing sensitivity and reproducibility at the prepared NMEs discussed previously (Chapter 4). These were constructed at an unmodified GCE, at a GCE modified with 40 µl of 150 µM C_{60} (Section 4.4.3) and at a GCE modified with functionalised MWCNTs (9 hours acid treated) (Section 4.4.2). Calibration curves generated at a GCE modified with functionalised SWCNTs (4 hours acid treatment) (Section 4.4.1) yielded a low degree of linearity and were not utilised in this study.

Figures 7.7, 7.8 and 7.9 represent the OSWVs for Reactive red containing effluent at an unmodified GCE, GCE-*f*MWCNT and GCE-C_{60}, respectively. For the purposes of these experiments 100% Reactive

Red effluent refers to undiluted effluent, whereas lower percentages refer to diluted volumes of effluent.

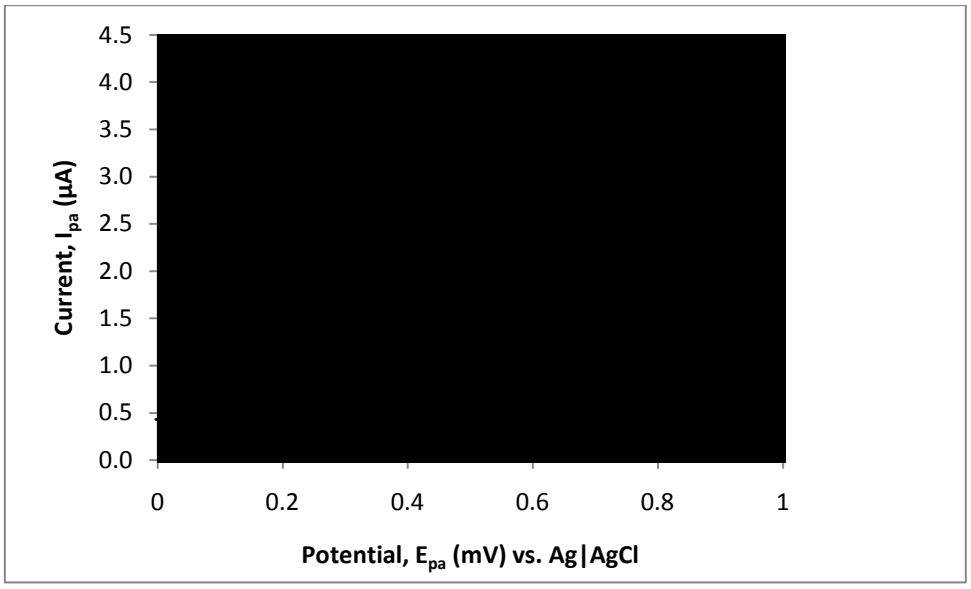

Figure 7.7 Osteryoung squarewave voltammograms at an unmodified GCE showing the increase in current response with increase in Reactive red (as % of total concentration in the effluent) between 10 %(i) and 100 % (vi). Dilutions were performed in *d*H_2O. Scan rate: 0.1 $V.s^{-1}$ vs. Ag|AgCl.

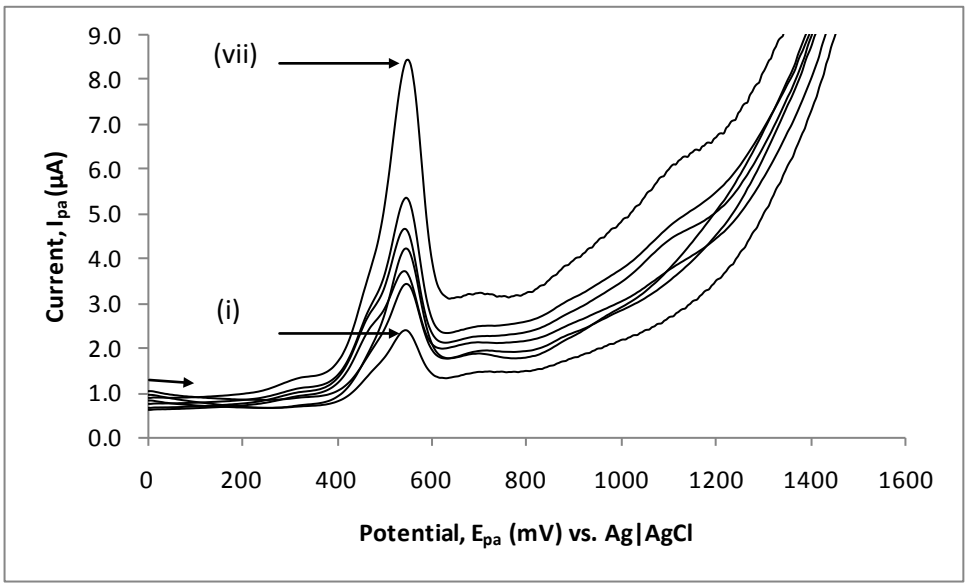

Figure 7.8 Osteryoung squarewave voltammograms at GCE-*f*MWCNTs showing the increase in current response with increase in Reactive red (as % of total concentration in the effluent) between 10 %(i) and 100% (vi).Dilutions were performed in *d*H_2O. Scan rate: 0.1 $V.s^{-1}$ vs. Ag|AgCl.

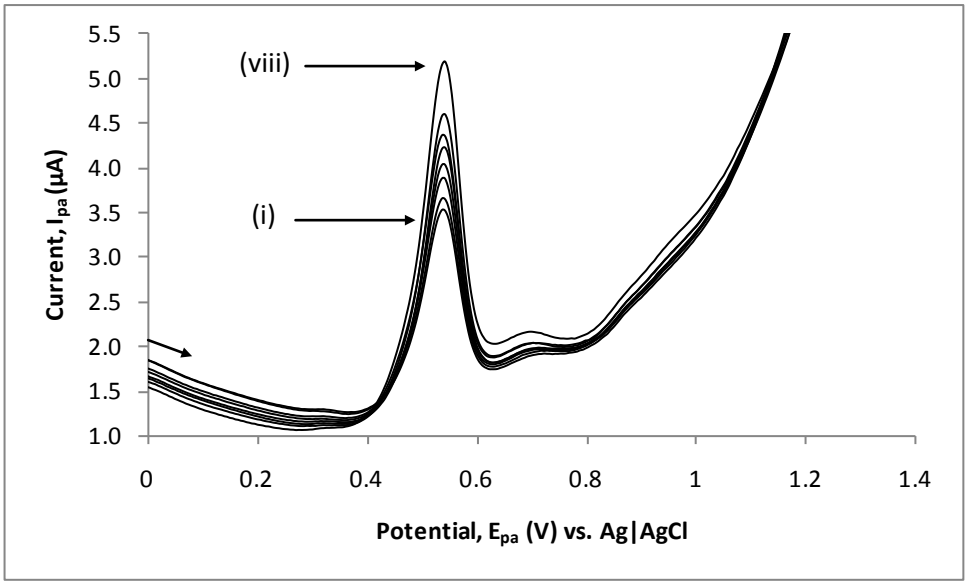

Figure 7.9 Osteryoung squarewave voltammograms at GCE-C_{60} showing the increase in current response with increase in Reactive red (as % of total concentration in the effluent) between 10 %(i) and 100 %viii). Dilutions were performed in *d*H_2O. Scan rate: 0.1 V.s^{-1} vs. Ag|AgCl.

The line graphs representing the OSWVs are shown in figure 7.10.

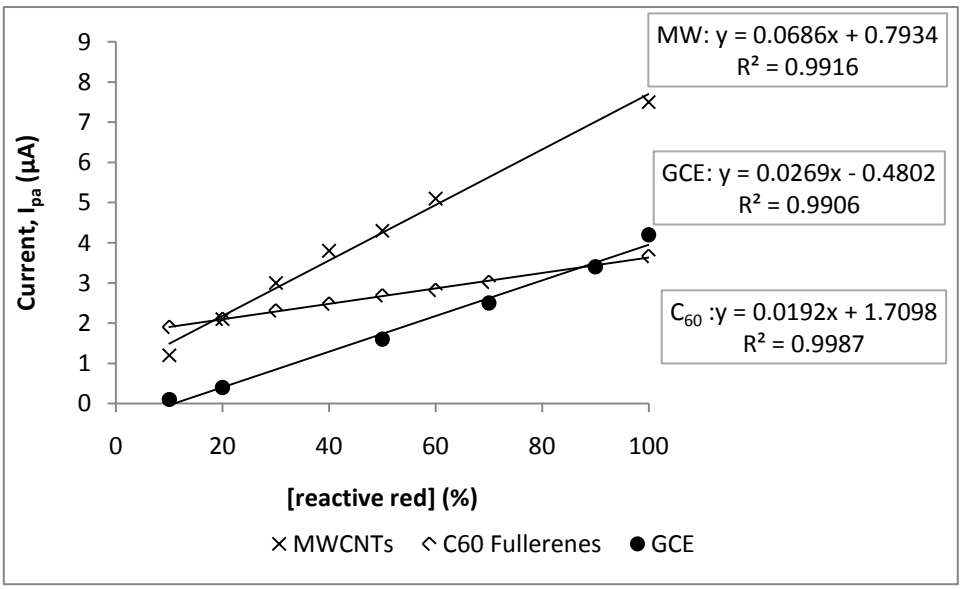

Figure 7.10 Current response at different percentages (v/v) of reactive red containing effluent at GCE, MW and C_{60} fullerene modified electrodes.

The reproducibility, accuracy, and sensitivity of Reactive red in effluent and quantification at the various electrodes (GCE, GCE-*f*MWCNTs, GCE-C_{60}) can be examined by a comparison of correlation coefficient, linearity and standard deviation, as in table 7.1.

Table 7.1 Comparative study showing differences in key factors between calibration curves for the quantification of Reactive red in effluent.

ELECTRODE	**SENSITIVITY** (μA/ % reactive red)	**CORRELATION COEFFICIENT, R^2**	**REPRODUCIBILITY*** (%)
GCE (unmodified)	8.47 C-0.12	0.9930	95.42
GCE-*f*MWCNTs	10.38 C + 2.22	0.9954	96.03
GCE-C_{60}	3.48 C + 2.15	0.9982	98.81

*Calculated as outlined in chapter 3.6.1

The generation of calibration curves for Reactive red in the actual effluent at the two NMEs (*f*MWCNTs and C_{60}) shows that GCE modified with *f*MWCNTs (9 hours acid treatment) yields the greatest sensitivity in the form of current response, while GCE-C_{60} exhibits the lowest sensitivity. Interestingly, an unmodified GCE exhibited greater sensitivity in comparison to GCE-C_{60}, which could possibly be attributed to the insulatory characteristics observed earlier (Section 4.4.3). However greater reproducibility for GCE-C_{60} in comparison to an unmodified GCE and GCE-*f*MWCNTs was observed. GCEs modified with *f*MWCNTs functionalised for 9 hours was opted for when further assessing the stability of Reactive red given the greater sensitivity recorded at this modified surface.

7.4.4 Biodegradation of Reactive red by *P. ostreatus*

7.4.4.1 Toxicity threshold determination

The initial toxicity determination of Reactive red to *P. ostreatus* was performed on potato dextrose agar (PDA) plates. Figure 7.11 shows a pure fungal culture of *P. ostreatus* assessed for its ability to degrade Reactive red.

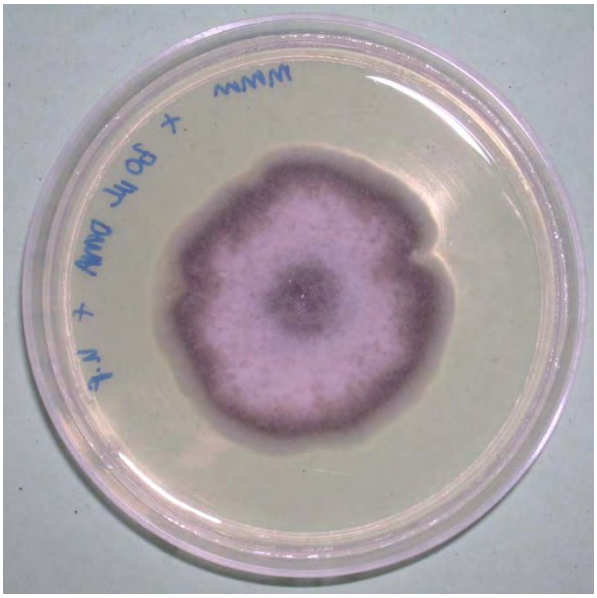

Figure 7.11 Pure culture of *P. ostreatus* grown on a potato dextrose agar plate.

In order to ascertain the toxicity threshold of the fungal species, *P. ostreatus* was inoculated onto PDA plates containing a range of concentrations of Reactive red. Growth of *P. ostreatus* was observed on all the concentrations of PDA plates spiked with Reactive red effluent (up to 100 %). While it was observed that at above 40 % Reactive Red effluent the growth of *P. ostreatus* was initially slower, within 2 days all the plates were covered in a fungal mat, showing *P. ostreatus* capability of growing in the presence of these concentrations of Reactive red. Effluent at 100 % was therefore utilised with no apparent retardation of the growth of *P. ostreatus* being demonstrated.

7.4.4.2 Semi-continuous batch reactor setup for the bioremediation of Reactive red by P. ostreatus

Figure 7.12 shows the semi-continuous batch reactor setup used in this study to monitor the biodegradation of Reactive red in 100 % textile effluent by *Pleurotus ostreatus*.

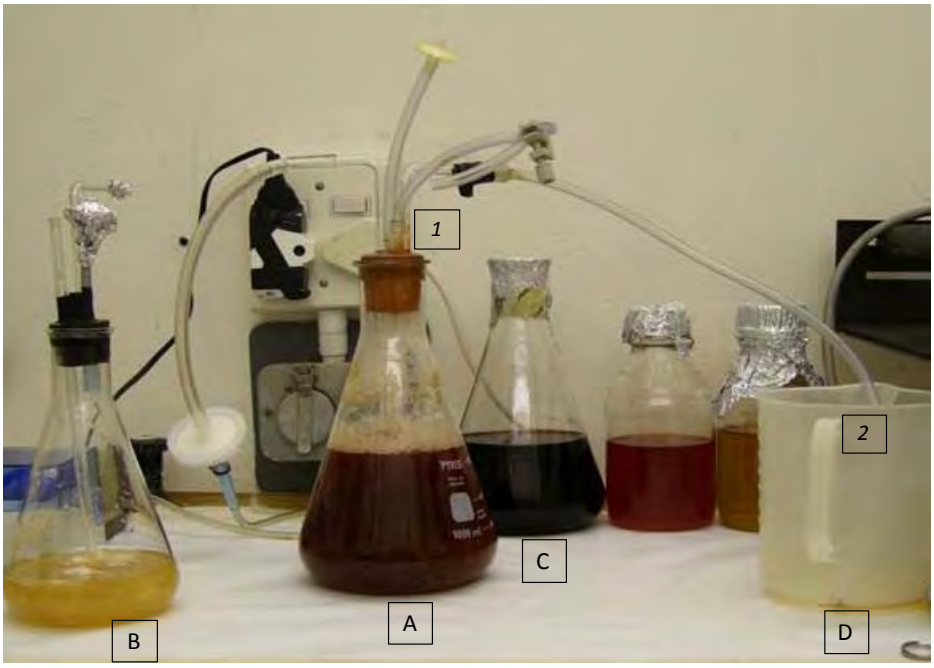

Figure 7.12 Photograph of the 1L semi-continuous batch reactor setup for the biodegradation of Reactive red by *Pleurotus ostreatus*. *Key*: (A): 1L batch reactor containing 100 % Reactive red + *P. ostreatus* inoculum, (B): fresh growth medium, (C): untreated 100 % Reactive red effluent, (D): spent growth medium + treated effluent, 1 and 2: sample points for the untreated and treated effluent, respectively.

In figure 7.12 a distinct change in the colour of the characteristic deep red colour of Reactive red effluent to a paler red occurs with time, which is indicative of the breakdown of the dye. Lignolytic fungi such as *P. ostreatus* are renowned for the decolourisation of phenolic and azo compounds (Nilsson *et al.* 2006). A control experiment was conducted where no *P. ostreatus* was added to the dye, and the colour remained unchanged.

Figure 7.13 (A) compares the initial Reactive red flask to one that had been treated for 36 hours, where the efficacy of fungal decolourisation of Reactive red over 36 hours is apparent. In figure 7.13 (B), the near complete dye decolourisation is clearly observed in the sample treated over 96 hours as compared to 24 hours.

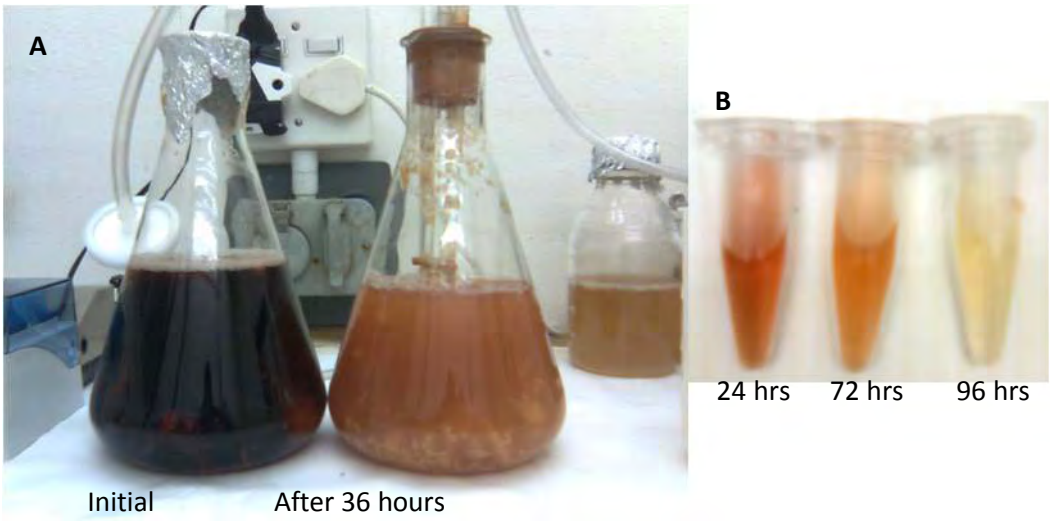

Figure 7.13 (A): Reactive red biodegradation by *Pleurotus ostreatus* at day 0 (left flask) and after 36 hours (right flask). (B): Eppendorf tubes showing the near complete biodegradation of Reactive red and the near removal of the distinctive red pigment at 96 hours.

7.4.4.3 Spectroscopic monitoring of the biodegradation of Reactive red by P. ostreatus.

Following centrifugation of the spent growth media and fungal biomass at 4500 RPM for 10 minutes, the supernatant was retained and a spectral scan performed between 400 nm and 650 nm at 3 different time intervals, namely 0 hours, 24 hours, and 72 hours respectively. Figure 7.14 shows the spectral scan.

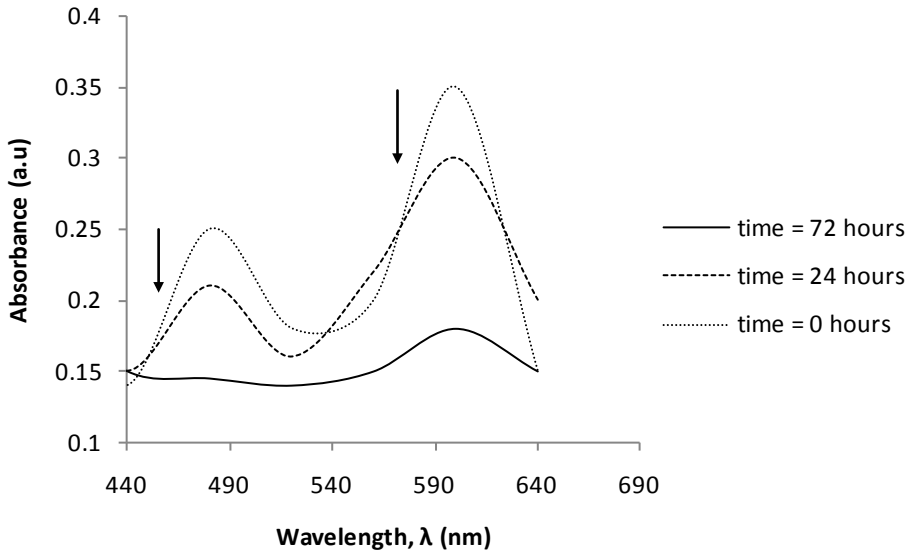

Figure 7.14 Spectral scans at 3 different time intervals in order to demonstrate the breakdown of Reactive red by *P. ostreatus.* Spectral scan window: 200 nm to 650 nm, at 1 nm increments.

The biodegradation of dyes by *Pleurotus ostreatus* is well documented with biodegradation pathways having been proposed by several authors (Vyas & Molitoris, 1995; Novotný *et al.*, 2001; Hou *et al.*, 2004; Palmieri *et al.*, 2004; Nilsson *et al.*, 2006). Wang *et al.* 2005 showed a decrease in the absorption peak found between 518 and 542 nm for azo bonds in the presence of known azo reductases, while Wang *et al* 2005 had observed a maximum for λ at 560 nm. In this study, λ_{max} was observed at 590 nm. The absorbance shift could have been attributed to interference from the composition of the growth medium and spent effluent in which the Reactive red was observed, since pure Reactive red in water exhibited λ_{max} between 540 and 560 nm. The peak at 590 nm was monitored every 12 hours, and by employing equation 8.01, the decolourisation extent was determined:

$$Decolorisation\ extent\ (\%) = \left(\frac{OD_1 - OD_t}{OD_1}\right) x\ 100 \qquad [7.01]$$

Where: OD_1 refers to the initial absorbance, and OD_t refers to the absorbance after incubation, at time t (Wang *et al.*, 2005).

Figure 7.15 shows the percentage decolourisation per 12 hour cycle.

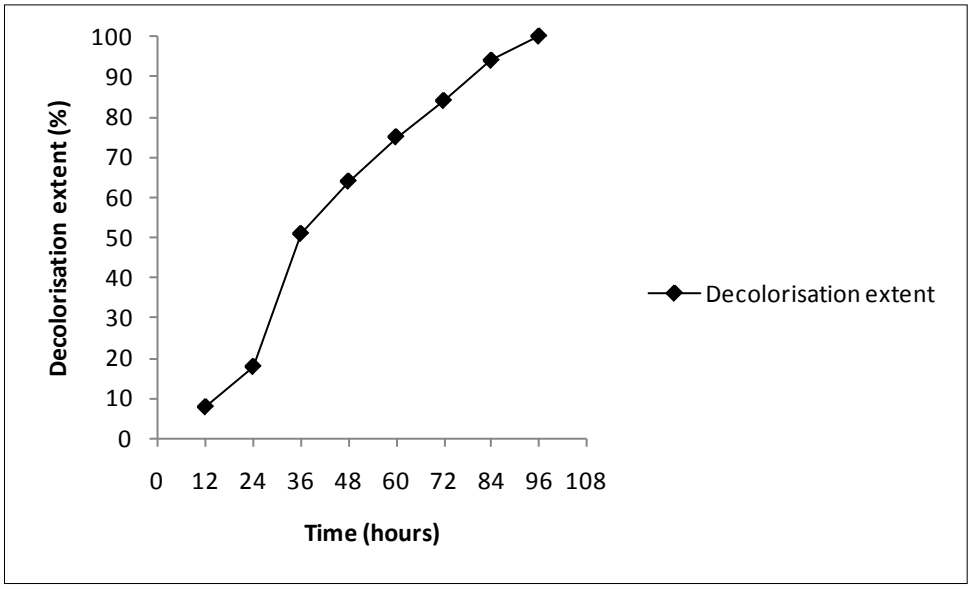

Figure 7.15 The extent of decolourisation (%) of Reactive red biodegradation per 12-hour interval, as determined spectrometrically at 590 nm.

In a proposed biodegradation pathway of Reactive red, Wang *et al.* (20085) suggest that an initial phase of biodegradation involves reductive cleavage catalysed by the enzyme lignin peroxidase. Consequently, the intermediate product undergoes desulphonation, giving rise to a 1-amino-2-naphthol moiety, which undergoes subsequent deamination to afford 2-naphthol, which is rapidly consumed as an energy source.

7.4.4.4 Electrochemical monitoring of the biodegradation of Reactive red by P. ostreatus.

Figure 7.16 are representative OSWVs illustrating the decrease in the peak attributed to Reactive red, indicative of the degradation of this compound at 0 hours, 24 hours and 72 hours respectively.

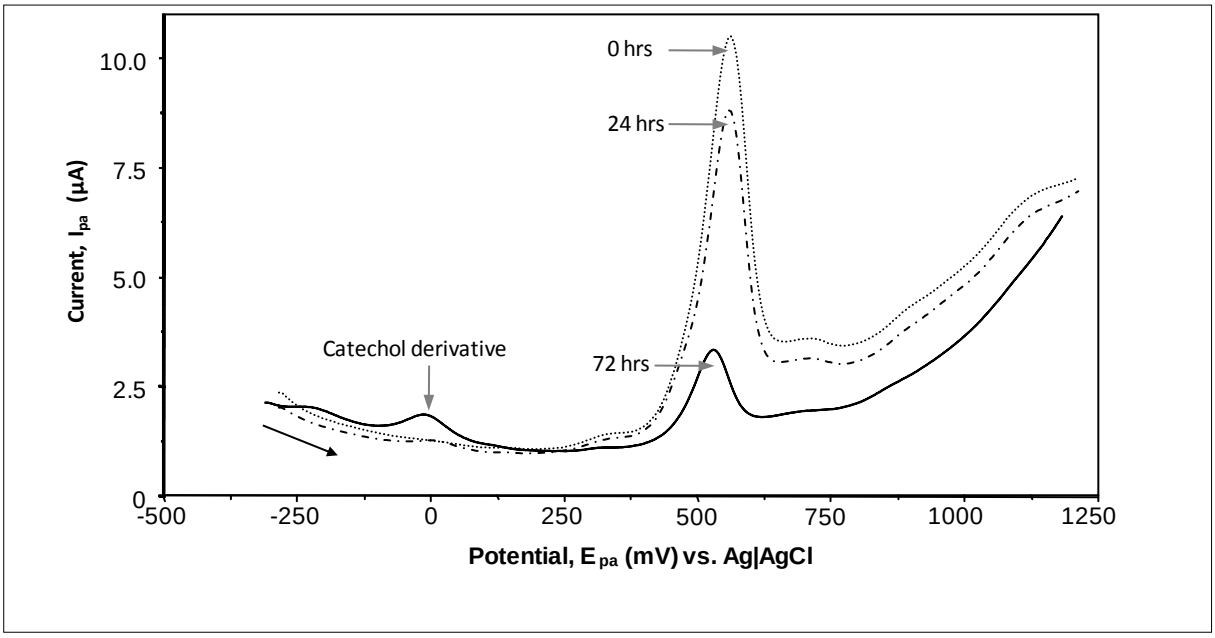

Figure 7.16 Square wave voltammograms showing the biodegradation over 72 hours of Reactive red in 100 % effluent by *Pleurotus ostreatus*. A catechol derivative forms as a by-product of the biodegradation. Working electrode: GCE-*f*MWCNT, scan rate: 0.1 $V.s^{-1}$. *Key*: dotted line: initial (0 hours) Reactive red anodic peak, dashed line: anodic peak after 24 hours and, solid line: Reactive red anodic peak after 72 hours.

In figure 7.16 a significant decrease in the prominent anodic peak for Reactive red (0.55 V) was observed, suggesting a decrease in the concentration of the anodic species. Interestingly, a peak is observed to form around 0 V that does not increase significantly in height from one time period to the next. Previous studies conducted on 3-methylcatechol (the product of 2,4-dimethylaniline hydrolysis), showed a similar trend (Brimecombe *et al.*, 2006), with the decrease in a prominent anodic peak between 0.55 V and 0.75 V, with the consequent formation of a smaller peak at 0 V

which was identified as being a catechol derivative. The electrochemical monitoring of the decrease of Reactive red in the batch reactor is represented in the line graph on figure 7.17.

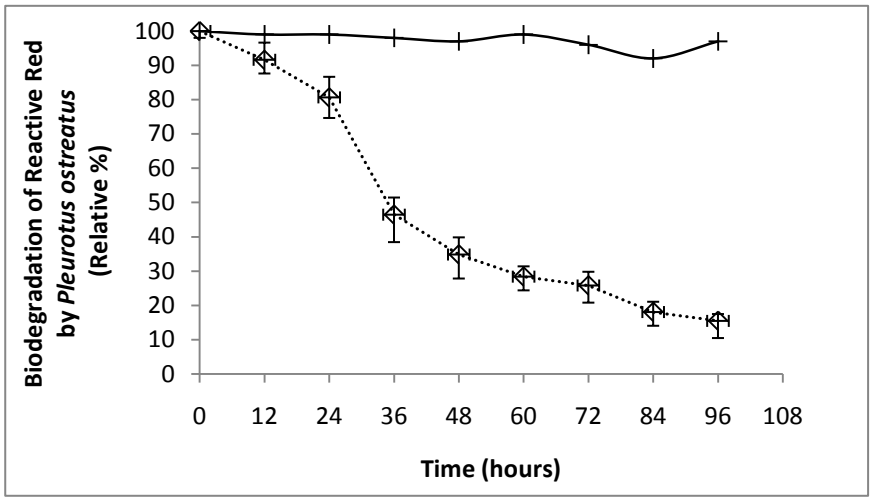

Figure 7.17 Relative percentage biodegradation efficacy of Reactive red by *Pleurotus ostreatus*, as measured using OSWV. *Key:* (+) control Reactive red sample with no *P. ostreatus*, (◊) Reactive red sample with *P. ostreatus* present. Scan rate: 100 $mV.s^{-1}$, GCE-*f*MWCNT vs. Ag|AgCl.

Figure 7.17 compares the breakdown of Reactive red by *P. ostreatus*, as compared to a negative control comprising only Reactive red with no *P. ostreatus* present. In the negative control sample [(+) on figure 7.17], no decrease in Reactive red concentration was expected. However in the presence of *P. ostreatus* the concentration of Reactive red was observed to decrease [(◊) on figure 7.17]. The recorded percentage biodegradation correlated well with the spectroscopically determined rate of degradation. For example, after 72 hours, 74 % degradation was recorded (Fig 7.17) compared to 83 % degradation observed spectroscopically (Fig 7.15). This also serves to highlight the sensitivity of the voltammetric detection method, where trace amounts of reactive red were measurable after 96 hours voltametrically (17 % effluent), while spectroscopic measurements had recorded 100 % decolourisation.

In figure 7.18 breakdown of Reactive red was initiated within the first 12 hours of acclimatisation, the highest rate of biodegradation observed to occur at 36 hours, with a near systematic decrease occurring between 36 to 96 hours. Similar studies record the highest degradation rate within the first 36 hours (Wang *et al.*, 2005). The rapid initiation of degradation is attributed to the rapid

acclimatization of *Pleurotus ostreatus* and availability of requisite enzymes typically involved in the cleavage of the azo dyes (Wesenberg *et al.* 2003, Forgacs *et al.* 2004, Nilsson *et al.* 2006).

7.5 Summary and Conclusions

Azo dye bioremediation by lignolytic fungi is well documented, however has only been monitored using spectroscopy. This limitation in the monitoring technique is problematic in many instances since turbidity of the real effluent samples interferes with the analyses. This issue was addressed in this study through the incorporation of an electrochemical approach. Accordingly, no sample pretreatment is required and the fungal biomass does not need to be removed prior to the analytical event, which is a prerequisite in many alternative diagnostic techniques. The distinctive anodic peak at 550 mV was utilized to electrochemically monitor the breakdown of Reactive red in the actual effluent. Additionally, no compounds that co-exist with Reactive red in the effluent were observed to interfere in the analysis. Application of the GCE-*f*MWCNTs showed promise in monitoring in situ the biodegradation of Reactive red in the effluent, with no sample pretreatment required, and with favourable performance compared to traditional spectroscopic methods. This preliminary study thus not only serves to exemplify the use of NME-GCEs in enhancing sensitivity of detection in real samples, but shows the feasibility of this approach for monitoring of degradation in complex media in the presence of biomass, warranting further investigations in future studies.

CHAPTER 8

CONCLUSIONS AND FUTURE RECOMMENDATIONS

8.1 Conclusions

The purpose of this study was two-fold: to explore the enhancement of nanomaterial modified electrodes and to test the feasibility and validity of these surfaces for target analytes of pharmaceutical and industrial relevance.

To this end, this study has provided a detailed examination of the optimisation of single-walled and multi-walled carbon nanotubes, and C_{60} fullerenes through functionalisation. Specifically, the study highlighted the importance of optimizing common procedures for CNT functionalisation, such as acid treatment, which impacts degree of surface functionalisation as well as on tubular structural integrity and hence performance of the nanomaterials in sensor applications. While this detailed study sought to resolve inconsistencies in the literature regarding CNT acid treatment, furthermore, the study provided new insight into the application of catechol for activation of SWCNT and MWCNT.

The study also provided the first voltammetric analysis of the anticancer drug wortmannin and the industrial dye Reactive red, serving as key target analytes for examination of the applicability of the nanomaterial modified electrodes (NME) designed in this study in a range of relevant matrices.

Through HRSEM, AFM, CV and EIS studies, the following key conclusions were reached:

1. Acid treatment of nanotubes (HNO_3:H_2SO_4 (1:3) *v/v*, sonication for time, *n*) is critical for optimised electrocatalytic performance of the sensor. Duration of the acid treatment affects the length of the nanotubes, as well as the amount of carboxylation occurring on the walls of the tubes. Over-exposure to the acid treatment results in the nanotubes losing their structural integrity, resulting in a loss of the sought after conductive properties. Shorter *f*MWCNTs did exhibit an order of organisation, as observed from the AFM images of MWCNTs functionalised for 9 hours. This observation of self assembly behaviour does hold promise in the form of reproducible sensor surfaces, for particular application in the bulk fabrication of sensor surfaces.
2. *f*SWCNTs undergo a more rigorous functionalisation than *f*MWCNTs which is most likely attributed to lower concentration of SWCNTs in the starting material. This results in

*f*SWCNTs ideal sensor performance being at 4 – 6 hours functionalisation, as opposed to 9 hours for MWCNTs.

3. Discrepancy exists in literature as to what the ideal acid treatment duration is. This study has, for the development of electrochemical sensor surfaces, normalised the optimisation time to 4 – 6 hours for *f*SWCNTS and 9 hours for *f*MWCNTs.
4. Electrochemical activation of the immobilised nanotube layer through cycling in catechol lowers the charge transfer resistance, R_{ct} therefore increasing the heterogeneous rate transfer, k_{app} which results in an increased current response, I_p.
5. Immobilisation of C_{60} onto a GCE was visualised as large aggregates, resulting in lowered k_{app} and ultimately smaller I_p outputs. Partial reduction of the C_{60} immobilised layer did decrease the R_{ct} marginally, which would be due to the incorporation of K^+ between aggregates of C_{60} on the electrode surface.

Each of the NMEs was further investigated through their performance in the detection of 2 different target analytes, namely wortmannin and reactive red. The purpose of these as target analyte to be used in this study was based on an existing demand. In the case of wortmannin, a probe that could monitor the concentration of wortmannin being synthesized in a bioreactor as well as in relevant biological matrices was proposed, while for reactive red an *in situ* compatible test for the intermittent monitoring of the target compound in effluent before and after bioremediation treatment would prove to be useful.

Of core importance was the examination of the performance of the NMEs for the detection of the target analytes in buffer and growth media (or effluent) given the particular demands of such analyses for rapid monitoring, low fouling of the sensor and minima pretreatment.

For the electrochemical detection of wortmannin, the following key features were established:

1. Wortmannin yields an electrochemically irreversible cathodic peak. The reduction of wortmannin affords a 4-electron mechanism with a diffusion coefficient of 1.19×10^{-7} $cm^2.s^{-1}$ in an ECE mechanism, with 2 electrons in the RLS

2. Wortmannin detection in Britton-Robinson buffer (pH 4.0) was achieved with a LOD of 0.102 nmol.cm^{-3} obtained at a GCE modified with *f*MWCNTs (functionalised for 9 hours). This value is more sensitive than a GCE (5.667 nmol.cm^{-3}) and more sensitive than the published LOD obtained using HPLC (0.233 nmol.cm^{-3}).
3. Wortmannin shows instability under physiological conditions, which is accelerated at higher alkaline conditions. Voltammetric methods allowed for the monitoring of wortmannin hydrolysis with the potential to shed new light on real time behavioural studies on the interaction with potential inhibitors as well as the fate of wortmannin, due to external factors such as pH.
4. A *f*MWCNT surface exhibited marked surface regeneration with subsequent scans. The lowered effect of surface passivation makes *f*MWCNTs an ideal candidate for a sensor scaffold for application in continuous monitoring systems for wortmannin.
5. The electrochemical reduction of wortmannin is minimally affected by known growth medium components, when the electrode is modified with *f*MWCNTs while an unmodified GCE was rapidly passivated with co-existing compounds.
6. The inclusion of an electrochemically based continuous monitoring system in a bioreactor during the biosynthesis of wortmannin, or as a single use electrode surface capable of accurately assessing the integrity of the wortmannin is thus highly feasible. This application would greatly influence the efficiency and accuracy of wortmannin research and associated developmental projects.

For the electrochemical assessment of the performance of NMEs for the electrochemical detection of Reactive red in industrial effluent, the following observations were made:

1. RR exhibits a prominent anodic peak that can be quantified with a LOD of ~ 10 % stock effluent concentration, at an unmodified GCE, which is lowered to ~ 3 % with the addition of *f*MWCNTs.
2. RR can be detected in the spent dye effluent, by employing GCE-*f*MWCNTs, without the need for sample preparation or the addition of a supporting electrolyte.
3. The breakdown of RR can be monitored electrochemically, the fate of which correlates favourably with what had been observed in literature by employing spectroscopic techniques.
4. The biodegradation of the RR by *Pleurotus ostreatus* is of prominent importance in the decolourisation and degradation of the effluent. The employed electrochemical approach

showed the ability to detect trace levels of RR, which would go undetected using spectroscopic approaches.

In conclusion, while this thesis covered fundamental approaches to sensor design through nanomaterial modified electrodes, the applications thereof are evident not merely in achieving sensitive target analyses, but as a valuable tool in shedding light for fundamental understanding of biological and biotechnological processes.

8.2 Future Recommendations

The particular outcome of this research has shown promise for continued research and development through integration thereof into the development of a variety of applications.

The utilisation of *f*MWCNTs for further developmental work into the construction of electrode surfaces is highly advised, based on the satisfactory and promising outcomes shown in this study for *f*MWCNTs incorporation into sensor construction.

Unless as produced SWCNTs can be obtained in larger quantities than 7 %, their feasibility for large scale industrial sensor application is limited. Additionally, alternative methods of constructing electrode surfaces with the inclusion of C_{60} could potentially be promising. An interesting study would involve assessing different methods of constructing NMEs based on C_{60} and SW/MWCNTs immobilisation or incorporation.

Some additional recommendations for each of Reactive red and wortmannin are summarised below:

For Reactive red:

- Obtain pure biodegradation products to confirm their identity.

- Establish a quantitative detection protocol for RR in buffer systems and compare sensitivity and reproducibility for its detection between pure RR detection and RR in effluent.

- Apply to the tannery working model (effluent storage tank) and monitor over time.

- This study could be used as an easy test to assess the degradation ability and rates of a variety of microbes, and could ultimately be used as a model for further such bioremediation detection processes.

For Wortmannin:

-The rapid hydrolysis of wortmannin under alkaline conditions, in addition to the biological hydrolysis that occurs in the bioreactor demands more information on a continuous basis on its fate, that can be obtained from employing the electrochemical protocols established in these studies. The information gained from these ongoing studies could greatly benefit the pharmaceutical companies synthesizing wortmannin.

- Further elucidation of the breakdown pathways for wortmannin, by studying the already established electrochemical breakdown, in conjunction with pure forms of the breakdown intermediates and products.

- Apply to the actual biosynthesis reactors and monitor wortmannin production and degradation.

- Standardise the acid treatment process for nanomaterials functionalization.

Future work on this topic should seek to develop sensor surfaces that can be validated in conformation with diagnostics regulations, for the development of technology that could be scaled-up and potentially commercialized. Based on the outcomes of this study, the feasibility of commercialization of this technology is not necessarily governed by the technology, but rather by the complexities involved in the commercialization process

REFERENCES

Abadulla E, Tzanov T, Costa S, Robra K-H, Cavaco-Paulo A, Gu¨bitz GM. (2000) Appl. Environ. Microbiol. 66:

Abdel-Hamid R (1988) Monatshefte für Chemie 119: 429.

Agarwal, K.C. 2001, book of Environmental Biology, Nidi Pub. Ltd. Bikaner.

Ajayan PM (1999) Chem. Rev. 99: 1787.

Alcock SJ, Turner APF (1994) Eng. Med. Biol. 13: 319.

Allen BL, Kichambare PD (2007) Adv. Mater. 19: 1439.

Bae E, Kim ND, Kwak BK, Park J, Lee J, Kim Y, Choi K, Yi J (2010) Carbon 48: 3676.

Banerjee S, Wong SS (2002) J. Phys. Chem. B. 106: 12144.

Banks CE, Croosley A, Salter C, Wilkins SJ, Compton RG (2006) Angew. Chem. Int. Ed. 45: 2533.

Banks CE, Davies TJ, Wildgoose GG, Compton RG (2005) Chem. Commun. 829.

Banks CE, Moore RR, Davies TJ, Compton RG (2004) Chem. Commun. 16: 1804–1805.

Barazzouk S, Hotchandani S, Kamat PV. (2002) J. Mater. Chem. 12: 2021.

Bard AJ, Faulkner LR (1980) Electrochemical methods. Fundamentals and applications. Canada: John Wiley & Sons, Inc, pp 7-44, 86-91, 119-130.

Barisci JN, Wallace GG, Baughman RH (2000) J. Electroanal. Chem. 488: 92.

Barsoukov E, MacDonald JR (Eds.)(2005)Impedance Spectroscopy: theory, experiment and applications. Wiley Interscience Publications (2nd edition).

Batchelor-McAuley C, Wildgoose GG, Compton RG, Shao L, Green MLH (2008) Sensors and Actuators B 132: 356.

Baughman RH, Zakhidov A, de Heer WA (2002) Science. 297: 787.

Bhushan B (Ed.) (2004) Springer Handbook of Nanotechnology. Springer-Verlag Germany. Pp 39 – 88.

Bockris JO'M, Reddy AKN, Gamboa-Aldeco M (2000) Modern Electrochemistry 2A. Fundamentals of Electrodics, 2nd Ed. Kluwer Academic/Plenum Publishers, Pp.1083, 2000.

Bosi S, Da Ros T, Spalluto G, Prato M (2003) Eur. J. Med. Chem. 38: 913.

Borchert M, Libra JA (2001) Biotech. Bioeng. 75(3): 313.

Brian PW, Curtis PJ. Hemming HG, Norris GLF (1957).Trans. Br. Mycol. Soc. 40: 365.

Brimecombe RD, Fogel R, Limson JL (2006) J. Agric. Food Chem. 54: 8799.

Britto PJ; Santhanam KSV, Alonso V, Rubio A, Ajayan PM (1998) Adv. Mater. 11: 154.

Britton HTS, Robinson RA (1931) 1456.

Brown ER, Large RF (1971) Physical Methods of Chemistry, Vol.1(IIA): Electrochemical Methods. Weissberger A, Rossiter B. (Eds.) Wiley-Interscience, New York.:

Bumpus JA, Aust SD (1987) BioEssays 6: 166-170

Burghard M (2005) Surf. Sci. Rep. 58: 1.

Campbell JK, Sun L, Crooks RM (1999) J. Am. Chem. Soc. 121: 3779.

Carliell CM, Barclay SJ, Naidoo N, Mulholland DA, Seniors E (1995) Water SA 21(1): 61.

Carlisle JJ, Wijayawardhana CA, Evans TA, Melaragno PR, Ailin- Pyzik IB (1996) J. Phys. Chem. 100 (38): 15532.

Caro CA, Bedioui F, Zagal JH (2002) Electrochim. Acta. 47: 1489.

Chandra U, Gilbert O, Swamy BEK, Bodke YD, Sherigara BS (2008) Int. J. Electrochem. Sci. 3: 1044.

Chattopadhyay D, Galeska L, Papadimitrakopoulos F (2003) J. Am. Chem. Soc. 125: 3370.

Chem. Phys. Lett. 221: 53.

Chen J, Hamon MA, Hu H, Chen Y, Rao AM, Eklund PC, Haddon RD (1998) Science. 282: 95.

Chen J, Rao AM, Lyuksyutov S, Itkis ME, Hamon MA, Hu H (2001) *J Phys Chem.* 105: 2525.

Chen JH, Li WZ, Wang DZ, Yang SX, Wen JG, Ren ZF (2002) Carbon 40: 1193.

Chen XL, Li WS, Tan CL, Li W, Wu YZ (2008) 184: 668.

Chou SG, Plentz F, Jiang J, Saito R, Nezich D, Ribeiro HB, Jorio A, Pimenta MA, Samsonidze GG, Santos AP, Zheng M, Onoa GB, Semke ED, Dresselhaus G, Dresselhaus MS (2005) Phys. Rev. Lett. 94:127402.

Chung K.-T, Stevens, SE (1993) Environ. Toxicol. Chem. 2: 2121.

Coleman JN, Khan U, Blau WJ, Gun'ko YK (2006) Carbon. 44: 1624

Compton RG, Spaman RA, Riley DJ, Wellington RG, Eklund JC, Fisher AC, Green MLH, Doothwaite RE, Stephens AHH, Turner J (1993) Electroanal. Chem. 344: 235.

Creemer LC, Kirst HA, Vlahos CJ, Schultz RM (1996) J. Med. Chem. 39: 5021.

Csiszár M, Szűcs Á, Tölgyesi M, Mechler Á, Nagy JB, Novák M (2001) J. Electroanal. Chem. 497: 69.

DeRosa MC**,** Crutchley RJ (2002) Coord. Chem. Rev. 233: 351.

D'Souza F, Rogers LM, O'Dell ES, Kochman A, Kutner W (2005) Bioelectrochemistry 66: 35.

Dennison MJ, Turner AFP (1995) Biotechnol. Adv. 13

Dillon AC, Jones KM, Bekkedahl TA, Kiang CH, Bethune DS, Heben MJ (1997) Nature 386: 387.

Drake GWF, Cassar MM (Eds.) (2006) Springer handbook of atomic, molecular and optical physics. Springer Science and Business Media Inc. Germany. Pp 594 – 596.

Dujardin E, Ebbesen TW, Krishnan A, Treacy MMJ (1998) Adv. Mater. 10: 611.

Ebbesen TW (1997) J. Phys. Chem. Of Solids 58 (11): 1979.

Echegoyen L, Echegoyen LE (1998) Acc. Chem. Res. 31: 593.

El-Samamody ES, Demadis KD, Meyer TJ, White PS (2001) Inorg. Chem. 40(15): 3677.

Engstrom CE (1982) Anal. Chem. 54: 2310.

Engstrom RC, Strasser VA (1984) Anal. Chem. 56: 136.

Erkurt EA, Unyayar A, Kumbur (2007) Process Biochem. 42(10): 1429.

Estrade-Szwarckopf H (2004) Carbon 42: 1713.

Forgacs Em Cserhati T, Oros G (2004) Environ. Int. 30(7): 953.

Frackowiak E, Delpeux S, Jurewicz K, Szostak K, Cazorla-Amoros D, Béguin (2002) Chem. Phys. Lett. 361: 35.

Froudakis GE (2001) Nano. lett. 1: 531.

Gavalas VG, Chaniotakis NA (2000) Anal. Chim. Acta.409: 131.

Geraldo DA, Togo CA, Limson J, Nyokong T (2008) Electrochim. Acta 53: 8051

Gharbi N, Pressac M, Hadchouel M, Szwarc H, Wilson SR, Moussa F (2005) *Nano. Lett.* 5(12): 2578

Gong K, Yan Y, Zhang M, Su L, Xiong S, Mao L (2005) Anal. Sci. 21: 1383.

González-Guerrero M; Melville LH; Ferrol N; Lott JNA; Azcón-Aguilar C; Peterson RL (2008) Canadian J Microbiol. 54(2): 103.

Gooding JJ (2005) Electrochim. Acta. 50: 3049.

Gooding JJ, Chou A, Liu J, Losic D, Shapter JG, Hibbert DB (2007) Electrochem. Commun. 9: 1677.

Goyal RN, Gupta VK, Chatterjee S (2009) Biosens. And Bioelectron. 1649.

Goyal RN, Gupta VK, Oyama M, Bachheti N (2007a) Talanta. 71(3): 1110.

Goyal RN, Gupta VK, Bachheti N (2007b) Anal. Chim. Acta 597(1): 82.

Goyal RN, Kaur D, Singh SP, Pandley AK (2008) Talanta. 75: 63.

Goyal RN, Singh SP (2006a) Electrochim. Acta 51(15): 3008.

Goyal RN, Singh SP (2006b) Talanta. 69(4): 932.

Goyal RN, Gupta VK, Oyama M, Bachheti N (2007) *Talanta.* 7(3): 1110.

Goyanes S, Rubiolo GR, Salazar A, Jimeno A, Corcuera MA, Mondragon I (2007) Diamond & Related Materials 16: 412.

Griese S, Kampouris DK, Kadara RO, Banks CE (2008) Electrochem. Commun. 10: 1633.

Grobert N (2007) Materials Today. 10(1-2): 28.

Guldi DM, Prato M (2000) Acc. Chem. Res. 33: 695.

Haddon RC (1992) Acc. Chem. Res. 25(3): 127.

Hansen SH, Olsson A, Casanova JE (1995) The Journal of Biological Chemistry 270(47): 28432.

Hao OJ, Kim H, Chiang PC (2000) Crit. Rev. Environ. Sci. Technol.30: 449.

Heng LY, Chou A, Yu J, Chen Y, Gooding JJ (2005) Electrochem. Commun. 7: 1457.

Herrera JE, Resasco DE (2003) Chem. Phys. Lett. 376: 302.

Hill DE, Lin Y, Rao AM, Allard LF, Sun YP (2002) Macromolecules. 35: 9466.

Hirsch A, Brettreich M (2005) Fullerenes: Chemistry and Reactions. Wiley-VCH Verlag GmbH & Co. KGaA. Weinheim. Germany.

Hsu CH, Mansfeld F (2001) Corrosion 57: 747.

Holleran JL, Egorin MJ, Zuhowski EG, Parise RA, Musser SM, Pan S-s (2003) Analytical Biochemistry 323: 19.

Holleran JL, Eiseman JJL, Parise RA, Musser SM, White KD, Covey JM, Forrest GL Pan S-s (2004) Drug Metab. Dispos. 32: 490.

Hou H, Zhou J, Wang J, Du C, Yan B (2004). Process Biochem. 39: 1415.

Hou P-X, Liu C, Cheng H-M (2008) Carbon 46: 2003.

Ibrahim MS, El-Maazawi MS, Al-Magboul KM, Kamal MM (2001) Determination of amitraz pesticide by adsorptive stripping voltammetry on the hanging mercury drop electrode. Mikrochim. Acta. 137: 215-220.

Iijima S (1991) Nature. 354: 56.

Iijima SS, Ichihashi T (1993) Nature. 363(6430): 603.

Isosaki M (2004) Biochem. Biophys. Res. Comm. 324(4): 1406.

Jang IY, Muramatsu H, Park KC, Kim YJ, Endo M (2009) Electrochem. Commun. 11: 719.

Jang JW, Lee DK, Lee CE, Lee TJ, Lee CJ, Noh SJ (2003) Solid State Commun. 127: 29.

Jehoulet C, Bard AJ, Wudl F (1991) J. Am. Chem. Soc. 113: 5456.

Jehoulet C, Obeng YS, Kim YT, Zhou F, Bard AJ (1992) J. AM. Chem. Soc. 114(11): 4237.

Jiang Q, Zhao Y, Lu XY, Zhu XT, Yang GQ, Song LJ, Cai YD, Ren XM, Qian L (2005) Chem. Phys. Lett. 410: 307.

Jurewicz K, Babel K, Peitrzak R, Delpeux S, Wachowska H (2006) Carbopn 44: 2368.

Jurkschat K, Ji X, Crossley A, Compton RG, Banks CE (2007) Analyst. 132: 21.

Kachoosangi RT, Wildgoose GG, Compton RG (2006) Electroanalysis 18(8): 741.

Kadish KM, Smith KM, Guilard R (Eds.)(2003) The porphyrin handbook. Volumes 15-20:Chapters 97-122. Academic Press, Boston.

Kalsberg WA, Thorp HH (1991) J. Electroanal. Chem. 314: 363.

Kapdan K, Kargi F (2002). Process Biochem. 37: 973.

Kastner J, Pichler T, Kuzmany H, Curran S, Blau W, Weldon DN, Delamesiere M, Draper S, Zandbergen H (1994)

Kawasaki S, Iwai Y, Hirose M (2009) Mat. Res. Bull. 44(2): 415.

Koehne J, Li J, Cassell AM, Chen H, Ye Q, Ng HT, Han J, Meyyappan M (2004) J. Mater. Chem. 14: 676.

Kimura K, Hattori S, Kabuyama Y, Shizawa Y, Takayanagi J, Nakamura S, Toki S, Matsuda Y, Onodera K, Fukui Y (1994) J. Biol. Chem. 18961.

Kissinger PT, Heineman WR (Eds). (1996) Laboratory Techniques in Electroanalytical Chemistry. Marcel Dekker, Inc. New York. Pp 165-194.

Kroto HW, Heath JR, O'Brien SC, Curl RF, Smalley RE (1985) Nature. 318: 162.

Kuznetsova A, Mawhinney DB, Naumenko V, Yates Jr JT, Liu J, Smalley RE (2000) Chem. Phys. Lett. 321: 292Lawrence et al (2005)

Lamprecht C, Liashkovich I, Neves V, Danzberger J, Heister E, Rangl M, Coley HM, McFadden J, Flahaut E, Gruber HJ, Hinterdorfer P, Kienberger F, Ebner A (2009) Nanotechnology. 20: 434001.

Laviron E (1979) J. Electroanal. Chem. 97: 135.

Lee RS, Kim HJ, Fischer JE, Thess, Smallely RE (1997) Nature 388: 255.

Leznoff CC, Lever ABP (Eds.)(1996) Phthalocyanines: properties and applications vol 4. VCH Publishers, New York.

Li X-y, Cui Y-h, Feng Y-j, Xie Z-m, Gu J-D (2005) Wat. Res. 39: 1972.

Li Y, Li H, Jia X, Hao J, Liu W (2006) Carbon. 44: 894.

Lin Y, Rao M, Sadanadan B, Kenik EA, Sun YP (2003) J. Phys. Chem. B. 106: 1294.

Liu K, Gao S (2005) Phys. Rev. Lett. 95: 226102.

Liu J, Rinzler AG, Dai H, Hafner JH, Bradley RK, Boul PJ, Lu A, Iverson T, Shelimov K, Huffman CB, Macias F, Shon YS, Randall T, Colbert DT, Smalley RE (1998) Science. 280: 1253.

Luong JHT, Male KB, Glennon JD (2008) J. Biotechnology Advances. 26: 92.

Marken F, Gerrard ML, Mellor IM, Mortimer RJ, Madden CE, Fletches S, Holt K, Foord JS, Dahm RH, Page F (2001) Electrochem. Commun. 3: 177.

Martinez-Calatayud J (1996) Flow injection analysis of pharmaceuticals: automation in the laboratory. Taylor & Francis Group, London UK.

Mazloum-Ardakania M, Taleata Z, Beitollahia H, Naeimib H (2010) J. Iran. Chem. Soc 7(1): 251.

M^{c}Cloud TG, Burnette A, Collins R, Graf S, Zhu J, Reeb S, Testerman R, Wang S-D, Newman DJ (1999) Development of a process for the production of the anticancer Lead compound Wortmannin by fermentation of *Penicillium duclauxii*.

Merkoc A, Pumera M, Llopis X, Pérez B, del Valle M, Alegret S (2005) Trends Anal. Chem. 24: 826.

Merkoci A (2006) Microchim. Acta. 152: 157.

Moore RR, Banks CE, Compton RG (2004) Anal. Chem. 76: 2677.

Musameh M, Lawrence NS, Wang J (2005) Electrochem. Commun. 7: 14.

Nicholson RS, Shain I (1964) Anal. Chem. 53: 2258.

Nigoić B et al. (2001) J. Pharm. Biomed. Anal. 26: 987.

Nilsson I, Möller A, Mattiasson B, Rubindamayugi MST, Welander U (2006). Enzyme Microb. Technol. 38: 94.

Nkosi D, Ozoemena KI (2008) Electrochim. Acta. 53: 2782.

Noel M, Vasu KI (1990) Cyclic voltammetry and the frontiers of electrochemistry, Aspect Publications, London.

Novotny C, Rawal B, Bhatt M, Patel M, Sasek V & Molitoris HP (2001) J. Biotechnol. 89: 113.

Nugent JM, Santhanam KSV, Rubio A, Ajayan PM (2001) Nano Lett. 1: 87.

Odom TW, Huang JL, Kim P, Lieber CM (1998) Nature. 391: 62.

Ozoemena KI, Nkosi D, Pillay J (2008) Electrochim. Acta. 53: 2844.

Ozoemena KI, Nyokong T, Nkosi D, Chambrier I, Cook MJ (2007) Electrochim. Acta 52: 4132.

Ozsoy HD, Unyayar A, Mazmancı MA (2005) Biodegradation 16: 195.

Padgornik H, Grgic I, Predih A(1999) Chemosphere 38 (6): 1353..

Palmieri G, Cennamo G, Sannia G (2004) Enz. Microbiol. Chen. 36(1): 17.

Pelekourtsa A, Missaelidis N, Jannakoudakis D (1997) Chim. Chron. 26: 39.

Pillay J, Ozoemena KI (2009) Electrochim. Acta 54: 5053.

Platzek T, Lang C, Grohmann G, Gi US, Baltes W (1999) Human Exp. Toxicol.18: 552.

Pohanka M, Skladal P, Kroca M (2007) Def. Sci. J. 57(3):185-93.

Retter U, Lohse H, Scholz F (Eds). (2002) Electrochemical impedance spectroscopy in electroanalytical methods. Springer, Berlin Heidelberg New York.

Robinson T, McMullan G, Marchant R, Nigam P (2001).Biores. Technol. 77: 247.

Rubianes MD, Rivas GA (2003) Electrochemistry Communications. 5: 689.

Sabatani E.; Rubinstein I, Maoz R, Sagiv J (1987) J. Electroanal. Chem. 219: 365.

Sano M, Kamino A, Okamura J, Shinkai S (2001) Langmuir 17: 5125.

Scharff P (1998) Carbon. 36(5-6): 481.

Shaffer MSP, Fan X, Windle AH (1998) Carbon. 36(11): 1603

Shaul GM, Holdsworth TJ, Dempsey CR, Dostal KA (1991) Chemosphere 22: 107.

Sherigara BS, Kutner W, D'Souza F (2003) Electroanalysis 15: 753.

Sjukic B, Banks CE, Compton RG (2006) Nano. Lett. 6: 1556.

Skunik M, Chojak M, Rutkowska IA, Kulesza PJ (2008) Electrochim. Acta 53: 3862.

Sotiropoulou S, Chaniotakis NA (2003) Anal. Bioanal. Chem. 375: 103.

Stephens PW (Eds.)(1993) Physics and Chemistry of fullerenes. World Scientific Publishing Co. (Pty) Ltd. USA. Pp. 208 – 209.

Strano MS, Dyke CA, Usrey ML, Barone PW, Allen MJ, Shan HW, Kittrell, Hauge RH, Tour JM, Smalley RE (2003) Science 301: 1519.

Szűcs A (2008) J. Electroanal. Chem. 623: 41.

Szűcs A, Loix A, Nagy JB, Lamberts L (1996) J. Electroanal. CHem. 402: 137.

Tan WT, Bond AM, Ngooi SW, Lim EB, Goh JK (2003) Anal. Chim. Acta. 491: 181.

Tekleab D, Czerw R, Carrol DL, Ajayan PM (2000) Appl. Phys. Lett. 76: 3594.

Trojanowicz M (2006) Trends in Analytical Chemistry. 25(5): 480.

Tsai Y-C, Li S-C, Liao S-W (2006) Biosens. Bioelectron. 22:495.

Valcárcel M, Simonet BM, Cardena S, Suarez B (2005) Anal. Bioanal. Chem. 382: 1783.

Vamvakaki V, Chaniotakis NA (2007) Sensors and Actuators B. 126: 193

Vamvakaki V, Tsagaraki K, Chaniotakis NA (2006) Anal. Chem. 78: 5538.

Vandevivere PC, Bianchi R, Verstraete W (1998) J. Chem. Technol. Biotechnol. 72: 289.

Vyas BR, Molitoris HP (1995) Appl. Environ. Microbiol. 61: 3919

Wang J (1994) Analytical Electrochemistry. VCH Publishers Inc. New York.

Wang J, Musameh M (2003) Carbon nanotube/teflon composite electrochemical sensors and biosensors. Anal. Chem. 75:2075-2079.

Wang Y, Iqbal Z, Malhotra SV (2005) Chem. Phys. Lett. 402: 96.

Wang J (2005) Electroanal. 17: 7.

Ward Jones SE, Campbell FW, Baron R, Xiao L, Compton RG (2008) J. Phys. Chem. C 112(46): 17820.

Wesenberg D, Kyriakides I, Agathos SN (2003) Biotechnol. Adv. 22(1-2): 161.

White NM, Turner JD (1997) Meas. Sci. Technol. 8: 1.

Wildgoose GG, Wilkins SJ, Williams GR, France RR, Carnahan DL, Jiang L, Jones TGJ, Compton RG (2005)

Wildgoose GG, Banks CE, Leventis HC, Compton RG (2006) Microchim. Acta 152: 187.

Wiles PG, Abrahamson J (1978) Carbon 16: 341.

Wipf P, Halter RJ (2005) Org. Biomol. Chem. 3: 2053.

Wymann WP, Zvelebil M, Laffar M (2003) Trends in Pharmacological Sciences.24(7): 366.

Xia JL, Chen F, Wiktor P, Ferry DK, Tao NJ (2010) Nano. Lett. 10(5):2144.

Xiao L, Wildgoose GC, Compton RG (2009) Sensors Actuators B 138: 524.

Xu J, Yudasaka M, Kouraba S, Sekido M, Yamamoto Y, Iijima S (2008) Chem. Phys. Lett. 461: 189.

Yadegari H. Jabbari A, Heli H, Moosavi-Movahedi AA< Karimian K, Khodadadi A (2008) Electrochim. Acta.53:

Yuan C, Shen L, Li D, Zhang F, Lu X, Zhang X (2010) Applied Surface Science 257: 440.

Yuan H, Barnes KR, Weissleder R, Cantley L, Josephson L (2007) Chemistry & Biology 14: 321.

Zare HR, Namazian M, Nasirizadeh N (2005) J. Electroanal. Chem. 584: 77.

Zare HR, Nasirizadeh N (2007) Electrochim. Acta 52: 4153.

Zhang J, Zou H, Qing Q, Yang Y, Li Q,, Liu Z, Guo X, Du Z (2003) J. Phys. Chem. B. 107: 3712.

Zhao J, Buldum A, Han J, Lu JP (2002) Nanotechnology. 13: 195.

Zhou F, Liu Z, Yu B, Chen M, Hao J, Liu W, Xue Q (2004) Surface Science 561: 1.

Zhou F, Yau SL, Jehoulet C, Laude DA, Guan Z, Bard AJ (1992) J. Phys. Chem. 96(11):4160-4162.

Zhou M, Guo J, Guo L-p, Bai J (2008) Anal. Chem. 80: 4642.